Pore Structure and Column Efficiency of Silica Monoliths in High Performance Liquid Chromatography (HPLC)

Dissertation zur Erlangung des Grades
„Doktor der Naturwissenschaften“
(Dr. rer. nat.)

vorgelegt dem Fachbereich Chemie und Pharmazie
der Johannes Gutenberg-Universität Mainz

von

Magister Romas Skudas
geboren in Kaunas, Litauen

April 2009, Mainz

Die vorliegende Arbeit wurde in der Zeit von Oktober 2004 bis April 2009 am Institüt für Anorganische Chemie und Analytische Chemie der Johannes Gutenberg-Universität Mainz durchgeführt.

Dekan:

Erstgutachten:
Zweitgutachten:

Tag der mündlichen Prüfung:

Zusammenfassung

Es wurde fünf verschiedene, physikalisch-chemische Methoden zur Charakterisierung der Porenstruktur von Silica Monolithen angewandt und ihre Ergebnisse kritisch evaluiert, insbesondere im Hinblick auf die Trennleistung monolithischer Säulen in der HPLC.

Es wurden drei verschiedenen Methoden für die Charakterisierung der Porenstruktur der Mesoporen von Silica Monolithen (mittlerer Porendurchmesser $2 < pd < 50$ nm) eingesetzt: a) Stickstoffsorptionsmessungen mit Auswertung nach die klassische Barrett, Joyner und Halenda (BJH) Methode und Non-Linear Density Functional Theory (NLDFT) – Methode; b) Die Inverse Größenausschluß-Chromatographie (ISEC) mit implementierte zwei Porenmodelle (Parallel Pore Model, PPM, sowie des Pore Network Models, PNM); c) und die Quecksilber-Porosimetrie. Alle drei angewandten Methoden ergaben nützliche Informationen mit den erwähnten Einschränkungen. Bevorzugt wurde die ISEC, weil diese Methode sowohl die Volumen- als auch die Anzahlverteilung der Poren liefert, sowie zusätzlich die Porenkonnektivität.

Es wurden zwei verschiedenen Methoden - die Quecksilber-Porosimetrie und die Flüssig-Penetrationsmethoden eingesetzt für die Charakterisierung der Porenstruktur der Durchflußporen (Makroporen mit $pd >> 50$ nm) von Silica Monolithen und ihre Ergebnisse evaluiert. Die Ergebnisse beider genannten Methoden wurden verglichen mit Ergebnissen Image-Analyse mit Hilfe der Raster-Elektronenmikroskopie. Hierbei zeigte sich, dass ein Vergleich bzw. eine Übereinstimmung der Ergebnisse sehr stark vom gewählten Porenmodell abhängt.

Im zweiten Teil der Arbeit wurde der Versuch unternommen, Rückschlüsse aus den Ergebnissen der Porenstrukturuntersuchungen auf die chromatographische Trennleistung der Monolithen zu gewinnen.

Zunächst deutete ein hohe Porenkonnenktivität (aus ISEC-Messungen) und ein geringes Entrapment (aus der Quecksilber-Porosimetrie) auf eine gute Kinetik des Massentransports hin, die auch experimentell in chromatographischen Messungen durch Ermittlung der Abhängigkeit der theoretischen Bodenhöhe von der linearen Flußgeschwindigkeit verifiziert wurde.

Die Ergebnisse erlaubten weiterhin in erster Nährung eine Abschätzung der optimalen Parameter der Porenstruktur von Monolithen bei der Flussigphasen-Trennung in der HPLC. Ein Ergebnis war, dass der durchschnittliche Porendurchmesser der Mesoporen aus der Anzahlverteilung etwa eine Größenordung größer sein sollte als der Molekülradius der zu

trennenden Komponenten. Das heißt, dass für die Trennung von Peptiden und erst recht von Proteinen entsprechend große Mesoporen oder sogar Makroporen im Monolithen vorhanden sein müssen.

Im Hinblick auf die Trennleistung von monolithischen Säulen ist nicht der durchschnittliche Durchflußporendurchmesser entscheidend, sondern das Oberflächen- zu Volumenverhältnis des Kiesegelgerüstes, das die Mesoporen enthält, sowie die Porosität der Makroporen und Mesoporen entscheidend sind Die Trennleistung nimmt zu mit abnehmendem Durchmesser der Durchflußporen, abnehmender Porosität der Durchflußporen und mit zunehmender Gesamtporosität des Monolithen. Allerdings sind diese Aussagen eingeschränkt bedingt durch die Heterogenität der monolithischen Säulen. Für die maximale Säulentrennleistung ist ein Durchmesser des Kieselsäureskeletts von ungefähr 0, 5 µm erforderlich, weiterhin eine homogene Verteilung der Durchflußporen.

Table of Contents

1. Introduction and objectives

High performance liquid chromatography (HPLC) is known to be the most versatile and effective separation method, which is able to resolve complex mixtures being composed of a variety of compounds and different structures. It is well established as a routine analytical platform in pharmaceutical industry, chemical industry and research institutions.

Chromatography is a separation of molecules based on the differences in their structure and/or composition. In general, chromatography involves moving a mixture of molecules to be separated over a stationary phase. If the molecules in the mixture have different interactions with the stationary phase, this would lead to resolution (separation). The first separations were performed at late 19th century [1, 2]. In 1903 M. Tswett proposed the term "Chromatography" for the isolation of chlorophyll constituents [3]. Soon it was recognized that specific separations could be performed only on more reproducible and more selective stationary phases [1, 4]. This improvement was possible via reduction of particle size and the increase of specific surface area [5]. The optimization of stationary phases led to the development of HPLC hardware, operating the separations at higher velocities and constant flow rates. Despite of extensive research on adsorbent improvement and column development it is a fact that the most common stationary phase is n-octadecyl bonded silica with an average particle diameter between 3 and 5 μm packed into stainless steel columns of a length between 50 to 250 mm and inner diameter of 4.0 or 4.6 mm applied in Reversed Phase HPLC.

Although a variety of other types of columns and separation modes are available other then the n-octadecyl bonded porous silica mode, the major intrinsic disadvantage of the porous particles is not yet solved – namely: How to overcome the slow diffusion of analytes in the pores of the particles which slows down the kinetics of the separation process? This becomes an even more stringed issue when high molecular mass samples, for example biopolymers, are intended to be resolved. A solution might be monolithic columns with a continuous bed that offer significant advantages over particle packed columns, namely, to increase the speed of separation at a lower column pressure drop than particle packed columns.

St. Hjerten was the first, who used the polymeric monoliths for the fast separation of biopolymers [6.], though the usefullness of monoliths as supports was already recognized in catalysis [7, 8] where their regular and open channels system provided a full access to the inner surface and generated a low-pressure drop as compared to packed reactors. Hjerten's work in polymeric monoliths was followed by T.Tennikova and F. Svec [9], while N. Shoga

and K. Nakanishi were the first ones who developed a template-supported synthesis for silica monoliths

[10-30]. These silica-based monoliths are composed of a single porous piece and exhibit two types of pores: flow-through pores in the micrometer (μm) size range (corresponding to the interparticle void space in the particulate supports) and mesopores in the nanometer (nm) size range (corresponding to the intraparticle pores in the particulate supports)(Fig.1). The ability to control and adjust both pore size regimes permits to design columns with the adequate mass transfer kinetics for defined analytes and allows controlling the hydrodynamic properties of the monolithic silica column such as the column back pressure and the flow rate (see publication I) giving an insight into the search for the analyte diffusion enhancement.

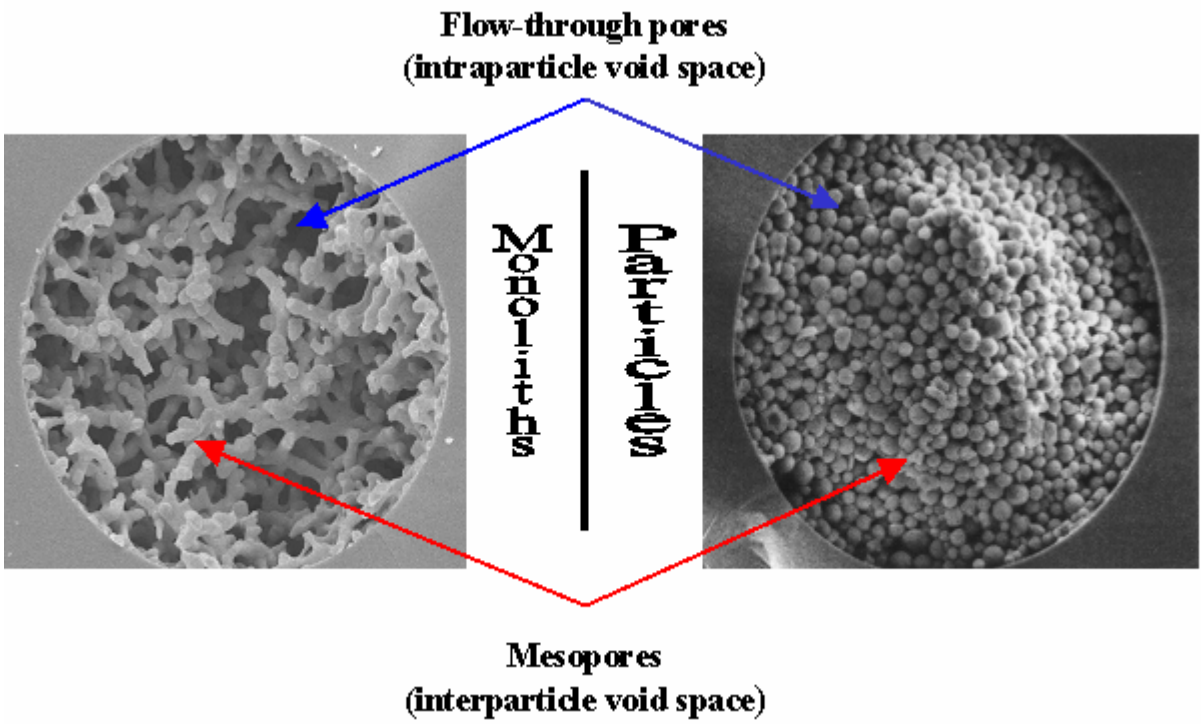

Figure 1. The structural differences of the monolithic and particulate stationary phase shown by the cross section of a particle packed (right hand site) and monolithic (left hand side) capillary column.

Though the basic idea of monolithic silica columns was to achieve a high resolution of low molecular weight compounds at a short analysis time and at a low pressure drop [28] the fundamental studies of this Ph.D. thesis is directed to the enhancement of the diffusion of the high molecular analytes in monolithic silica columns. The selection of high molecular mass analytes, namely peptides and proteins, is addressed to meet the challenges of postgenomic life science research, development and enhanced processing.

The challenges of this Ph.D. thesis are to reliably characterize the pore structural parameters of monoliths and to link these parameters with the hydrodynamic and kinetic properties of the column, such as the column pressure drop, the column efficiency, the speed of analysis and other target parameters through the control of the column morphology and the variation of the pore structural parameters of silica monoliths providing a unique opportunity to design columns for targeted applications with optimum hydrodynamic and mass transfer kinetics.

The major objectives of this Ph.D. thesis are:

1) The critical examination and improvement of the existing pore structural characterization methods and to assess reliable pore characterization values of the monolithic silica samples;
2) The link of the assessed pore characterization values of monolithic silica samples with the mass transfer and hydrodynamic properties of the monolithic silica columns for high molecular weight compounds;
3) The prediction and test of the optimum regimes of the pore structural parameters for the enhanced diffusion of high molecular weight analytes.

2. The assessment of the pore structural parameters of the silica monoliths

Though the application of HPLC has gained a substantial interest in solving daily analytical problems, the knowledge about the complexity of this process is usually rather low. The separation in the column is a very complex process, which depends on numerous parameters, properties, and conditions. Minor changes of any of these often lead to drastic changes of the results. One can distinguish five main key constituents of the chromatographic system: the flow velocity, the axial dispersion coefficient, the mass transfer coefficient, the adsorption capacity and the effective diffusion coefficient [31]. Each of these constituents is influenced by various key parameters: analyte properties, mobile phase properties, adsorbent properties and column properties. Each of the key parameter consists of further properties, for example – adsorbent properties are: the internal porosity, the pore size, the surface area, the type of support material, the surface chemistry, the external porosity and the flow resistance.

Such a complex process is hard to follow if it is viewed as the whole, but breaking into separate parts gives an insight into understanding and possible influence. For example, adsorbent parameter consists of the internal porosity, the pore size and the surface chemistry, that influence the adsorption capacity of the column and the effective diffusion coefficient of the analytes, while the external porosity and the flow resistance influence the flow velocity parameter, the axial dispersion coefficient and the mass transfer coefficient (Fig. 2).

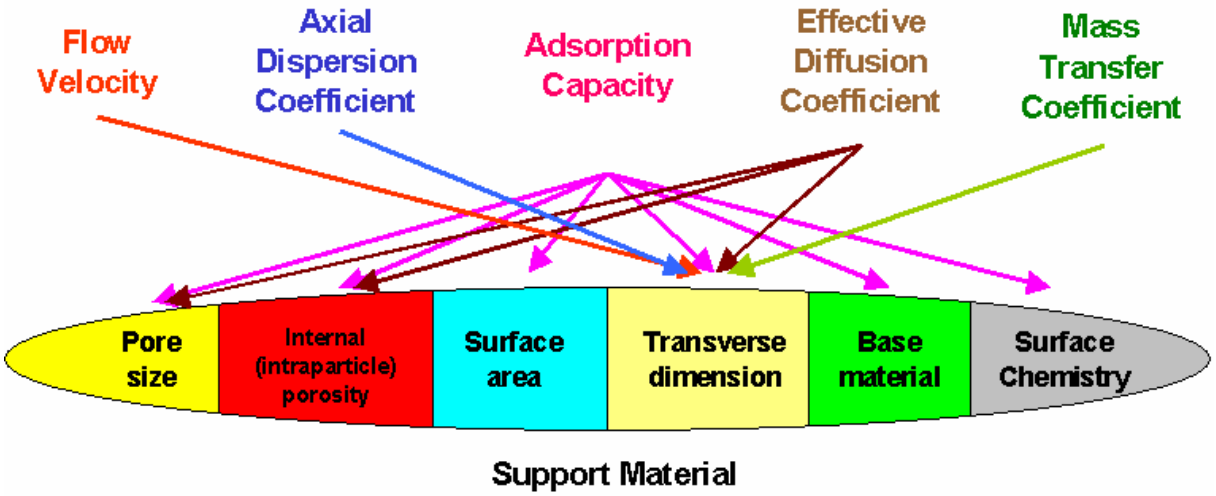

Figure 2. Chromatographic system constituents associated to key parameters of monolithic columns

The optimization process of such complex system is not trivial, but possible, especially if optimization is performed step-wise. The mobile phase could be optimized by

changing its composition and the separation temperature, the analyte properties are case dependent and usually are less influenced, while the influence of the stationary phase properties could be elucidated if one has a degree of freedom to manufacture them with desired properties. The monolithic silica columns enhance the level of freedom, enabling an independent change of the pore size, internal porosity, transverse dimension, external porosity and surface chemistry through the control of forming the structure during the templated sol-gel synthesis. Particulate supports are, in this case, limiting since the external porosity and the transverse dimension are dependent on the particle size.

This unique level of freedom of monolithic structures gives the possibility to optimize support material properties for enhanced column performance. The first step includes a critical examination and improvement of the existing pore structural characterization methods.

The methods of choice for the mesopore characterization were nitrogen sorption, the Inverse Size Exclusion Chromatography (ISEC) and Mercury Porosimetr (MP) .These methods provide information about the internal porosity, intra-particle (intra-skeleton) pore volume, number distribution and connectivity. The flow-through pore values of external porosity, pore size and distribution as well as connectivity were obtained via mercury porosimetry, liquid penetration and image analysis.

Physisorption of nitrogen at 77 K was the first choice to study porous characteristics of monoliths. The isotherm obtained from these measurements provides information on the specific surface area, the specific pore volume and the mesopore size distribution in the range between 0.5 – 200 nm [32-34].

Size Exclusion Chromatography (SEC) [35-38] is a robust chromatographic technique used for the size and mass separation of polymers. Assuming a relationship between the pore size and the molecular size of polymer standards, the porosity and mesopore size distribution values of porous particles can be assessed by ISEC. ISEC is a particularly useful method for the characterization of the porous adsorbent in the column, since the parameters are obtained under liquid phase conditions.

MP as one of liquid intrusion techniques [39, 40] is an especially attractive method due to the advanced textural analysis of the porous sample. This technique may provide not only information about the surface area and pore size distribution from μm to nm size range, but may be also used to investigate parameters such as the tortuosity, permeability, fractal dimension and compressibility of porous materials. Therefore, this technique was especially attractive for characterization of silica monoliths having a bimodal pore size distribution.

Liquid permeability could be employed to determine the flow through pore size distribution of monolithic samples, though usually it is applied for the measurement of an average particle size for the particulate supports. This method enables the assessment of external porosity and flow resistance characteristics [41-43].

Microscopy is a valuable tool for the investigation of the flow-through pore diameter and the skeleton diameter of monolithic silicas [44 - 46]. Recent development if the three-dimentional (3D) images of the characterized structure from the magnetic resonance imaging [47] and microscopic images enables one to transfer these data to the computer simulation platform [48, 49]. These approaches enable to choose routes to improve the performance of monolithic structures using the computational estimation of the plate height data [50], domain size-induced heterogeneity effects [46, 51], optimal external porosity effects [52], and a correlation of the column pressure drop [53].

Monolithic silica research samples were supplied by Merck KGaA, Darmstadt, Germany. Their properties are displayed in Figure 3 based on the different functional groups bonded to the surface and preliminary pore characterization results performed by Merck KGaA.

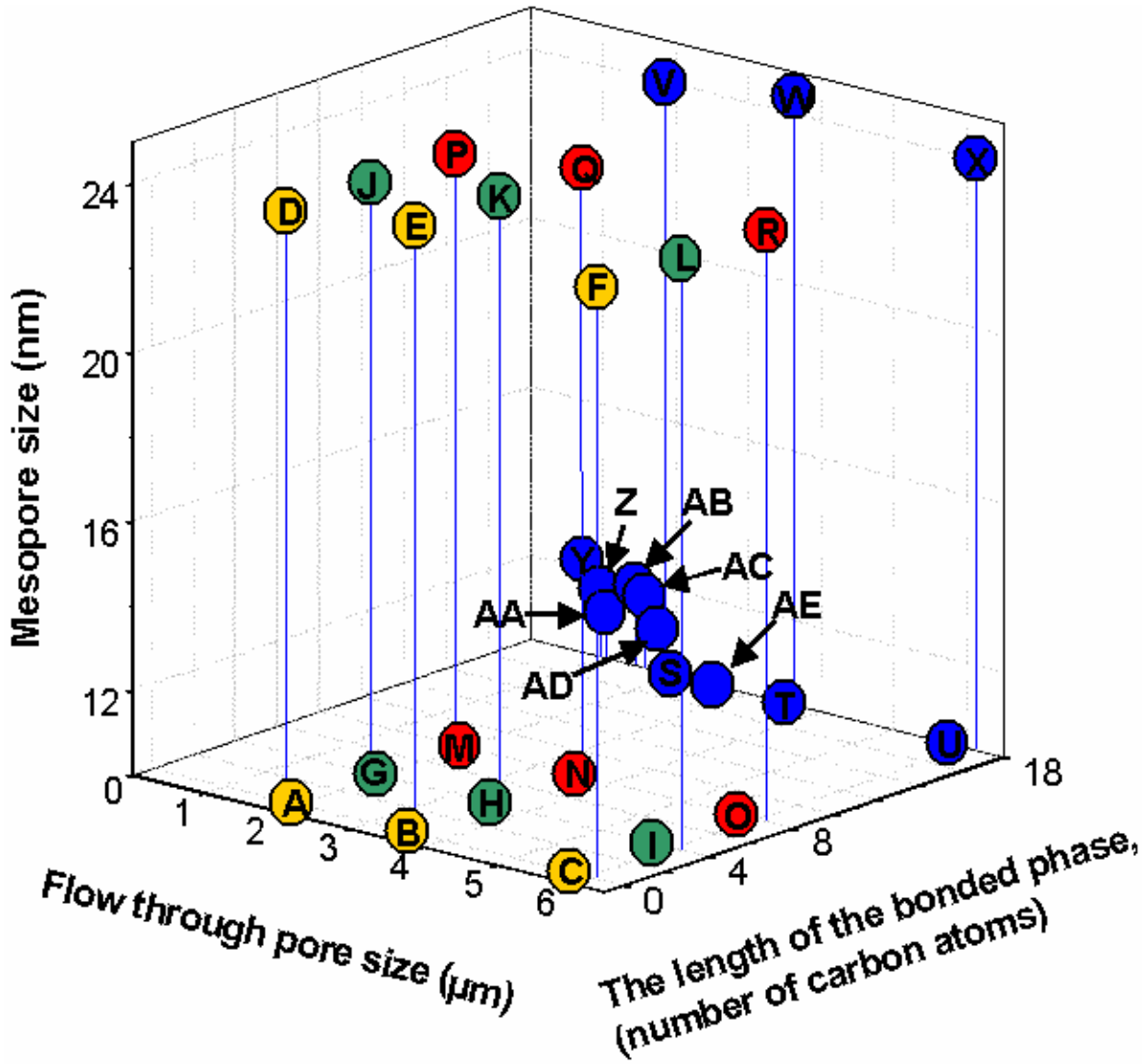

Figure 3. Preliminary pore characterization results and the length of bonded n-alkyl groups of monolithic silica research samples, where A represents monolithic silica sample Tr2783/1, B – Tr2786/1, C – TG36/1, D – Tr2783/2, E – Tr2786/2, F – TG36/2, G – Fr905, H – Fr911, I – Fr917, J – Fr906, K – Fr917, L – Fr918, M – Fr1103, N – Fr1109, O – Fr1115, P – Fr1104, Q – Fr1110, R – Fr1116, S - 787, T - 803, U - 842, V – 800, W – 811, X – 843, Y – KN349, Z – KN341, AA – KN344, AB – KN253, AC – KN252, AD – KN255, AE – KN345.

The range of the chosen samples covered the flow through pore range from 0,7 µm to 6 µm, the mesopore range from 10 - 25 nm and bonded surface functional groups from n-butyl to n-octadecyl as well as unmodified (native) monolithic silica research samples. For chromatographic applications monolithic silica columns were gladded with poly-ether-ether-ketone (PEEK) by a propriety process of Merck KGaA, Darmstadt, Germany. PEEK is one of the highest rated thermoplastic materials in terms of heat resistance, it has excellent chemical resistance, high strength and good resistance to burning. To encase the silica sorbent in PEEK, the PEEK plastic cover is shrink wrapped onto the silica rods to ensure that there is no void space between the silica and the PEEK material.

The named characterization methods were applied to measure the pore structural data of given monolithic silica samples, to enable a comparison and the validity of data and to assess their impact on the mass transfer kinetics in the separation of peptides and proteins.

2.1 Monolith characterization via Inverse Size Exclusion Chromatography

ISEC is a method used to determine the intra-particle pore size distribution of a column stationary phase based on measuring the residence times of solutes (polystyrenes, dextrans, etc.) of varying molecular diameter under the conditions where solute adsorption, intraparticle diffusion resistance, longitudinal (hydrodynamic) dispersion and other mass transfer processes are minimized [54].

ISEC was introduced in 1978 by Halasz et. al. [55] who determined the pore size distribution of porous materials, followed by Knox et. al. [56]. Gorbunov et al. [35] provided a thorough review of ISEC and suggested an accurate method for determining the pore volume distributions. Calculated values of the average pore size and width of the distribution were based on the experimental partition coefficient of macromolecules chosen which is explicitly defined so that the volume partitioning of solutes was considered only to occur in the intraparticle pores (mesopores).

As a consequence, the described model was dependent on the morphology of the porous adsorbent, and inapplicable for the characterization of stationary phases where the volume partitioning of solutes is occuring in the intraparticle and interparticle pores. To overcome such a drawback, a general model was developed based on the first moments of the column response to a pulse injection making it independent of the morphology of the porous material (see publication II).

A parallel pore model (PPM) and a pore network model (PNM) were applied to provide the state-of-art methods for the calculation of various pore characteristics from the ISEC experiments (see publication II). The PPM provides the state-of-art method for the calculation of the mesopore and flow-through pore volume distribution from the experimentally measured partition coefficients of a homologous set of polymer standards based on the first moments of the column response to a pulse injection. The PNM allows to obtain the pore connectivity factor, an indirect measure of mass transfer resistance in the mesopores, and the mesopore number distribution. Since the PNM is an idealization that assumes an infinite pore connectivity, it does not adequately represent the finite connected porous network occurring in the real porous network. But it is used to provide an initial guess for the non-linear regression of the experimental data that later is used in the PNM to obtain the actual pore connectivity values.

In Figure 3, the experimentally measured ISEC curves for two silica monoliths (787 and 800) alongside with the theoretical predictions obtained by fitting the PPM and PNM are presented.

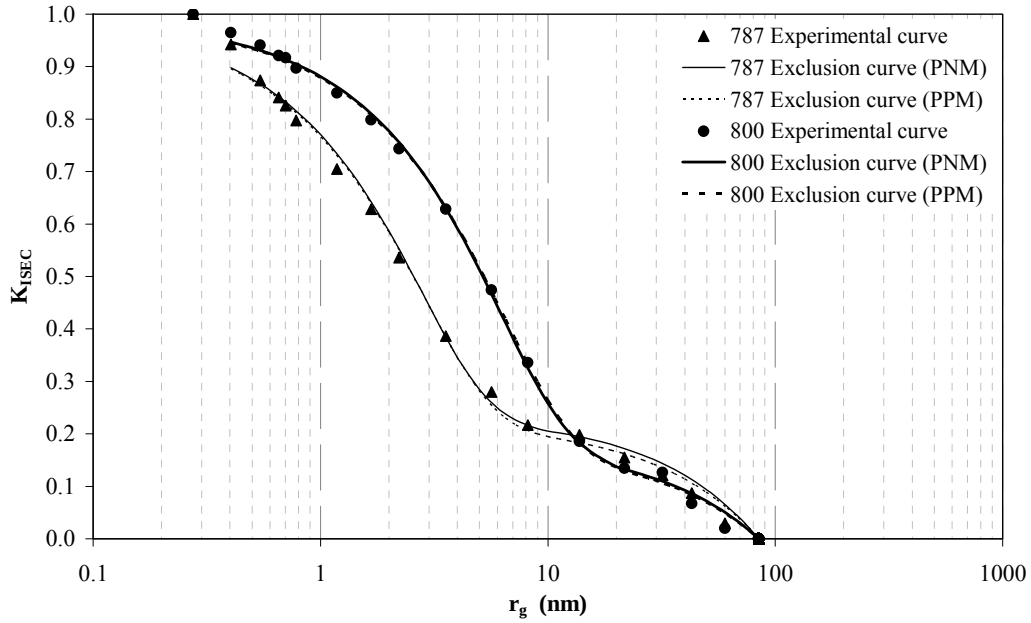

Figure 3. Experimentally measured exclusion curves by ISEC for silica monoliths 787 and 800 along with theoretical exclusion curves obtained from regressing the data with the parallel pore model and the pore network model.

The values for the flow-through pore void fraction, ε_b (0,5 for column 787 and 0,48 for column 800) and the average mesopore size based on volume distribution (16,3 nm for column 787 with a distribution of 4,92 nm, and 36,4 nm for column 800 with a distribution of 11,3 respectively) were obtained from regression of the parallel pore model to the experimental data.

The values for pore connectivity n_T were greater then 10 for both columns, the parameters of the average pore size and distribution based on the number distribution (average pore size based 11,0 nm for column 787 and 23,3 for column 800, and pore size distribution was 4,82 nm for column 787 and 11,1 for column 800) and parameters for the average pore size and distribution based on volume distribution (average pore size was 15,8 nm for column 787 and 34,8 for column 800, and pore size distribution was 4,15 nm for column 787 and 9,14 for column 800) were obtained from the regression of the pore network model to the experimental data.

Mesopore structural characterization results obtained from the pore network model indicated that the values of the pore connectivity, n_T, for all the monoliths studied were 10 or

greater. This is an indication that the mesopore topology within the silica skeleton could be considered to be almost infinitely connected with the respect to the volume-partitioning phenomenon and not hindering the mass transfer kinetics.

Conclusion

Due to the fact that the experimental exclusion curves of silica monoliths had two inflection points, the existing model of Gorbunov et al. [35] could not provide a satisfactory fit to the data obtained for monolithic silica columns. The developed parallel pore model and pore network model provided a satisfactory fit to the experimental data allowing to obtain not only the average pore size and distribution based on the volume distribution, but also the average pore size and distribution based on the number distribution and the pore connectivity values.

2.2 Monolith characterization via Nitrogen sorption

Nitrogen sorption is commonly used method for the characterization of the pore properties of porous substances. It is based on the measuring the nitrogen adsorption and desorption isotherms. The volume of adsorbed nitrogen as a function of the partial equilibrium pressure represents the adsorption branch of the isotherm, and the volume of desorbed nitrogen as a function of the partial equilibrium pressure represents the desorption branch of the isotherm. Brunauer et al. [57] proposed five types of characteristic isotherms, which were later completed by adding the sixth one [58].

The assessment of pore structure via nitrogen sorption measurements is based on the application of the Kelvin equation using the method of Barrett-Joyner-Halenda (BJH) [59] to evaluate the data from the isotherm adsorption and desorption branch. The extracted data are used to obtain the specific surface area according to the Brunauer-Emmet-Teller (BET) [60] method, the specific pore volume according to the Gutwitsch (G) method [61] and the pore volume distribution according to the method of Barrett-Joyner-Halenda (BJH) [59].

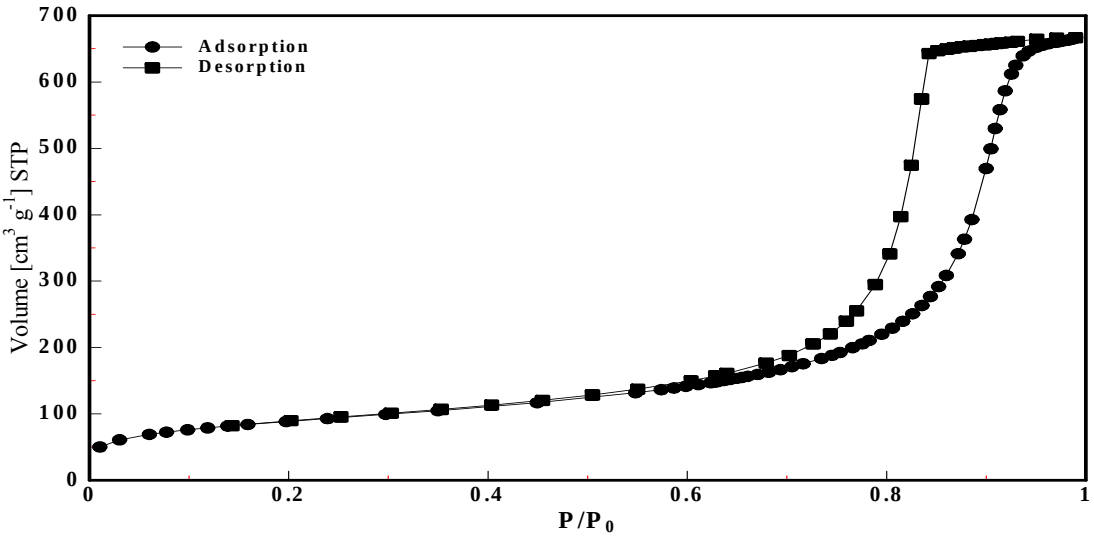

Figure 5. Nitrogen sorption at 77.4 K on the native silica monolith Tr2783/1.

Nitrogen adsorption/desorption data obtained at 77.4 K on the native silica monolith Tr2783/1 are displayed in Figure 5. The type IV isotherm [48] reveals a hysteresis loop indicative of pore condensation. The hysteresis loop can be classified as to between type H1 and H2. This would indicate that in the addition to the intrinsic reasons for the hysteresis, (i.e. the delay in condensation is caused by the metastable pore fluid) and the pore blocking/percolation effects are present which lead to the delay in the position of the desorption branch. The calculated specific surface area (BET method) was 298 m²/g for the monolithic silica sample Tr2783/1, the specific pore volume (G method) – 0, 88 cm³/g, and the average pore size according to the volume distribution (BJH method) was 10.9 nm (see publication III).

Due to the fact that the BJH method fails to describe correctly the adsorption and the phase behaviour of fluids in small mesopores, it leads to a significant underestimation of the pore size (for the pore widths which are smaller than. 20 nm). Theoretical approaches such as the Non Local Density Functional Theory (NLDFT) [63, 64] are able to describe the configuration of the adsorbed phase on a molecular level, and therefore allow obtaining an accurate pore size distribution. In addition, the application of the NLDFT correctly predicts that the adsorption branch of a hysteretic adsorption isotherm is not at the thermodynamic equilibrium, i.e. the pore condensation occurs with a delay due to the metastable pore fluid. Hence, in case hysteresis is only caused by the metastable pore fluid and no networking effects are present, the desorption branch of the hysteresis loop reflects the thermodynamic equilibrium transition and the pore size distribution calculated from the desorption branch by applying the NLDFT equilibrium method and from the adsorption branch by applying the so-

called NLDFT metastable adsorption branch kernel (which takes into account the delay in condensation) should agree. Data comparison of applying these two kernels on the adsorption and desorption branches of the nitrogen isotherm are in chapter 2.6 alongside with the results of the results of MP and ISEC.

Conclusion

Since BJH method used for nitrogen sorption data interpretation leads to a significant underestimation of the pore size for the pore widths that are smaller then 20 nm, we applied NLDFT equilibrium method. The chosen NLDFT method is more accurate due to the ability to describe the configuration of the adsorbed phase on a molecular level and assumption that the adsorption branch of a hysteretic adsorption isotherm is not at the thermodynamic equilibrium.

2.3 Monolith characterization via Mercury Porosimetry (MP)

The assessment of the pore structure via mercury intrusion is based on the application of pressure to force mercury into the pores. Thus, a progressive increase in the hydrostatic pressure is applied to enable the mercury to enter the pores with decreasing order of width. Accordingly, there is an inverse relationship between the applied pressure and the pore diameter which in the simplest case of the cylindrical pores is given by the Washburn equation [62].

MP enables to determine the average pore diameter in the range between 40 μm and 4 nm, the porosity of these pores and their specific surface area. Furthermore, the technique can provide useful information with respect to the pore shape, network effects, the skeleton and bulk density [39, 40, 65, 66] (see publication III). Therefore we used this technique for the characterization of the monolithic silica samples.

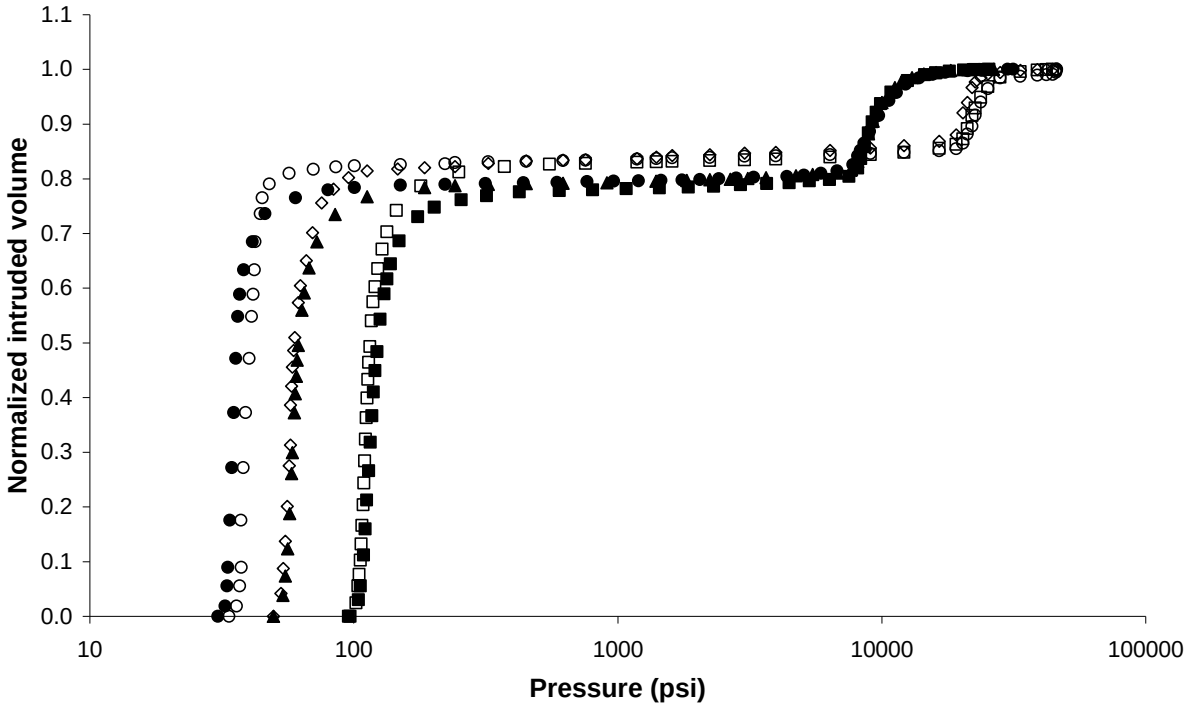

Figure 6. Mercury intrusion curves of investigated silica monoliths: □ – "787" monolithic silica rod grafted with n-octadecyl chains, ■ – "800" monolithic silica rod grafted with n-octadecyl chains, ◊ - "803" monolithic silica rod grafted with n-octadecyl chains, ▲ – "811" monolithic silica rod grafted with n-octadecyl chains, ○ – "842" monolithic silica rod grafted with n-octadecyl chains, ● – "843" monolithic silica rod grafted with n-octadecyl chains.

The mercury intrusion curves (Fig. 6) indicate that the pore structure is bimodal having pores located in the silica skeleton (mesopores) and the flow-through pores. The plateau region at pressures of 1,000 psi in the mercury intrusion curves clearly separates the two pore size regimes and allows one to calculate the corresponding surface area and porosity values of the two types of pores.

Therefore MP could be used to assess not only the mesopore size and distribution but also provides a possibility for comprehensive structural characterization of bimodal silica monoliths, namely the flow-through pores as well (see publication III). Furthermore, a significant feature of mercury porosimetry curves is the occurrence of hysteresis between the intrusion and extrusion branch. In addition, entrapment is often observed, i.e. mercury remains contained in the porous network after extrusion.

The importance of understanding the hysteresis and entrapment phenomena has been recognized since a long time [67-69] because it is most important to be able to obtain an unambiguous pore size analysis [70-72]. Though different mechanisms have been proposed to explain intrusion/extrusion hysteresis [71, 73-77], it is now generally accepted that pore blocking effects are associated with the rupture of mercury bridges in pore constrictions

during extrusion leading to mercury entrapment in ink-bottle pores. The fragmentation slows down the rate of mass transfer of fluid from the porous material. The decrease of mass transfer rate causes a significant reduction in separation efficiency in HPLC.

The striking feature of the intrusion/extrusion behaviour into native silica monoliths and n-octadecyl grafted silica monolith samples is the fact that they do not show any appreciable amount of entrapment. This also indicates that the flow-through porous framework of some samples (for example TG36/2) that showed moderate amount of entrapment appears to be much more heterogeneous/disordered as compared to the silica monoliths samples which do not show entrapment. As displayed in Figure 6, no entrapment occurs for monoliths Tr2783/1 and Tr2783/2 which have almost an identical flow-through pore system with regard to porosity and pore size distribution, but mercury entrapment is observed in TG36-2 monolith, which exhibits higher flow-through pore sizes and a more disordered framework.

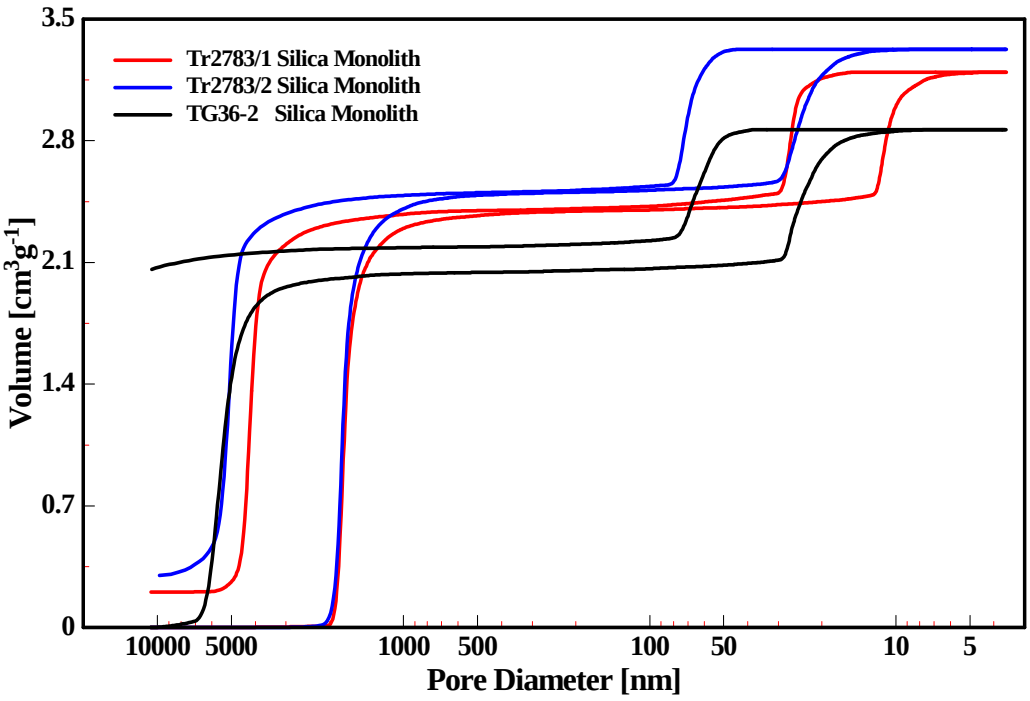

Figure 7. Hystereses curves between mercury intrusion and extrusion branch for some selected native silica monoliths

The results of a systematic study of the mercury intrusion/extrusion behavior into native silica monoliths and monoliths with bonded n-alkyl groups reveals that the flow-through pore (or through pore) structure, which controls the mass transfer to and from the mesopores, mainly controls the entrapment behavior. It appears that entrapment is more likely to occur when the flow-through pore system is heterogeneous and disordered (which would restrict mass transfer) as indicated by a wide pore size distribution coupled with relatively low

porosity. Vice versa, the lack of entrapment after extrusion from the monolith mesopore system indicates enhanced transport properties which is in accord with an ordered, highly porous flow-through pore system.

Conclusion

Mercury porosimetry (intrusion/extrusion) does not only allow to obtain a complete pore structure analysis over the complete range of macro- and mesopores, but might serve as tool to estimate the mass transport properties of silica monoliths employed in liquid phase separation processes.

The examination of silica monolith flow-through pore system via mercury porosimetry led to the significant improvement in understanding the relationship between the flow-through pore structure and mass transfer resistance in the mesopores. The obtained results could be directly linked with the column performance of peptidic analytes and proteins in HPLC.

2.4 Monolith characterization via Liquid Permeability (LP)

Liquid permeability (LP) has been applied to a lesser extent then the mercury porosimetry although it bears a high potential of information. The liquid permeability (the flow resistance) is dependant on the external surface area to volume ratio of the porous material. Pioneering work in this field has been done by Washburn [41], who studied the dynamic invasion of a fluid into capillaries and by Carman [42], who used the concept of hydraulic radius to define equilibrium positions of fluid-fluid interfaces in tubes of different cross section. The flow of a liquid through a porous material was described by the Hagen-Poiseuille and by the Kozeny-Carman [43] equations.

According to the Poiseuille equation for cylindrical capillaries, the steady state volume flux (the rate of volume flow across the cross section A_c) J_v can be obtained from the average fluid velocity and the pressure drop [78, 79]. The Kozeny-Carman equation is then employed for the calculation of the effective diameter of the equivalent pores in the porous bed from the permeability and porosity data [80]. The Hagen-Poiseuille approach was based on the assumption of cylindrical pores whereas the Kozeny-Carman approach assumed pores as voids between closely packed spheres of equal size.

Various papers have been published dealing with the Kozeny-Carman approach at the characterization of silica based monoliths. The most fundamental work was done by Minakushi [81], Leinweber [30, 82], and Vervoort [83, 84] resulting in various interpretations

of the flow resistance values. The same relative particle diameters were obtained, but certain specific approximations were applied for the calculation of the flow-through pore sizes. A notable progress was made by introducing the term of domain size being the sum of the skeleton diameter and the diameter of the flow-through pore [85]. Though this assumption did not reflect the real silica based monolithic support, it enabled to use the liquid permeability data to characterize the monolith regardless of its format and chemistry.

Alternatively, we developed an approach for monolithic silica flow-through pore characterization (see details in article IV) via the liquid permeability method, which was based not on the Kozeny-Carman approach but on the Hagen-Poiseuille equation. The assumption of cylindrical pores fits best to the flow-through pore morphology of the silica monolith. No approximations are necessary to link the particle size with the flow-through pore diameter.

Table 1: Flow-through pore characteristics of silica monoliths assessed by the permeability of a liquid.

Monolithic silica sample	Minakuchi				Skudas			
	Equivalent particle diameter, D_{perm} (µm)		Average flow-through pore diameter D_f (µm)		Average flow-through pore diameter D_f (µm)		Average skeleton diameter, D_s (µm)	
787	8.352	10.51*	5.563	7.013*	1.934	2.436*	1.685	2.123*
800	7.161	8.99*	4.771	5.990*	1.871	2.363*	1.569	1.990*
803	8.475	8.36*	5.652	5.571*	3.524	3.475*	2.466	2.433*
811	14.771	16.84*	9.851	11.234*	3.874	4.411*	3.243	3.692*
842	20.484	19.96*	13.662	13.302*	6.133	5.974*	4.891	4.761*
843	20.542	19.48*	13.691	12,993*	6.424	6.093*	5.043	4.783*
KN 253	1.908	1.94*	1.272	1.290*	1.181	1.201*	0.687	0.696*
KN 341	1.817	1.81*	1.211	1.209*	0.959	0.957*	0.603	0.601*
KN 255	2.673	2.77*	1.782	1.849*	1.574	1.635*	0.938	0.974*
KN 349	1.642	1.64*	1.095	1.092*	0.666	0.665*	0.471	0.474*
KN 345	5.518	6,03*	3.679	4.021*	2.488	2.719*	1.681	1.837*
KN 344	2.398	2.43*	1.599	1.623*	0.921	0.934*	0.666	0.676*
KN 252	2.249	2.32*	1.499	1.545*	1.333	1.374*	0.791	0.816*

Values with * were obtained using methanol as a solvent.

The results in Table 1 first clearly reveal major differences between the Kozeny – Carman (as indicated by Minakuchi) and the Hagen-Poiseuille approach (as indicated by

Skudas). Second they reveal that the permeability method could be used not only to obtain flow-through pore values but also skeleton diameters (for details see article IV). Moreover, surface area of the skeletons and volume of the skeleton ratios were calculated.

Conclusion

The critical examination of liquid permeability let to the development of alternative experimental data, which characterizes monolithic structures. It was found that not the flow-through pore size influences the mobile phase flow through the monolithic column resistance values, but the ratio between the external surface area to volume of the monolithic material. To obtain this data, Hagen-Poiseuille theoretical approach of flow resistance in the cylinders was used to exclude numerous approximations and limitations of usually applied Kozeny-Carman theoretical approach of flow resistance in the packed beds.

2.5 Monolith characterization via Scanning Electron Microscopy (SEM)

SEM is a method of imaging the sample surface by scanning it with a high-energy beam of electrons in a raster scan pattern. The electrons interact with the atoms that make up the sample producing signals that contain information about the sample's surface topography, composition and other properties such as electrical conductivity.

The first SEM image was obtained by Knoll, who in 1935 obtained an image of silicon steel showing electron channeling contrast [86]. Further pioneering work on the physical principles of the SEM and beam specimen interactions was performed by von Ardenne in 1937 [87, 88] who produced a British patent [89] but never made a practical instrument. The SEM was further developed by Prof. C. Oatley and his postgraduate student Stewart and was the first marketed in 1965 by the Cambridge Instrument Company as the "Stereoscan".

SEM was used to give a direct image of the flow-through pore system of monolithic silica samples (Figure 8). Two methods were applied to assess the average flow-through pore diameter and skeleton diameter: direct scale measurement and the "Pixcavator" program. The direct measurement was performed via segmenting each image into relative areas and measuring the characteristic parameters via given scale. The average values were withdrawn from all measured values. The values estimated by the "Pixcavator" program were based on the area estimation via integrating the number of pixels in that area. The area was defined by the colour. Since the flow-through pores were in most cases black, the estimation of all the pixels in the area was performed by calculation of their number and multiplying by the area of one pixel. The obtained relative area of a single flow-through pore was then assumed to be

equal to the area of circle (meaning a round shaped pore) and the diameter of this circle was taken as the diameter of the flow-through pore.

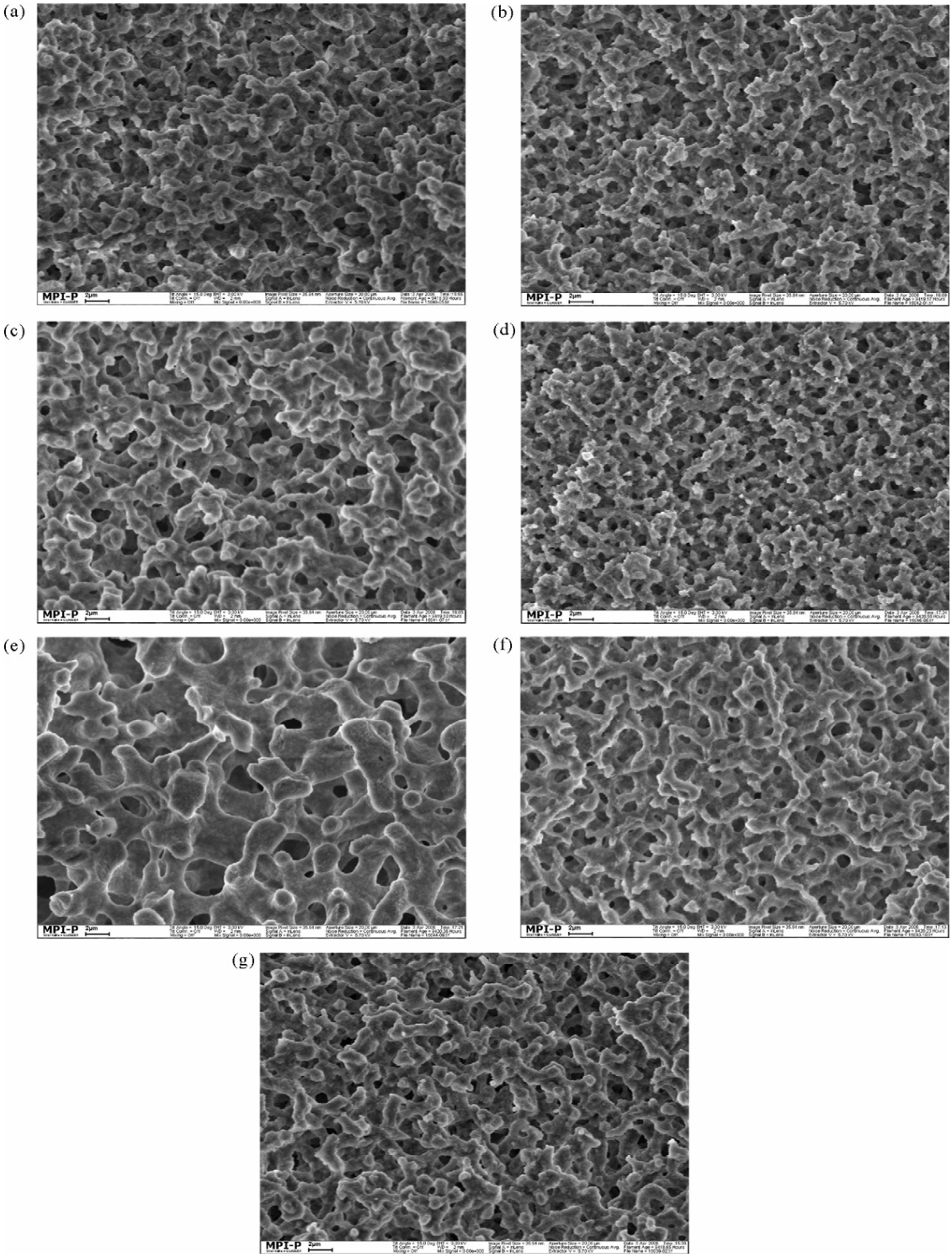

Figure 8. The electron scanning micrographs of monolithic research silica samples: (a) KN 253, (b) KN 341, (c) KN 255, (d) KN 349, (e) KN 345, (f) KN 344, (g) KN 252.

The detailed image analysis revealed not only cylindrical silica structure skeletons, but also various forms by which these skeletons are connected. This causes a wide distribution of skeleton diameter values as well (see details in article IV). As a consequence, the external surface area of such monolithic structure is smaller if compared to the ideal cylindrical morphology when the volume and the average structural diameters are equal. This leads to smaller flow-resistance and enhanced mass transfer values.

Conclusion

The application of SEM for the characterization of monolithic silicas led not only to the estimation of the flow-through pore size and silica skeleton size, but revealed that the external surface area of the studied monoliths is smaller than compared to the ideal cylindrical morphology.

2.6 Comparison of the mesopore characterization data

The mesopore size distribution obtained from MP, ISEC, and nitrogen sorption are compared in Figure 9.

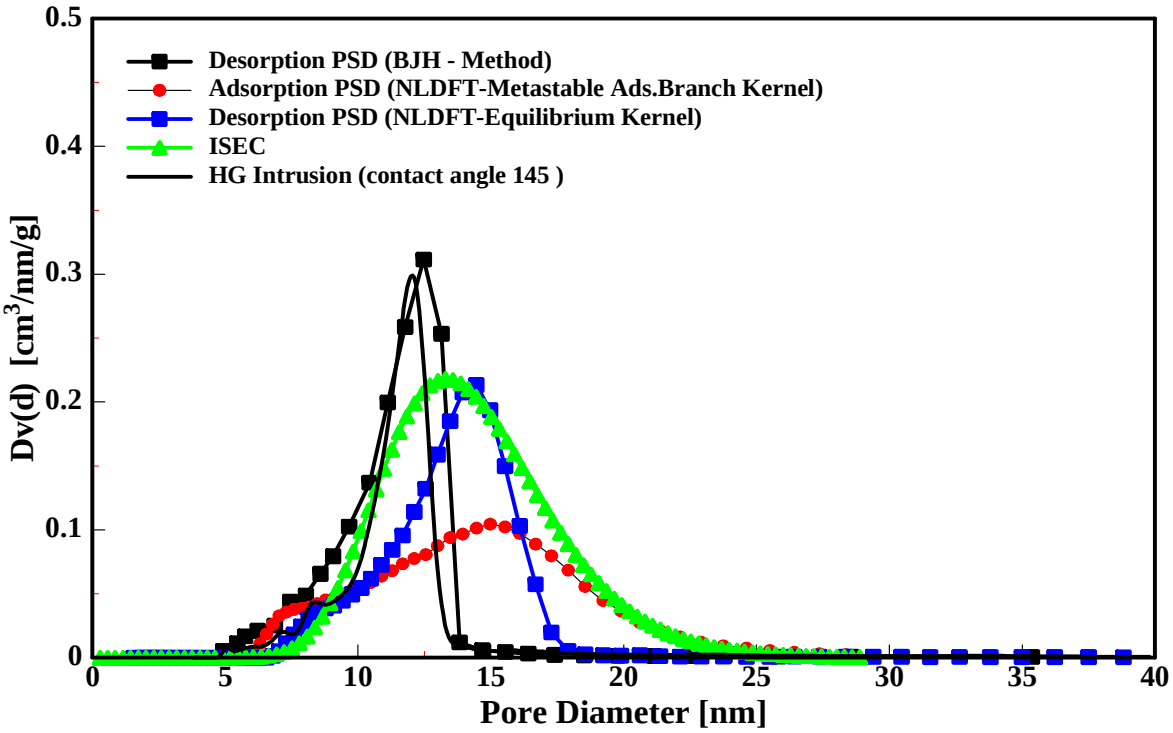

Figure 9. Comparison of mesopore size distribution curves for the native silica monolith Tr2783/1 obtained from nitrogen sorption by applying NLDFT and the BJH method, ISEC andMP.

A good agreement was obtained between the pore size distribution (psd) curves by applying the BJH method [59] using the desorption branch of nitrogen sorption method with the psd curves obtained from MP by applying the Washburn equation and a contact angle of 145°. Applying the NLDFT-metastable adsorption branch kernel and the NLDFT-equilibrium kernel methods on the nitrogen isotherm of sample Tr2783/1 reveals that the mode pore diameters (most frequent pore diameters, or maximum of the psd curve) agree well, but the mode pore diameter obtained from the desorption branch is slightly shifted to the smaller values. Furthermore, the psd curve is much narrower as compared to the psd obtained from the adsorption branch of the nitrogen isotherm indicating the presence of some network/pore blocking effects.

The data presented in Figure 9 also indicate that (as to be expected) the BJH method (nitrogen sorption) and mercury intrusion method applying 145° contact angle significantly underestimate the pore size compared to the NLDFT pore size method (nitrogen sorption). Interestingly, the width of the pore size distribution curve obtained by ISEC agrees reasonably well with the psd curve obtained from the NLDFT adsorption branch.

Concluding remarks

The results indicate that all the investigated methods are useful for the mesopore characterization with the respect to the pore size distribution by volume, but special care should be chosen for the correct data interpretation.

2.7 Comparison of the flow-through pore characterization data

For the comparison of the flow-through pore size values the Pearson correlation coefficient, *rp*, was calculated (see Table 2). The best correlation coefficient values were obtained for mercury intrusion and image analysis using the "Pixcavator" program, *rp* = 0.998; mercury intrusion and permeability of water using Gusev's model [90] gave *rp* = 0.998 and the Skudas model [92], *rp* = 0.998.

Table 2. Pearson correlation coefficient (r_P), calculated for the flow-through pore diameters obtained by mercury intrusion, image analysis and liquid permeability for monolithic research silica columns

Characterization methods		Mercury intrusion	Image analysis		Permeability of a liquid					
			Direct analysis	*"Pixc."*	*Gusev (H_2O)*	*Gusev (CH_3OH)*	*Minakuchi (H_2O)*	*Minakuchi (CH_3OH)*	*Skudas (H_2O)*	*Skudas (CH_3OH)*
Mercury intrusion			***0.991***	***0.998***	***0.998***	0.985	0.958	0.918	***0.998***	0.986
Image Analysis	**Direct analysis**	***0.991***		0.986	***0.991***	0.985	0.971	0.939	***0.992***	0.987
	"Pixcavator"	***0.998***	0.986		***0.997***	0.987	0.957	0.919	***0.996***	0.986

Characterization methods		Mercury intrusion	Image analysis		Permeability of a liquid					
			Direct analysis	*"Pixc."*	*Gusev (H_2O)*	*Gusev (CH_3OH)*	*Minakuchi (H_2O)*	*Minakuchi (CH_3OH)*	*Skudas (H_2O)*	*Skudas (CH_3OH)*
Permeability of a liquid	*Gusev (H_2O)*	***0.998***	***0.991***	***0.997***		0.989	0.968	0.930	***1.000***	***0.990***
	Gusev (CH_3OH)	0.985	0.985	0.987	0.989		0.983	0.965	***0.990***	***1.000***
	Minakuchi (H_2O)	0.958	0.971	0.957	0.968	0.983		0.989	0.970	0.983
	Minakuchi (CH_3OH)	0.918	0.939	0.919	0.930	0.965	0.989		0.933	0.965
	Skudas (H_2O)	***0.998***	***0.992***	***0.996***	***1.000***	***0.990***	0.970	0.933		***0.991***
	Skudas (CH_3OH)	0.986	0.987	0.986	***0.990***	***1.000***	0.983	0.965	***0.991***	

As mentioned before, the Kozeny-Carman theory does not fit to the calculation of pore characteristic values of silica monoliths. The obtained Pearson's correlation coefficients obtained were < 0.95.

When one compares the flow-through pore diameters by liquid permeability approaches, and mercury intrusion, one notices slight differences (Fig. 9).

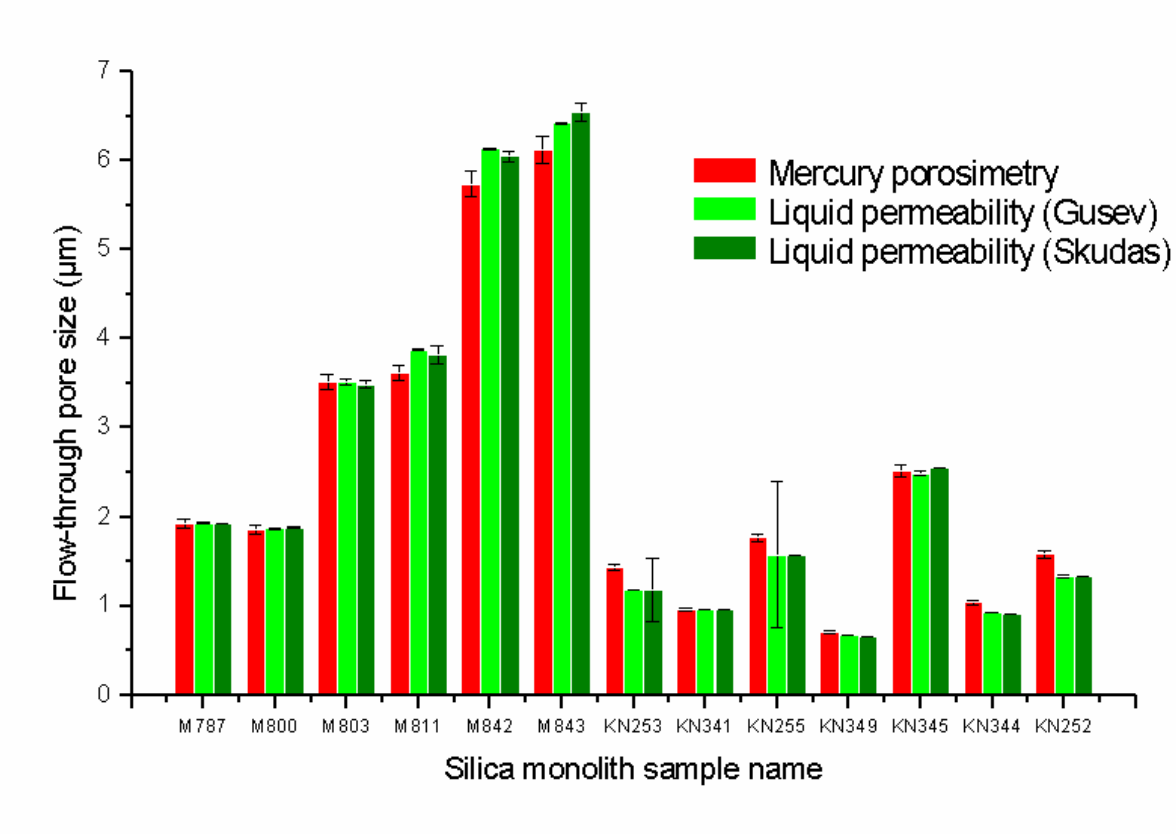

Figure 10. Average flow-through pore diameters and standard deviation of silica monoliths obtained by mercury porosimetry, liquid permeability method according to Gusev [58], and liquid permeability method according to Skudas (see article IV).

These might be due to the fact, that not all the pores were permeable at the same extent. The larger pores (explicitly columns 842 and 843) have a higher permeability than the others (which) since the flow rate is proportional to the pore diameter to the fourth. Therefore the estimated flow-through pore diameter values are larger as well (see details in article IV). It could be concluded that obviously not all of the surface area has access to the liquid at the same ratio.

Concluding remarks

MP, imaging and image analysis and liquid permeability could be used to distinguish reliably the flow-through pore diameters for the monolithic silica columns, but special care should be taken about the chosen theoretical model.

3. Relationship between the pore structure of silica monoliths and their column efficiency in HPLC

3.1. Modelling parameters, approaches and results

In general there are three major criteria in characterizing a HPLC column:

(a) **The hydrodynamic properties** (expressed by the dependency of the column back pressure on the flow-rate of the eluent) provide an insight into the flow behaviour. From these data the column permeability can be calculated and compared with the expected value based on the average particle diameter and the column dimensions;

(b) **The kinetic properties** of the column expressing the mass transfer kinetics of analytes are the measure of the peak dispersion of a column. The peak dispersion is characterized by the theoretical plate height (H) and the number of theoretical plates (N). A more detailed diagnosis of the kinetic performance is based on the dependency of the plate height (H) as the function of the linear velocity (u) of the eluent;

(c) **The thermodynamic properties** are expressed by the retention coefficients and the selectivity coefficient of test solutes under constant conditions.

The hydrodynamic properties were already investigated in the liquid permeability part, where we combined the column pressure vs. flow dependency with the parameter of the external surface area to the volume ratio of the silica monoliths. We found that this ratio should be as small as possible to assure the smallest flow resistance (for details see article IV**).**

The first researchers who systematically studied peak dispersion phenomena were Martin et al. [92], Van Deemter et al. [93] and Giddings [94, 95]. The treatment of the mass transfer processes and the distribution equilibrium between the mobile and stationary phase in a column lead to equations which link the theoretical plate height as the decisive column performance parameter to properties such as linear velocity of eluent, diffusion coefficient of analyte, retention coefficient of analyte, column porosity, etc.

Van Deemter proposed an equation, which described the column performance as a function of the linear velocity for a packed column in gas chromatography coated with a stationary liquid layer. Similar equations, however, with other terms were derived for LC by numerous researchers (see review article III**).** It became common practice to refer to all H vs.u plots collectively as Van Deemter plots. A minimum in the plate height vs. linear velocity curve is observed where the column performance is the highest. Knox suggested a three-term

equation to describe the dependency of the theoretical plate height H of a column as a function of the linear velocity of the eluent:

$$H = A + \frac{B}{u} + Cu \qquad 1$$

The A-term stands for the eddy diffusion and corresponds to the convective dispersion by flow through the tortuous column bed, the B-term stands for the longitudinal molecular diffusion and expresses the dispersion due to longitudinal molecular diffusion and the C-term stands for the mass transfer resistance and is a measure of the equilibration of the analyte between the stationary and mobile phase in a column. While using different linear velocity values, the H value of chosen analyte is measured and the H. vs u curve is obtained. The H vs u curve is dominated at the left hand side by the minimum of the longitudianl molecular diffusion term and at the right hand side by the mass transfer resistance term at higher linear velocities.

Since the given Knox equation is suited for particle packed columns and not the monolithic ones, we had to develop an equation which links the plate height of monolithic columns with the common mass transfer kinetics of an analyte and the properties of the monolithic columns (see article II):

$$H = \frac{K_b D_L}{2u} + \left[2L\left(\frac{K_b D_L}{uL}\right)^2 \left(e^{(-uL)/(K_b D_L)} - 1\right)\right] + \left[\frac{\varepsilon_b(1-\varepsilon_b)\left(\varepsilon_p K_p + K_{eq}\right)^2}{\left[\varepsilon_b K_b + (1-\varepsilon_b)\left(\varepsilon_p K_p + K_{eq}\right)\right]^2} \frac{R_p}{k_f}\right] u + \left[\frac{\varepsilon_b(1-\varepsilon_b)\left(\varepsilon_p K_p + K_{eq}\right)^2}{4\left[\varepsilon_b K_b + (1-\varepsilon_b)\left(\varepsilon_p K_p + K_{eq}\right)\right]^2} \frac{R_p^2}{\varepsilon_p K_p D_p}\right] u \qquad 1$$

In the equation H stands for the height equivalent of a theoretical plate (HETP), or plate height, u is the linear flow velocity of the eluent, R_p denotes the radius of the silica skeletons, ε_b is the void fraction of the flow-through pores void space in the column, the K_b represents the volume partition coefficient of the finite sized molecule in the flow-through porous void space of the monolithic column, ε_p is the void fraction of the monolithic skeleton, K_p represents the volume partition coefficient of the finite sized molecule in the mesoporous void space of the skeleton, D_p denotes the effective diffusion coefficient of the analyte in the confined mesoporous space of the skeleton, K_{eq} represents the equilibrium adsorption constant

of the linear adsorption isotherm, k_f denotes the film mass transfer coefficient of the analyte, D_L represents the axial dispersion coefficient of the solute in the mobile phase, L is the length of the column.

Applying this equation, we were able to link the structural parameters of silica monoliths with their chromatographic efficiency. For example, Figure 11 demonstrates the dependency of the column back pressure on the number of the theoretical plates for a solute of one nanometre (nm) molecular diameter. The graph indicates no significant changes in plate numbers when the flow-through pore diameter is varied at constant surface area to volume ratio of the skeletons and the external porosity (ε_b). The lines represent results from modelling where the curves of flow-through pore diameters between 1 μm and 10 μm do not scatter. The column efficiency is not dependent on the flow-through pore diameter. The surface area to volume ratio of the skeletons as well as external porosity are decisive.

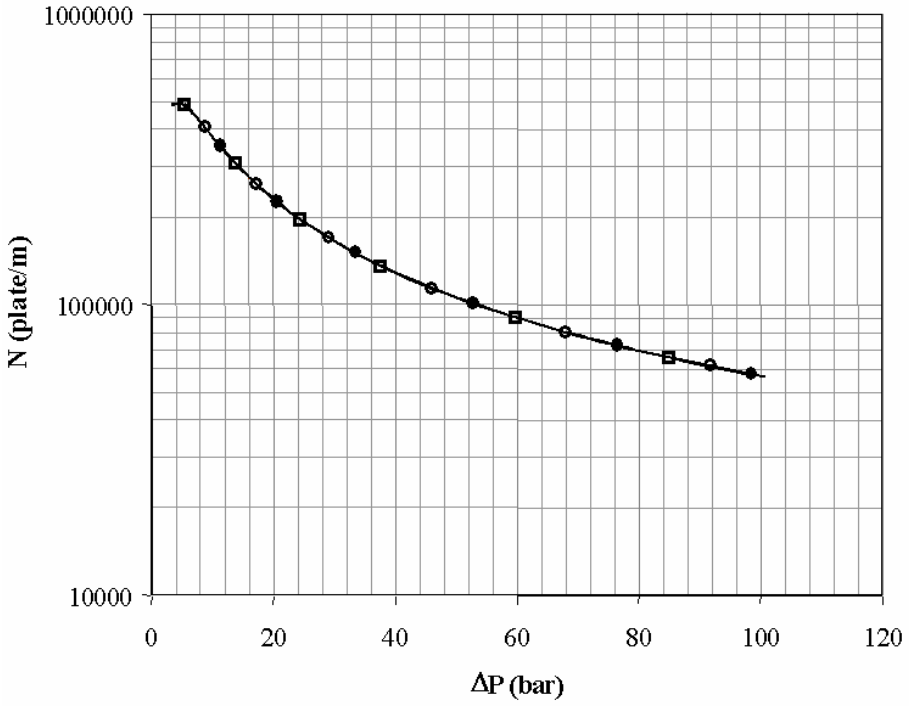

Figure 11. The plate number of monolithic silica columns as a function of column back-pressure for different flow-through pore diameters. The analyte radius (r) was 0.50 nm; K_{eq} – 10; ε_t – 0.800; ε_b – 0.500; ε_p – 0.600; $P_{d,mes}$ – 10 nm were kept constant. D_f was changed in the range from 1 μm to 10 μm (-○- 1 μm, -● - 4 μm, ,- ■ - 10 μm).

In order to measure the influence of the silica monoliths properties on the column efficiency, the following parameters were taken into account: the specific surface area, the specific pore volume and the external porosity, as well as the internal porosity, the mesopore average size, the mesopore distribution and the connectivity values. The power of each characteristic parameter could be evaluated to the overall separation performance.

3.2 Impact of the mesopore parameters on the column efficiency

The impact of the mesopore structural characteristics of *n*-octadecyl bonded silica monoliths on the column performance for peptide and protein probes in RPLC were quantitatively determined. Monolithic silica columns of various mesopore sizes were evaluated via HETP curves for lysozyme and cytochrome C (see article V for details).

In Figure 12, the influence of the mesopore diameter (~10 and ~25 nm) of the monolithic silica columns on column efficiency of lysozyme and cytochrome C separation was investigated. Based on the value of the minimum plate height and the slope of the mass transfer dominated portion of the HETP curves, the efficiency of each column was related to the value of the mesopore diameter. As indicated in Fig. 12, the measured minimum plate height values for lysozyme and cytochrome *C* were similar (49–53µm) for monolithic silica columns having mesopores of ~10.9 and ~25 nm but the average linear velocity (u_{av}) where the minimum plate height occurred was higher for the monolithic silica columns having a mesopore diameter of ~25 nm. The minimum plate height values appeared at linear velocities of ~0.6 mm/s for the monolithic silica columns having a nominal mesopore diameter of ~25 nm, while for the columns having a nominal mesopore diameter of ~10.9 nm, the minimum plate height occurred at ~0.2 mm/s. Furthermore, it is evident from Fig. 12 that the slope of the HETP curves at higher velocities is smaller for columns having nominal mesopore diameters of ~25 nm than the slope of the HETP curves for monoliths having nominal mesopore diameters of ~10.9 nm in the same velocity domain.

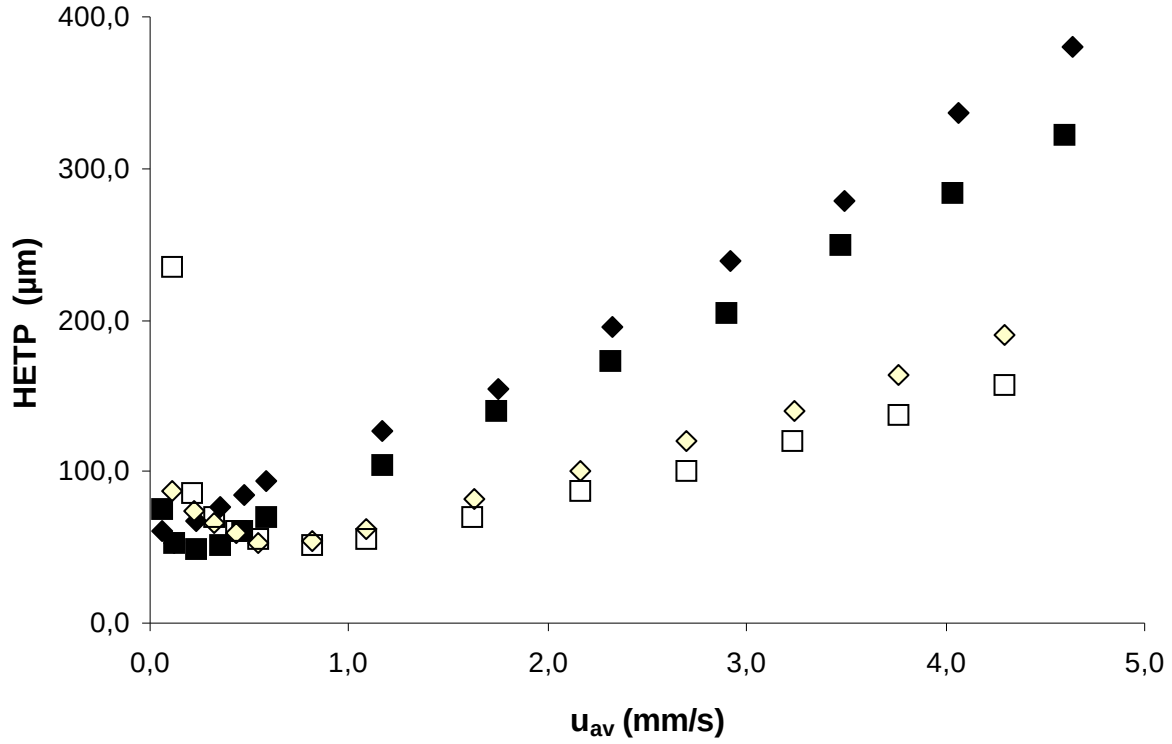

Figure 12. Plate height vs. linear velocity curves for lysozyme and cytochrome *C* on C18e monolithic silica columns of average through-pore diameter of 1.8–1.9 µm: ♦ measured efficiency values on column 787 (1,8 µm flow-through pores and 10,9 nm mesopores) for lysozyme; ■ measured efficiency values on column 787 for cytochrome C; ◊ measured efficiency values on column 800 (1,9 µm flow-through pores and 25 nm mesopores) for lysozyme; □ measured efficiency values on column 842 for cytochrome C.

Concluding remarks

It was found that the monolithic silica columns with the larger mesopore diameter (~25 nm) provided less mass transfer resistance in the mesoporous structure of the skeleton due to the fact that there is less steric hindrance and frictional resistance to diffusion of the large lysozyme and cytochrome *C* molecules when the mesopores are considerably larger (~5 times) than the analytes. Thus, the monolithic columns having larger mesopore diameters (~25 nm) enables to operate the column at higher flow rates which allows for shorter analysis times without loosing separation efficiency.

Apart from providing high column efficiency at high flow rates, the most prominent feature of the HETP versus velocity curves for monolithic silica columns having nominal mesopore diameters of ~25 nm was a very shallow curvature near the minimum. This is due to the low mass transfer resistance and short diffusion path lengths in the mesoporous structure of the silica skeleton. For the monolithic silica column having ~25 nm mesopores, the measured HETP values varied between ~100 and ~250 µm when the average linear

velocity was increased from 0.5 to 4 mm/s. While for the monolithic silica column having mesopores of 10.9 nm, the measured HETP values increased from ~150 to ~1000 µm over the same linear velocity range.

3.3 Impact of the flow-through pore parameters on the column efficiency

In Figure 13, the effect of the through-pore size on the plate height vs. linear velocity dependencies are presented for the columns having a nominal mesopore diameter of ~25 nm. The minimum HETP values obtained with lysozyme for the monolithic silica columns having through-pores of 1.9, 3.5, and 6.0 µm were ~50, ~100, ~150µm, respectively. The same tendencies were obtained for cytochrome *C*. The magnitude of band broadening was dependant on the average through-pore diameter, and tended to diminish with decreasing through-pore size. Again, this result is due to the fact that the diffusion path length through the mesoporous void space of the skeleton increases as the diameter of the through-pores increases.

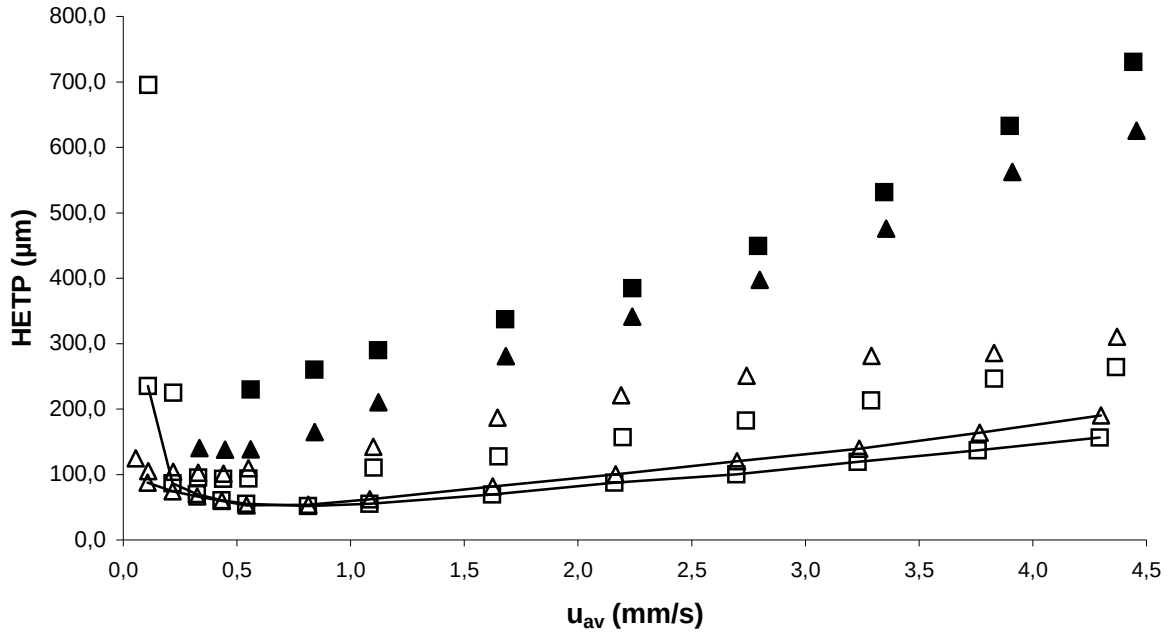

Figure 13. Plate height vs. linear velocity curves for lysozyme and cytochrome *C* on C18e monolithic silica columns of average mesopore diameter of 24–25 nm: —□— measured efficiency values on column 800 (1,9 µm flow-through pores and 25 nm mesopores) for cytochrome C; —Δ— measured efficiency values on column 800 for lysozyme; □ measured efficiency values on column 811 (3,5 µm flow-through pores and 24 nm mesopores) for cytochrome C; Δ measured efficiency values on column 811 for lysozyme; ■ measured efficiency values on column 842 (5,74 µm flow-through pores and 24,4 nm mesopores) for cytochrome C; ▲ measured efficiency values on column 842 for lysozyme.

Concluding remarks

Clearly, since the average size of the skeleton were greater with enlarged through-pore diameter, the diffusion path length through the mesoporous skeleton was increasing which lead to the loss of column efficiency as the nominal through-pore diameter increased. This result is analogous when increasing the particle diameter in a packed bed.

3.4. Impact of the structural parameters of silica monoliths with regard to fast mass transfer kinetics in HPLC

The monolithic silica columns with large mesopores and small through-pores showed higher separation efficiency than those with smaller mesopores and larger through-pores. The best column performance within the tested RP-18e columns for lysozyme was found for RP-18e column 800 (HETP = 45 µm), as displayed in Figure 14.

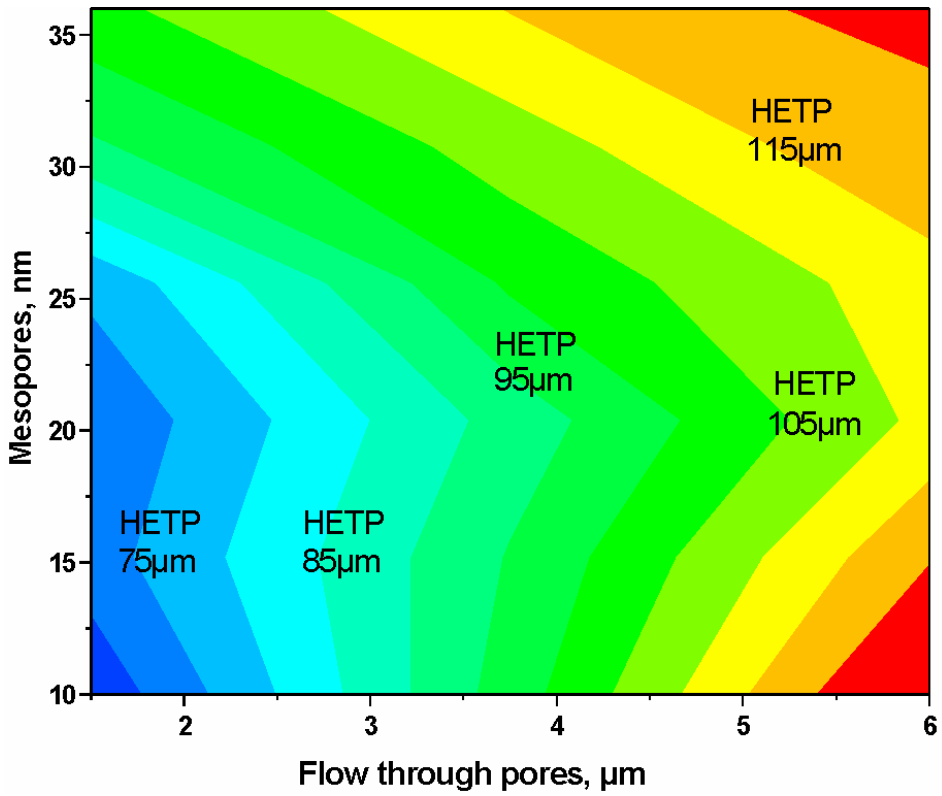

Figure 14. Dependency of column efficiency at minimum plate height of RP-18e monolithic silica columns on the flow through pore diameter and the mesopore diameter

It was found that as the diameter of the through-pores decreases, the column efficiency increases. The columns with the small-sized skeletons and mesopores large enough not to hinder the mass transfer rate of molecules in the mesoporous void space of the skeleton would give the lowest HETP values. The mesopore sizes have to be adapted to the molecular size of the analyte in particular to peptides and proteins. Consequently, the larger set of mesopores studied with a nominal diameter of ~25 nm provided the most efficient column performance because they provided less resistance to mass transfer in the mesoporous of the skeleton (see details in article V).

The comprehensive characterization of the selected monolithic silica structure parameters (see article II) as well as the results of modelling of the column efficiency enabled us to compare the experimental and predicted results (Figure 15).

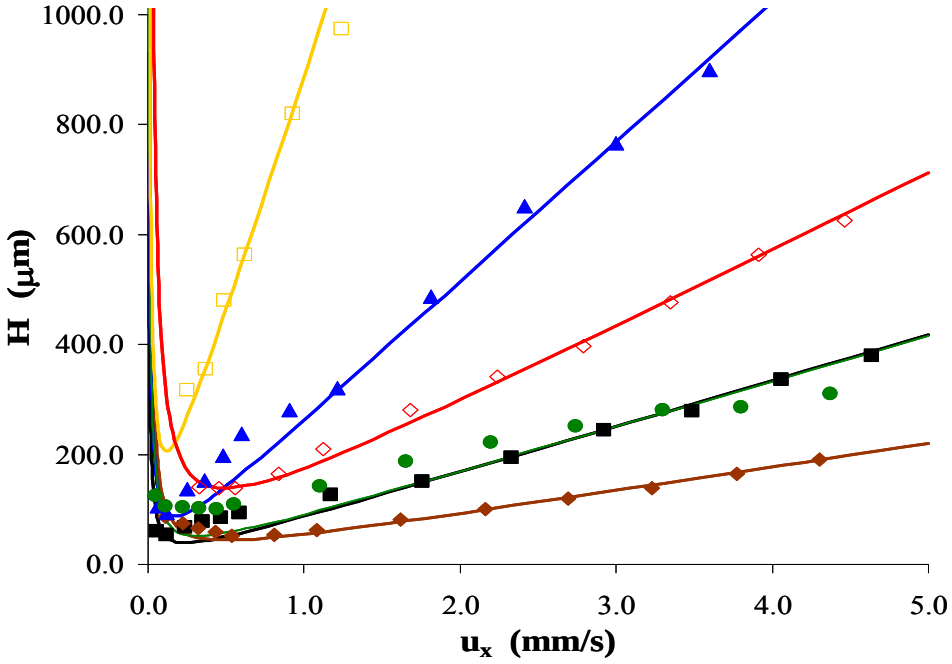

Figure 15. Theoretical and experimental HETP versus linear velocity curves for the monolithic silica columns for lysozyme as solute: ■ measured values for 787 (1,8 µm flow-through pores and 10,9 nm mesopores) monolithic silica column; ▬ calculated values for 787 monolithic silica column; ♦ measured values for 800 (1,9 µm flow-through pores and 25 nm mesopores) monolithic silica column; ▬ calculated values for 800 monolithic silica column; ▲ measured values for 803 (3,5 µm flow-through pores and 10 nm mesopores) monolithic silica column; ▬ calculated values for 803 monolithic silica column; ● measured values for 811 (3,4 µm flow-through pores and 24 nm mesopores) monolithic silica column; ▬ calculated values for 811 monolithic silica column; □ measured values for 842 (5,74 µm flow-through pores and 10 nm mesopores) monolithic silica column; ▬ calculated values for 842 monolithic silica column and ○ measured values for 843 (6 µm flow-through pores and 24,4 nm mesopores) monolithic silica column; ▬ calculated values for 843 monolithic silica column.

Further, the axial dispersion coefficient for the retained solute lysozyme and the size of the skeletons of silica monoliths were calculated as an average value from mercury intrusion, image analysis and permeability of a liquid. The graphic data shown in Figure 15 indicate a fairly good agreement between the theoretical and the experimental data. This means in addition that our assumptions on the impact of the surface area to volume ratio of the skeletons and external porosity influence on the column efficiency were correct. This enabled us to assess the conditions for the minimum plate height values for the investigated monolithic silica research columns.

In monoliths, the axial dispersion is significant since it increases with increasing flow-through pore size and their porosity. As a consequence this will lead to a significant decrease of the column efficiency. The size of the monolithic skeleton strongly depends on the flow-through pore size (it increases with increasing flow-through pore size) and this leads to a diminution of the column efficiency. Thus, for the optimum column efficiency one needs to reduce the flow-through porosity and flow-through pore size and increase the mesoporosity to maintain the overall porosity. The results of maximum column efficiency of all tested column values, (see article V) suggest that there is a limit of optimum performance of tested monolithic silica research columns. The best performance was obtained with a column that did not feature the smallest skeleton diameter values or the highest surface to volume ratios. This finding corresponds to the earlier conclusions by Billen et. al. [101] on the limit of column performance. In our case, this limit is between 0,45 μm and 0,62 μm of the skeleton diameter. The same corresponds to the surface to volume ratio from 4,819 Mm^{-1} to 7,018 Mm^{-1}.

Concluding remarks

Our results give clear evidence that if the surface area to volume ratios of the skeletons are optimized by controlling the average skeleton sizes and the external porosity of the monolithic columns, the efficiency of such supports might also reach a limit. However, this assumption is true only in the case of adjusted mesopore size and adjusted mesoporosity to the selected analyte.

4. Summary and Conclusions

Five different methods were critically examined to characterize the pore structure of the silica monoliths. The mesopore characterization was performed using: a) the classical BJH method of nitrogen sorption data, which showed overestimated values in the mesopore distribution and was improved by using the NLDFT method, b) the ISEC method implementing the PPM and PNM models, which were especially developed for monolithic silicas, that contrary to the particulate supports, demonstrate the two inflection points in the ISEC curve, enabling the calculation of pore connectivity, a measure for the mass transfer kinetics in the mesopore network, c) the mercury porosimetry using a new recommended mercury contact angle values.

The results of the characterization of mesopores of monolithic silica columns by the three methods indicated that all methods were useful with respect to the pore size distribution by volume, but only the ISEC method with implemented PPM and PNM models gave the average pore size and distribution based on the number average and the pore connectivity values.

The characterization of the flow-through pore was performed by two different methods: a) the mercury porosimetry, which was used not only for average flow-through pore value estimation, but also the assessment of entrapment. It was found that the mass transfer from the flow-through pores to mesopores was not hindered in case of small sized flow-through pores with a narrow distribution, b) the liquid penetration where the average flow-through pore values were obtained via existing equations and improved by the additional methods developed according to Hagen-Poiseuille rules. The result was that not the flow-through pore size influences the column bock pressure, but the surface area to volume ratio of silica skeleton is most decisive. Thus the monolith with lowest ratio values will be the most permeable.

The flow-through pore characterization results obtained by mercury porosimetry and liquid permeability were compared with the ones from imaging and image analysis. All named methods enable a reliable characterization of the flow-through pore diameters for the monolithic silica columns, but special care should be taken about the chosen theoretical model.

The measured pore characterization parameters were then linked with the mass transfer properties of monolithic silica columns. As indicated by the ISEC results, no restrictions in mass transfer resistance were noticed in mesopores due to their high connectivity. The mercury porosimetry results also gave evidence that no restrictions occur for mass transfer

from flow-through pores to mesopores in the small scaled silica monoliths with narrow distribution.

The prediction of the optimum regimes of the pore structural parameters for the given target parameters in HPLC separations was performed. It was found that a low mass transfer resistance in the mesopore volume is achieved when the nominal diameter of the number average size distribution of the mesopores is appr. an order of magnitude larger that the molecular radius of the analyte. The effective diffusion coefficient of an analyte molecule in the mesopore volume is strongly dependent on the value of the nominal pore diameter of the number averaged pore size distribution. The mesopore size has to be adapted to the molecular size of the analyte, in particular for peptides and proteins.

The study on flow-through pores of silica monoliths demonstrated that the surface to volume of the skeletons ratio and external porosity are decisive for the column efficiency. The latter is independent from the flow-through pore diameter. The flow-through pore characteristics by direct and indirect approaches were assessed and theoretical column efficiency curves were derived. The study showed that next to the surface to volume ratio, the total porosity and its distribution of the flow-through pores and mesopores have a substantial effect on the column plate number, especially as the extent of adsorption increases. The column efficiency is increasing with decreasing flow through pore diameter, decreasing with external porosity, and increasing with total porosity. Though this tendency has a limit due to heterogeneity of the studied monolithic samples. We found that the maximum efficiency of the studied monolithic research columns could be reached at a skeleton diameter of ~ 0.5 μm. Furthermore when the intention is to maximize the column efficiency, more homogeneous monoliths should be prepared.

5. References and selected reading

1. U. Wintermeyer in *Packings and Stationary Phases in Chromatographic Techniques* (Ed.: K.K. Unger) M. Dekker, New York, **1990**, pp. 87 – 234.
2. L.S. Ettre in *HPLC - Advances and Perspectives, Vol.1* (Ed.: Cs. Horvath), Academic Press, New York, **1980**, pp. 2 – 75.
3. L.S. Ettre, *Chromatographia*, **1996**, *42*, 343 – 351.
4. R. Kuhn, *Naturw.,* **1931**, *19*, 306.
5. J.F.K. Huber, *Ber. Bunsenges. Physik. Chem.,* **1973**, *77*, 179 – 184.
6. S. Hjerten, *J. Chromatogr. A*, **1989**, *473*, 273 – 275.
7. E.S.J. Cox in *Handbook of Heterogeneous Catalasis, Vol.4* (Eds. G.Ertl, H. Knözinger, J. Weitkamp), VCH, Weinheim, **1997**, pp. 1559 – 1633.
8. F.J. Janssen in *Handbook of Heterogeneous Catalasis, Vol.4* (Eds. G.Ertl, H. Knözinger, J. Weitkamp), VCH, Weinheim, **1997**, pp. 1633 – 1677.
9. *Monolithic Materials: preparation, properties and applications* (Ed.: F. Svec, T.B. Tennikova, Z. Deyl), Elsevier, Amsterdam, **2003.**
10. Nakanishi, K., Soga, N., J. Am. Ceram. Soc. 74 (1991) 2518.
11. Nakanishi, K., Soga, N., J. Non-Cryst. Solids 139 (1992) 1.
12. Nakanishi, K., Soga, N., J. Non-Cryst. Solids 139 (1992) 14.
13. Minakuchi, H., Nakanishi, K., Soga, N., Ishizuka, N., Tanaka, N., Anal. Chem. 68 (1996) 3498.
14. Nakanishi, K., Minakuchi, H., Soga, N., Tanaka, N., J. Sol-Gel. Sci. Technol. 8 (1997) 547.
15. Minakuchi, H., Nakanishi, K., Soga, N., Ishizuka, N., Tanaka, N., J. Chromatogr. A 762 (1997) 135.
16. Nakanishi, K., Minakuchi, H., Soga, N., Tanaka, N., J. Sol-Gel. Sci. Technol. 13 (1998) 163.
17. Ishizuka, N., Minakuchi, H., Nakanishi, K., Soga, N., Hosoya, K., Tanaka, N., J. Chromatogr. A 797 (1998) 133.
18. Cabrera, K., Wieland, G., Lubda, D., Nakanishi, K., Soga, N., Minakuchi, H., Unger, K.K., TrAC 17 (1998) 50.
19. Nakanishi, K., J. Sol-Gel Sci. Technol. 19 (2000) 65.
20. Ishizuka, N., Nakanishi, K., Hirao, K., J. Sol-Gel. Sci. Technol. 19 (2000) 371.

21. Cabrera, K., Lubda, D., Minakuchi, H., Nakanishi, K., J. High Resolut. Chromatogr. Commun. 23 (2000) 81.
22. Nakanishi, K., Cabrera, K., Lubda, D., J. High Resolut. Chromatogr. 23 (2000) 111.
23. Zoellner, P., Leitner, A., Lubda, D., Cabrera, K., Lindner, W., Chromatographia 52 (2000) 818.
24. Lubda, D., Cabrera, K., Minakuchi, H., Nakanishi, K., J. Sol-Gel Sci. Technol. 23 (2002) 185.
25. Motokawa, M., Kobayashi, H., Ishizuka, N., Minakuchi, H., Nakanishi, K., Jinnai, H., Hosoya, K., Ikegami, T., Tanaka, N., J. Chromatogr. A 961 (2002) 53.
26. Tanaka, N., Kobayashi, H., Ishizuka, N., Minakuchi, H., Nakanishi, K., Hosoya, K., Ikegami, T., J. Chromatogr. A 965 (2002) 35.
27. Tanaka, N., Kobayashi, H., Anal. Bioanal. Chem. 376 (2003) 298.
28. Siouffi, A.-M., J. Chromatogr. A 1000 (2003) 801.
29. Cabrera, K., J. Sep. Sci. 27 (2004) 843.
30. Leinweber, F. C., Lubda, D., Cabrera, K., Tallarek, U., Anal. Chem. 74 (2002) 2470.
31. Dong, M. W., "Modern HPLC for practicing scientists", John Wiley & Sons Inc., New Jersey (2006).
32. Gregg, S. J., Sing, K. S. W., "Adsorption Surface Area and Porosity", 2nd ed., Academic Press, London (1982) p. 303.
33. Rouquerol, F., Rouquerol, J., Sing, K. S. W.; "Adsorption by Powders and Porous Solids", Academic Press, London (1991) p. 467.
34. Lowell, S., Shields, J. E., "Powder, Surface Area and Porosity", 3rd. ed., Chapman & Hall, London (1991) p. 250.
35. Gorbunov, A. A., Solovyova, L. Ya., Pasechnik, V.A., J.Chromatogr. 448 (1988) 307;
36. Hagel, L., Östberg, M., Andersson, T., J. Chromatogr. A 743 (1996) 33.
37. Goto, M., McCoy, B.J., Chem. Eng. Sci. 55 (2000) 723.
38. Al-Bokari, M., Cherrak, D., Guiochon, G., J. Chromatogr. A 975 (2002) 275.
39. Ritter, H. L., Drake, L. C., Ind. Eng. Chem. Anal. Chem. 17 (1945) 782;
40. Drake, L. C., Ritter, H. L., Ind. Eng. Chem. Anal. Ed. 17 (1945) 787;
41. Washburn, W., Phys. Rev. 17 (1921) 273;
42. Carman, P. C., Soil Sci. 52 (1941) 1;

43. Carman, P.C., “Flow of Gases through Porous Media”, Butterworths, London (1956) Chap.1;
44. D. Lubda, J. Chromatogr. A 1083 (2005) 14.
45. H. Minakuchi, J. Chromatogr. A 797 (1998) 121.
46. N. Vervoort, Anal. Chem. 77 (2005) 3986.
47. M. D. Montminy, J. Colloid Interf. Sci. 280 (2004) 202, C.A. Baldwin, J. Colloid Interf. Sci. 181 (1996) 79.
48. H. Jinnai, Langmuir 17 (2001) 619.
49. J. Courtois, Anal. Chem. 79 (2007) 335.
50. P. Gzil, J. Sep. Sci. 29 (2006) 1675.
51. J. Billen, Anal. Chem. 78 (2006) 6191.
52. P. Gzil, Anal. Chem. 76 (2004) 6707.
53. N. Vervoort, Anal. Chem. 75 (2003) 843.
54. J.F. Parcher, Anal. Chem. 1997 229A.
55. I. Halasz, Angew. Chemie, Int. Ed., 17, 1978, 901.
56. J. Knox, J. Chromatogr., 326, 1984, 311.
57. S. Brunauer, J. Am. Chem. Soc. 62, 1940, 1723-1732
58. IUPAC, Recommendations, Pure Appl. Chem. 66, 1994, 1739-1758.
59. Barrett, E. P., Joyner, L. G., Halenda, P. P., J. Amer. Chem. Soc. 73 (1951) 373;
60. Brunauer, S., Emmet, P.H., Teller E., J. Am. Chem. Soc. 60 (1938) 309;
61. Gurwitsch, L. G., J. Phys. Chem. Soc. Russia 47 (1915) 805;
62. Washburn, E. W., Proc. Natl. Acad. Sci. U.S.A. 7 (1921) 115;
63. Thommes, M.; In: “Nanoporous Materials, Science & Engineering”, Lu, G. Q., Zhao, X. S. (Editors), Imperial College Press, New York (2004) Chapter 11;
64. Neimark, A. V, Ravikovitch, P. I., Microporous Mesoporous Mater. 44 (**2001**) 697;
65. Lowell, S., Shields, J., Thomas, M.A., Thommes, M., “Characterization of Porous Solids and Powders: Surface Area, Pore Size and Density”, Springer, The Netherlands (2004);
66. León y León, Adv. Colloid Interface Sci. 76 (1998) 341;
67. Neimark, A.V., Colloid Journal of the USSR 46 (1984) 639;
68. Tsakiroglou, Payatakes, A.C., Adv. Colloid Interface Sci. 75 (1998) 215;
69. Rigby, S., in: “Characterization of Porous Solids VI”, Rodriguez-Reinoso, F., MacEnaney, B., Rouquerol, J., Unger, K. (Editors), “Studies in Surface Science and Catalysis”, Vol. 144, Elsevier , Amsterdam (2002) p. 1854;

70. Rigby, S. P., Evbuoumwan, I. O., Watt-Smith, M. J., Edler, K., Fletcher, R.S., Part. Part. Syst. Charact. (**2006)** 82;
71. Day, M., Parker, I. B., Bell, J., Thomas, M., Fltecher, R., Duffie J., in: "Characterization of Porous Solids II", Rouquerol, J., Rodriguez-Reinoso, F., Sing, K. S. W., Unger, K.K. (Editors) Amsterdam (1991) p. 75;
72. Day, M., Parker, I. B., Bell, J., Fletcher, R., Duffe, J., Sing, K. S. W., Nicholson, D., in: "Characterization of Porous Solids III", Rouquerol, J., Rodriguez-Reinoso, F., Sing, K. S. W., Unger, K. K. (Editors), "Studies in Surface Science and Catalysis", Vol. 87, Elsevier, Amsterdam (1994) p. 225;
73. Giesche, H., Part. Part. Syst. Charact. 23 (**2006**) 9;
74. Giesche, H., Mat. Res. Soc. Symp. Proc. 431 (1996) 151;
75. Lowell, S., Shields, J. E., J. Colloid. Interface Sci. 80 (1981) 192;
76. Lowell, S., Shields, J. E., J. Colloid. Interface Sci. 83 (1981) 273;
77. Salmas, G., Androutsopolous, G. J., J. Colloid Interface Sci. 239 (2001) 178;
78. Petropoulos, J. H., Petrou, J. K., Kanellopoulos, N. K., Chem. Eng. Sci. 44 (1989) 2967;
79. Petropoulus, J. H., Petrou, J. K., Sep. Technol. 2 (1992) 162;
80. Gusev, I., J. Chromatogr. A 855 (1999) 273;
81. Minakuchi, H., Nakanischi, K., Soga, N., Ishizuka, N., Tanaka, N., J. Chromatogr. A 797 (1998) 121;
82. Leinweber, F. C., Tallarek, U., J. Chromatogr. A 1006 (2003) 207;
83. Vervoort, U., Gzil, P., Baron, G. V., Desmet, G., Anal. Chem. 75 (2003) 843;
84. Vervoort, N., Saito, H., Nakanischi, K., Desmet, G., Anal. Chem. 77 (2005) 3986;
85. Gzil, P., Vervoort, N., Baron, G. V., Desmet, G., Anal. Chem. 76 (2004) 6707;
86. M. Knoll, Zeitschrift für technische Physik, 16, 1935, 467-475.
87. M. von Ardenne, Zietschrift für Physik, 108, 1937, 553-572;
88. M. von Ardenne, Zietschrift für technische Physik, 19, 1937, 407-416.
89. M. von Ardenne GB patent 511204.
90. I. Gusev, J. Chromatogr. A 855 (1999) 273.
91. R. Skudas, B.A. Grimes, O. Kornysova, D. Lubda, K.K.Unger, presented at the 30th International Symposium on High Performance Chromatography and Related Techniques, Stockholm, Sweden, June 25–28, 2005.
92. Martin J. P., Synge, R. L., Biochem. J. 35 (1941) 1358;

93. van Deemter, J. J., Zuiderweg, F. J., Klinkenberg, A., Chem. Eng. Sci. 5 (1956) 271;
94. Giddings, J. C., J. Chromatogr. 5 (1961) 47;
95. Giddings, J. C., J. Chromatogr. 5 (1961) 61;
96. Ishizuka, N., Minakuchi, H., Nakanishi, K., Hirao, K., Tanaka, N., Colloids Surf. A 187 (2001) 273;
97. Liapis, A. I., Meyers, J. J., Crosser, O. K., J. Chromatogr. A 865 (1999) 13;
98. Meyers, J. J., Liapis, A. I., J. Chromatogr. A 852 (1999) 3;
99. Vervoort, N., Gzil, P., Baron, G. V., Desmet, G., J. Chromatogr. A 1030 (2004) 177;
100. Gritti, F., Piatkowski, W., Guiochon, G., J. Chromatogr. A 978 (2002) 81;
101. Billen, J., Gzil, P., Desmet, G., Anal. Chem. 78 (2006) 6191;

6 List of publications

1. K. K. Unger, R. Skudas, M. M. Schulte, J. Chromatogr. A, 1184 (2008) 393-415
2. B. A. Grimes, R. Skudas, K. K. Unger, D. Lubda, J. Chromatogr. A, 1144 (2007) 14-29;
3. M. Thommes, R. Skudas, K.K. Unger, D. Lubda, J. Chromatogr. A, 1191 (2008) 57-66;
4. R. Skudas, B. A. Grimes, M. Thommes, K. K. Unger, J. Chromatogr. A, 1216 (2009) 2625-2636;
5. R. Skudas, B. A. Grimes, E. Machtejevas, V. Kudirkaite, O. Kornysova, T. P. Hennessy, D. Lubda, K. K. Unger, J. Chromatogr. A, 1144 (2007) 72-84.

7. Glossary of symbols

A_c	the rate of volume flow across the cross section
BET	Brunauer-Emmet-Teller theory for specific surface area determination from nitrogen sorption data
BJH	Barret-Joyner-Halenda method for deriving mean pore size distribution from nitrogen sorption data
C18	n-octadecyl bonded silica phase
D_f	the average diameter of the flow through pores of silica monoliths
D_L	the axial dispersion coefficient of the solute in the mobile phase
D_p	the effective diffusion coefficient of the analyte in the confined mesoporous space of the skeleton
ε_b	the void fraction of the flow-through pores void space in the column
ε_p	the void fraction of the monolithic skeleton
ε_t	the total void fraction of the monolithic silica column
G	Guzrwitsch method to calculate the specific pore volume from nitrogen sorption data
H	the height equivalent of a theoretical plate or plate height
HETP	the height equivalent of the theoretical plate H
HPLC	High performance liquid chromatography
ISEC	inverse size exclusion chromatography
IUPAC	International Unity of Pure and Applied Chemistry
J_v	the steady state volume flux
K_b	the volume partition coefficient of the finite sized molecule in the flow-through porous void space of the monolithic column
K_{eq}	the equilibrium adsorption constant of the linear adsorption isotherm

k_f	the film mass transfer coefficient of the analyte
K_p	the volume partition coefficient of the finite sized molecule in the mesoporous void space of the skeleton
L	the length of the column
LC	liquid chromatography
µm	micro meter
N	number of theoretical plates
NLDFT	Nonlocal Density Functional Theory for deriving mean pore size distribution from nitrogen sorption data
nm	nano meter; 1nm=10°A
n_T	pore connectivity
$p_{d,mes}$	average mesopore size distribution
PNM	pore network model
PPM	parallel pore model
r_m	analyte radius
R_p	the radius of the monolithic silica skeletons
RP	Reversed Phase
SEC	Size Exclusion Chromatography
u	the linear flow velocity of the eluent
u_{av}	the average linear velocity through the bed

Available online at www.sciencedirect.com
ScienceDirect
Journal of Chromatography A, 1184 (2008) 393–415
JOURNAL OF CHROMATOGRAPHY A
www.elsevier.com/locate/chroma

Review

I

Particle packed columns and monolithic columns in high-performance liquid chromatography-comparison and critical appraisal

Klaus K. Unger[a,*], Romas Skudas[a], Michael M. Schulte[b]

[a] *Institut für Anorganische Chemie und Analytische Chemie, Johannes Gutenberg-Universität-Mainz, Duesbergweg 10-14, D-55099 Mainz, Germany*
[b] *Performance & Life Science Chemicals R&D, Merck KGaA, Frankfurter Land Str. 250, 64293 Darmstadt, Germany*

Available online 23 December 2007

Dedicated to Professor K.S.W. Sing, Professor emeritus at the former Department of Chemistry, Brunel University, Uxbridge, UK for his strong support over thirty years.

Abstract

The review highlights the fundamentals and the most prominent achievements in the field of high-performance liquid chromatography (HPLC) column development over a period of nearly 50 years. After a short introduction on the structure and function of HPLC columns, the first part treats the major steps and processes in the manufacture of a particle packed column: synthesis and control of particle morphology, sizing and size analysis, packing procedures and performance characterization. The next section is devoted to three subjects, which reflect the recent development and the main future directions of packed columns: minimum particle size of packing, totally porous vs. core/shell particles and column miniaturization. In the last section an analysis is given on an alternative to packed columns—monolithic columns, which have gained considerable attraction. The challenges are: improved packing design based on modeling and simulation for targeted applications, and enhanced robustness and reproducibility of monolithic columns. In the field of miniaturization, particularly in chip-based nano-LC systems, monoliths offer a great potential for the separation of complex mixtures e.g. in life science.

Keywords: Particle packed columns; Monolithic columns; High-performance liquid chromatography; Fundamental aspects and recent developments

Contents

* Corresponding author. Tel.: +49 6151 152630; fax: +49 6151 152631.
E-mail address: k.k.unger@web.de (K.K. Unger).

0021-9673/$ – see front matter © 2007 Elsevier B.V. All rights reserved.
doi:10.1016/j.chroma.2007.11.118

I

1. Introduction

The consumption of analytical columns worldwide is estimated to be ca 2 million per year. If one assumes that each HPLC instrument requires five columns per year on average, one can easily estimate the number of HPLC instruments. These figures clearly indicate that a HPLC column is a widely used consumable; nevertheless, its impact on system performance is considerably higher than its cost contribution.

Only a minority of users, however, can imagine the complex structure of HPLC columns. Typically, an analytical column has an inner diameter (I.D.) of 4.6 mm and a length of 100 mm and is packed with 5 μm spherical particles. A simple calculation shows that such a column contains roughly 10 billion particles in a dense array taking into account that the column porosity is 40%.

It should be emphasized that it took more than 20 years before scientists and engineers were able to design and manufacture such columns in reproducible enough fashion to meet the stringent demands in quality control of modern analytical laboratories. It is evident that many innovative and experienced investigators have contributed to achieve these results.

This happened less in a planned concerted action but more in a frog-leap way with alternating technical and technological advances between equipment, e.g. high pressure pumps, sensitive UV-detectors, particle synthesis and characterization and corresponding column hardware design, until the idea was accepted, realized and integrated into a convincing technical approach.

The majority of the pioneers of modern liquid chromatography started from gas chromatography, while others had a background in inorganic, organic, physical or surface chemistry, in physics, or in chemical and mechanical engineering.

It took several decades before scientists invented, as an alternative to particle packed beds, columns made of a single monolithic block, composed of porous polymers or porous silica. The development of monoliths was born in the field of ceramics, where they were used as carriers in the field of catalytic conversion of automobile exhaust gases which were converted into non-toxic effluents such as water, nitrogen and carbon dioxide. Monoliths composed of high temperature stable oxides were manufactured as solid porous rods with regular channels with millimetre openings. The open structure of such monoliths enabled a fast reaction of the exhaust gas with the catalytic components deposited at the surface of the channels of the monoliths [1]. While such monoliths were made by extrusion of a paste composed of powdered and highly dispersed oxides and oxihydrates, attempts were made to generate monoliths with defined and controlled pore system via the sol–gel route using porogens. Pioneering work was done by Soga and Nakanishi at the Kyoto University, Japan [2,3]. Tanaka at the Kyoto Institute of Technology [4] was the first who recognized the value of porous monolithic rods as columns for HPLC. The basic idea was to employ such monoliths as stable and reproducible columns enabling a much faster separation at lower pressure than particle packed beds were able to achieve. Simultaneously, Tennikova et al. synthesized rigid porous monoliths made of cross-linked polymers [5].

The development of porous microparticles and porous monoliths were one significant achievement among other drivers e.g. in instrumentation which provided the basis for the widespread application of HPLC in pharmaceutical and industrial analysis. The hyphenation of HPLC as a multidimensional technique coupled to mass spectrometric detection was another significant step towards solving complex analytical tasks. Looking forward one can assume that combining reliable equipment with sensitive detection is likely to become one of the most powerful analytical methods available for modern life science approaches such as proteomics, peptidomics, metabolomics. Yet this field is still in its infancy as compared to routine HPLC analysis in pharmaceutical industry, where the majority of today's produced columns are applied and consumed.

This article will focus on aspects of column structure in connection with the expected chromatographic resolution and will critically examine the limitations and pitfalls in column design and development drawing on 50 years experience in this field. In addition, an attempt is made to compare and critically review

the two types of sorbents, namely packed particulate beds and monolithic structures applied to HPLC.

2. Particle packed columns

2.1. Structure and function of a high-performance liquid chromatography column

The selective separation of a complex mixture into individual species by column liquid chromatography requires a sufficiently large surface of the adsorbent particles with interactive surface sites to selectively retain analytes based on their chemical composition and structure. Usually a column packed with porous micron-sized particles (see Fig. 1) is applied in order to achieve this separation. In elution chromatography, the sample is transported by a convective flow through the packed column. The convective flow is generated by a pump (pressure driven mode). As the particles possess pores of the order of 10 nm, the internal surface carrying the molecular discriminators has to be reached by diffusion of the analytes. Diffusion of solutes in a liquid phase is usually three orders of magnitude slower than in the gas phase for small to medium sized molecules. In addition, diffusion into and out of tortuous pores (pore diffusion) reduces significantly the diffusivity as compared to diffusion in the liquid bulk phase. A central problem in HPLC is therefore to overcome the limitations of hindered mass transfer of solutes due to pore diffusion by providing sufficient access to the interactive surface sites. One way is to reduce the average particle size of the packing to minimize the diffusion path length by using micro particulate packings. Unfortunately, any reduction in particle size results in increased column pressure drop. Another alternative is to introduce a bimodal pore size distribution within the particles with mesopores to generate sufficient surface area and macropores to enhance the mass transfer kinetics. Those flow-through pores with sizes larger than 80 nm enable a convective flow within the particle.

The most powerful means, however, is to use an electrical field along the packed column (electrically driven chromatography in packed capillaries is called capillary electrochromatography or CEC). In the case of silica particles as a packing material, which carry a negative surface charge, and a buffer as an eluent, an electroosmotic flow (EOF) directed to the cathode is generated, which leads to a convective flow within the porous particles. As a result, the mass transfer kinetics are drastically enhanced, which is reflected in achieving large numbers of theoretical plates of such columns [7]. Although CEC became popular at the beginning of 1990s, the potential of this approach was hardly recognized. The theoretical treatment is still in its infancy and thus a basic understanding of the mass transfer and distribution equilibrium, particularly for charged analytes, is lacking [8–12].

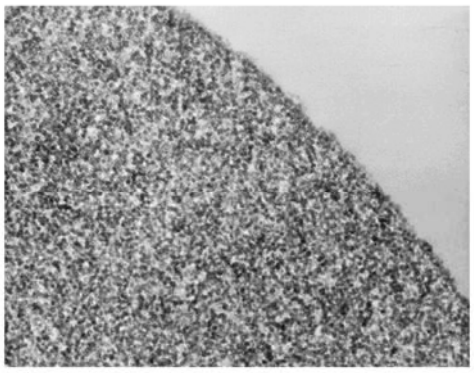

Fig. 1. Transmission electron micrograph of a porous silica microparticle (magnification ×150,000 times) (reproduced by the permission of author [6]).

2.2. How to make a high-performance liquid chromatography column?

A HPLC column is normally a stainless steel tube with 4.0 or 4.6 mm I.D. densely packed with micron size silica particles. The pathway from a mirror-finished tube to a packed HPLC column comprises a sequence of carefully controlled steps. The first is the synthesis and manufacturing of spherical particles (see Section 2.2.1). The second is the sizing and size classification (see Section 2.2.2). The surface functionalization usually involves several steps on its own. Next, a particle suspension is prepared, which is filtered at high flow-rate and increasing pressure through the column (column packing) (see Section 2.2.3). The column has to be flushed and conditioned and subjected to tests to assess the column performance and selectivity (see Section 2.2.4). Fig. 2 shows a scheme of the manufacturing process of an *n*-octadecyl bonded silica material of 5 μm average particle size [13].

2.2.1. Synthesis and particle formation

Classical LC is performed with irregularly shaped silica particles of 30–40 μm, 40–60 μm or larger sizes. These particles are obtained by consecutive grinding or milling of larger particles e.g. of silica xerogel lumps, followed by size classification, commonly performed with sieves of a given aperture. This holds for particles larger than 25 μm. Microparticulate packings are classified employing the air elutriation technique. In this way packings of 5–10 μm were made at the beginning of HPLC. There have been heavy scientific debates at the beginning of HPLC mainly at the annual Zlatkis Meetings in Houston, TX, USA, between 1969 and 1975, whether irregular or spherical particles would be the preferred packings of HPLC columns with respect to pressure drop, column stability and column performance. This discussion is still ongoing. To go deeper into such comparison, it must be said that not only the particle morphology must be taken into account but also the particle size distribution, the amount of fines and the type of packing procedure. A study under these aspects was performed by Verzele et al. [14]. In the period between 1970 and 1995 the columns with irregular particles were replaced by those packed with spherical particles at least for analytical columns. Spherical or spheroidal particles were produced from synthetic cross-linked polymers according to specific synthesis procedures. Packings

I

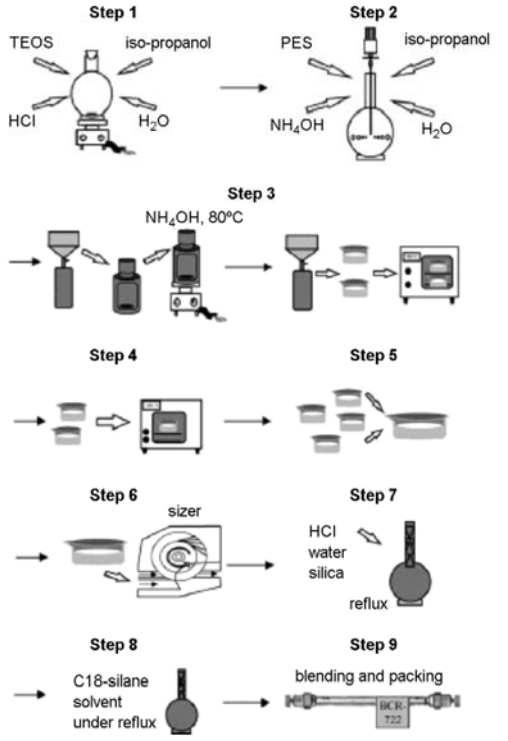

Fig. 2. A scheme of the manufacturing processes of an *n*-octadecyl bonded silica material for liquid chromatography. The synthesis comprise: PES (polyethoxysilane) synthesis (step 1); conversion of PES into hydrogel beads (step 2); washing, aging and drying (step 3); calcination (step 4); blending of individual batches into a master batch (step 5); size classification (step 6); rehydroxylation (step 7); silanazition (step 8); and blending and packing material into HPLC columns (step 9) [13].

with irregular particles, in particular silica, are still on the market.

At the beginning of the seventies no spherical silica particles in the size range between 5 and 10 μm were available and appropriate synthesis protocols had to be developed.

Several synthetic routes and processes can be employed to generate spherical particles, which are specific for each material. For the manufacture of spherical silica particles the following processes were employed:

(1) subjecting colloidal silica dispersions to gelling into a two phase system [15,16];
(2) hydrolysis and polycondensation of polyethoxysiloxane (PES) to silica hydrogel beads under stirring in a two-phase system [17–23];
(3) agglutination of silica sols in presence of a polymer followed by calcination of the beads [24];
(4) spray drying of silica sol suspensions [25];
(5) formation and growing of silica nano particles in suspensions [26,27].

The silica sources were sodium silicates, stabilized silica sol suspensions and alkoxysilanes. In some cases templates, porogens and detergents were added to adjust and to control the pore structural parameters and to achieve the spherical morphology. Afterwards, the additives had to be thoroughly removed by washing after or the dried particles had to be subjected to a controlled calcination up to 600 °C to burn out the organic constituents.

The major goals of the manufacturing processes were to achieve a spherical morphology of the particles and simultaneously adjust and control the pore structural parameters such as the specific surface area, the specific pore volume or particle porosity and the average pore diameter.

The following values were reported for the most commonly used silica based packing materials employed as base materials for the separation of low molecular weight analytes (MW < 1000 Da):

(i) specific surface area, a_s (BET): 100–400 m^2/g;
(ii) specific pore volume, v_p: 0.4–1.0 mL/g;
(iii) average pore diameter, p_d: 6–50 nm.

Packings suitable for the separation of synthetic polymers and biopolymers possess larger pores of average pore diameter >50 nm. Correspondingly the specific surface area of these materials becomes smaller than 50 m^2/g.

One has to take into account that these values decrease after the surface functionalization. The extent of decrease depends on the chemistry or the way the modification is performed (e.g. silanization, polymer coating, etc.).

Generally, a decision has to be made, whether the packing is employed for the separation of low molecular weight analytes (MW < 1000 Da) or for the separation of high molecular weight compounds (MW ≫ 10,000 Da). As a rule of thumb, for efficient separation, the average pore diameter of an adsorbent particle should be four times larger than the hydrodynamic diameter of the analytes, in order to minimize hindered diffusion and to enhance mass transfer kinetics [28].

The major field of application is the resolution of low molecular weight fine chemicals and pharmaceuticals. Here, an average pore diameter of ca. 10–12 nm is sufficient, which results in a specific surface area of roughly 300 m^2/g. An average pore diameter of 30 nm is needed to resolve analytes of a molecular weight between 20,000 and 50,000 Da. For polymers of larger molecular weight an average pore diameter of 50 or even 100 nm is required. The specific surface area then is notably lower. However, in surface–solute interactions with biopolymers by ion-exchange chromatography (IEC), hydrophobic interaction chromatography (HIC), reversed-phase liquid chromatography (RPLC), etc., the magnitude of the specific surface is not the critical parameter as a result of the strong interactions between the biopolymer and the active sites of the surface. Studies on biopolymer separations with nonporous 2 μm particles and a specific surface area of only 5 m^2/g in RPLC, HIC and IEC

modes have demonstrated that fast and high-resolution separations can be achieved [29–32].

In terms of pore size and pore size distribution, two aspects have to be considered. First, a packing material should be free of micropores (pores < 2 nm). Micropores generate a high surface area, with a high adsorption potential. In addition, small pores lead to small mass transfer kinetics by slowing down the diffusion of solute molecules in the pores. The second issue is that the pores of packing should be highly interconnected to facilitate the mass transfer of analytes during the chromatographic separation process. The aspect of pore connectivity, which is well known in the design of heterogeneous catalysts, has received considerable attention during the last decade in the field of modelling and simulation of pore structures [33–35].

When discussing pore structural parameters and comparing different packing materials one should keep in mind that the specific surface area according to BET is determined with nitrogen – a small probe molecule in the gas phase at 77 K. HPLC takes place in a liquid phase and separates molecules, which typically are considerably larger than the nitrogen molecule. Thus the magnitude of the specific surface area according to BET, in such case, is not a proper measure of the accessibility of pores in the liquid phase. As a consequence, the effective surface area for specific interactions may be much smaller.

The same distinction holds for the characterization of the pore size, or more precisely the pore volume distribution of packings. Usually, the pore size distribution is derived from the desorption branch of the nitrogen sorption isotherm at 77 K by application of the Kelvin equation with appropriate corrections [36]. An alternative method, known as inverse size-exclusion chromatography (ISEC) using polymer standards [37–42] can be applied to overcome the drawbacks of gas sorption methods, since ISEC is based on liquid chromatographic measurements and more relevant specific surface areas and pore volume distribution values are obtained. This holds for both inorganic porous adsorbents with various surface modifications [43] as well as for swellable cross-linked organic polymers [44,45]. Various reviews [41,46] showed the applicability and reliability of the method, without taking of the pore connectivity and pore shape into account. Grimes et al. [42] recently achieved to estimate the pore connectivity.

The reported parameters can be expressed in relation to the unit of mass of adsorbent and packing. However, it is generally more relevant to refer to unit of column volume. Instead of using the bulk density of particles, the packing density is the most reliable parameter, i.e. the mass of particle being packed per unit volume of the column. The packing density ranges between 0.4 g/cm^3 for highly porous particles with a specific pore volume larger then 1 g/cm^3 up to 0.8 g/cm^3 for low porosity particles having a specific pore volume of approximately 0.4 g/cm^3. For example, highly ordered mesoporous silica of type MCM-41 (mobil composition of matter), first introduced by researchers from Mobil Oil Corp., USA, possess a high specific surface area in excess of 1000 m^2/g and a high specific pore volume of larger than 1 cm^3/g [47,48]. The bulk and packing density, however, is relatively low and thus the specific surface area per unit volume becomes by a factor of ~2 smaller then the value per unit mass. This becomes important when one compares different column packings. In consequence the pore structural parameters should be expressed per unit volume.

2.2.2. Sizing and size analysis

At the early application of HPLC, the packings of choice were irregularly shaped native silica particles operated with organic eluents in the so-called normal-phase chromatography mode. The first action was to mill and to grind larger silica xerogel particles to batches with the desired particle size. At this time no technical means were available to fractionate or size micro particulate packings. Sieving, as done traditionally, was not an efficient and economic process. Therefore, in the 1970s, based on their experience in air stream technology for aircrafts, Alpine (Augsburg, Germany) developed and introduced novel equipment for sizing based on the phenomenon of air elutriation. The core of the Alpine Zig-Zag siever was a metal wheel with zig-zag channels rotating at high speed, which gives a separation into coarse and fine particles. Removing particles at the upper and the lower end of the particle size distribution had to be repeated until a desired particle size distribution was achieved. The classification was accompanied by particle analysis to control the sizing process [49,50].

The smaller the particle – the higher the rotation speed of the wheel had to be. The particles were subjected to high abrasion forces while running through the channels of the siever and thus fines were formed, often adhering to the surface of larger particles. Based on the relationship between particle size and rotation speed the lower limit of sizing silica particles was ca. 2 μm. The sizing process usually resulted in substantial material losses, depending on how narrow the intended size distribution was. Losses of 50% (w/w) were common. In addition, the silica became polluted with iron; the latter had to be removed by an acid treatment of the sized material [13]. Apart from air elutriation [51], other methods can be applied [52] e.g. sedimentation of the dilute silica suspension in the counter current mode [53].

Particle size analysis is an essential tool to control the result of sizing. Nowadays, a number of effective technologies are available to assess the particles size distribution in the range between 1 and 10 μm. More than 50 different methods have been described in the literature for the analysis of particle shape and size distribution. They mainly differ in the applied measuring principle, the particle size range they can be used for, the information they are extracting from the particles and the necessary measuring time.

The most common measuring principles for the determination of particle size distributions of chromatographic packings are listed in Table 1. They can be grouped into five different categories according to their measuring principle: Sieve- and classification analysis, light scattering, sedimentation analysis, electronic measurements and microscopic principles.

The most common particle size analysis methods are collected and briefly described in Appendix A.

Each instrument is based on a given principal and measuring technique and thus provides a specific and varying average of the particle diameter – d_p. The particle diameter can be expressed as the number average – d_{pn}, the surface average – d_{ps}, the weight

Table 1
The measuring principles for the determination of particle size distributions of chromatographic packings

Method	Particle size range (μm)	Information from single particles or multitude	Form information	Separating method	System manufacturers (web address)
Sieve analysis					
Dry sieving	>20	Single	No	Yes	Retsch (www.retsch.de
Air sieving	>5	Single	No	Yes	
Sonic sieving	>5	Single	No	Yes	Gilsonic (www.christison.com)
Light scattering					
Laser diffraction	0.05–30	Multitude	No	No	Malvern (www.malvern.co.uk); Helos
Turbidimetric systems	0.05–30	Multitude	No	No	
Single-particle optical sensing (SPOS)	0.5–400	Single	No	Yes	Nicomp, Particle Sizing Systems (www.pssnicomp.com)
Light obscuration (AccuSizer)					
Sedimentation					
Pipette analysis	0.5–300	Multitude	No	Yes	
Sedimentation balance	0.5–300	Multitude	No	Yes	
Photo- or X-ray sedimentation	>2	Multitude	No	Yes	
Centrifugal sedimentation	0.0005–50	Single	No	Yes	CPS instruments (www.cpsinstruments-eu.com)
Resistazone counters					
Electrical sensing zone (ESZ) method	0.4–1200	Single	No	No	Coulter Counter (www.beckman.com)
Optical methods					
Light microscopy	0.5–250	Single	Yes	No	Image analysis: SigmaScan (www.spssscience.com)
Electron microscopy	0.001–10 (100)	Single	Yes	No	
Flow through photometry	2–9000	Single	Yes	Yes	
Flow cytometry (Sysmex)	0.7–160	Single	Yes	Yes	Malvern (www.malvern.co.uk)
Field flow fractionation					
Gravitational FFF	10–100	Multitude	No	Yes	Postnova analytics (www.postnova.com)
Centrifugal sedimentation FFF	2–15	Multitude	No	Yes	

average – d_{pw} and the volume average – d_{pv}. For statistical reasons ranking of averages is as follows [54]:

$$d_{p_n} < d_{p_s} < d_{p_w} < d_{p_v}$$

The smallest value is the number average; the largest is the volume average in this series. Assuming that the weight of the spherical particle $w_i \approx s_i d_i \approx n_i d_i^2$, where s_i is the surface area of the spherical particle of diameter d_i and n_i is the number of the spherical particles, the weight average can be expressed by a surface average and the number average [18,55].

The particle size distribution can be presented as a cumulative distribution or as a differential distribution. There are three different average values: the mean, the median and the mode [55]. Table 2 gives an example of certain characteristic values of silica packing. In HPLC, the volume average of the particle size is the most informative one, because it refers to the volume of the column. However, the number average is also useful to visualize the fine particle and their distribution.

There has been much discussion on how narrow a particle size distribution should be to generate the most stable packing and the highest column performance. As a rule of thumb the ratio of the d_{p90} value (average value at 90% of the cumulative distribution) to the d_{p10} value (average value at 10% of the cumulative distribution) should amount from 1.5 to 2.0 for particles in the range of 3–7 μm (analytical HPLC columns) [56].

2.2.3. Packing procedures

In the early stages of LC, columns were obtained by dry packing 30–40 μm particles into glass columns using a methodology, that involved repeated damping (mechanically tapping the column or lifting it up in the air and letting it drop) of the packed column. [57]. The first HPLC columns were also dry-packed into stainless steel columns with microparticulate packings by Huber and Kraak at the University of Amsterdam by mechanically pushing the particles into the column blank with a rod.

Enormous efforts were undertaken to develop an efficient packing procedure for micro particulate packings in stainless steel columns [58]. The most common one is the slurry technique: a dilute suspension of the particles is forced under high pressure and high flow-rate into the column. The column end contains a porous frit, which retains the particles. When 4.6 mm I.D. 250 mm long columns are packed with 5 μm particles, the back pressure may rise up to 500 bar at flow rates in excess of 10 mL/min. Such procedure would require a high pressure pump and a properly designed stainless steel reservoir.

The steps are as follows [59]:

Table 2
Summary of a particle size measurement (volume and number statistics), performed with Particle Sizing Systems, Santa Barbara, California, U.S.A. (data supplied by Dr. F. Krebs, Merck KGaA, Darmstadt)

Volume statistics (geometric) 6.01					
Calculations from 0.96 to 33.50%					
Volume		100.0%		Coinc. connected	195,770
Mean		8.267 μm		SD	0.091
Median		8.236 μm			
Mean/median ratio		1.004		Variance	0.0082
Mode		8.089 μm		Skewness:-4.625e-001 left skewed	
%	<5.000	<10.00	<50.00	<90.00	<95.00
Size (μm)	6.067	6.475	8.236	10.74	11.54
d_{p90}/d_{p10}		1.66			
Number statistics (geometric) 6.01					
Calculations from 0.96 to 33.50%					
Number		100.0%		Coinc. connected	195,770
Mean		6.240 μm		SD	0.221
Median		7.138 μm			
Mean/median ratio		0.874		Variance	0.049
Mode		7.341 μm		Skewness:-2.010e-001 left skewed	
%	<5.000	<10.00	<50.00	<90.00	<95.00
Size (μm)	1.545	2.865	7.138	9.344	10.09
d_{p90}/d_{p10}		3.26			

(i) preparation of a stable suspension of highly dispersed particles;
(ii) filling of the column at high flow rates of >10 mL/min and high pressures up to 500 bar employing a stainless steel reservoir;
(iii) washing the column and conditioning with the eluent.

As a rule of thumb the packing pressure should always be significantly higher than the working pressure. A stable column has a porosity between 35 and 45%. This value does not correspond to the densest packing order, which is 26% for a hexagonally close packed bed [60]. However, the packing density varies close to the wall as compared to the center. Inhomogeneities in the packing due to wall effects are assumed for approximately 20 particle diameters. Such packing inhomogeneities can result in channel formation and voiding effects, diminishing the expected column performance. Most experience was gained on the packing of 3–10 μm particles in stainless steel columns. It took column manufacturers approximately 10 years to develop procedures to reproducibly pack analytical columns of 4 and 4.6 mm I.D., respectively. The main outcome is discussed in the paper of Kirkland and DeStefano [61]: "A very important aspect identified was that the particles must be totally suspended and not aggregated in the slurry liquid to be used for the packing process. Higher packing pressures generally were found favoured for both performance and stability. This high-pressure operation requires good strength in particles, which is characteristic of porous silica micro spheres used in the test; irregular particles were deficient in this regard. The low viscosity slurry method was identified as superior over high-density techniques for packing silica micro spheres, and the constant pressure packing method invariably was favoured over the constant flow rate. It was found that thin screens for capturing the packing at column inlets and outlets produced the highest column efficiency. However, this material is less useful for preparing long-term stable columns, and thin porous frits generally are preferred for this purpose. There was no performance advantage found for packing the column in an upwards vs. downwards direction, but the downwards approach is more convenient."

Particles larger than 10 μm could be packed by the dynamic axial compression technique in preparative columns of 50 mm inner diameter and larger. In general, there exist two methods to fill columns in preparative scale: this is dry packing and slurry packing (filtration technique) methods. Even though the dry filling method is easy to perform, the slurry method gives, especially for smaller particles, more efficient and more reproducible columns [62]. For extended stability and reproducibility of the packing processes in the preparative mode, new techniques were developed, such as dynamically axial compression [63–67] and radial compression [68–73]. These methods allow one to change the packed bed volume, through solving the instability problem in the packed bed, which is due to the formation of channels, voids and inhomogeneous dense packing formed by slurry packing process.

The packing of microbore columns (I.D. between 1 and 3 mm) and of fused silica capillaries (I.D. between 200 and 20 μm I.D.) requires different conditions and extended experience. Different column packing techniques could be applied, such as: dry packing [74], high-pressure slurry packing [75], packing using supercritical carbon dioxide [76], electrokinetic packing [77], and packing with centripetal forces [78]. Though different packing methods allows one to obtain a stable capillary column, the preparation of robust frits is not easy. The most common technique is the fusing of silica particles [79,80]. Although

I

silica particles can be fused together, the general observation was that after such a treatment the column performance had decreased, still leaving the problem of the frit preparation in the capillary columns an unresolved issue.

Particular effort is required to pack columns with particles smaller than 3 μm. The adhesion forces between the particles become much larger then for particles with $d_p > 5$ μm and thus stable suspension have to be prepared with highly dispersed individual particles before slurry packing.

A number of research projects related to the characterization of column bed structure involved the application of techniques such as NMR imaging [81–84], pulsed-field-gradient NMR spectroscopy [85–87], hydrodynamic chromatography [88], and visual monitoring of elution bands in glass columns [89].

2.2.4. *Evaluation of the column performance*

In general there are three major criteria in characterizing a HPLC column:

(a) The hydrodynamic properties expressed by the column pressure vs. flow dependency provide an insight into the flow behaviour. From these data the column permeability can be calculated and compared with the expected value based on the average particle diameter and the column dimensions.
(b) The kinetic properties of the column expressing the mass transfer kinetics of analytes are a measure of the peak dispersion of a column. The peak dispersion is characterized by the theoretical plate height (H) and the number of theoretical plates (N). A more detailed diagnosis of the kinetic performance is based on the dependency of the plate height (H) as the function of the linear velocity (u) of the eluent.
(c) The thermodynamic properties are expressed by the retention coefficients and the selectivity coefficient of test solutes under constant conditions.

2.2.4.1. Hydrodynamic properties. The column pressure drop Δp is proportional to the viscosity η of the eluent, the column length (L) and the linear velocity of the eluent u and inversely proportional to the average particle diameter (d_p) of the packing squared (Eq. (1)):

$$\Delta p = \frac{\Phi \eta L u}{d_p^2} \quad (1)$$

where Φ is the column resistance factor, which varies between 500 and 1000 for a well packed column [90]. The operating pressures of reversed phase columns of 4 mm I.D. and 100 mm length usually range between 50 and 100 bar. Changes of the column backpressure are commonly a strong indicator that the column bed structure alters and the column performance declines. The column pressure drop becomes significant when the particles of the packing are smaller then 2 μm (see Section 2.3.1.) The column pressure is important for particles of all sizes, as it plays a central role in maximizing plates/time or optimizing the performance of a given column. There are many review articles, which discuss the critical role of pressure in both using columns and evaluating their performance [91,92].

2.2.4.2. Peak dispersion. The first researchers who systematically studied peak dispersion phenomena were Martin and Synge [93], van Deemter et al. [94] and Giddings [95,96]. The treatment of the mass transfer processes and the distribution equlibria between the mobile and stationary phase in a column lead to equations which link the theoretical plate height as the decisive column performance parameter to the properties of the LC systems such as linear velocity of eluent, diffusion coefficient of analyte, retention coefficient of analyte, column porosity, etc.

van Deemter proposed an equation, which described the column performance as a function of the linear velocity for a packed column in gas chromatography coated with a stationary liquid layer. Similar equations, however, with other terms were derived for LC by numerous researchers (see Table 3). It became common practice to refer to all H vs. u plots collectively as van Deemter plots. A minimum in the plate height vs. linear velocity curve is observed where the column performance is the highest. Knox suggested a three term equation to describe the dependency of the theoretical plate height H of a column as a function

Table 3
Comparison of plate height models (reproduced by the permission of the authors [97])

	Model	Limiting case for large ν (velocity)
van Deemter et al. [94]	$h = A + \frac{B}{\nu} + C\nu$	$h + A + C\nu$
Giddings [96]	$h = \frac{1}{1/A + 1/E\nu} + \frac{B}{\nu} + C\nu$	$h + A + C\nu$
Snyder (1969)	$h = A\nu^n$ $(0.3 \le n \le 0.7)$	
Huber and Hulsman (1976)	$h = \frac{1}{1/A + 1/E\nu^{1/2}} + \frac{B}{\nu} + C\nu + D\nu^{1/2}$	$h = A + c\nu + D\nu^{1/2}$
Kennedy and Knox [128]	$h = A\nu^{1/3} + \frac{B}{\nu} + C\nu$	$h = A\nu^{1/3} + C\nu$
Horvath and Lin (1978)	$h = \frac{1}{1/A + 1/E\nu^{1/3}} + \frac{B}{\nu} + C\nu + D\nu^{1/3}$	$h = A + c\nu + D\nu^{2/3}$
van Krefeld and van den Hoed (1978); Afeyan et. al (1990)	$h = \frac{1}{1/A + 1/E\nu} + \frac{B}{\nu} + F$	$h = A + F$
Yang et al. (1992)	$h = A + \frac{B}{\nu} + \frac{DC\nu}{D + C\nu}$	$h = A + D$

of the linear velocity of the eluent by Eq. (2):

$$H_{\text{total}} = \frac{L}{N} = Au^{1/3} + \frac{B}{u} + Cu \quad (2)$$

where H_{total}, is the total theoretical plate height of a column; u, is the linear velocity of the eluent and A, B and C are constants.

The A-term corresponds to the convective dispersion by flow through the tortuous column bed, the B-term expresses the dispersion due to longitudinal molecular diffusion and the C-term is a measure of the equilibration of the analyte between the stationary and mobile phase in a column. H_{total} vs. u is dominated at the left hand side of the minimum by B and at the right hand side by the term C at higher linear velocities. Well packed columns have the approximate values of $A<1$, $B\cong 2$ and $C<0.1$. [98].

It is useful to convert H and u to dimensionless parameters by Eqs. (3) and (4):

$$h = \frac{H}{d_{\text{p}}} (\text{reduced theoretical plate height}) \quad (3)$$

$$v = \frac{ud_{\text{p}}}{D_{\text{m}}} (\text{reduced linear velocity}) \quad (4)$$

where D_{m} is the diffusion coefficient of the analyte in the mobile phase.

The application of reduced parameter is quite common for chemical engineers comparing the performance of columns in unit operations such as distillation, extraction, adsorption. Typical reduced parameters are: the Peclet number (Eq. (5)), the Sherwood number (Eq. (6)) and the Reynolds number (Eq. (7)):

$$Pe = \frac{d_{\text{p}}u}{D_{\text{m}}} (\text{Peclet number}) \quad (5)$$

$$Sh = \frac{k_{\text{if}}d_{\text{p}}}{D_{\text{m}}} (\text{Sherwood number}) \quad (6)$$

$$Re = \frac{ud_{\text{p}}}{\upsilon_{\text{m}}} (\text{Reynolds number}) \quad (7)$$

where d_{p} is the average particle size; u, linear velocity of the eluent; k_{if}, partial mass transport coefficient in the flowing medium, and υ_{m} is the kinetic viscosity of the mobile phase [99]. The Peclet number is then identical with the reduced velocity (see Eqs. (4) and (5)).

The particular advantage of this approach is the ability to compare the performance of columns packed with particles of different sizes.

Unger et al. [100] demonstrated experimentally that the course of the reduced plate height-reduced linear velocity plots are similar for all types of packings independent of whether they are irregular or spherical, for silicas and aluminas of widely differing average particle diameter.

A more detailed analysis of the H vs. u curves published in the LC literature is often not possible for the following reasons: Firstly, the plate height is commonly measured by simple approximations and not accurately by the method of statistical moments. Secondly, the measurements were performed on instruments, which had substantial dead volumes, and no corrections were performed to correct the total plate height with respect to the extra-column contributions. Needless to say, plate height measurements should be performed at isocratic conditions. A recent investigation including a number of commercial columns packed with micron size particles has indicated that the impact of these terms in assessing the column performance has to be re-investigated [101]. Still, the usual aim in column design is the need to make C-term of H vs. u curve as small as possible, what would allow a fast and efficient separation, even at higher linear velocities, where $v \gg 10$.

The optimum linear velocity is v_{opt} was found to be between 2 and 5 with reduced plate heights between 2 and 5. In other words, at the best conditions the plate height values correspond to twice the average particle diameter. H value have been reported which are smaller than 2 [102].

The current trend in column development is to make the analysis faster and more sensitive with respect to detection. One alternative is to reduce the particle size on the expense of column pressure drop using classical packing materials. The other alternative is to change the particle design or to apply electrically driven chromatography such as CEC. We will treat this issue in more detail in the next section.

A more advanced concept on the characterization of the column performance was pioneered by Poppe [91], which was further developed by Tanaka et al. [103] and Gzil et al. [104]. Poppe introduced the so-called kinetic plots: plate time ($\log(t_0/N)$) as a function of the number of theoretical plates N, where t_0 is the elution time of a non-retained compound. In order to assess the limits of column performance as a function of particle size, column pressure drop, etc. Tanaka et al. [103] applied kinetic plots to compare monolithic silica columns with particle packed columns. The experimentally obtained kinetic plots clearly indicated the advantage of monolithic column structures over particle packed columns with respect to maximum column performance.

The increase of the plate numbers of a HPLC column or the number of plates per unit time of the LC system, however, is only one side of the coin and very much resembles the situation in HPLC at the middle 1970s. It should be remembered that the chromatographic resolution R_{s} is mainly governed by the selectivity of the phase system (stationary and mobile phase) rather than by the column performance. Thus the message is to develop highly selective stationary phases with acceptable column performance and column stability. As the emphasis of this article is not directed to stationary phase development, the reader is referred to numerous literature sources [105–110].

2.3. Selected topics

2.3.1. The ultimate minimum particle size in high-performance liquid chromatography – fiction and facts

The subject of minimum particle size in HPLC was already discussed in depth at the advent of HPLC by several researchers. In 1975 Halasz stated in a paper: "At a column pressure of approximately 500 bar, the temperature of the eluent may increase up to 35 °C. Temperature and viscosity gradients exist in axial and radial directions inside the column. For routine work the particle size should be $5\,\mu\text{m} < d_{\text{p}} < 3\,\mu\text{m}$. The mini-

I

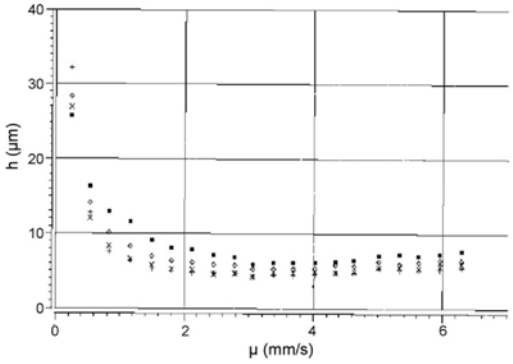

Fig. 3. Plate height–linear velocity plots on a 2 µm nonporous RP 18 silica column. Conditions: column 53 × 4.6 mm, Monospher RP18 d_p = 2.1 µm, eluent: water/acetontrile 60/40 (v/v), detection UV 254 nm, flow-cell volume 0.6 µL, detector constant 50 ms, injection volume 0. 5 µL, solutes: (■), naphthalene (k' = 0.39); (◇), anthracene (k' = 1.18); ×, pyrene (k' = 1.74); and +, chrysen (k' = 2.99) (reproduced by the permission of authors [114]).

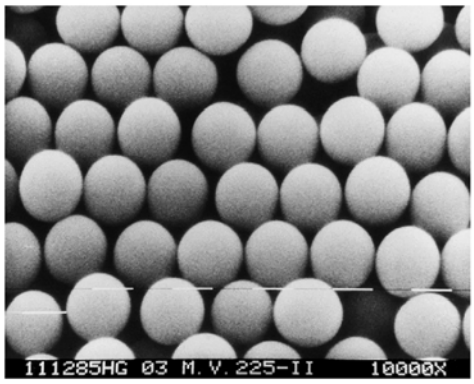

Fig. 4. An electron scanning micrograph of 2 µm nonporous silica particles (reproduced by the permission of authors [114]).

mum particle size in LC is between 1 and 3 µm [111]". Knox performed a number of calculations assuming a given number of theoretical plates and a limiting pressure drop of 400 bar and came to similar conclusions with respect to the minimum particle size [112]. Heat effects were discussed by Poppe et al. [113].

The major advantages in using columns with sub 2-µm particles were the gain in higher column efficiency, short analysis time by raising the flow-rate and high detection sensitivity, particularly when working with mass spectrometry as detector/separator.

However, columns packed with such particles need a special LC system. Shortening the connecting tubes and reducing the tube diameter should minimize extra column effects. To reduce frictional heating and minimize temperature effect the column diameter should be reduced to 2 mm or smaller. Columns should be short in length and possess frits with the desired porosity to retain the particles. The injection volume should be small as well as the volume of the detector cell, in case UV detection is applied. A source of information is an article by Giesche et al. [114], who studied the packing technology, column bed structure and chromatographic performance of columns packed with nonporous 1–2 µm size reversed phase silicas.

Employing 2 µm nonporous C18 bonded silica particles plate height values between 5 and 8 µm were generated at linear eluent velocities between 2 and 6 mm/s. At a flow-rate of 2.5 mL/min the column pressure drop was 500 bar (column dimensions 53 × 4.6 mm). Fig. 3 shows the corresponding plate height-linear flow velocity curves of analytes with retention coefficients between k = 0.39 and 2.99 for such a column. To keep extra-column effects to a minimum, the injection volume was 0.6 µL, the volume of the detector cell 0.3 µL and the time constant of the UV detector <60 ms. Such columns enabled ultra-fast separations of analytes in less then 60 s [115]. Fig. 4 exhibits an electron scanning micrograph of such particles. As the particles were totally non-porous, the specific surface area per milliliter of column volume was in the order of approximately 5 m^2/mL. Consequently, the mass loadability was by a factor of 100 lower than that of a common analytical column. To achieve the same retention of analytes in the reversed phase mode as compared to a 4.6 mm I.D. analytical column packed with 5 µm particles, the water content of the eluent had to raised from 40/60 to 80/20 water/acetonitrile volumetric ratio. The column was extremely mechanically stable up to packing pressures of 2000 bar because the particles were non-porous.

MacNair et al. [116] demonstrated that such particles could also be packed into fused silica capillary columns generating several thousand plates per meter of column length at elevated pressure in excess of 1000 bar.

With the breakthrough of coupling HPLC with mass spectrometric detection the way was open to connect columns packed with porous sub-2 µm particles with an LC instrument designed for higher pressures and coupled to MS. The result was a substantial increase in sensitivity and sample throughput (Acquity UPLC system of Waters) [117,118].

An essential element of the Acquity UPLC system are Water's novel XTerra columns based on the concept of particle hybrid technology [119].

The term hybrid stands for porous inorganic/organic particles with an inorganic skeleton and a bonded organic moiety distributed in the bulk phase as well as at the surface. The first attempts to synthesize silica-organic hybrid-particles were made by two routes [120]:

(i) hydrolyzing a tetraalkoxysilane and an organotrialkoxysilane to a poly(organoalkoxysiloxane);
(ii) adding an organotrialkoxysilane to a poly(alkoxysiloxane).

Both intermediate products were subjected to complete hydrolysis and condensation at a two-phase system under vigorous stirring, whereby spherical organo-silica particles were formed.

The particular feature of Waters novel hybrid technology was the use of ethane bridged silanes (e.g. (bistriethoxysilyl)ethane) and tetraethoxysilane to form a bridged poly(ethoxysiloxane). The bridged ethylsiloxane silica (called BEH) was synthesized as porous sub 2 μm particles with a narrow particle size distribution. Due to the ethyl bridge the particles display a high mechanical stability and an enhanced pH stability in the pH range between 1 and 12. XTerra materials and columns are available with different kinds of organic moieties and surface chemistries [121].

In order to avoid the application of high pressure Advanced Materials Technology, Chadds Ford, PA, USA have recently introduced particles with a solid core and a porous shell, as explained in Section 2.3.2.

A promising alternative to using submicron particles is to employ them in CEC. In this case, the electrical field generates the flow and plate heights of 1–2d_p have been generated. Porous silica beads with an average particle diameter between 0.2 and 3 μm, *n*-octyl surface functionalized have been studied in 100 μm I.D. fused silica capillaries in CEC [122].

Thus there is still a need for fundamental studies on CEC to elucidate the retention mechanism for polar and charged analytes and to design appropriate systems. Furthermore, CEC is much more complex than pressure driven LC with regard to two phenomena: (i) the EOF is not constant but varies as a function of many system- and operational parameters and (ii) retention and selectivity in CEC is changing when the field strength alters [123].

2.3.2. *Totally porous vs. core/shell particles*

The development of efficient packing materials in HPLC was never a straightforward approach. There were false starts and intermediate solutions, which in the long run proved to be unsuccessful. An example was the introduction of porous layer beads. Before totally porous particles were applied in HPLC, porous layer beads were introduced as packings based on the pioneering work of Horvath and co-workers [124,125]. The objective was to enhance the mass transfer kinetics of solutes by reducing the diffusion path length. Due to the large particle diameter the columns generated relatively low backpressure and were dry packed by damping. Although the specific surface area was considerably larger as compared to nonporous 2 μm particles the mass loadability was limited. Such products are still commercially available and employed as packings in precolumns.

The porous layer bead particles consisted of an impermeable core of 30–40 μm diameter and a porous silica shell of approximately 1 μm thickness. They were operated in the normal-phase LC mode. The porous layer contained mesopores and the specific surface areas ranged between 1 and 30 m^2/g [126]. Chromatographic tests of commercial products in normal-phase chromatography gave plate height values in the range of 1–4 mm at a linear velocity of 2.5 cm/s. The measured plate is mainly determined by the A-Term, which represents the packing quality of the column bed. At higher velocities, the C term of plate height curves was relatively small and this enabled one to obtain efficient and fast separations [126].

An investigation was subsequently made of the impact of the estimated thickness of the porous layer d_s in the range between $0.5 < d_s < 0.9$ μm at constant particle size and constant pore diameter of the porous layer on the theoretical plate height of selected solutes in normal-phase chromatography. A relationship of $H = d_s^{1.4}$ was obtained which is to be expected [127]. Comparative column performance studies of porous layer beads and totally porous particles were carried out by Kennedy and Knox [128] at the same time.

Recently, Advanced Materials Technology has introduced a novel type of a column known as Halo HPLC column, which is based on a fused core particle technology developed by Kirkland. The 2.7 μm silica particles are composed of a solid core of 1.7 μm thickness surrounded by a porous layer of 0.5 μm. The particles possess a specific surface area of 150 m^2/g and an average pore diameter of 9 nm. They are available with a variety of bonded reversed phase chemistry [129]. The column I.D. is 2.1, 3.0 and 4.6 mm, respectively. Columns packed with such particles show low mass transfer resistance values at high linear velocities enabling very fast separations of low molecular weight analytes in less then one minute at column back pressures of approximately 300 bar.

Recently Gritty and Guiochon [101] performed a comparative study on the performance of micron size RP silica columns including the Halo column at a wide range of the mobile phase velocities. The Halo column performed best for low molecular compounds (e.g. naphthalene), but is not as good as the other studied columns using insulin as solute. The relatively high C-term of the Halo column at high flow rates was attributed to the roughness of the external surface of the Halo particles which might generate a high film mass transfer resistance.

2.3.3. *Column miniaturization: from meso to micro to nano – where is the end?*

Column miniaturization has been under discussion for many years, particularly since 1980 when fused silica capillaries of I.D. in 100 μm range were first manufactured. They were first applied in gas chromatography with liquid stationary phase coatings inside. It is beyond the scope of this article to provide an in depth survey of micro bore and capillary columns in HPLC [92,130]. The main idea to reduce the column diameter was to minimize the dilution of the sample to be resolved and to achieve higher peak heights as compared to the 4.6 mm I.D. columns, while maintaining the column efficiency.

The next step in I.D. diminution was to introduce Microbore stainless steel columns of 1–2 mm I.D. Such columns can be still operated with a conventional HPLC system. Systematic studies on the packing procedure and the efficiency of such columns revealed that indeed the same column performance could be achieved as compared to 4 mm I.D. columns using the same packing materials. The critical issue is the column hardware and the packing process. The stainless steel tubings should be stable to high pressures and contain a mirror finish of the inside wall. The packing pressure is commonly above 1000 bar. The optimum packing pressure is dependant on the type of silica packing.

Table 4
A survey of HPLC columns of varying I.D. and the corresponding flow-rates

Column I.D. (μm)	Flow rate (μL/min)	Column volume (μL)	Mass of silica per column (mg)	Mass loadability per column (μg)
4600	1000	1660	1100	110
4000	760	1260	830	83
2000	190	310	210	21
1000	47	80	50	5
300	4.3	7	5	0.5
100	0.5	0.8	0.5	0.05
50	0.125	0.2	0.13	0.01
10	0.005	0.08	0.05	0.005

Assumptions: column dimensions, $L = 100$ mm, total column porosity $\varepsilon_t = 0.7$, skeleton porosity $\varepsilon_s = 0.3$, silica skeleton density 2.2 g/cm^3. A mass loadability of 0.1 mg/g of stationary phase was assumed (reproduced by the permission of authors [132]).

Roumeliotis et al. [131] increased packing pressures to 2000 bar and the silicas were still mechanically stable. To achieve the expected column performance several factors (injection volume, detection volume, connecting tubes) have to be considered to minimize the contributions of extra-column effects to the total peak dispersion. It should be emphasized that 1 mm bore columns require a very low peak broadening system, minimizing extra-column-volume contribution otherwise the plate number are adversely effected. Table 4 provides a survey of HPLC columns of varying I.D. and the corresponding flow-rates [132].

Viewing Table 4 it becomes evident, that the operation of micro and nano columns require low volume flow-rates for which classical HPLC instruments that run with columns of 1.0–4.6 mm I.D. are not designed. Consequently, a micro-LC and nano-LC system, respectively, is required to match the flow-rate in the microliter to nanoliter/min range. Such systems are not only operated under isocratic conditions, but also under gradient elution conditions. Rapp and Tallarek have reviewed the state-of-art in the generation and control of micro- and nanoliter flow rates with special emphasis on feasibility, automation, delay times and dead volumes [133]. In addition, the volume of detector cells has to be reduced.

The range of 300–20 μm column I.D. is covered by fused silica capillaries coated outside with a poly(ethyleneimine) layer. They can be operated as open tubes and packed tubes. The smallest I.D. capillary columns applied had an I.D. of 20 μm [134].

For the operation of capillary columns, special equipment is required. One has to make sure that for the range of 10–300 μm column I.D. the approximately typical flow rate (linear eluent velocities between 1 and 10 mm/s) is in the range from 10 nL/min to 100 μL/min and the pressure limit up to 5000 psi [135]. Various injection systems and detectors are applicable. Also one needs special frits and column connections. The packing of fused silica capillaries is achieved by slurry packing, but a miniaturized packing device should be employed.

Another important aspect using micro and nano-LC columns relates to the mass loadability of the column, which is a measure of the column capacity [136,137]. Analytical columns are commonly operated in the linear range where the retention coefficient of an analyte and the plate number N is constant and independent of the sample size. Further increase of the sample size leads to a diminution of the retention coefficient k and a drastic decrease of column plate number N. At further increase of the sample size, the column is overloaded. The linear range, where analytical columns could be operated without overload was arbitrarily defined as the linear capacity corresponding to the sample mass per gram of the stationary phase causing a 10% decrease of k and a 50% decrease of N for a given solute [57]. However, the mass loadability or column capacity is affected by a number of the parameters such as the composition and type of eluent, the type of stationary phase (e.g. the chain length of an alkylbonded silica), the type of solute (ionic, neutral, basic, acidic) and its molecular weight. As a rule of thumb, the mass loadability for reversed phase C18 column is about 2 mg of sample per gram of stationary phase for a low molecular weight solute. It accounts to about 10 mg/g of stationary phase for peptides and increases to about 100 mg/g of stationary phase for proteins on an ion-exchange column. Mc Calley et al. [138,139] and Buckenmeiser et al. [140] have studied over-loading effects for various solutes on a large number of columns (reversed phase silicas, polymeric columns) and came to much more refined conclusions.

By decreasing the column I.D. the mass of packing or stationary phase decreases proportionally too (see Table 4). In other words, a packed 100 μm I.D. column contains ca. 0.13 mg of packing and the mass loadability is estimated to be 0.01 μg.

The lowest I.D. of capillary columns is reported to be 10 and 20 μm. The latter were packed with 0.8 μm reversed-phase silica particles [134]. The capillary columns were employed in ultrahigh-throughput proteomics using fast RPLC separations with electrospray ionization (ESI) MS/MS. Also monolithic C18 bonded silica columns were manufactured and tested for the same purpose by the same group [141].

There are a number of inherent problems associated with the manufacture and operation of these capillary columns:

(a) packing of capillaries with particulate materials or/and manufacture of stable and homogeneous monolithic columns;
(b) selection of appropriate frit systems in case of particle packed capillaries to avoid significant extra-column volume contributions;
(c) connection to the mass spectrometer.

To overcome these problems a microfluidic chip was designed by Agilent Technologies, Germany to be used at nano- and

pico-litre flow-rates which integrates most of the functional components of a conventional nano column LC/MS directly to a chip.

3. Monolithic columns

3.1. The basic idea and the pioneers

As compared to particle bed columns, monolithic columns represent a single piece made of porous cross-linked polymer or porous silica. Monoliths are made in different formats as porous rods, generated in thin capillaries or made as thin membranes or disks.

When one critically judges the progress made with particle packed columns in HPLC over the last 50 years and consider the problems caused by the assembly of particles in a column it becomes immediately obvious, that the search for alternatives is a logical consequence. Cross-linked polymers are ideally suited to be synthesized in a confined space. Thus, the initial attempts were made with polyurethane foams to be applied in size exclusion chromatography and in gas chromatography [142–144]. Hjerten was the first one who developed continuous polymer beds based on polyacrylamide for the fast separation of biopolymers [145]. Tennikova and Svec synthesized poly(glycidyl methacrylate ethylene dimethacrylate) polymers as disks called macroporous polymer membranes [5] which were commercialized later by BIA Separations, Lubljana, Slovenia under the trade name Convective Interaction Media (CIM). Svec and Frechet [146] extended the family of continuous polymer beds by poly(styrene divinylbenzene) copolymers. Later on Premstaller et al. [147] extended the approach to prepare functionalized polymeric capillaries for the separation of nucleic acids. Buchmeiser et al. [148] introduced the ring-opening metathesis polymerization (abbreviated as ROMP) as an alternative synthetic route to free radical polymerization which enabled the syntheses of materials with a controlled pore structure and surface functionality.

Polysaccharides such as agarose, cellulose and cross-linked dextran were also employed as such [149,150] or used by supports in layered stacks and rolled layer [151,152]. Polysaccharides suffer from weak mechanical stability.

Parallel to the development of cross-linked polymers, Soga and Nakanishi made the fundamental studies [2,3,153] to synthesize continuous beds made of porous silica. The specific feature was that the monoliths contained a discrete bimodal pore size distribution made by large flow through pores in the micrometer pore size range and smaller diffusive pores (meso pores) in the nm size range. Tanaka immediately recognized the added value of the so-called "silica rods" as monolithic columns in HPLC and made the pioneering investigations in close collaboration with Nakanishi and co-workers.

Based on this concept Merck, Darmstadt, Germany, introduced monolithic columns as 4.6 mm columns and as 100 μm I.D. capillaries.

The major goals of applying monolithic columns in HPLC were to achieve high-speed separations; low column backpressure and fast mass transfer kinetics [154].

3.2. Monolithic silica columns

3.2.1. Formation processes and pore structure control of silica monoliths

The starting silica sources are tetramethoxysilane, tertraethoxysilane or *n*-alkyltrialkoxysilanes which are subjected to acid catalyzed hydrolysis and condensation in presence of water soluble polymers such as polyethyleneglycols and polyacrylic acid and surfactants as additives. The multicomponent solution converts into a sol–gel system by a nucleation and growth mechanism in which small fractions of a finely dispersed phase grow in size (see Fig. 5a) being limited by a thermally activated diffusion process. A second process, called spinodal decomposition, takes place leading to a co-continuous domain structure, which remains stable over an extended period of time (see Fig. 5b). The gel morphology is controlled by the kinetics of two competitive processes: the domain coarsening and the structure freezing by the sol–gel transition. The resulting gels are aged and a solvent exchange is performed to tailor the pore structure. The macroporous gel domains are filled with the polymer, which has been burned out by calcination after drying. The mesopore structure and mesopore size is adjusted by hydrothermal treatment conditions. In this way the process enables to generate two continuous pore systems and to adjust and control the pore size, and porosity of macropores and mesopores independently [2–4,153,156–171].

The manufacturing process of monolithic silica rods with 4.6 mm I.D. comprises the following consecutive steps: preparation of the starting sol, phase separation and gelation, aging and drying. After drying the rods are cladded with poly(ether ether ketone) (PEEK). Surface functionalization is performed in situ. The product is called Chromolith Performance and marketed by Merck, Darmstadt, Germany.

In case of fused silica capillaries the formation of the monolithic structure occurs within the capillary. Fig. 6 shows an electron scanning micrograph of the cross section of a 100 μm I.D. capillary.

The bimodal pore structure of a Chromolith column is characterized by a distinct bimodal pore structure: macropores of 2 μm in diameter and mesopores with an average pore diameter of approximately 13 nm. The total porosity of the monolithic column amounts to 80% and higher, the larger proportion accounts for the macropores. The mesopores generate a specific surface area of approximately 300 m^2/g.

Silica monoliths (rods) of 4.6 mm I.D. size were characterized by the classical pore structure analysis such as nitrogen sorption at 77 K, mercury intrusion, scanning electron microscopy (SEM) and transmission electron microscopy (TEM). As a result the mesopore volume and macropore volume distribution were assessed to detect the size of diffusive pore and the size of flow through pores. Tanaka and co-worker introduced the parameter of domain size as a measure being the sum of the thickness of the silica skeleton and the flow through pore diameter. These authors stated that large ratios of flow through pores to the skeleton size and a high porosity lead to high column efficiencies per unit pressure drop [158].

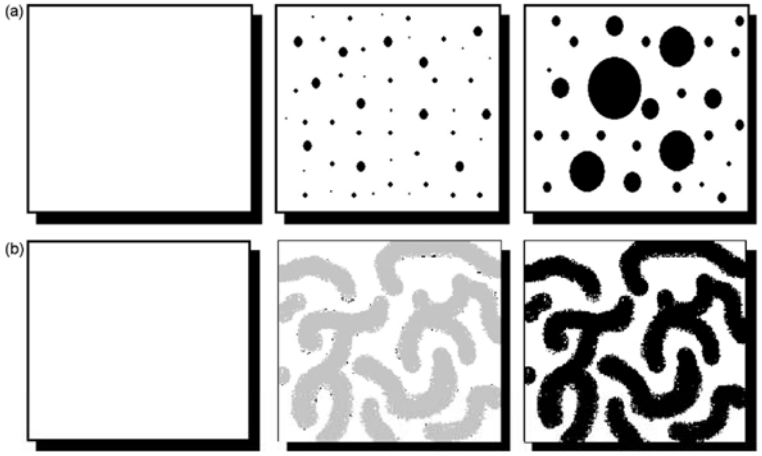

Fig. 5. (a) Nucleation and growth (diffusion limited) of silica-based monoliths, where dispersed domains with sharp interfaces grow by diffusion-controlled kinetics (reproduced by the permission of author [155]). (b) Spinoidal decomposition (spontaneous) of silica-based monoliths, where interconnected domains with diffuse interfaces grow exponentially with time (reproduced by the permission of author [155]).

Unger et al. [172] examined the column performance and hydrodynamic properties of a series of native silica monoliths of 4.6 mm I.D. with graded macropore size between 1.9 and 6 μm at constant mesopore size of 12 nm. They also determined the pore connectivity of the mesopores using the model of Meyers et al. [173,174]. They found, that the pore connectivity n_T had a tendency to decrease with increasing macropore diameter. Increasing macropore size lead also to increased theoretical plate heights at $u_{optimumn}$ of the plate height linear velocity dependencies. The column pressure drop vs. volume flow-rate dependencies were lowest for the highest macropore diameter and increased with smaller flow-through pores.

Tallarek and co-workers introduced the equivalent sphere dimension as a parameter to compare monolithic silica columns and microparticulate packed silica columns [175–177]. They claimed that silica monoliths have to be described by two characteristic lengths: a characteristic length for the band dispersion d_{disp} derived from the C-term of the H vs. u curve and a particle diameter d_{perm} representing the hydraulic permeability. As a result of this analysis applying insulin and angiotensin as analytes on a C18 modified monolith they found that d_{disp} was 3.9 and 2.5 μm, respectively, and d_{perm} 15.6 μm. In other words the C18 bonded silica monolithic showed a column performance equivalent to approximately 3 μm packed column and a column permeability comparable to approximately 15 μm packed column.

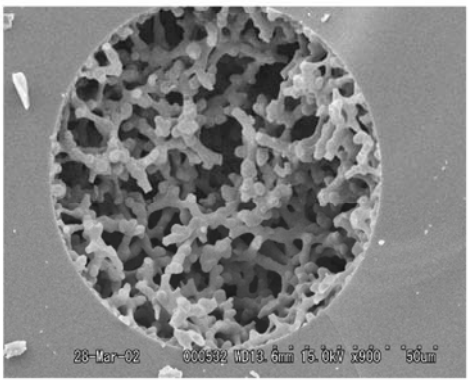

Fig. 6. An electron scanning micrograph of the cross section of a 100 μm I.D. capillary (reproduced by the permission of author [155]).

The structure of silica monoliths and the flexibility to tailor the pore structure and the column format have initiated a number of systematic studies to model and to simulate the pore structure by the pore network model und to compare the results of model analysis with particle packed columns [178,179]. Liapis et al. stated [179]: "The results of this work indicate that since in monoliths the size of through-pores could be controlled independently from the size of the skeletons, then if one could construct monolith structures having (a) relatively large through-pores with high through-pore connectivity that can provide high flow-rates at low pressure drops and (b) small-sized skeletons with mesopores having an appropriate pore size distribution (mesopores having diameters that are relatively large when compared with the diameter of the diffusing solute) and high pore connectivity, n_T, the following positive results, which are necessary for obtaining efficient separations, could be realized: (i) the value of the pore diffusion coefficient, D_{mp}, of the solute would be large, (ii) the diffusion path length in the skeletons would be short, (iii) the diffusion velocity, v_D, would be high, and (iv) the diffusion response time, t_{drt}, would be small. Monoliths with such pore structures could provide more efficient separations with respect to (a) dynamic adsorptive capacity and (b) required

pressure drop for a given flow-rate, than columns packed with porous particles."

The classical methods in characterizing the pore structure of monoliths, particular those in the capillary format have two major disadvantages: the conditions at which the materials are characterized do not resemble those applied in liquid phase adsorption processes as HPLC. Secondly, the amounts of stationary phase in monolithic silica capillaries are too small to be applied to classical characterization methods.

For these reasons we have focused on ISEC as an in situ characterization method [42]. ISEC is a well-known procedure [37–41]. We have improved the approach by including the parallel pore model (PPM) and the pore network model (PNM) to enable the calculation of several characteristic parameters from ISEC experiments. It should be emphasized in this context that the calculations are also valid for particle packed columns [42]: "The PPM and PNM proposed in this work are able to determine the void fractions of the macropores and silica skeleton, the pore connectivity of the mesopores, as well as the pore number distribution (PND) and pore volume distribution (PVD) of the mesopores. The results indicate that the mesoporous structure of all materials studied is well connected as evidenced by the similarities between the PVDs calculated with the PPM and the PNM, and by the high pore connectivity values obtained from the PNM. Due to the fact that the proposed models can predict the existence of the second inflection point in the exclusion curves, the proposed models could be more applicable than other models for ISEC characterization of chromatographic columns with small diameter macropores (interstitial pores) and/or large macropore (interstitial pore) void fractions. It should be noted that the PNM can always be applied without the use of the PPM, since the PPM is an idealization that considers an infinitely connected porous medium and for materials having a low (<6) pore connectivity the PPM would force the PVD to a lower average diameter and larger distribution width as opposed to properly accounting for the network effects present in the real porous medium."

The logical next step is to use the results of modelling and simulation and to connect them to chromatographic performance parameters such as plate height, chromatographic resolution or peak capacity and column capacity. This allows one to optimize the parameters of the pore structure of monoliths with respect to certain target parameters provided one has the necessary know-how in the synthesis to achieve the desired values of parameters.

Key parameters in modelling and simulation of monoliths are [180]:

(i) ΔP: column back pressure (linked to the volumetric flow rate, Q_v);
(ii) r_m: analyte characteristic molecular radius;
(iii) K_{eq}: analyte equilibrium adsorption constant;
(iv) ε_t: total column void fraction;
(v) ε_b: through-pore (macropore) void fraction;
(vi) ε_p: skeleton-pore (mesopore) void fraction;
(vii) D_0: skeleton diameter (characteristic transverse dimension) of the monolith;
(viii) $p_{d,mac}$: nominal diameter of the through-pores;
(ix) $p_{d,mes}$: nominal diameter of the skeleton-pores.

Another more pragmatic means is to experimentally measure chromatographic data such as plate height vs. linear velocity curves and resolution parameters and to connect the findings with the pore structural characteristics of the monolithic columns [181].

Even though the potential of using monolithic silica columns for peptide and protein separation was recognized [171,182–184], the pore structure of the monoliths needed to be adapted to the peptidic analytes to ensure a rapid mass transfer and a high accessibility of the stationary surface [181].

Numerous theoretical models proved this assumption of high porosity, high homogeneity and small-sized skeletons with mesopores large enough not to hinder the passage of the molecules in and out of the pore [178,179,185–187]. First, it was proven by a series of theoretical calculations, that a perfectly ordered flow-through pore network, instead of traditionally used packed bed columns, would gain efficiency in LC separation [188,189]. It was shown as well that a considered monolithic micro-structure column would allow to perform $N > 100{,}000$ plate separations in a few hundreds of seconds [190]. The further theoretical analysis led to the conclusion that the large porosity supports can always potentially yield shorter analysis times or larger plate numbers than small porosity supports but need sub micrometer feature sizes to actually achieve this [185,186]. If a strong improvement of the structural homogeneity (assuming constant domain size conditions) or a degree of the domain size (assuming constant homogeneity conditions) would be achieved by monolithic column synthesis, such a support would have an applicable potential, where no existing chromatographic supports seems to be able to operate [191].

3.2.2. Chromatographic properties

Major chromatographic features of monolithic silica columns arise from the large through-pore size/skeleton size ratios and high porosities, resulting in high permeability and large number of theoretical plates per unit pressure drop. High permeability and small diffusion path length provided by the presence of large through-pores and relatively small-sized skeletons resulted in the lower plate height and the lower pressure drop with monolithic silica columns compared with a particle-packed column, making faster separations possible with current instrumentation. Fig. 7 displays the potential of applying the monolithic silica column in gradient separation. For the detailed survey on articles touching the relationship between structural properties of silica monoliths and their chromatographic performance and selectivity see Table 5.

3.3. Polymer-based monolithic columns

3.3.1. Synthesis approaches and characterization

As compared to the formation of silica monoliths the formation of porous cross-linked polymeric monoliths has a wide variety of facets in terms of starting monomers, co-monomers, initiators, solvents and porogens.

Table 5
Survey on important research articles connecting the structural properties with the chromatographic properties of silica monoliths

Properties	Subject and specific features in brief
Fast separation property due to the low-pressure drop across the column	Monolithic silica rod columns can be prepared with independent control of the mesopores and the through-pores (macropores) [2–4,153,156–172]. As a result, chromatographic columns with higher total porosity and bigger through-pore sizes as compared to particulate ones are obtained [4,158,169,192–194,175]. This enables one to perform faster separations [139,172,176,195–198,182,199–206].
High-efficiency property due to the fast mass transfer kinetics and high binding capacity of monolithic silica columns	Monolithic silica columns show high efficiency on the basis of the small-sized silica skeletons providing sufficient surface area for the separation and fast mass transfer kinetics due to the large-sized through-pores. Such monolithic silica columns were used as a robust and efficient separation medium for the peptide mapping by reversed-phase HPLC [206], separation of biological macromolecules [198,182] as well as separation of low molecular weight analytes [207,187,208–210].
Applications	
Analysis of low molecular weight analytes	The structure and performance of monolithic silica based columns appeared to be very suitable for the resolution of low molecular weight analytes up to 10 kDa [207,187,208–210].
High throughput analysis of drugs and metabolites	Monolithic high throughput characteristic application in the rapid separation of: microcystins and nodularin [197], methylphenidate [211] and other drugs and their metabolites [212–216] proved to be beneficial in separation time if compared with conventional particulate columns.
Separation of environmentally relevant substances and food additives	Monolithic silica columns have been applied in: separations of pollutants or ions in water [217–224] and various applications in the field of food analysis [225–227].
Separation of enantiomers	Monolithic silica columns have been used in the field of enantiomeric separation as a robust and efficient separation media [217,228–230].
Separation of complex biological samples	Monolithic high-throughput characteristic application in the metabonomic studies of biofluid samples [196], the peptide mapping by reversed-phase HPLC [194,175,197,182,206,231] and biological macromolecules [198,232,233].
Separation of complex biological samples in multidimensional HPLC	The low flow resistance feature of the monolithic silica columns enables one to use such separation media in the complicated multidimensional HPLC, where usually column back pressure is one of the decisive factors [234–238].

The syntheses of macroporous cross-linked polymers, their structural characterization and their application in size-exclusion chromatography (SEC) is described in depth in a survey article by Seidl et al. [239]. The most in depth monograph in this field was published by. Svec et al. [240]. The tailoring of the morphology of polymeric monoliths is shown for methacrylate-ester based monoliths by Eltink et al. [241].

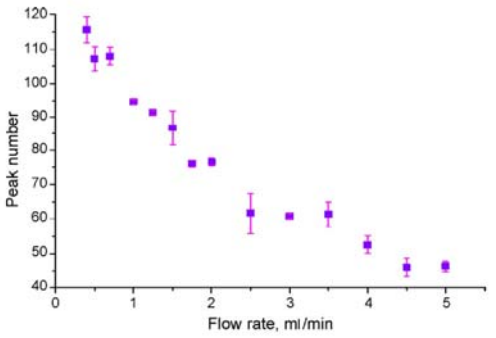

Fig. 7. Peak number as a function on the flow rate at gradient elution on a reversed phase monolithic column. The peak number was calculated according to a program integrated in Agilent software. The peak number is assumed to be proportional to the chromatographic resolution (reproduced by the permission of E. Machtejevas, Merck, Darmstadt, Germany). Conditions: system, standard Agilent HPLC 1100 system; column, chromolith 100 × 4.6 mm I.D. thermostatted at 25 °C; sample, 48 μg (2 μL) human hemofiltrate; mobile phases, (A) H_2O + 0.1% TFA, (B) ACN + 0.1% TFA; gradient volume, 20 mL; and gradient time, 0 min 95% A and 5% B; 20 min 50% A and 50% B; 22 min 0% A and 100% B.

Typically, the pore texture of polymeric monoliths can be described as an assembly of fused micro globules with graded densities. The interstices generate a macroporous system with pore diameters in excess of 100 nm. The reported specific surface area is much smaller than those of monolithic silicas (<50 m^2/g). It seems that smaller pores (mesopores and micropores) are often present to a minor degree, their appearance depends on the solvent and the swelling properties of the material.

One major advantage of polymeric monoliths over silica monoliths is the fact that the surface functionality can be generated and controlled by the use of appropriate co-monomers. Thus hydrophobic, hydrophilic, polar and charged surfaces can be obtained. Also polymeric monoliths are manufactured in a wide variety of column formats as thin membranes, disks, capillary columns and large bore preparative columns.

3.3.2. *Chromatographic properties*

For the detailed survey on the chromatographic properties of polymeric monoliths, we refer to selected reading [242–245].

In general, polymeric-based monolithic columns, concerning their chromatographic properties, are applied in two areas:

(i) as monolithic capillaries with hydrophobic and other functionalities as capillaries in the separation of peptides and proteins, particular in the proteomics field [246–249];
(ii) as disks, rods and other formats in the isolation and purification of biopolymers. Poly(methylmethacrylate) monoliths

Table 6
Structural and chromatographic parameters of monolithic silica columns Chromolith® Performance (RP 18e) and microparticulate silica columns (C18 reversed phase)

Property	Monolithic silicas (chromolith)	Microparticulate silicas
Pore structural data		
Pore modality	Bimodal	Bimodal
Meso pore diameter	13 nm	7–30 nm
Column porosity and specific pore volume, respectively	Column porosity >80%, and pore volume approximately 1 cm^3/g	Specific pore volume of the particles 0.3–1.1 cm^3/g: column porosity depends on the packing density of particles and can be in the range of 40–60%
Macropore diameter	2 μm (flow through pores)	Interstitial pores (pore size approximately 40% of average particle size)
Column macroporosity	Approximately 55%	35–50% (interstitial column porosity)
Specific surface area	300 m^2/g	70–510 m^2/g
Chromatographic parameters		
Column format (*L*; I.D.)	100 mm; 4.6 mm	100–250 mm, 4–4.6 mm
Column hardware	PEEK	Usually stainless steel
Column pressure drop	<20 bar at 1 mL/min	40–150 bar at 1 mL/min
Volume flow-rate range	0.01 mL/min–10 mL/min	0.01 mL/min–5 mL/min
Plate height values[a]	Approximately 12 μm	>9 μm
Plate number values[a]	Approximately 80,000 N/m	30,000–110,000 N/m

Comparison data on commonly used C18 phases, of average particle size from 4 to 10 μm.
[a] Values are given for a neutral compound.

are marketed by BIA Separations as Convective Interaction Media (CIM).

The column performance characteristics of poly (methylmethacrylate) monolithic capillaries under the aspects of kinetic plots was studied in detail by Eeltink et al. [241].

4. Comparison of the structure and performance of particle packed and monolithic columns

The column performance of a 5 μm C 18 bonded silica column was compared with a monolithic C 18 bonded silica column in Reversed Phase HPLC under isocratic conditions. The particle packed column showed a plate height *H* of 10–15 μm at a linear velocity of 1 mm/s. The *H* vs. *u*. curve of the monolithic column followed the same course but remained nearly parallel to the abscissa up to a linear velocity of 7 mm/s. At this high velocity the packed column could not be operated due to the high column back pressure. The monolithic RP column showed a column back pressure which was three to five times lower than the particle packed column [169].

A fundamental examination on the chromatographic performance of monolithic silica columns as compared to particle packed columns was made by Leinweber et al. [175]. The band dispersion characteristics of insulin and angiotensin II on monolithic C18 bonded silica columns were examined. From the *H* vs. *u* curves the mechanical and non-mechanical contribution of the dispersion to the total plate height was analyzed. The superposition of the reduced plate height – reduced velocity curves indicated that the mass transfer properties of the monolithic columns in the mesopores corresponded to that of packed columns with an equivalent dispersion particle diameter of 3 μm.

Table 7
Comparison of pore structural and operational parameters of monolithic polymeric columns and research monolithic silica columns

Property	Cross-linked polymeric monoliths	Silica monoliths
Pore modality	Unimodal (broad)	Bimodal (macro + meso)
Macropore diameter	0.05–10.0 μm	1–10 μm
Macroporosity	10–95%	40–70%
Total column porosity	Low-density and high density monoliths	0.8–0.9
Pore morphology	Globular structure	Spongy and worm-like structure
Surface functionality	Adjusted by functional co-monomers	Introduced by grafting from and grafting on surface modification
Column format	Preparative size to capillary formats	Analytical, microbore, capillary formats
Column pressure drop	Distinct higher column back pressure as compared to monolithic silica columns	1/3–1/5 as compared to 5 μm packed columns
Linear velocity range	1–7 mm/s and higher	1–7 mm/s and higher
Plate height and plate numbers	$H = 5–10$ μm at optimum *u*	$H = 5–10$ μm at optimum *u*
pH range for application	Acidic to strong alkaline	Acidic to pH 8
Typical application areas	Separation of peptides and proteins (analytical) Isolation and purification of biopolymers	Separation of low molecular weight compounds and peptides

I

The through pore system of the monolithic column controlling the hydraulic permeability was translated into an interstitial pore system of a packed bed. The comparison resulted in a equivalent permeability particle diameter of 15 μm.

Tanaka et al. [169] applied the kinetic plots ($\log t_0/N$ vs. N) as a measure to demonstrate the superior performance of monolithic silica capillary columns vs. microparticle packed beds in the capillary format.

In a more fundamental study Gzil et al. [185] treated the impact of variable bed porosity on the chromatographic performance parameters. They defined limiting cases for separations requiring small plate number and high plate numbers and linked this parameter to the optimum external porosity.

Tables 6 and 7 provide a comparison of the structural and chromatographic properties of monolithic silica columns and microparticulate silica columns (Table 6) and the characteristics of polymer based and monolithic silicas (Table 7).

5. Conclusion – where are we now and where are we going?

5.1. Where are the needs and where are the alternatives?

The success of HPLC as a widely accepted separation technique and platform at analytical scale, preparative scale and process scale was a result of an interdisciplinary and integrated research and development combined with a rapid technology transfer into effective, versatile robust and reliable systems. The central and most essential part of an HPLC system is the separation column. More than 20 years of academic, technical and engineering knowledge and experience have been invested into the manufacture of selective, efficient, reproducible and robust columns. Most of the achievements made are based on experimental and technical experience knowing the needs of the users and the demands in the respective application areas rather then on a solid fundamental theoretical basis.

Contrary to many predictions and expectations, 4 and 4.6 mm I.D. columns packed with microparticulate C18 bonded silicas dominate the market. There is a slight tendency to the use of miniaturized column formats [250,251]. This means that microparticulate packed C18 columns will maintain its leading position as benchmark columns in the future. The high surface area and the relatively high mass loadability make them most suitable as working horses in HPLC technology.

Miniaturized columns such as micro bore and fused silica capillaries cover only a minor part in application. They are mostly applied in research laboratories. The reasons for this fact are that firstly one needs a miniaturized HPLC equipment (at least for fused silica capillaries) and secondly, experience and skills are required to operate such systems in an optimum way.

Monolithic columns are still the major subject of extensive research. Monolithic columns as compared to particulate ones have the ability and potential of designing an optimum structure, which will lead to designed columns with optimum performance and selectivity for the various facets of application areas. Apart from this option monolithic columns offer a high robustness and easier maintenance than packed columns with frits.

Most of the modelling and simulation activities are seen in the field of monolithic silicas. There is still an unexplored potential in the fundamental understanding and design of polymer-based monoliths.

The results obtained on columns packed with 2 μm spherical particles hyphenated to mass spectrometers as second separators and detector will meet the current demands on sensitive and fast high resolution separations in pharmaceutical and chemical analysis.

The future challenges and highest demands on liquid based separation techniques will originate in life science applications. On the top is the search for biomarkers for diagnostic purposes and the development of therapeutics. Related to that is the isolation and purification of biotech products such as recombinant proteins and vaccines by bio-processing.

The sample mixtures in bio fluids from human sources, animals and plants are extremely complex with regard to chemical composition and structure. They contain a large number of chemical entities and cover a large range of abundance ratio.

The resolution of such complex mixtures can be only accomplished by using multidimensional LC systems with selective phase systems in combination with powerful detection system as e.g. mass spectrometers. Selectivity is the key target parameter and can be achieved by a design of novel materials with superior mass transfer properties and advanced surface functionalities.

The potential of packing and stationary phase design and development has not been explored to the full extent.

Other powerful separation techniques based on electro-driven systems are still in their infancy and promise a high potential of selective molecular recognition for polar and charged analytes.

Acknowledgements

The authors are grateful to Dr. J. J. Kirkland, Dr. R. Ditz and Professor K. Sing for critical comments and suggestions to improve the manuscript as well as to Merck KGaA, Darmstadt, Germany for financial, material, and intellectual support for this work.

Appendix A. Survey on the most common methods of particle size analysis of HPLC packings

A.1. Sieve and classification analysis

One of the oldest and easiest methods to determine the particle size distribution is the sieve analysis. Because of its ease of use this method is widely applied in official methods, e.g. many pharmacopoeias (USP, Ph.Eur.). The mesh width of sieves, used for sieve analysis, is standardized according to DIN-methods (DIN 4188) or US-standard methods (ASTM E11-70/E 161-70). The most serious drawback of sieve analysis is the application range, which is to particles >20 μm. For the analysis of finer powders the sieve analysis has to be combined with other methods.

A.2. Light scattering

When light hits a collective of particles it is partly absorbed and partly diffracted. The angle and the intensity of the diffracted light are depending on the size of the particle. At a constant wavelength large particles diffract the light into small scattering angles and small particles with low intensity into high scattering angles. The intensity of the diffracted light can be used for quantification. Several systems with different geometric design of the equipment have been developed over the last few years. Most of the systems use lasers as the source of focused light. As light scattering is a technique, which is applied to a multitude of particles, the biggest problems stems from the deconvolution of the obtained light pattern.

When comparing particle size distributions it is very important to know which instrument is used, because the recorded values can be considerably affected by differences in optics design, software algorithms and sample preparation and concentration [252–254].

A.3. Sedimentation

The sedimentation of a particle in a liquid is dependent on its size, density and form in accordance with Stoke's law (Eq. (8)):

$$d_p = \sqrt{\frac{18\eta}{(\rho - \rho_0)g}}\sqrt{\frac{h}{t}} \quad (8)$$

g, gravitation; h, falling height; t, falling time; η, viscosity; $(\rho - \rho_0)$, difference in density between the particle and the dispersion solvent.

For particles as small as 0.5 μm the measurement can be done under the earth's gravity. One of the oldest instruments for sedimentation analysis is the ANDREASEN-pipette, where at definite times samples are withdrawn from a sedimenting suspension and the mass fraction is determined by weighing. Modern systems are working with light or X-ray detection of the particles passing by the analysis window. To speed up analysis time the sample cell itself can be moved at a given rate passing the detector (wide-angle scanning photo-sedimentometer).

Some prerequisites must be fulfilled for sedimentation analysis: the sedimentation liquid has to be totally inert and must have a density, which is lower than the particle density. No convection within the liquid should take place due to temperature or density gradients. As a high particle concentration can cause density gradients, the particle concentration should be below 1%. For systems working with the earth's gravitation the minimum particle diameter is around 1 μm because of the Brownian motion, which disturbs the measurement of smaller particles.

Sedimentation analysis gives relatively high resolution results and is used for a wide range of materials, including the determination of agglomerates [255].

A.4. Electronic measurements

The change of the electrical resistance is measured in an electro zone stream counter. The system most commonly used is the Coulter Counter. The particles of interest have to be suspended in a conducting electrolyte and are passed through an orifice, which is situated between two electrodes. For the conducting electrolyte the same prerequisites have to be fulfilled as for the suspension liquid in sedimentation analysis. In most cases sodium chloride solutions at low concentrations are used. The particles within the suspension liquid are forced through the small orifice by means of a controlled vacuum. On either side of the orifice two electrodes are mounted. Due to the presence of a particle within the inspection zone, which exhibits a high electrical field, the resistance of the electrolyte changes, generating a voltage pulse the amplitude of which is assumed to be proportional to the volume of the particles.

A.5. Microscopic methods

Microscopic methods are characterized by a particular disadvantage and one great advantage. The disadvantage is given by the fact that only a small population of particles is used for the determination of the particle size distribution. Before the programs of computer-automated image analysis became available the determination of the particles size distribution was very tedious and laborious since it involved direct comparison with sets of reference circles (the reticule, engraved on the eyepiece of the microscope). Even with the newest powerful image analysis programs hundreds of digitized images may be required to get enough information to establish statistical significance for the particle size determination.

The biggest advantage, which all image analysis systems have in common, is the shape information obtained from single particles. Only by using microscopic techniques is it possible to judge the quality of a chromatographic sorbent in terms of its physical uniformity. The most valuable information obtained from microscopy is the determination of fines in the micrometer and sub-micron range attached to particles (Fig. 8A) and the identification of miss-formed and broken particles (Fig. 8B).

A.6. Field flow fractionation

The combination of two different forces is used in the field flow fractionation technique (FFF), where a gravitational (GFFF) or centrifugal field is applied perpendicular to a flow direction. The particles are placed in an empty capillary and moved by the liquid flow in one direction. Due to the applied field the particles are forced according to their size towards a wall of the capillary. The particles are driven by the mobile phase towards the capillary outlet at different velocities depending on their size. The particle size distribution is recorded by an UV-detector placed at the end of the capillary. With this instrumental setup it is possible to determine the particle size distribution of chromatographic sorbents either of inorganic or organic nature in the particle size range from 1 to 100 μm [256–258]. The method is supposed to be accurate, fast and inexpensive, as standard HPLC equipment can be used for the measurement. Only recently first attempts have been made to set up a standardless method for the measurement of silica particles. The method

I

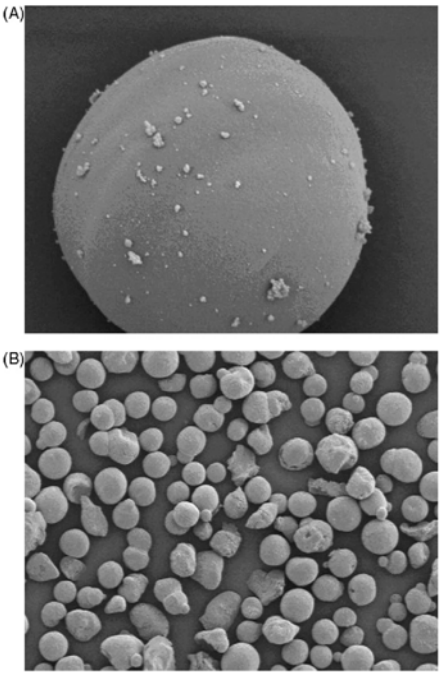

Fig. 8. Scanning electron microscopy-pictures of different silica sorbents (reproduced by permission of Merck, Darmstadt, Germany). (A) Nucleoprep 100-30 (25–40 μm) (magnification ×3000), small attached particles. (B) Zorbax LP 100/40 Si (40 μm) (magnification ×100), high content of misformed and broken particles.

allows the direct conversion of fractograms into quantitative, size-distribution profiles without calibration of the system [259].

References

[1] W. Weigert, E. Koberstein, Angew. Chem. 88 (1976) 657.
[2] K. Nakanishi, N. Soga, J. Am. Ceram. Soc. 74 (1991) 2518.
[3] K. Nakanishi, N. Soga, J. Non Cryst. Solids 139 (1992) 1.
[4] H. Minakuchi, K. Nakanishi, N. Soga, N. Ishizuka, N. Tanaka, Anal. Chem. 68 (1996) 3498.
[5] T.B. Tennikova, F. Svec, B.G. Belenkii, J. Liq. Chromatogr. 13 (1990) 63.
[6] C. du Fresne von Hohenesche, Ph.D. thesis, University of Mainz, 2002.
[7] S. Luedtke, Th. Adam, K.K. Unger, J. Chromatogr. A 786 (1997) 229.
[8] B.A. Grimes, S. Lüdtke, K.K. Unger, A.I. Liapis, J. Chromatogr. A 979 (2002) 447.
[9] I. Nischang, G. Chen, U. Tallarek, J. Chromatogr. A 1109 (2006) 32.
[10] F.C. Leinweber, U. Tallarek, J. Phys. Chem. B. 109 (2005) 21481.
[11] F. Leinweber, M. Pfafferodt, A. Seidel-Morgenstern, U. Tallarek, Anal. Chem. 77 (2005) 5839.
[12] I. Nischang, K. Spannmann, U. Tallarek, Anal. Chem. 78 (2006) 3601.
[13] C. du Fresne von Hohenesche, V. Ehwald, K.K. Unger, J. Chromatogr. A 1025 (2004) 177.
[14] M. Verzele, C. Dewaele, J. Chromatogr. 391 (1987) 111.
[15] P.G. Bird, US Pat. 2,244 325, assigned to P. G. Bird (1945).
[16] W. Stöber, A. Fink, E. Bohm, J. Colloid Interface Sci. 26 (1968) 62.
[17] R.K. Iler, The Chemistry of Silica, Wiley, New York, 1979, p. 866.
[18] K.K. Unger, Porous Silica, its Properties and Use as a Support in Column Liquid Chromatography, Elsevier, Amsterdam, 1979, p. 77.
[19] D. Barby, in: G.D. Parfitt, G.S.W. Sing (Eds.), Characterization of Powder Substances, Academic Press, London, UK, 1976, p. 353.
[20] C.J. Brinker, G.W. Scherer, Sol–Gel Science, Academic Press, New York, 1990, p. 303.
[21] L.L. Hench, J.K. West, Chem. Rev. 90 (1990) 33.
[22] G.W. Scherer, J. Non-Cryst. Solids 147 (1992) 363.
[23] G.W. Scherer, in: A.S. Mujumdar (Ed.), Drying'92, Elsevier, Amsterdam, 1992, p. 92.
[24] Ullmann's Encyclopedia of Industrial Chemistry, vol. A23, Silica, VCH, Weinheim, 1993, Chapter 6.
[25] H. Reinhardt, A. Becker, R. Kuhlmann, P. Nauroth (Degussa AG) DE-OS 3 639 845, 1986.
[26] G. Buechel, M. Gruen, K.K. Unger, A. Matsumoto, K. Tsutsumi, J. Supramolec. Sci. 5 (1998) 253.
[27] K.K. Unger, D. Kumar, M. Gruen, G. Buechel, S. Luedtke, Th. Adam, K. Schumacher, S. Renker, J. Chromatogr. A 892 (2000) 47.
[28] B.A. Grimes, A.I. Liapis, personal communication.
[29] K.K. Unger, G. Jilge, J.N. Kinkel, M.T.W. Hearn, J. Chromatogr. 359 (1986) 61.
[30] G. Jilge, R. Janzen, H. Giesche, K.K. Unger, J.N. Kinkel, M.T.W. Hearn, J. Chromatogr. 397 (1987) 71.
[31] R. Janzen, K.K. Unger, H. Giesche, J.N. Kinkel, M.T.W. Hearn, J. Chromatogr. 397 (1987) 91.
[32] G. Jilge, K.K. Unger, U. Esser, H.-J. Schäfer, G. Rathgeber, W. Müller, J. Chromatogr. (1989) 135.
[33] J.J. Meyers, A.I. Liapis, J. Chromatogr. A 827 (1998) 197.
[34] J.J. Meyers, et al., J. Chromatogr. A 908 (2001) 35.
[35] A.I. Liapis, J. Chromatogr. A 865 (1999) 13.
[36] F. Rouquerol, J. Rouquerol, K.S.W. Sing, Adsorption by Powders and Porous Solids, Academic Press, London, 1999.
[37] I. Halasz, K. Martin, Ber. Bunsenges. Phys. Chem. 79 (1975) 731.
[38] I. Halasz, K. Martin, Angew. Chem., Int. Ed. Engl. 17 (1978) 901.
[39] J.H. Knox, H.P. Scott, J. Chromatogr. 316 (1984) 311.
[40] A.A. Gorbunov, L. Ya. Solovyova, V.A. Pasechnik, Vysokomol. Soedin. Ser. A 26 (1984) 967.
[41] A.A. Gorbunov, L.Ya. Solovyova, V.A. Pasechnik, J. Chromatogr. 448 (1988) 307.
[42] B.A. Grimes, R. Skudas, K.K. Unger, D. Lubda, J. Chromatogr. A 1144 (2007) 14.
[43] A. Kurganov, V. Davankov, T. Isajeva, J. Chromatogr. A 660 (1994) 97.
[44] M. Ousalem, X.X. Zhu, J. Hradil, J. Chromatogr. A 903 (2000) 13.
[45] K. Jerabek, K.J. Shea, D.Y. Sasaki, G.J. Stoddard, J. Polym. Sci. A: Polym. Chem. 30 (2003) 605.
[46] Y. Yao, A.M. Lenhoff, J. Chromatogr. A 1037 (2004) 273.
[47] J.S. Beck, J.C. Vartuli, W.J. Roth, M.E. Leonowicz, C.T. Kresge, K.D Schmitt, C.T.-W. Chu, D.H. Olson, E.W Sheppard, S.B. McCullen, J.B. Higgins, J.L. Schlenker, J. Am. Chem. Soc. 114 (10) (1992) 834.
[48] C.T. Kresge, M.E. Leonowicz, W.J. Roth, J.C. Vartulli, J.C. Beck, Nature 359 (1992) 710.
[49] O. Lauer, Grain Size Measurements on Commercial Powders, Alpine, Augsburg, 1962.
[50] Process Technology for Tomorrow, Hosokawa Alpine Augsburg, Germany, 2007.
[51] M. Shapiro, V. Galperin, Chem. Eng. Proc. 44 (2005) 279.
[52] J.H. Perry, Chemical Engineers Handbook, third ed., McGraw Hill, New York, 1950.
[53] R.H. Davis, A. Acrivos, Ann. Rev. Fluid Mech. 17 (1985) 91.
[54] J.T. Roscoe, Fundamental Research Statistics for the Behavioral Sciences, Holt, Rinehart and Winston, New York, 1975.
[55] T. Allen, Particle Size Measurement, Chapman and Hall, London, 1974.
[56] Kromasil – for your analytical HPLC, Eka Chemicals, Bohus, Sweden, 2006.
[57] L.R. Snyder, J.J. Kirkland, Introduction to Modern Liquid Chromatography, second ed., Wiley, New York, 1979, Chapter 5.
[58] J.J. Kirkland, J. Chromatogr. Sci. 9 (1971) 206.

[59] U.D. Neue, HPLC columns, Wiley-VCH, New York, 1997, p. 93 (Chapter 5).
[60] R.G. Avery, J.D. Ramsay, J. Colloid Interface Sci. 42 (1973) 597.
[61] J.J. Kirkland, J.J. DeStefano, J. Chromatogr. A 1126 (2006) 50.
[62] J. Dingenen, Anal. Mag. 26 (1998) M18.
[63] E. Godbille, P. Devaux, J. Chromatogr. 122 (1976) 317.
[64] H. Colin, P. Hilaireau, J. de Tournemire, LC–GC 8 (1990) 302.
[65] D.-R. Wu, K. Lohse, J. Chromatogr. A 658 (1994) 381.
[66] M. Sarker, G. Guiochon, J. Chromatogr. A 702 (1995) 27.
[67] M. Sarker, G. Guiochon, J. Chromatogr. A 709 (1995) 227.
[68] J.N. Little, R.L. Cotter, J.A. Prendergast, P.D. McDonald, J. Chromatogr. 126 (1976) 439.
[69] P.D. McDonald, R.V. Vivilecchia, D.R. Lorenz, US Patent 4,211,658 (1980).
[70] C.W. Rausch, Y. Tuvin, U.D. Neue, US Patent 4,228,007 (1980).
[71] P.D. McDonald, C.W. Rausch, US Patent 4,250,035 (1981).
[72] M. Sarker, G. Guiochon, J. Chromatogr. A 683 (1994) 293.
[73] M. Sarker, Y. Yun, G. Guiochon, J. Chromatogr. A 728 (1996) 3.
[74] L.A. Colon, T.D. Maloney, A.M. Fermier, J. Chromatogr. A 887 (2000) 43.
[75] R.J. Boughtflower, T. Underwood, C.J. Paterson, Chromatographia 40 (1995) 329.
[76] M.M. Robson, S. Roulin, S.M. Shariff, M.W. Raynor, K.D. Bartle, A.A. Clifford, P. Meyers, C.M. Euerby, C.M. Johnson, Chromatographia 43 (1996) 313.
[77] R. Stol, M. Mazereeuw, U.R. Tjaden, J. van der Greef, J. Chromatogr. A 873 (2000) 293.
[78] A.M. Fermier, L. Colon, J. Microcolumn Sep. 10 (1998) 439.
[79] T. Adam, K.K. Unger, M.M. Dittmann, G.P. Rozing, J. Chromatogr. A 887 (2000) 327.
[80] C. Fujimoto, Anal. Sci. 18 (2002) 19.
[81] J.B. Miller, TrAC 10 (1991) 9.
[82] E. Bayer, W. Müller, M. Ilg, K. Albert, Angew. Chem. 101 (1989) 1033.
[83] U. Tallarek, E. Bayer, D. van Dusschoten, T. Scheenen, H. Van As, G. Guichon, U.D. Neue, AIChE J. 44 (1998) 1962.
[84] U. Tallarek, E. Baumeister, K. Albert, E. Bayer, G. Guiochon, J. Chromatogr. A 696 (1995) 1.
[85] J. Kärger, H. Pfeifer, W. Heink, Adv. Mag. Reson. 12 (1988) 1.
[86] U. Tallarek, D. van Dusschoten, M. Von As, E. Bayer, G. Guiochon, J. Phys. Chem. B 102 (1998) 3486.
[87] U. Tallarek, F.J. Vergeldt, H. Van As, J. Phys. Chem. B 103 (1999) 7654.
[88] J. Kraak, R. Ostervink, H. Poppe, U. Esser, K.K. Unger, Chromatographia 27 (1989) 585.
[89] M. Hallmann, Ph.D. thesis, University Mainz, Germany, 1995.
[90] J.H. Knox, High Performance Liquid Chromatography, Edinburgh University Press, Edinburgh, Scotland, 1978, p. 9.
[91] H. Poppe, J. Chromatogr. A 778 (1997) 3.
[92] G. Guiochon, in: Cs. Horvath (Ed.), Optimization in Liquid Chromatography, HPLC, Advances and Perspectives, Academic Press, London, 1980, p. 1.
[93] J.P. Martin, R.L. Synge, Biochem. J. 35 (1941) 1358.
[94] J.J. van Deemter, F.J. Zuiderweg, A. Klinkenberg, Chem. Eng. Sci. 5 (1956) 271.
[95] J.C. Giddings, J. Chromatogr. 5 (1961) 47.
[96] J.C. Giddings, J. Chromatogr. 5 (1961) 61.
[97] K.H. Hamaker, M.R. Ladisch, Sep. Purif. Methods 25 (1996) 47.
[98] A. Bristow, J.H. Knox, Chromatographia 10 (1977) 279.
[99] J.F.K. Huber, Ber. Bunsenges. Phys. Chem. 77 (1973) 179.
[100] K.K. Unger, W. Messer, K.F. Krebs, J. Chromatogr. A 149 (1978) 1.
[101] F. Gritti, G. Guiochon, J. Chromatogr. A 1166 (2007) 30.
[102] R.W. Stout, J.J. Destefano, L.R. Snyder, J. Chromatogr. 282 (1983) 263.
[103] N. Tanaka, H. Kobayashi, N. Ishizuka, H. Minaguchi, K. Nakanishi, K. Hosoya, T. Ikegami, J. Chromatogr. A 965 (2002) 35.
[104] P. Gzil, N. Verwoort, G.V. Baron, G. Desmet, Anal. Chem. 76 (2004) 6707.
[105] E.C. Vonk, B.M.W. Langeveld-Voss, J.L.J. van Dongen, R.A.J. Janssen, H.A. Claessens, C.A. Cramers, J. Chromatogr. A 911 (2001) 13.
[106] A. Mendez, E. Bosch, M. Roses, U.D. Neue, J. Chromatogr. A 986 (2003) 33.
[107] P. Dehouck, D. Visky, Z. Kovacs, B. Noszal, E. Adams, J. Hoogmartens, LC–GC Europe (2003) 2.
[108] N.S. Wilson, J. Gilroy, J.W. Dolan, L.R. Snyder, J. Chromatogr. A 1026 (2004) 91.
[109] L.R. Snyder, J.W. Dolan, P.W. Carr, J. Chromatogr. A 1060 (2004) 77.
[110] L.R. Snyder, J.W. Dolan, P.W. Carr, Anal. Chem. (2007) 3255.
[111] I. Halasz, R. Endele, J. Asshauer, J. Chromatogr. 122 (1975) 37.
[112] J.H. Knox, J. Chromatogr. Sci. 15 (1977) 352.
[113] H. Poppe, J.C. Kraak, J.F.K. Huber, J.H.M. van der Berg, Chromatographia 14 (1981) 515.
[114] H. Giesche, K.K. Unger, U. Esser, B. Erray, U. Trüdinger, J. Chromatogr. 465 (1989) 39.
[115] T. Issaeva, A. Kourganov, K.K. Unger, J. Chromatogr. A 846 (1999) 13.
[116] J. MacNair, K.D. Patel, J.W. Jorgensen, Anal. Chem. 71 (1999) 700.
[117] H. Engelhardt, J. Asshauer, U. Neue, N. Weigand, Anal. Chem. 46 (1974) 336A.
[118] J.R. Mazzeo, U.D. Neue, M. Kele, R.S. Plumb, Anal. Chem. (2005) 460A.
[119] Patent WO 03/014450A1, PCT/US02/25193, February 20, 2003.
[120] K.K. Unger, N. Becker, P. Roumeliotis, J. Chromatogr. 125 (1976) 115.
[121] E.S. Grumbach, Th.E. Wheat, J.R. Masseo, Aquity UPLC System, Application Notebook, Waters, Milford, MA, March 2006, p. 6.
[122] S. Luedtke, Th. Adam, N. von Doehren, K.K. Unger, J. Chromatogr. A 887 (2000) 339.
[123] I. Nischang, U. Tallarek, Electrophoresis 28 (2007) 611.
[124] C.G. Hovath, B.A. Preiss, S.R. Lipsky, Anal. Chem. 39 (1967) 1422.
[125] C.G. Hovath, S.R. Lipsky, Anal. Chem. 41 (1969) 1227.
[126] K. Unger, P. Ringe, J. Schick-Kalb, B. Straube, Z. Anal. Chem. 264 (1973) 267.
[127] K.K. Unger, J. Schick-Kalb, B. Straube, in: S. Modry, M. Svata (Eds.), Pore Structure and Properties of Materials, Academia, Prague, 1974, p. B47.
[128] G.J. Kennedy, J.H. Knox, J. Chromatogr. Sci. 10 (1972) 549.
[129] K.K. Unger, J. Chromatogr. A 1000 (2004) 1 (Table 3, p. 4).
[130] J.P.C. Vissers, J. Chromatogr. A 856 (1999) 117.
[131] P. Roumeliotis, M. Chatziathanassiou, K.K. Unger, Chromatographia 19 (1984) 145.
[132] G. Rozing, LC–GC–LC Col. Technol. Suppl. June (2004) 12–16.
[133] E. Rapp, U. Tallarek, J. Sep. Sci. 26 (2003) 453.
[134] Y. Shen, R.D. Smith, K.K. Unger, D. Kumar, D. Lubda, Anal. Chem. 77 (2005) 6692.
[135] G. Rozing, Recent developments in LC column technology, LC–GC June (2003) 2–7.
[136] J.H. Knox, H.M. Pyper, J. Chromatogr. 363 (1986) 1.
[137] L.R. Snyder, J.J. Kirkland, J.L. Glajch, Practical HPLC Method Development, second ed., Wiley, New York, 1997, p. 50.
[138] D.M. McCalley, J. Chromatogr. A 793 (1998) 31.
[139] D.M. McCalley, Anal. Chem. 75 (2003) 3404.
[140] St.M.C. Buckenmeiser, D.M. McCalley, M.R Euerby, Anal. Chem. 74 (2004) 4672.
[141] Q. Luo, Y. Shen, K.K. Hixon, R. Zhao, F. Yang, R.J. Moore, H.M. Mottaz, R.D. Smith, Anal. Chem. 77 (2005) 5028.
[142] M. Kubin, P. Spacek, P. Chromecek, Coll. Czechosl. Chem. Commun. 32 (1967) 3881.
[143] W.D. Ross, R.T. Jefferson, J. Chromatogr. Sci. 8 (1970) 386.
[144] F.D. Hileman, R.E. Sievers, G.G. Hess, W.D. Ross, Anal. Chem. 45 (1973) 1126.
[145] S. Hjerten, J.L. Liao, R. Zhang, J. Chromatogr. A 473 (1989) 273.
[146] F. Svec, J.M.J. Frechet, Anal. Chem. 54 (1992) 820.
[147] A. Premstaller, H. Oberacher, C.G. Huber, Anal. Chem. 72 (2000) 4386.
[148] M.R. Buchmeiser, N. Atzl, G.K. Bonn, J. Am. Chem. Soc. 119 (1997) 9166.
[149] P.-E. Gustavsson, P.-O. Larsson, J. Chromatogr. A 925 (2001) 69.
[150] M. Khayyami, M.T. Perez Pita, N. Pena Garcia, G. Johansson, B. Danielsson, P.-O. Larsson, Talanta 45 (1998) 557.
[151] D. Zhou, H. Zou, J. Ni, L. Yang, L. Jia, Q. Zhang, Y. Zhang, Anal. Chem. 71 (1999) 155.

I

[152] K. Hamaker, S.-L. Rau, R. Hendrickson, J. Liu, C.M. Iadisch, M.R. Ladisch, Ind. Eng. Chem. Res. 38 (1999) 865.
[153] K. Nakanishi, N. Soga, J. Non Cryst. Solids 139 (1992) 14.
[154] A.M. Siuoffi, J. Chromatogr. A 1000 (2003) 801.
[155] D. Lubda, Ph.D. thesis, University of Vienna, 2004.
[156] K. Nakanishi, J. Porous Mater. 4 (1997) 67.
[157] K. Nakanishi, H. Minakuchi, N. Soga, N. Tanaka, J. Sol–Gel. Sci. Technol. 8 (1997) 547.
[158] H. Minakuchi, K. Nakanishi, N. Soga, N. Ishizuka, N. Tanaka, J. Chromatogr. A 762 (1997) 135.
[159] K. Nakanishi, H. Minakuchi, N. Soga, N. Tanaka, J. Sol–Gel. Sci. Technol. 13 (1998) 163.
[160] N. Ishizuka, H. Minakuchi, K. Nakanishi, N. Soga, K. Hosoya, N. Tanaka, J. Chromatogr. A 797 (1998) 133.
[161] K. Cabrera, G. Wieland, D. Lubda, K. Nakanishi, N. Soga, H. Minakuchi, K.K. Unger, TrAC 17 (1998) 50.
[162] K. Nakanishi, J. Sol–Gel Sci. Technol. 19 (2000) 65.
[163] N. Ishizuka, K. Nakanishi, K. Hirao, J. Sol–Gel. Sci. Technol. 19 (2000) 371.
[164] K. Cabrera, D. Lubda, H. Minakuchi, K. Nakanishi, J. High Resolut. Chromatogr. Commun. 23 (2000) 81.
[165] K. Nakanishi, K. Cabrera, D. Lubda, J. High Resolut. Chromatogr. 23 (2000) 111.
[166] P. Zoellner, A. Leitner, D. Lubda, K. Cabrera, W. Lindner, Chromatographia 52 (2000) 818.
[167] D. Lubda, K. Cabrera, H. Minakuchi, K. Nakanishi, J. Sol–Gel Sci. Technol. 23 (2002) 185.
[168] M. Motokawa, H. Kobayashi, N. Ishizuka, H. Minakuchi, K. Nakanishi, H. Jinnai, K. Hosoya, T. Ikegami, N. Tanaka, J. Chromatogr. A 961 (2002) 53.
[169] N. Tanaka, H. Kobayashi, N. Ishizuka, H. Minakuchi, K. Nakanishi, K. Hosoya, T. Ikegami, J. Chromatogr. A 965 (2002) 35.
[170] N. Tanaka, H. Kobayashi, Anal. Bioanal. Chem. 376 (2003) 298.
[171] K. Cabrera, J. Sep. Sci. 27 (2004) 843.
[172] K.K. Unger, B. Bidlingmaier, C. du Fresne von Hohenesche, D. Lubda, in: F. Rodriguez-Reinoso, B. McEnany, J. Rouquerol, K.K. Unger (Eds.), Characterization of Porous Solids VI, Elsevier, Amsterdam, 2002, p. 115.
[173] J.J. Meyers, S. Nahar, D.K. Ludlow, A.I. Liapis, J. Chromatogr. A 907 (2001) 57.
[174] J.J. Meyers, O.K. Crosser, A.I. Liapis, J. Chromatogr. A 908 (2001) 35.
[175] F.C. Leinweber, D. Lubda, K. Cabrera, U. Tallarek, Anal. Chem. 74 (2002) 2470.
[176] U. Tallarek, F.C. Leinweber, A. Seidel-Morgenstern, Chem. Eng. Technol. 25 (2002) 1177.
[177] F.C. Leinweber, U. Tallarek, J. Chromatogr. A 1006 (2003) 207.
[178] J.J. Meyers, A.I. Liapis, J. Chromatogr. A 852 (1999) 3.
[179] A.I. Liapis, J.J. Meyers, O.K. Crosser, J. Chromatogr. A 865 (1999) 13.
[180] B.A. Brian, R. Skudas, K.K. Unger, in preparation.
[181] R. Skudas, B.A. Grimes, E. Machtejevas, V. Kudirkaite, T.P. Hnnessy, D. Lubda, K.K. Unger, J. Chromatogr. A 1144 (2007) 72.
[182] L. Xiong, R. Zhang, F.E. Regnier, J. Chromatogr. A 1030 (2004) 187.
[183] B. Barroso, D. Lubda, R. Bischoff, J. Proteome Res. 2 (2003) 633.
[184] L. Rieux, H. Niederlander, E. Verpoorte, R. Bischoff, J. Sep. Sci. 28 (2005) 1628.
[185] P. Gzil, N. Vervoort, G.V. Baron, G. Desmet, Anal. Chem. 76 (2004) 6707.
[186] N. Vervoort, P. Gzil, G.V. Baron, G. Desmet, J. Chromatogr. A 1030 (2004) 177.
[187] F. Gritti, W. Piatkowski, G. Guiochon, J. Chromatogr. A 978 (2002) 81.
[188] P. Gzil, N. Vervoort, G.V. Baron, G. Desmet, Anal. Chem. 75 (2003) 6244.
[189] J. De Smet, P. Gzil, N. Vervoort, H. Verelst, G.V. Baron, G. Desmet, Anal. Chem. 76 (2004) 3716.
[190] P. Gzil, G.V. Baron, G. Desmet, J. Chromatogr. A 991 (2003) 169.
[191] P. Gzil, J. De Smet, G. Desmet, J. Sep. Sci. 29 (2006) 1675.
[192] H. Minakuchi, N. Ishizuka, K. Nakanishi, N. Soga, N. Tanaka, J. Chromatogr. A 797 (1998) 121.
[193] H. Minakuchi, N. Ishizuka, K. Nakanishi, N. Soga, N Tanaka, J. Chromatogr. A 797 (1998) 133.
[194] H. Minakuchi, N. Ishizuka, K. Nakanishi, N. Soga, N. Tanaka, J. Chromatogr. A 828 (1998) 83.
[195] B. Bidlingmaier, N. von Doehren, K.K. Unger, J. Chromatogr. A 832 (1999) 11.
[196] H. Pham-Tuan, L. Kaskavelis, C.A. Daykin, H.-G. Janssen, J. Chromatogr. B 789 (2003) 283.
[197] L. Spoof, J. Meriluoto, J. Chromatogr. A 947 (2002) 237.
[198] L. Rieux, H. Niederländer, E. Verpoorte, R. Bischoff, J. Sep. Sci. 28 (2005) 1628.
[199] Y. Chun, C.F. Poole, J. Chromatogr. A 1003 (2003) 113.
[200] M.R. Euerby, P. Petersson, J. Chromatogr. A 994 (2003) 13.
[201] J.J. Gilroy, J.W. Dolan, L.R. Snyder, J. Chromatogr. A 1000 (2003) 801.
[202] F. Gritti, G. Guiochon, Anal. Chem. 75 (2003) 5726.
[203] P. Jandera, M. Halama, K. Novotna, S. Buncekova, Chromatographia 57 (2003) 153.
[204] D.V. McCalley, J. Chromatogr. A 987 (2003) 17.
[205] C. Stella, P. Seuret, S. Rudaz, P.-A. Carrupt, J.-Y. Gauvrit, P. Lanteri, J.-L. Veuthey, Chimia 57 (2003) 210.
[206] T.P. Hennessy, R.I. Boysen, M.I. Huber, K.K. Unger, M.T.W. Hearn, J. Chromatogr. A 1009 (2003) 15.
[207] B. Chankvetnadze, C. Yamamoto, Y. Okamoto, Chem. Lett. 32 (2003) 850.
[208] F.C. Leinweber, D.G. Schmid, D. Lubda, K.-H. Weismüller, G. Jung, U. Tallarek, Rapid Commun. Mass Spectrom. 17 (2003) 1180.
[209] D. Lubda, K. Cabrera, N. Nakanischi, W. Lindner, Anal. Bioanal. Chem. 377 (2003) 892.
[210] D. Lubda, W. Lindner, J. Chromatogr. A 1036 (2004) 135.
[211] N. Barbarin, B.D. Mawhinney, R. Black, J. Henion, J. Chromatogr. B 783 (2003) 73.
[212] Y. Hsieh, G. Wang, Y. Wang, S. Chackalamannil, J.-M. Brisson, K. Ng, W.A. Korfmacher, Rapid Commun. Mass Spectrom. 16 (2002) 944.
[213] A.M. van Nederkassel, A. Aerts, A. Dierick, D.L. Massart, Y. Van der Heyden, J. Pharm. Biomed. Anal. 32 (2003) 233.
[214] G. Dear, R. Plumb, D. Mallet, Rapid Commun. Mass Spectrom. 15 (2001) 152.
[215] K. Pihlainen, E. Sippola, R. Kostiainen, J. Chromatogr. A 994 (2003) 93.
[216] F. Gerber, M. Krummen, H. Potgeter, A. Roth, Ch. Siffrin, Ch. Spoendlin, J. Chromatogr. A 1036 (2004) 127.
[217] Q. Xu, M. Mori, K. Tanaka, M. Ikedo, W. Hu, J. Chromatogr. A 1026 (2004) 191.
[218] T. Koal, A. Asperger, J. Efer, W. Engewald, Chromatographia 57 (2003) 93.
[219] Q. Xu, K. Tanaka, M. Mori, M.I.H. Helaleh, H. Toada, W. Hu, K. Hasebe, Chromatographia 57 (2003) 19.
[220] Q. Xu, K. Tanaka, M. Mori, M.I.H. Helaleh, W. Hu, K. Hasebe, H. Toada, J. Chromatogr. A 997 (2003) 183.
[221] A. Asperger, J. Efer, Th. Koal, W. Engewald, J. Chromatogr. A 960 (2002) 109.
[222] J. Efer, Th. Koal, A. Asperger, W. Engewald, GIT Special Sep. 22 (2002) 58.
[223] A. Asperger, J. Efer, Th. Koal, W. Engewald, J. Chromatogr. A 937 (2001) 65.
[224] P. Hatsis, Ch.A. Lucy, Analyst 127 (2002) 451.
[225] P. Zollner, A. Leitner, D. Lubda, K. Cabrera, W. Lindner, Chromatographia 52 (2000) 818.
[226] M. Castellari, E. Sartini, A. Fabiabi, G. Arfelli, A. Amati, J. Chromatogr. A 973 (2002) 221.
[227] A. Jakab, E. Forgacs, Chromatographia 56 (2002) 69.
[228] D. Lubda, K. Cabrera, K. Nakanishi, W. Lindner, Anal. Bioanal. Chem. 377 (2003) 892.
[229] G. Massolini, E. Calleri, A. Lavecchia, F. Loiodice, D. Lubda, C. Temporini, G. Fracchiolla, P. Tortorella, E. Novellino, G. Caccialanza, Anal. Chem. 75 (2003) 535.
[230] E. Calleri, C. Temporini, G. Massolini, G. Caccialanza, J. Pharm. Biomed. Anal. 35 (2004) 243.
[231] V.V. Tolstikov, A. Lommen, K. Nakanishi, N. Tanaka, O. Fiehn, Anal. Chem. 75 (2003) 6737.
[232] A.J. Shah, F. Crespi, C. Heidbreder, J. Chromatogr. B 781 (2002) 151.

[233] B. Barroso, D. Lubda, R. Bischoff, J. Prot. Res. 2 (2003) 633.
[234] N. Tanaka, H. Kimura, D. Tokuda, K. Hosoya, T. Ikegami, N. Ishizuka, H. Minakuchi, K. Nakanishi, Y. Shintani, M. Furona, K. Cabrera, Anal. Chem. 76 (2004) 1273.
[235] C.J. Venkatramani, Y. Zelechonok, Anal. Chem. 75 (2003) 3484.
[236] T. Murahashi, Analyst 128 (2003) 611.
[237] T. Ikegami, T. Hara, H. Kimura, H. Kobayashi, K. Hosoya, K. Cabrera, N. Tanaka, J. Chromatogr. A 1106 (2006) 112.
[238] E. Machtejevas, S. Andrecht, D. Lubda, K.K. Unger, J. Chromatogr. A 1144 (2007) 97.
[239] J. Seidl, J. Malinski, K. Dusek, W. Heitz, Adv. Polymer Sci. 5 (1967) 113.
[240] Monolithic Materials: Preparation, Properties and Applications, F. Svec, T.B. Tennikova, Z. Deyl (Eds.), J. Chromatogr. Lib., Elsevier, Amsterdam, 2003.
[241] S. Eltink, J.M. Herrero-Martinez, G.P. Rozing, P.J. Shoemakers, W.Th. Kok, Anal. Chem. 77 (2005) 7342.
[242] Special Issue on Momolithic Columns, J. High Resolut. Chromatogr. 23 (2000) 3–116.
[243] D. Josic, J.G. Clifton, J. Chromatogr. 1144 (2007) 2.
[244] A. Podgornik, Advantages of Chromatographic Monoliths, Monolith Summer School, Portoroz, Slovenia, 27–31 May 2006.
[245] S. Eeltink, Ph.D. thesis, University of Amsterdam, 2005.
[246] H. Oberacher, C.G. Huber, Trends Anal. Chem. 21 (2002) 166.
[247] B. Mayr, K. Eder, M.R. Buchmeiser, C.G. Huber, Anal. Chem. 74 (2002) 6080.
[248] W. Walcher, H. Oberacher, S. Troiani, G. Hölzl, P.J. Oefner, L. Zolla, C.G. Huber, J. Chromatogr. B 782 (2002) 111.
[249] H. Oberacher, A. Premstaller, C.G. Huber, J. Chromatogr. A 1030 (2004) 201.
[250] R.E. Majors, LC–GC N. Am. 24 (2006) 248.
[251] R.E. Majors, LC–GC N. Am. 24 (2006) 356.
[252] M. Wedd, GIT-Labor-Fachz. 44 (2000) 610.
[253] D. Nicoli, P. OïHagan, G. Pokrajac, K. Hasapidis, Int. Lab. 30 (2000) 16.
[254] D. Driscoll, F. Etzler, T. Barber, J. Nehne, W. Niemann, B. Bistrian, Int. J. Pharm. 219 (2001) 21.
[255] R. Trottier, B. Kaye, Size Measurement of Particles, Encyclopedia of Polymer Science and Technology, Wiley, New York, 1987, p. 267.
[256] P. Reschiglian, G. Torsi, Chromatographia 40 (1995) 467.
[257] J. Pazourek, J. Microcol. Sep 9 (1997) 611.
[258] P.J.P. Cardot, J.-M. Launay, M. Martin, J. Liq. Chromatogr. Rel. Technol. 20 (1997) 2543.
[259] P. Reschiglian, D. Melucci, G. Torsi, A. Zattoni, Chromatographia 51 (2000) 87.

Available online at www.sciencedirect.com
ScienceDirect
Journal of Chromatography A, 1144 (2007) 14–29
JOURNAL OF CHROMATOGRAPHY A
www.elsevier.com/locate/chroma

Pore structural characterization of monolithic silica columns by inverse size-exclusion chromatography

Brian A. Grimes [a,*], Romas Skudas [a], Klaus K. Unger [a], Dieter Lubda [b]

[a] *Institut für Anorganische Chemie und Analytische Chemie, Johannes Gutenberg Universität-Mainz, Duesbergweg 10-14, D-55099 Mainz, Germany*
[b] *PLS Merck KGaA, Frankfurterstrasse 250, D-64271 Darmstadt, Germany*

Available online 28 November 2006

II

Abstract

In this work, a parallel pore model (PPM) and a pore network model (PNM) are developed to provide a state-of-art method for the calculation of several characteristic pore structural parameters from inverse size-exclusion chromatography (ISEC) experiments. The proposed PPM and PNM could be applicable to both monoliths and columns packed with porous particles. The PPM and PNM proposed in this work are able to predict the existence of the second inflection point in the experimental exclusion curve that has been observed for monolithic materials by accounting for volume partitioning of the polymer standards in the macropores of the column. The appearance and prominence of the second inflection point in the exclusion curve is determined to depend strongly on the void fraction of the macropores (flow-through pores), (b) the nominal diameter of the macropores, and (c) the radius of gyration of the largest polymer standard employed in the determination of the experimental ISEC exclusion curve. The conditions that dictate the appearance and prominence of the second inflection point in the exclusion curve are presented. The proposed models are applied to experimentally measured ISEC exclusion curves of six silica monoliths having different macropore and mesopore diameters. The PPM and PNM proposed in this work are able to determine the void fractions of the macropores and silica skeleton, the pore connectivity of the mesopores, as well as the pore number distribution (PND) and pore volume distribution (PVD) of the mesopores. The results indicate that the mesoporous structure of all materials studied is well connected as evidenced by the similarities between the PVDs calculated with the PPM and the PNM, and by the high pore connectivity values obtained from the PNM. Due to the fact that the proposed models can predict the existence of the second inflection point in the exclusion curves, the proposed models could be more applicable than other models for ISEC characterization of chromatographic columns with small diameter macropores (interstitial pores) and/or large macropore (interstitial pore) void fractions. It should be noted that the PNM can always be applied without the use of the PPM, since the PPM is an idealization that considers an infinitely connected porous medium and for materials having a low (<6) pore connectivity the PPM would force the PVD to a lower average diameter and larger distribution width as opposed to properly accounting for the network effects present in the real porous medium.

Keywords: Inverse size-exclusion chromatography; Silica monolith; Parallel pore model; Pore network model; Pore size distribution; Pore volume distribution; Pore number distribution; Pore connectivity

1. Introduction

Monolithic columns have gained substantial interest in high-performance liquid chromatography (HPLC) as compared to microparticulate packed columns [1–38]. While polymer-based monoliths [1–18] found widespread application in the field of analysis and preparative isolation of biopolymers, silica-based monolithic columns [19–38] appear to be more suitable for the resolution of low molecular weight analytes up to 10 kDa [39–43]. Polymer-based monoliths [1–18] possess a pronounced macropore structure with pore diameters in excess of 50 nm. Silica monoliths [19–38] exhibit a distinct bimodal pore volume distribution with macropores (flow-through pores) of approximately 2 μm diameter and mesopores (diffusional pores) of approximately 10 nm diameter. Such columns are commercialized as Chromolith columns by Merck (Darmstadt, Germany), as *n*-octadecylbonded stationary phases and enable fast separations at substantially low column back pressures. For example,

* Corresponding author. Tel.: +49 6151 728 209; fax: +49 6151 729 535.
E-mail address: b.a.grimes@web.de (B.A. Grimes).

0021-9673/$ – see front matter © 2006 Elsevier B.V. All rights reserved.
doi:10.1016/j.chroma.2006.11.007

II

such columns exhibit a column performance equivalent to 3 μm packed columns and a column back pressure equivalent to 13 μm packed columns [44].

Further development and optimization of monolithic silica columns with respect to higher column performance and higher speed of analysis at an acceptable column pressure drop can be accomplished in two ways: empirically by systematically varying the pore structural parameters of the monoliths and monitoring their chromatographic properties, or by modeling and simulation tools predicting optimum properties with regard to column performance. The latter are based on pore structural models and generate parameters that are related to the chromatographic properties via mass transfer kinetics and equilibrium constants [45–52]. In this context, the reliable characterization of monoliths becomes an essential tool for modeling and simulation. Instead of performing a comprehensive physicochemical characterization and chromatographic testing, ISEC was the pore structural characterization method of choice for the following reasons: (a) ISEC is based upon a common liquid phase-based separation process that is similar to SEC and HPLC application scenarios, (b) a well-developed theoretical framework is published in the literature [53–62], (c) the method can be fully automated with high reproducibility, and (d) ISEC is particularly attractive for assessing the pore structural data of monolithic silica capillaries with diameters of 100 μm and smaller as an situ-method.

One of the first models for SEC was suggested by van Kreveld and van den Hoed [53]. They [53] employed a uniform-sized random sphere model to characterize the average sphere radius of Porosil silica gel beads based on a known particle void volume. Furthermore, van Kreveld and van den Hoed [54] thoroughly described the mass transfer phenomena in SEC and proved the assumption that the elution volume behavior of a homologous set of unretained polymer standards was governed by the steric exclusion effect and that the elution volume of the polymer standards should be independent of the flow rate if the first moment of the individual chromatograms is used as the retention time, t_R. Halasz and Martin [55] also suggested a model for partitioning in SEC. However, this model [55] assumes that the volume partition coefficient of a non-rigid macromolecule in an individual pore is unity when the molecular radius of the macromolecule is smaller than the pore radius. This assumption [55] is contradictory to macromolecule partitioning theory [63–68] as pointed out by Knox and Scott [56] as well as Gorbunov et al. [57], and will consequently give pore volume distributions that are far too wide [57]. Knox and Scott [56] employed a non-uniform-sized random sphere model to predict SEC calibration curves (exclusion curves); their model [56] provided an excellent correlation to experimental data but was computationally cumbersome. They [56] also suggested a model for the SEC exclusion curve for rigid spherical macromolecules that could easily provide the pore volume distribution of the porous material with numerical differentiation of the exclusion curve. This model [56] is based on the inversion of a first-kind Fredholm equation representing the partitioning of macromolecules in all elements of the stationary phase and the pore volume distributions are expressed in terms of the derivatives of the experimental exclusion curve. However, great uncertainties could arise in numerically calculating the higher order derivatives of the experimental exclusion curve [57]. Gorbunov et al. [57] provided a thorough review of SEC as chromatographic porosimetry (or ISEC) and suggested that a more accurate method for determining pore volume distributions would be to directly solve the first-kind Fredholm equation while using an appropriate function that represents the partitioning of flexible macromolecules in the individual pores [63–68] as the kernel function. Hagel et al. [58] presented the model of Gorbunov et al. [57] in summation (rather than integral) form and discussed the effect of the data point density and locations on the calculated values of the average pore size and the width of the distribution. Goto and McCoy [59] provided a model for ISEC with polydisperse pore and solute sizes by obtaining the zeroth, first, and second moments of the column response to a pulse injection from the differential mass balance equations for the particles and packed chromatographic column that account for a finite solute size. Al-Bokari et al. [60] presented a model to determine the mesopore volume distribution in silica monoliths as well as the individual macropore and mesopore volume void fractions by exploiting the unusual feature of a second inflection point in the exclusion curves measured for silica monoliths. However, this model [60] uses the inaccurate model of Halasz and Martin [55] to obtain the mesopore volume distribution from the experimental exclusion curves and relies on the extrapolation of an empirical model beyond the domain of the experimental data to determine the individual volume void fractions of the macropores and mesopores. It should be noted that in all the SEC and ISEC models for packed columns discussed above [53–59], the experimental partition coefficient, K_{ISEC}, is explicitly defined such that volume partitioning of solutes is considered only to occur in the intraparticle pores (mesopores).

In this work, a state-of-art calculation method for the pore number and volume distributions by ISEC that employs a parallel pore model (PPM) and a pore network model (PNM) is presented, and the potential of ISEC for the characterization and optimization of monolithic silica columns is discussed. A general mathematical model for the exclusion curve of a homologous set of flexible straight-chain polymer standards is developed based on the first moments of the column response to a pulse injection and formulated in a manner that is similar to typical experimental calculations of the ISEC exclusion curve.

2. Mathematical formulation

2.1. General expressions for the moments of the column response to a pulse injection

A radially homogenous monolith having a bimodal porous structure consisting of macropores (flow-through pores) and mesopores is considered. The solid phase (skeleton) of the monolith contains the mesopores and is surrounded by macropores, which form a continuous network throughout the column [49,69]. The skeleton of the monolith is taken to be physicochemically homogeneous and could be approximated by

cylindrical geometry [49,69]. The column is considered to be filled with an incompressible liquid that does not adsorb onto the stationary phase and flow only occurs in the macropores [49,69]. In the model system, a single analyte is injected into the column as a pulse, and eluted under isocratic conditions. The concentration of the analyte is considered to be dilute such that its adsorption isotherm can be taken to be linear [69]. Furthermore, the analyte is considered to have a finite size represented by a characteristic molecular radius, r_m. Under isothermal conditions, the differential mass balance for the analyte in the stagnant liquid inside the skeleton is given by Eq. (1). The initial and boundary conditions of Eq. (1) are given by Eqs. (2)–(4).

$$\varepsilon_p K_p \frac{\partial C_p}{\partial t} + K_{eq} \frac{\partial C_s}{\partial t} - \varepsilon_p K_p D_p \left[\frac{\partial^2 C_p}{\partial r^2} + \frac{1}{r} \frac{\partial C_p}{\partial r} \right] = 0 \quad (1)$$

$$\text{at } t = 0, \quad C_p = 0, \quad \text{for } 0 \le r \le R_p \quad (2)$$

$$\text{at } r = 0, \quad C_p \text{ is finite}, \quad \text{for } t > 0 \quad (3)$$

$$\text{at } r = R_p, \quad k_f(C_b - C_p|_{r=R_p}) = \varepsilon_p K_p D_p \left. \frac{\partial C_p}{\partial r} \right|_{r=R_p}, \quad \text{for } t > 0 \quad (4)$$

In Eqs. (1)–(4), t represents the time, r the radial position of the cylindrical skeleton elements, C_p the concentration of the analyte in the stagnant liquid inside the mesopores, C_b the concentration of the analyte in the liquid flowing through the macropores, C_s the concentration of the analyte in the adsorbed phase per unit skeleton volume, R_p the radius of the skeleton elements, D_p the effective diffusion coefficient of the analyte in the confined mesoporous space of the skeleton, K_{eq} the equilibrium adsorption constant of the linear adsorption isotherm, k_f the film mass transfer coefficient of the analyte, ε_p the void fraction of the monolithic skeleton, and K_p represents the volume partition coefficient of the finite sized analyte in the mesoporous void space of the skeleton. The value of K_p can be obtained from Eq. (5).

$$K_p = \int_{p_d=0}^{\infty} K_{sp}(r_m, \xi) f_p(\xi)\, d\xi \quad (5)$$

In Eq. (5), ξ is a dummy variable of integration, r_m the characteristic molecular radius of the analyte, p_d the diameter of the mesopores, $f_p(p_d)$ the pore volume distribution of the mesopores which represents the distribution of mesopore diameters relative to the total volume of mesopores, and K_{sp} represents the function that describes the volume partitioning of the analyte in a single pore [63–68]. In ISEC, a homologous set of polymeric standards is employed to determine the exclusion curve. In a single pore of cylindrical geometry, the functional form of K_{sp} for a flexible linear polymer having an infinite number of infinitely small segments is given by the expression developed by Casassa [63],

$$K_{sp} = 4\sum_{m=1}^{\infty} \frac{1}{\lambda_m^2} \exp\left[-\lambda_m^2 \left(\frac{2r_g}{p_d} \right) \right] \quad (6a)$$

where λ_m denotes the mth root of the zeroth order Bessel function of the first kind and r_g represents the radius of gyration of the polymer. It is important to note that the radius of gyration, r_g, is generally considered to represent the characteristic molecular radius, r_m, of the polymer standards employed as analytes in ISEC and, thus, r_m and r_g can be taken to be equivalent ($r_m = r_g$). In a single cylindrical pore, the functional form of K_{sp} for flexible linear polymers having an finite number of segments with a finite length is given by the following expression developed by Davidson et al. [68]:

$$\ln(K_{sp}) = \ln\left(4\sum_{m=1}^{\infty} \frac{1}{\lambda_m^2} \exp\left[-\lambda_m^2 \left(\frac{2r_g}{p_d} \right) \right] \right) + \frac{\ell}{p_d} \left[0.49 + 1.09 \left(\frac{2r_g}{p_d} \right) + 1.79 \left(\frac{2r_g}{p_d} \right)^2 \right] \quad (6b)$$

By evaluating the Laplace transform of Eqs. (1)–(4) and normalizing the spatial variable, r, by the radius of the skeleton such that $\rho = r/R_p$, one obtains the following expressions for the differential mass balance of the analyte in the stagnant liquid of the mesoporous skeleton and its boundary conditions:

$$\rho^2 \frac{d^2 \bar{C}_p}{d\rho^2} + \rho \frac{d\bar{C}_p}{d\rho} - \rho^2 \omega^2 \bar{C}_p = 0 \quad (7)$$

$$\text{at } \rho = 0, \quad \bar{C}_p \text{ is finite} \quad (8)$$

$$\text{at } \rho = 1, \quad \bar{C}_b - \bar{C}_p|_{\rho=1} = \gamma \left. \frac{d\bar{C}_p}{d\rho} \right|_{\rho=1} \quad (9)$$

where

$$\omega = \beta\sqrt{s} \quad (10)$$

$$\beta = \sqrt{\frac{R_p^2}{D_p}\left(1 + \frac{K_{eq}}{\varepsilon_p K_p} \right)} \quad (11)$$

$$\gamma = \frac{\varepsilon_p K_p D_p}{k_f R_p} \quad (12)$$

In Eqs. (7)–(12), the variables with an overhead bar represent the Laplace transform of the given variable, and s denotes the independent variable of the Laplace transform domain. The solution to Eqs. (7)–(9) is given by Eq. (13).

$$\bar{C}_p = \bar{C}_b \frac{I_0(\omega\rho)}{I_0(\omega) + \gamma\omega I_1(\omega)} \quad (13)$$

In Eq. (13), I_0 denotes the modified Bessel function of the first kind of zero order and I_1 represents the first order modified Bessel function of the first kind. In order to simplify the calculation for the moments of the chromatogram, it would be advantageous at this point to evaluate the limits of $\bar{C}_p$ at $\rho = 1$, as the value of s approaches zero, along with the limits of its first and second derivative with respect to s.

$$\lim_{s\to 0} \bar{C}_p|_{\rho=1} = \lim_{s\to 0} \frac{I_0(\beta\sqrt{s})}{I_0(\beta\sqrt{s}) + \gamma\beta\sqrt{s} I_1(\beta\sqrt{s})} = 1 \quad (14)$$

$$\lim_{s\to 0}\left.\frac{\partial \bar{C}_p}{\partial s}\right|_{\rho=1} = \lim_{s\to 0}\frac{1}{2}\gamma\beta^2\frac{[I_1(\beta\sqrt{s})-I_0(\beta\sqrt{s})][I_1(\beta\sqrt{s})+I_0(\beta\sqrt{s})]}{[I_0(\beta\sqrt{s})+\gamma\beta\sqrt{s}I_1(\beta\sqrt{s})]^2} = -\frac{1}{2}\gamma\beta^2 \tag{15}$$

$$\lim_{s\to 0}\left.\frac{\partial^2 \bar{C}_p}{\partial s^2}\right|_{\rho=1} = \lim_{s\to 0}\frac{\gamma\beta^2}{2[I_0(\beta\sqrt{s})+\gamma\beta\sqrt{s}I_1(\beta\sqrt{s})]^3}\left[\frac{\beta I_0(\beta\sqrt{s})^2 I_1(\beta\sqrt{s})}{\sqrt{s}}+\gamma\beta^2 I_0(\beta\sqrt{s})^3-\gamma\beta^2 I_0(\beta\sqrt{s})I_1(\beta\sqrt{s})^2 - \frac{I_0(\beta\sqrt{s})I_1(\beta\sqrt{s})^2}{s}-\frac{\beta I_1(\beta\sqrt{s})}{\sqrt{s}}-\frac{\gamma\beta I_1(\beta\sqrt{s})^3}{\sqrt{s}}\right] = \frac{1}{2}\gamma^2\beta^4+\frac{1}{8}\gamma\beta^4 \tag{16}$$

II

The differential mass balance for the analyte in the flowing liquid of the macropores is given by Eq. (17). The initial and boundary conditions of Eq. (17) are given by Eqs. (18)–(20).

$$\varepsilon_b K_b\frac{\partial C_b}{\partial t}+u_0\frac{\partial C_b}{\partial z}+(1-\varepsilon_b)\frac{2}{R_p}k_f(C_b-C_p|_{r=R_p}) - \varepsilon_b K_b D_L\frac{\partial^2 C_b}{\partial z^2}=0 \tag{17}$$

$$\text{at } t=0,\quad C_b=0,\quad \text{for } 0\le z\le L \tag{18}$$

$$\text{at } z=0,\quad u_0\delta(t)=u_0 C_b|_{z=0}-\varepsilon_b K_b D_L\left.\frac{\partial C_b}{\partial z}\right|_{z=0}, \quad \text{for } t>0 \tag{19}$$

$$\text{at } z=L,\quad \left.\frac{\partial C_b}{\partial z}\right|_{z=L}=0,\quad \text{for } t>0 \tag{20}$$

In Eqs. (17)–(20), z is the spatial variable along the axis of the column, u_0 the superficial velocity of the mobile phase in the column, D_L the axial dispersion coefficient of the solute in the flowing liquid phase, L the length of the column, $\delta(t)$ the Dirac delta function which represents a pulse injection of the solute into the column, ε_b the void fraction of the macroporous void space in the column, and K_b represents the volume partition coefficient of the finite sized analyte in the macroporous void space of the monolithic column. The value of K_b can be obtained from Eq. (21).

$$K_b=\int_{p_d=0}^{\infty}K_{sp}(r_m,\xi)f_b(\xi)\,d\xi \tag{21}$$

In Eq. (21), r_m is the characteristic molecular radius of the analyte (which for the polymer standards most commonly used in ISEC should be equivalent to the radius of gyration, r_g, of the polymer standard), p_d the diameter of the macropores, $f_b(p_d)$ the pore volume distribution of the macropores that represents the distribution of macropore sizes relative to the total volume of macropores, and K_{sp} represents the function that describes the partitioning of the analyte in a single pore which is given by Eq. (6a) or (6b).

By evaluating the Laplace transform of Eqs. (17)–(20) and normalizing the spatial variable z by the length, L, of the column such that $\zeta=z/L$, one obtains the following expressions for the differential mass balance of the analyte in the liquid flowing through the macroporous void space of the column and its boundary conditions:

$$\frac{d^2\bar{C}_b}{d\zeta^2}-\varphi\frac{d\bar{C}_b}{d\zeta}-g(s)\bar{C}_b=0 \tag{22}$$

$$\text{at } \zeta=0,\quad \varphi=\varphi\bar{C}_b|_{\zeta=0}-\left.\frac{d\bar{C}_b}{d\zeta}\right|_{\zeta=0} \tag{23}$$

$$\text{at } \zeta=1,\quad \left.\frac{d\bar{C}_b}{d\zeta}\right|_{\zeta=1}=0 \tag{24}$$

where

$$g(s)=\chi s+\kappa(1-\bar{C}_p|_{\rho=1}) \tag{25}$$

$$\varphi=\frac{u_0 L}{\varepsilon_b K_b D_L} \tag{26}$$

$$\chi=\frac{L^2}{D_L} \tag{27}$$

$$\kappa=\frac{(1-\varepsilon_b)}{\varepsilon_b K_b}\frac{2}{R_p}\chi k_f. \tag{28}$$

In order to easily evaluate the moments of the chromatogram, it would be advantageous at this point to evaluate the limits of $g(s)$ along with its first and second derivative with respect to s, as the value of s approaches zero. By considering Eq. (25) and its derivatives with respect to s, along with the limits given in Eqs. (14)–(16), one obtains the following expressions:

$$\lim_{s\to 0}g(s)=0 \tag{29}$$

$$\lim_{s\to 0}\frac{\partial g}{\partial s}=\lim_{s\to 0}\chi-\kappa\left.\frac{\partial \bar{C}_p}{\partial s}\right|_{\rho=1}=\chi-\frac{1}{2}\kappa\gamma\beta^2 \tag{30}$$

$$\lim_{s\to 0}\frac{\partial^2 g}{\partial s^2}=\lim_{s\to 0}-\kappa\left.\frac{\partial^2 \bar{C}_p}{\partial s^2}\right|_{\rho=1}=\frac{1}{2}\kappa\gamma^2\beta^4+\frac{1}{8}\kappa\gamma\beta^4 \tag{31}$$

The solution to Eqs. (22)–(24) is given by Eq. (32) as follows:

$$\bar{C}_b=\varphi\left[\frac{m_2 e^{m_2+m_1\zeta}-m_1 e^{m_1+m_2\zeta}}{m_2(\varphi-m_1)e^{m_2}-m_1(\varphi-m_2)e^{m_1}}\right] \tag{32}$$

where

$$m_1=\tfrac{1}{2}(\varphi+h(s)) \tag{33}$$

$$m_2=\tfrac{1}{2}(\varphi-h(s)) \tag{34}$$

$$h(s)=\sqrt{\varphi^2+4g(s)} \tag{35}$$

It follows from Eq. (32) that the Laplace transform domain solution of C_b at the column exit ($\zeta = 1$) should be expressed as follows:

$$\bar{C}_b|_{\zeta=1} = 4\varphi\, e^{\varphi/2}\left[\frac{h}{(\varphi+h)^2\, e^{h/2} - (\varphi-h)^2\, e^{-h/2}}\right] \tag{36}$$

Again, in order to simplify the calculation of the moments of the chromatogram, it is advantageous at this point to evaluate the limit of $h(s)$ and its first and second derivative with respect to s, as s approaches zero. By considering Eq. (35) along with the limits presented in Eqs. (29)–(31), one obtains the following expressions:

$$\lim_{s\to 0} h(s) = \varphi \tag{37}$$

$$\lim_{s\to 0}\frac{\partial h}{\partial s} = \lim_{s\to 0}\frac{2}{\sqrt{\varphi^2+4g(s)}}\frac{\partial g}{\partial s} = \frac{1}{\varphi}(2\chi - \kappa\gamma\beta^2) \tag{38}$$

$$\begin{aligned}\lim_{s\to 0}\frac{\partial^2 h}{\partial s^2} &= \lim_{s\to 0}\frac{2}{[\varphi^2+4g(s)]^{1/2}}\frac{\partial^2 g}{\partial s^2} - \frac{4}{[\varphi^2+4g(s)]^{3/2}}\left(\frac{\partial g}{\partial s}\right)^2 \\ &= -\frac{1}{\varphi}\left(\kappa\gamma^2\beta^4 + \frac{1}{4}\kappa\gamma\beta^4\right) - \frac{1}{\varphi^3}\left(\chi + \frac{1}{2}\kappa\gamma\beta^2\right)^2\end{aligned} \tag{39}$$

The nth moment of Eq. (36) is equivalent to the nth moment of the chromatogram [69–72] provided that the detector is located sufficiently close to the column exit such that extra-column peak dispersion could be considered to be negligible. Therefore, the zeroth moment, μ_0, first moment, μ_1, and second moment, μ_2, of the chromatogram for the single analyte could be expressed [69–72], respectively, as follows:

$$\mu_0 = \lim_{s\to 0}\bar{C}_b|_{\zeta=1} = 1 \tag{40}$$

$$\begin{aligned}\mu_1 &= \lim_{s\to 0} -\left.\frac{\partial \bar{C}_b}{\partial s}\right|_{\zeta=1} = -\lim_{h\to\varphi}\left.\frac{\partial \bar{C}_b}{\partial h}\right|_{\zeta=1}\lim_{s\to 0}\frac{\partial h}{\partial s} \\ &= \frac{L}{u_0}\left[\varepsilon_b K_b + (1-\varepsilon_b)\varepsilon_p K_p\left(1+\frac{K_{eq}}{\varepsilon_p K_p}\right)\right]\end{aligned} \tag{41}$$

$$\begin{aligned}\mu_2 &= \lim_{s\to 0}\left.\frac{\partial^2 \bar{C}_b}{\partial s^2}\right|_{\zeta=1} = \lim_{h\to\varphi}\left.\frac{\partial^2 \bar{C}_b}{\partial h^2}\right|_{\zeta=1}\lim_{s\to 0}\left(\frac{\partial h}{\partial s}\right)^2 + \lim_{h\to\varphi}\left.\frac{\partial \bar{C}_b}{\partial h}\right|_{\zeta=1}\lim_{s\to 0}\frac{\partial^2 h}{\partial s^2} = \frac{1}{2}\frac{\varepsilon_b K_b D_L}{u_0 L}\mu_1^2 \\ &+ \left[1 + 2\left(\frac{\varepsilon_b K_b D_L}{u_0 L}\right)^2\left(e^{(-u_0 L)/(\varepsilon_b K_b D_L)} - 1\right)\right]\mu_1^2 + \frac{L}{u_0}(1-\varepsilon_b)\varepsilon_p K_p\left(1+\frac{K_{eq}}{\varepsilon_p K_p}\right)^2\left[\frac{R_p}{k_f}\varepsilon_p K_p + \frac{R_p^2}{4D_p}\right]\end{aligned} \tag{42}$$

Eqs. (40)–(42) represent the zeroth, first, and second moments, respectively, of the column response to a pulse injection. Upon comparison of Eq. (41) to expressions developed for μ_1 of columns packed with porous spherical particles [70–72], it becomes clear that the first moment, μ_1, of the column response to a pulse injection is independent of the morphology of the stationary phase and, thus, Eq. (41) could represent μ_1 for a chromatographic column having a stationary phase of any morphology (e.g., a column packed with porous spherical particles or a monolith having a porous skeleton).

Although it is not required for characterization of porous media with ISEC, at this point for completeness, it would be beneficial to provide the expression for the height equivalent of a theoretical plate (HETP), or plate height, H, that can be obtained from the moments, μ_0, μ_1, and μ_2, presented in Eqs. (40)–(42), respectively.

$$\begin{aligned}H = \frac{K_b D_L}{2u} &+ \left[2L\left(\frac{K_b D_L}{uL}\right)^2\left(e^{(-uL)/(K_b D_L)} - 1\right)\right] \\ &+ \left[\frac{\varepsilon_b(1-\varepsilon_b)(\varepsilon_p K_p + K_{eq})^2}{[\varepsilon_b K_b + (1-\varepsilon_b)(\varepsilon_p K_p + K_{eq})]^2}\frac{R_p}{k_f}\right]u \\ &+ \left[\frac{\varepsilon_b(1-\varepsilon_b)(\varepsilon_p K_p + K_{eq})^2}{4[\varepsilon_b K_b + (1-\varepsilon_b)(\varepsilon_p K_p + K_{eq})]^2}\frac{R_p^2}{\varepsilon_p K_p D_p}\right]u\end{aligned} \tag{43}$$

In Eq. (43), u represents the linear velocity of the mobile phase. It should be noted that the second term on the right-hand-side of Eq. (43) represents the band broadening due to dispersion at the entrance of the column (see Eq. (19)) and has a negligible contribution to the plate height unless the column length is very short.

2.2. Experimental calculation of ISEC exclusion curves

In a typical experimental determination of an ISEC exclusion curve [57,61,73], an inert tracer molecule and a homologous set of N polymer standards are eluted individually through the column. The retention times, $t_{R,i}$ ($i = 0, 1, 2, \ldots, N$), of the inert tracer molecule ($i = 0$) and polymer standard i ($i = 1, 2, \ldots, N$) along with the elution volumes, $V_{E,i}$ ($i = 0, 1, 2, \ldots, N$), of the inert tracer molecule ($i = 0$) and polymer standard i ($i = 1, 2, \ldots, N$) are determined to obtain the experimental ISEC partition coefficient, K_{ISEC}, as a function of the radius of gyration, $r_{g,i}$ ($i = 1, 2, \ldots, N$) of the polymers. It should be noted here that in order to satisfy the quasi-equilibrium conditions required for ISEC calculations, the first moment of the chromatograms should be used as the retention time [53,54,62]. After the elution volumes have been calculated, one can obtain the experimental ISEC partition coefficient, $K_{ISEC}(i)$, for each molecule i ($i = 0, 1, 2, \ldots, N$) as follows [57,61,73]:

$$K_{ISEC}(i) = \frac{V_{E,i} - V_{E,N}}{V_{E,0} - V_{E,N}}, \quad \text{for } i = 0, 1, 2, \ldots, N \tag{44}$$

where $K_{ISEC}(i)$ represents the experimental ISEC partition coefficient of molecule i ($i = 0, 1, 2, \ldots, N$), and $V_{E,i}$ denotes the elution volume of molecule i ($i = 0, 1, 2, \ldots, N$). Furthermore, the total void fraction of the column, ε_t, can be obtained from

II

the following expression:

$$\varepsilon_t = \frac{V_{E,0} - V_d}{\pi R^2 L} \quad (45)$$

where R denotes the radius of the column and V_d represents the column dead volume.

2.3. Parallel pore model for ISEC

Due to the fact that the elution volumes used in Eq. (44) are obtained from the first moment, μ_1, of the individual chromatograms of the standards [53,54,62], it follows that the exclusion curve could be modeled in terms of the first moments, $\mu_{1,i}$ ($i=0, 1, 2, \ldots, N$), of the column response to a pulse injection. For a given molecule i ($i=0, 1, 2, \ldots, N$), Eq. (44) can be expressed in terms of the first moments, $\mu_{1,i}$ ($i=0, 1, 2, \ldots, N$), as follows:

$$K_{ISEC}(i) = \frac{Q_i\mu_{1,i} - Q_N\mu_{1,N}}{Q_0\mu_{1,0} - Q_N\mu_{1,N}}, \quad \text{for } i = 0, 1, 2, \ldots, N \quad (46)$$

where Q_i denotes the volumetric flow rate employed in the chromatographic measurement of molecule i ($i=0, 1, 2, \ldots, N$) and $\mu_{1,i}$ represents the first moment of the chromatogram obtained for molecule i ($i=0, 1, 2, \ldots, N$). As shown in Eq. (41), for any stationary phase morphology (e.g., columns packed with spherical particles or cylindrical particles, or monoliths having spherical or cylindrical skeleton elements), and also when considering (i) axial dispersion to be functioning, (ii) film (external) mass transfer resistance to be functioning, (iii) intraparticle (internal) mass transfer resistance to be functioning, and (iv) no adsorption to be occurring, the first moment of the column response to a pulse injection is given by Eq. (47).

$$\mu_{1,i} = \frac{L}{u_{0,i}}[\varepsilon_b K_{b,i} + (1-\varepsilon_b)\varepsilon_p K_{p,i}], \quad \text{for } i = 0, 1, 2, \ldots, N \quad (47)$$

In Eq. (47), $u_{0,i}$ is the superficial column velocity used in the chromatographic measurement of molecule i ($i=0, 1, 2, \ldots, N$), $K_{p,i}$ the volume partition coefficient of molecule i ($i=0, 1, 2, \ldots, N$) in the pores of the stationary phase (mesopores), and $K_{b,i}$ represents the volume partition coefficient of molecule i ($i=0, 1, 2, \ldots, N$) in the void space where bulk flow occurs (macropores). Since the total porosity, ε_t, of the column can be determined experimentally as shown in Eq. (45), it is useful to employ the expression given by Eq. (48) to express the void fraction of the skeleton, ε_p, in terms of ε_t and ε_b.

$$\varepsilon_p = \frac{\varepsilon_t - \varepsilon_b}{1 - \varepsilon_b} \quad (48)$$

By combining Eqs. (46)–(48), and considering that the polymer standards are eluted through the column at the same volumetric flow rate ($L/u_{0,i}$ is then constant for all molecules i ($i=0, 1, 2, \ldots, N$), we can obtain the following expression for the experimentally measured partition coefficient in terms of the pore volume distributions f_b and f_p as well as the porosities ε_t and ε_b as follows:

$$K_{ISEC}(i) = \frac{\int_{p_d=0}^{\infty} K_{sp}(r_{g,i}, \xi)[\varepsilon_b f_b(\xi) + (\varepsilon_t - \varepsilon_b) f_p(\xi)]\, d\xi - \int_{p_d=0}^{\infty} K_{sp}(r_{g,N}, \xi)[\varepsilon_b f_b(\xi) + (\varepsilon_t - \varepsilon_b) f_p(\xi)]\, d\xi}{\int_{p_d=0}^{\infty} K_{sp}(r_{g,0}, \xi)[\varepsilon_b f_b(\xi) + (\varepsilon_t - \varepsilon_b) f_p(\xi)]\, d\xi - \int_{p_d=0}^{\infty} K_{sp}(r_{g,N}, \xi)[\varepsilon_b f_b(\xi) + (\varepsilon_t - \varepsilon_b) f_p(\xi)]\, d\xi},$$
$$\text{for } i = 1, 2, \ldots, N \quad (49)$$

Eq. (49) represents the experimentally measured partition coefficient in inverse size-exclusion chromatography based on the first moments of the column response to a pulse injection. It is important to note here that in Eq. (49), the accessible pore volume of the inert tracer ($i=0$) can be taken to be equal to the total column porosity, ε_t, due to the fact that (a) the elution volume, $V_{E,0}$, of the inert tracer ($i=0$) is generally taken to be equal to the total pore volume of the column (inclusive of the macropore volume and the mesopore volume), and (b) the inert tracer molecule ($i=0$) is usually not a flexible polymer and, thus, Eq. (6a) or (6b) cannot be used to describe the partitioning of the inert tracer ($i=0$) in a single pore, while employing a function in place of Eq. (6a) or (6b) that would consider the inert tracer ($i=0$) as a hard sphere [64] leads to a discontinuity in the exclusion curve. Furthermore, it is important to stress that when the first moments, $\mu_{1,i}$ ($i=0, 1, 2, \ldots, N$) of the experimentally measured chromatograms are used to represent the retention times, $t_{R,i}$ ($i=0, 1, 2, \ldots, N$), then it is not necessary to achieve quasi-equilibrium conditions (that is, mass transfer resistance by axial dispersion, external film mass transfer, and restricted diffusion in the pores do not factor into the calculation) as the elution volumes, $V_{E,i}$ ($i=0, 1, 2, \ldots, N$), will be independent of the volumetric flow rate, as noted by van Kreveld and van den Hoed [54].

If one considers (a) that the extent of volume partitioning of the molecules in the interstitial pores of a packed bed or the flow-through pores of a monolith is negligible, and (b) that the excluded volume of the smallest molecule (the inert tracer) is negligible, such that $K_{b,0} \to 1$, $K_{p,0} \to 1$, $K_{b,N} \to 1$, $K_{p,N} \to 0$, and $K_{b,i} \to 0$ ($i=0, 1, 2, \ldots, N$), then $K_{ISEC}(i) \to K_{p,i}$ and Eq. (49) reduces to the expression developed by Gorbunov et al. [57]:

$$K_{ISEC}(i) \to K_{p,i} = \int_{p_d=0}^{\infty} K_{sp}(r_{g,i}, \xi) f_p(\xi)\, d\xi,$$
$$\text{for } i = 0, 1, 2, \ldots, N \quad (50)$$

For columns having large diameters of the bulk flow pores (interstitial pores in packed beds or flow-through pores in monoliths) relative to the largest molecular weight standard employed and low values of ε_b, Eq. (50) is suitable to use to represent the experimentally measured exclusion curve. However, for columns packed with small particles which have smaller diameter interstitial pores relative to the largest polymer standards and for many monoliths having a porous skeleton, which generally have a high values of ε_b and smaller diameter flow-through pores relative to

the largest polymer standards, Eq. (49) should be employed to characterize the mesopore structural parameters with ISEC.

2.4. Pore network model for ISEC

In a pore network model, a finite number of pore diameters, N_{pore}, are randomly chosen from a pore number distribution, $f_{p,n}(p_d)$ (this represents the distribution of mesopore sizes relative to the total number of mesopores), and topologically mapped onto a three-dimensional distorted [52,74] cubic lattice of interconnected cylindrical pores having a regular array of nodes (the lattice size, L_D, is the same along the x, y, and z coordinates of the lattice and, thus, $x \times y \times z$: $L_D \times L_D \times L_D$). The nodes are connected to each other by bonds (pores) of the pore network; nearest neighbor and next-to-nearest neighbor connections are considered in the distorted cubic lattice and, thus, the coordination number of the lattice is 18. The total number of pores, N_{pore}, is determined [74] from the pore connectivity, n_T, where $N_{pore} = 0.5n_T(L_D^3)$. A spine of bulk flow pores (these are considered to be the interstitial pores of a packed bed or the macroporous flow-through pores of a monolith) is added so that it transects the lattice [52,74] and is considered to be the point where the probe molecules enter the internal (mesopore) void space. Periodic boundary conditions are applied to all six faces of the cubic lattice because the system is considered to be at quasi-equilibrium and, thus, the top and bottom faces (which are perpendicular to the macroporous spine) of the lattice do not have to be open for bulk transport of material. This represents a departure from the periodic boundary conditions applied previously in network modeling theory [45–52,74] which considered the top and bottom faces of the lattice to be open and accessible to the bulk liquid. In several of these works [46–50,74], it was necessary to open the top and bottom faces of the lattice to accommodate a mass flux, or fluid flow. However, since pore characterization experiments such as ISEC, mercury porosimetry, or gas sorption occur under quasi- or true equilibrium conditions, there is no reason to open the top and bottom faces of the lattice to accommodate a mass flux or fluid flow and, thus, the bulk liquid is only considered to be accessible from the macroporous spine. By closing all six faces of the cubic lattice for the quasi-equilibrium process modeled, the simulation results become consistent with increases in the lattice dimension, L_D, as opposed to what has been presented elsewhere in the literature [45–52,74] and the number of realizations required for each point on the exclusion curve does not have to be large to obtain a smooth curve; the number of realizations could be as low as 8, although in this work, 20 realizations were performed with the network model at each point on the exclusion curve. It was found through numerous simulations with this model that a lattice dimension, L_D, of 13 ($L_D = 13$) was sufficient to provide consistent results for all porous media studied. It is important to note that for other intrusive pore characterization methods [52,74] that require the system to reach equilibrium (e.g., mercury porosimetry and gas sorption), this approach of applying periodic boundary conditions to all six sides of the cubic lattice is applicable and should provide consistent simulation results with increasing values of the lattice dimension, L_D.

The length of the mesopores are taken to be equal to their diameter [45–52,74], however, in order to match the model porosity to the porosity of the real porous medium, the length, $\ell_{p,s}$, of the "spinal" pores must be scaled according to Eq. (51).

$$\ell_{p,s} = \frac{4\varepsilon_b}{\varepsilon_p(1-\varepsilon_b)\pi p_{d,m}^2 L_D} \tag{51}$$

In Eq. (51), $p_{d,m}$ represents the nominal pore diameter of the "spinal" macropores.

The model of Casassa [63] or Davidson et al. [68] (Eqs. (6a) and (6b), respectively) for cylindrical pores could be applied to describe the partitioning function K_{sp} in each pore of the lattice. In order to determine the percolation effects on the exclusion properties of the porous medium, the lattice is scanned outward from the spine [74]; if the radius of a pore is smaller than the effective radius, r_e, of the given molecule ($r_e = 0.5r_g\sqrt{\pi}$), the pore is considered, for all practical purposes, to be inaccessible to the molecule and, thus, will block the percolation pathway, otherwise, the pore is considered to be accessible. The lattice is scanned repeatedly until no more accessible pores are found. The partition coefficient can then be obtained from Eq. (52).

$$K_{ISEC}(i) = \frac{\sum_{n=1}^{N_{pore}} \nu_{n,i} K_{sp}(r_{g,i}, p_{d,n})[\pi \ell_{p,n}(p_{d,n}^2/4)] - \sum_{n=1}^{N_{pore}} \nu_{n,N} K_{sp}(r_{g,N}, p_{d,n})[\pi \ell_{p,n}(p_{d,n}^2/4)]}{\sum_{n=1}^{N_{pore}} \nu_{n,0} K_{sp}(r_{g,0}, p_{d,n})[\pi \ell_{p,n}(p_{d,n}^2/4)] - \sum_{n=1}^{N_{pore}} \nu_{n,N} K_{sp}(r_{g,N}, p_{d,n})[\pi \ell_{p,n}(p_{d,n}^2/4)]},$$
$$\text{for } i = 1, 2, \ldots, N \tag{52}$$

In Eq. (52), $\nu_{n,i}$ ($n = 1, 2, \ldots, N_{pore}$; $i = 1, 2, \ldots, N$) is equal to unity if pore n is accessible to molecule i, while $\nu_{n,i}$ is equal to zero if pore n is inaccessible to molecule i. The values of $\nu_{n,i}$ ($n = 1, 2, \ldots, N_{pore}$; $i = 1, 2, \ldots, N$) are determined from the scanning algorithm discussed above. In Eq. (52), the volume partition coefficient of the inert tracer ($i = 0$) could be taken to be equal to unity for the reasons discussed above for the PPM. It should be mentioned here that since the PPM (Eq. (49)) is an idealization (that is, it assumes an infinite connectivity) that does not adequately represent the finite connected porous network occurring in real porous media, the PNM (Eq. (52)) alone is adequate to employ for the characterization of porous media by ISEC. This is because at high values of the pore connectivity, n_T, the PNM can always predict the same results as the PPM, while at low values of n_T, the PPM cannot predict the same behavior as the PNM. However, it is useful to use the PPM to provide an initial guess for the non-linear regression of the experimental data with the PNM.

3. Experimental description

3.1. Chemicals and samples

Tetrahydrofuran (for liquid chromatography) and 2-propanol (for liquid chromatography) were obtained from Merck. Poly-

II

mer standards of polystyrene – molecular weights 162, 309, 514, 707, 795, 1920, 3460, 51,500, 524,000 – and polystyrol – molecular weights 5610, 12,500, 27,500, 125,000, 271,000, 864,000, 1,530,000 – were obtained from Polymer Standards Service (Mainz, Germany). Polystyrene standards of molecular weights 950 and 2,750,000 (for lipophilic gel permeation chromatography) were obtained from Merck. All samples had the polydispersity values lower than 1.10 except for the sample of molecular mass 2,750,000, which had a polydispersity value lower then 1.3.

3.2. Chromatographic measurements

All experiments were run on a Bischoff Liquid Chromatographic system (LC-CaDI controller with two HPLC compact pumps 2250, UV detector Lambda 1010, auto-sampler Model 718AL), obtained from Bischoff Chromatography (Leonberg, Germany). The configuration was controlled by McDAcq32 software (Bischoff Chromatography).

Measurements were made with Chromolith Performance RP18e columns (100 mm × 4.6 mm) having inter-skeleton macropore sizes in the range from 1.8 to 6.0 μm and 10 to 25 nm intra-skeleton mesopore sizes. These monolithic columns were obtained as a research sample from Merck. Pore volume distributions were independently measured by nitrogen adsorption and mercury porosimetry at Merck.

All experiments were performed under isocratic elution for each polymer standard sample. The pump was set to provide a volumetric flow rate of 0.5 mL/min for all chromatographic measurements. The injection volume was 2 μL and detection was carried out at 254 nm. The measurements were carried out tree times. Data emerge as mean values from three independent runs.

4. Results and discussion

In the parallel pore model presented above, a Gaussian distribution is employed to represent the pore volume distribution (PVD) of the mesopores located inside the skeleton of the monolith. The Gaussian distribution was chosen because the average value and standard deviation are explicit parameters in the distribution equation and it has been shown [57] that the ISEC exclusion curve is very insensitive to the functional form of the pore volume distribution. As mentioned above, the PVD represents the distribution of mesopore diameters relative to the total mesopore volume and is denoted as $f_p(p_d)$. In Eq. (53), the functional form of the Gaussian distribution is presented which represents the PVD of the mesopores that is employed in the PPM.

$$f_p(p_d) = \frac{1}{p_{dv,std}\sqrt{2\pi}} \exp\left[-\frac{1}{2}\left(\frac{p_d - p_{dv,ave}}{p_{dv,std}}\right)^2\right] \quad (53)$$

In Eq. (53), $p_{dv,ave}$ represents the average diameter of the pores in the distribution, while $p_{dv,std}$ represents the standard deviation of the pore diameters in the distribution. It must be mentioned here that ISEC can only account for the full distribution of the mesopores because as one employs larger and larger standards to characterize partitioning in the macropores, the column will become blocked and, thus, the full exclusion curve for the macropores cannot be measured. That is, only the concave down portion of the exclusion curve for the macropores can be measured. Due to the fact that the concave up portion of the exclusion curve is most affected by the distribution width [57,58], the distribution of the macropores is taken to be a uniform distribution centered around the nominal macropore diameter, $p_{d,m}$.

Similarly for the pore network model, a Gaussian distribution is employed to represent the pore number distribution (PND) of the mesopores. It is important to note again that the PND represents the distribution of mesopore diameters relative to the total mesopore number and is denoted as $f_{p,n}(p_d)$. In Eq. (54), the functional form of the Gaussian distribution is presented which represents the PND of the mesopores that is employed in the PNM.

$$f_{p,n}(p_d) = \frac{1}{p_{dn,std}\sqrt{2\pi}} \exp\left[-\frac{1}{2}\left(\frac{p_d - p_{dn,ave}}{p_{dn,std}}\right)^2\right] \quad (54)$$

In Eq. (54), $p_{dn,ave}$ represents the average diameter of the pores in the distribution, while $p_{dn,std}$ represents the standard deviation of the pore diameters in the distribution. The PVD, $f_p(p_d)$, of the PNM can be obtained from the PND, $f_{p,n}(p_d)$, by employing the following expression [74]:

$$f_p(p_d) = \frac{N_{pore} - L_D}{V_{p,meso}} \left(\frac{\pi}{4} p_d^3\right) f_{p,n}(p_d) \quad (55)$$

In Eq. (55), $V_{p,meso}$ denotes the total volume of mesopores in the pore network model. The average diameter, $p_{dv,ave}$, and standard deviation, $p_{dv,std}$, of the PVD of the PNM can be obtained by evaluating the first and second moments of the PVD obtained from Eq. (55).

In Fig. 1a and b, theoretically calculated ISEC exclusion curves (K_{ISEC} versus r_g) are presented for various values of the macropore void fraction, ε_b. The material modeled in Fig. 1a and b has a mesoporous skeleton with macroporous flow-through pores and, thus, could be taken to represent a silica monolith [19–38]. In Fig. 1a, the ISEC exclusion curves are calculated with the PPM presented above (Eq. (49)), while in Fig. 1b, the calculations are made with the PNM presented above (Eq. (52)). In Fig. 1a, the total porosity, ε_t, of the column is taken to be equal to 0.85, the nominal diameter of the macropores is equal to 2.0 nm, the average diameter of the PVD, $p_{dv,ave}$, and the standard deviation of the PVD, $p_{dv,std}$, are set at 15.0 and 4.0 nm, respectively. In Fig. 1b, the total porosity and the nominal diameter of the macropores have the same values as those reported for Fig. 1a, the average diameter of the PND, $p_{dn,ave}$, and the standard deviation of the PND, $p_{dn,std}$, are set at 15.0 and 4.0 nm, respectively; these parameters for the PND of the PNM provide an average diameter, $p_{dv,ave}$, of 17.8 nm and a standard deviation, $p_{dv,std}$, of 3.69 nm for the PVD of the PNM. Additionally, in Fig. 1b, the pore connectivity, n_T, of the lattice is taken to be equal to 10, the dimension of the cubic, L_D, lattice is 13, and the number of realizations [45–52,74] performed with the network is 20. It should be noted here that for all simulations presented

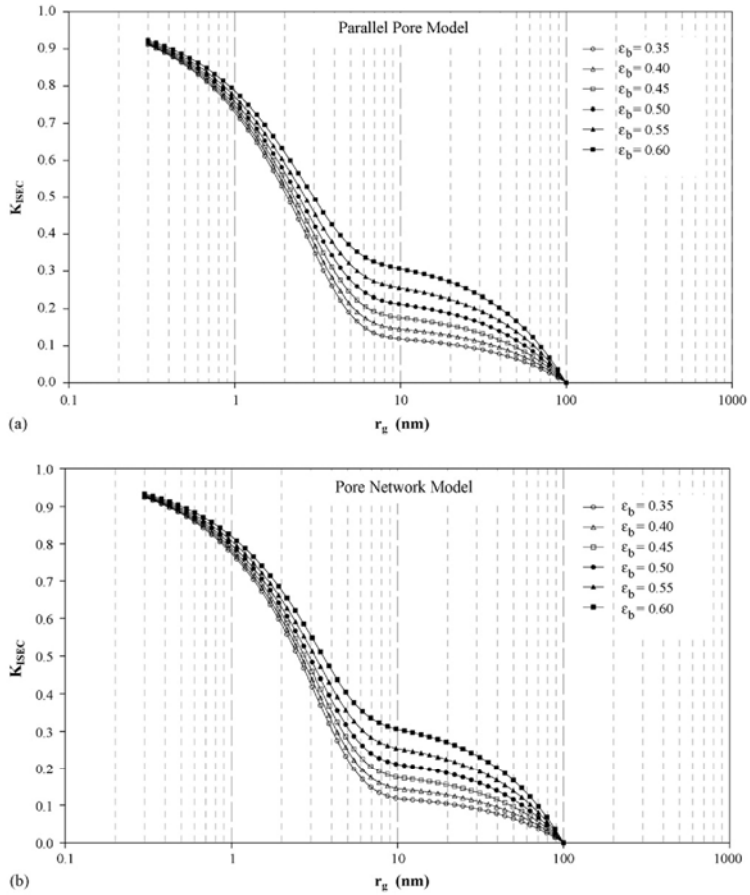

Fig. 1. Theoretical exclusion curves for monoliths having a mesoporous skeleton and macroporous flow-through pores for various values of the void fraction of the macropores, ε_b. Calculations done with the: (a) parallel pore model (PPM) and (b) pore network model (PNM).

in this work, Eq. (6a) was employed to represent the partitioning of the polymer standards in the individual pores. It is clear from both Fig. 1a and b that the models presented above in Eqs. (49) and (52), respectively, predict two inflection points in the exclusion curves for the systems studied. Such exclusion curves with two inflection points have been observed previously for monoliths [60,75]. This second inflection point in the exclusion curves (that appears at the foot of the curve) could be due to the partitioning of the polymer standards in the macropores. Such a result would indicate that it is not necessarily true under all conditions that the elution volume of the largest standard used in the ISEC calibration represents the volume of the macropore void space in the monolith (or in the case of a packed bed, the volume of the interstitial pore void space). That is, under certain conditions, the following equation (Eq. (56)) for the elution volume of a molecule, V_E, of molecule i expressed in terms of: (a) the volume, V_b, of the macropores in a monolith or interstitial pores in a packed bed, (b) the volume, V_p, of the pores in the skeleton of a monolith or the particles in a packed bed, and (c) the experimentally measured partition coefficient, K_{ISEC}, may not always be valid.

$$V_E = V_b + K_{ISEC} V_p \tag{56}$$

Indeed, one may find that for certain systems the macropore volume is decreasing as they inject larger and larger standards into the column. Therefore, it is necessary to define the characteristics of a chromatographic system that provide significant partitioning in the macropores. As indicated by the results in Fig. 1a and b, increasing the macropore void volume, ε_b, increases the prominence of volume partitioning in the macropores. Due to the fact that the macropore void fraction, ε_b, in silica monoliths is much larger than the interstitial void fraction of a column packed with porous particles [19–38], one reason behind the relatively more

II

common appearance of the second inflection point in the exclusion curve for silica monoliths becomes apparent. Furthermore, it is very important to note that as the value of ε_b increases and the partitioning in the macropores becomes more prominent, the value of the partition coefficient, K_{ISEC}, increases for any given value of the radius of gyration, r_g, despite the fact that the PVD and PND of the mesopores was held constant for all simulations. This result is also due to the fact that volume partitioning is more prominent in the macropores as the value of ε_b increases. But this result does not indicate that one would find that the average pore diameter and standard deviation of the mesopores would increase with increasing values of ε_b if one were to use a set of polymer standards where the largest molecule is, in a practical sense, just at the exclusion limit of the mesopores ($r_g \sim 10$–15 nm for the results in Fig. 1a and b) and model the exclusion curve with the methods suggested by Gorbunov et al. [57] or Hagel et al. [58]. However, if one does not recognize that the second inflection point arises from volume partitioning in the macropores and considers the entire exclusion curve to represent volume partitioning in the mesopore volume as shown in Eq. (56) (which is the common assumption in ISEC [55–58,60,61]), then by employing a bimodal pore volume distribution for the mesopores, one would always find that the nominal radius of the larger pore set is equal to the radius of gyration of the largest polymer employed [75]. Finally, by comparing Fig. 1a and b, one can observe that the lower portion of the exclusion curves that represent the volume partitioning of the molecules in the macropores are almost identical when calculated with the PPM and the PNM. The upper portion of the exclusion curves that represent the volume partitioning of the molecules in the mesopores has slightly larger values of K_{ISEC} for the PNM relative to the PPM. This is simply due to the fact that the average diameter, $p_{dv,ave}$, and standard deviation, $p_{dv,std}$, are slightly larger for the PNM than the PPM. The similarity between the two curves indicates that a pore connectivity, n_T, value of 10 provides enough alternate pathways through the porous media such that the connectivity of the material could be considered infinite and equivalent to the PPM which assumes infinite connectivity [74]. Numerous simulations with the PNM over a wide range of PND parameters (not shown in this work) indicates that for n_T values of 10 and greater, there is no noticeable change in the behavior of the exclusion curve and these curves are exactly similar to an exclusion curve calculated with the PPM having the same PVD.

In Fig. 2a and b, theoretically calculated ISEC exclusion curves (K_{ISEC} versus r_g) are presented for what can be considered to be a silica monolith [19–38] and the values of the nominal macropore diameter, $p_{d,m}$, are varied. In Fig. 2a, the ISEC exclusion curves are calculated with the PPM presented above (Eq. (49)), while in Fig. 2b, the calculations are made with the PNM presented above (Eq. (52)). In Fig. 2a and b, the macropore void fraction is taken to be equal to 0.50, while all other parameters have the same values as those reported above for Fig. 1a and b. Again, Fig. 2a and b depict the second inflection point in the exclusion curve for the monolith modeled and the prominence of the partitioning in the macropores decreases as the nominal diameter of the macropores, $p_{d,m}$, increases. Again this result provides strong evidence that the second inflection point observed in the exclusion curves for monoliths arises from volume partitioning of solutes in the macropores. It should be clear by now that the appearance and prominence of the second inflection point is dictated by the following three factors: (a) the macropore void fraction, ε_b (or the interstitial void fraction of a column packed with porous particles), (b) the nominal diameter of the macropores, $p_{d,m}$ (or the diameter of the interstitial pores in a column packed with porous particles), and (c) the gyration radius of the largest polymer standard employed in the determination of the exclusion curve. Numerous simulations have determined [62] that the second inflection point in the exclusion curve appears and becomes prominent when the ratio ($r_{g,N}/p_{d,m}$) of the radius of gyration, $r_{g,N}$, of the largest polymer standard employed in the ISEC experiment to the nominal diameter, $p_{d,m}$, of the macropores becomes larger than 0.0025 when the macropore void fraction, ε_b, is equal to 0.30, and when $r_{g,N}/p_{d,m}$ becomes larger than 0.0017 when ε_b is equal to 0.50.

In Figs. 3–5, the experimentally measured ISEC exclusion curves are presented for the six silica monoliths (monoliths 787, 800, 803, 811, 842, and 843) as well as the theoretical predictions obtained by fitting the PPM and PNM presented in this work to the experimental data. The six silica monoliths can be considered to be grouped into three pairs (787 and 800; 803 and 811; 842 and 843) where each pair has similar nominal macropore diameters while the nominal mesopore diameters of each member of a pair are different. The macropore diameters of each monolith were determined by mercury intrusion (data not shown) and are summarized in Table 1. Table 1 indicates that the nominal macropore diameter, $p_{d,m}$, of silica monolith pair 787 and 800 are 1.8 and 1.9 μm, respectively, the values of $p_{d,m}$ for the silica monolith pair 803 and 811 are 3.5 and 3.4 μm, respectively, while the values of $p_{d,m}$ for the silica monolith pair 842 and 843 are 5.7 and 6.0 μm, respectively. The total porosity, ε_t, of each column was determined by dividing the elution volume of toluene, $V_{E,0}$, by the volume of the empty column, and are presented in Table 1; the values of ε_t for all monoliths are in the range of 0.82 and 0.92 indicating that these monoliths are highly porous. The PPM (Eq. (49)) could be employed to simultaneously regress the parameters $p_{dv,ave}$ and $p_{dv,std}$ of the PVD and either the macropore void fraction, ε_b, or the nominal pore diameter, $p_{d,m}$, of the macropores. Due to the fact that the values of $p_{d,m}$ were previously obtained from mercury porosimetry, the parameters $p_{dv,ave}$, $p_{dv,std}$, and ε_b were simultaneously obtained for all monoliths from non-linear regression of the experimental exclusion curves with the PPM (Eq. (49)) by employing the IMSL subroutine DRNLIN [76]. It should be noted that if one had obtained the value of ε_b from another independent experiment, then one could also use Eq. (49) to determine the values of $p_{dv,ave}$, $p_{dv,std}$, and $p_{d,m}$ by non-linear regression of the experimental data with Eq. (49). It should also be mentioned here that the regression was performed employing only the data points for the flexible polymer standards ($i = 1, 2, \ldots, N$) due to the reasons discussed above following Eq. (49). The results obtained from the ISEC characterization of the silica monoliths are summarized in Table 2. Furthermore, it is clear from Figs. 3–5 that the agreement between theory and experiment is excellent. Once

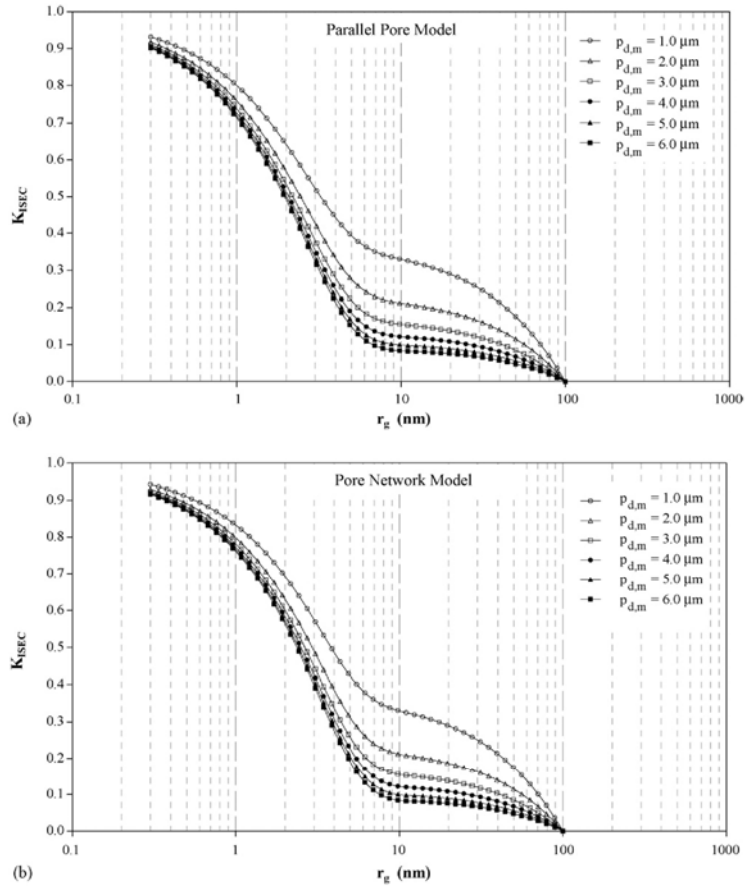

Fig. 2. Theoretical exclusion curves for monoliths having a mesoporous skeleton and macroporous flow-through pores for various values of the nominal diameter of the macropores, $p_{d,m}$. Calculations done with the: (a) parallel pore model (PPM) and (b) pore network model (PNM).

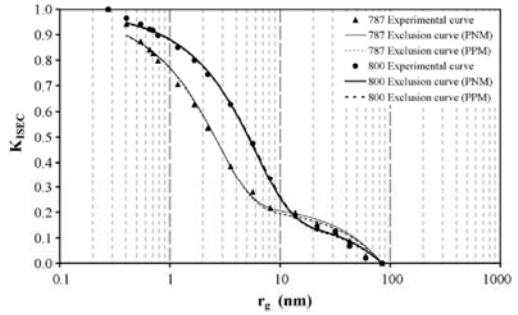

Fig. 3. Experimentally measured exclusion curves for silica monoliths 787 and 800 along with theoretical exclusion curves obtained from regressing the data with the parallel pore model (PPM) (Eq. (49)) and the pore network model (PNM) (Eq. (52)).

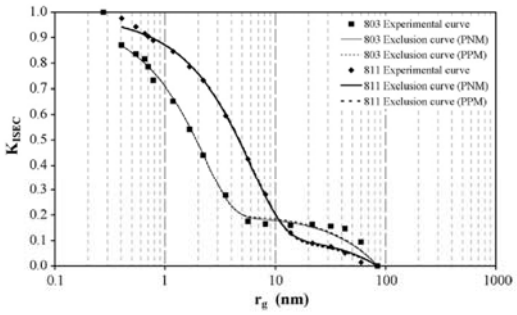

Fig. 4. Experimentally measured exclusion curves for silica monoliths 803 and 811 along with theoretical exclusion curves obtained from regressing the data with the parallel pore model (PPM) (Eq. (49)) and the pore network model (PNM) (Eq. (52)).

II

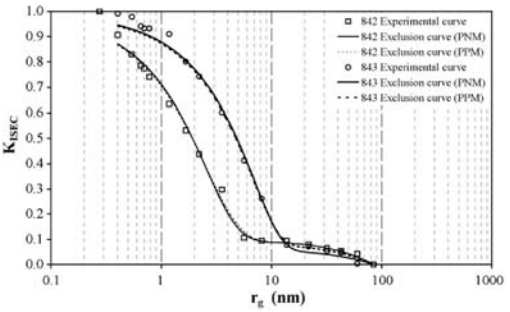

Fig. 5. Experimentally measured exclusion curves for silica monoliths 842 and 843 along with theoretical exclusion curves obtained from regressing the data with the parallel pore model (PPM) (Eq. (49)) and the pore network model (PNM) (Eq. (52)).

Table 1
Summary of the macropore diameters and individual void fractions of the column, macropores, and mesopores for the six silica monoliths

Material	$p_{d,m}$ (μm)	ε_t	ε_b	ε_p
787	1.8	0.86	0.50	0.72
800	1.9	0.92	0.48	0.84
803	3.5	0.85	0.61	0.62
811	3.4	0.90	0.48	0.81
842	5.7	0.82	0.52	0.62
843	6.0	0.88	0.54	0.74

the values of ε_t and ε_b were obtained for each column, the value of the void fraction of the skeleton, ε_p, can be obtained from Eq. (48). It should be noted that the method described in this work for determining the values of the individual void fractions of the macropores and mesopores, ε_b and ε_p, respectively, is clearly advantageous to the method proposed by Al-Bokari et al. [60] due to the fact that one does not have to extrapolate a linear empirical model of a non-linear curve beyond the range of the experimental data points. The calculation method for ε_b presented in this work is based on first principles and a theoretical description of actual experimental calculation methods. Once the silica monoliths had been characterized with the PPM, the PNM presented in Eq. (52) was employed to determine the values of the pore connectivity, n_T, the parameters $p_{dn,ave}$ and $p_{dn,std}$ of the PND as well as the parameters $p_{dv,ave}$ and $p_{dv,std}$ of the PVD (the parameters $p_{dv,ave}$ and $p_{dv,std}$ were not part of

Table 2
Values of the macropore void fraction, ε_b, and parameters of the pore volume distribution (PVD), $p_{dv,ave}$ and $p_{dv,std}$, obtained from the regression of the parallel pore model (PPM) (Eq. (49)) to the experimental data

Material	ε_b	$p_{dv,ave}$ (nm)	$p_{dv,std}$ (nm)
787	0.50	16.3	4.92
800	0.48	36.4	11.3
803	0.61	12.0	0.55
811	0.48	35.3	9.53
842	0.52	14.8	4.43
843	0.54	34.8	0.09

Table 3
Values of the pore connectivity, n_T, the parameters of the pore number distribution (PND), $p_{dn,ave}$ and $p_{dn,std}$, and the parameters of the pore volume distribution (PVD), $p_{dv,ave}$ and $p_{dv,std}$, obtained from the regression of the pore network model (PNM) (Eq. (52)) to the experimental data

Material	n_T	$p_{dn,ave}$ (nm)	$p_{dn,std}$ (nm)	$p_{dv,ave}$ (nm)	$p_{dv,std}$ (nm)
787	>10	11.0	4.82	15.8	4.15
800	>10	23.3	11.1	34.8	9.14
803	>10	11.5	1.73	12.3	1.68
811	>10	25.0	10.0	34.4	8.74
842	>10	11.5	3.70	14.5	3.33
843	>10	36.0	3.00	36.7	2.97

the regression, but can be calculated from $f_{p,H}(p_d)$ according to Eq. (55)). It should be noted that for each silica monolith, the value of ε_b obtained from the PPM was employed as a constant in the PNM and not as a regression parameter due to the fact that the lower part of the curve containing the second inflection point where changes in the value of ε_b are most significant is not affected when the calculations are made with the PNM as opposed to the PPM as discussed for Figs. 1a and b. The best fit values of n_T, $p_{dn,ave}$, and $p_{dn,std}$ were obtained by employing an iterative grid search [57]. The results obtained with the PNM are summarized in Table 3. Again, it is clear from Figs. 3–5 that the agreement between experiment and theory is excellent. The results in Table 3 indicate that the pore connectivity, n_T, of the mesopores is greater than 10 which, as discussed above, indicates that the mesopore network is sufficiently well connected such that it behaves as it is infinitely connected with regard to the volume partitioning phenomenon. This result becomes clear when one compares the values of $p_{dv,ave}$ obtained from the PPM and PNM presented in Tables 2 and 3, respectively, which are very similar; if the value of the pore connectivity, n_T, is less than ideal ($n_T < 10$), then the PVD obtained from the PNM would be shifted to larger diameters and narrower than the PVD obtained from the PPM due to the fact that the assumption of infinite connectivity in the PPM would force the nominal pore diameter to a lower value and increase the standard deviation of the distribution in order to account for the pore volume excluded due to poor network percolation. Such large connectivity values are common for mesoporous materials with a large pore volume fraction; applications of PNM (Eq. (52)) to macroporous ($p_{dv,ave} \sim 100$ nm) polymeric particles [62] consistently provides values of the pore connectivity, n_T, that are less than 10, and the resulting PVD calculated from the PNM differs substantially from the PVD calculated with the PPM. It should be noted here that the value of the pore connectivity, n_T, does not physically represent the average number of intersecting pores within the volume of the real porous media [77]. Strictly speaking, n_T is simply a parameter of the model network which can account for the alternate pathways for mass transfer within the real porous medium. This is similar to the fact that the pore diameters reported from all indirect pore characterization (e.g., ISEC, Hg intrusion, gas sorption) methods do not represent the actual pore diameters within the real porous media, but only the pore diameters of equivalent cylinders that provide the same surface to volume ratio of the real porous media. Nonetheless,

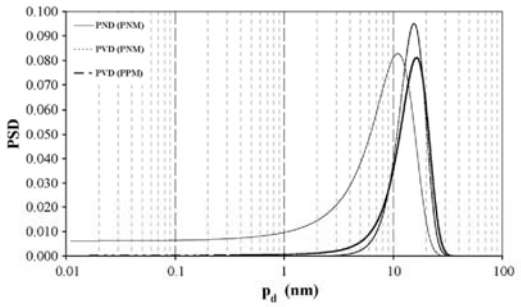

Fig. 6. Pore volume distribution (PVD) obtained from the parallel pore model (PPM) (Eq. (49)) and the pore number distribution (PND) and PVD obtained from the pore network model (PNM) (Eq. (52)) for silica monolith 787.

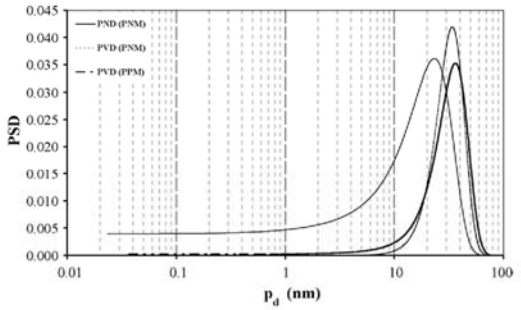

Fig. 7. Pore volume distribution (PVD) obtained from the parallel pore model (PPM) (Eq. (49)) and the pore number distribution (PND) and PVD obtained from the pore network model (PNM) (Eq. (52)) for silica monolith 800.

the PNM provides a fast and easy way to characterize the topology of the porous medium and will be useful until advanced microscopy and 3-D imaging [78–81] becomes widely applied to porous media.

In Figs. 6–11, the PVDs of the mesopores calculated from the PPM regression along with the PNDs and PVDs of the mesopores calculated from the PNM regression are presented for silica monoliths 787, 800, 803, 811, 842, and 843, respectively. For the pore size distributions (PSDs) of silica monoliths 787, 800, 811, and 842 shown in Figs. 6, 7, 9 and 10, respectively, it is clear that the PND obtained from the PNM are shifted to the left (to smaller pore diameters) of the PVDs obtained from both

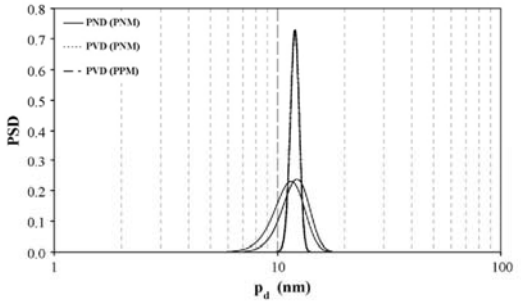

Fig. 8. Pore volume distribution (PVD) obtained from the parallel pore model (PPM) (Eq. (49)) and the pore number distribution (PND) and PVD obtained from the pore network model (PNM) (Eq. (52)) for silica monolith 803.

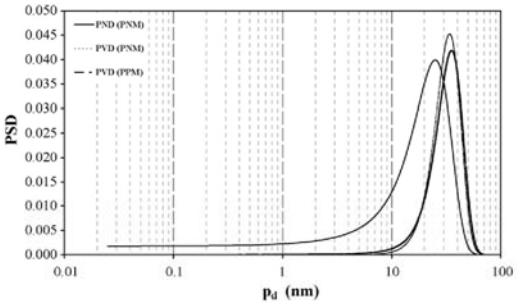

Fig. 9. Pore volume distribution (PVD) obtained from the parallel pore model (PPM) (Eq. (49)) and the pore number distribution (PND) and PVD obtained from the pore network model (PNM) (Eq. (52)) for silica monolith 811.

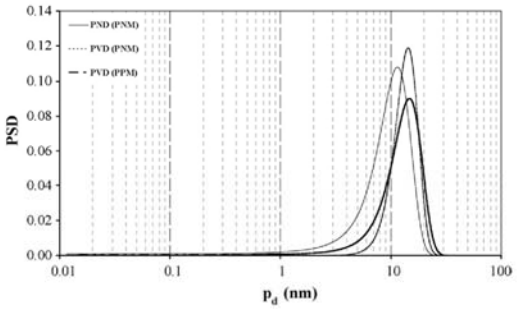

Fig. 10. Pore volume distribution (PVD) obtained from the parallel pore model (PPM) (Eq. (49)) and the pore number distribution (PND) and PVD obtained from the pore network model (PNM) (Eq. (52)) for silica monolith 842.

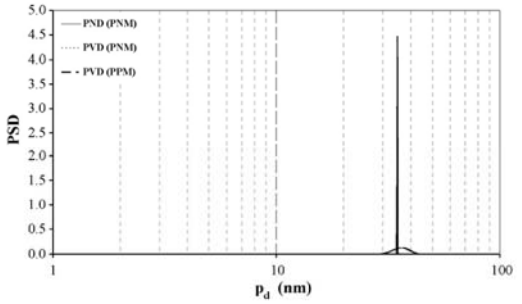

Fig. 11. Pore volume distribution (PVD) obtained from the parallel pore model (PPM) (Eq. (49)) and the pore number distribution (PND) and PVD obtained from the pore network model (PNM) (Eq. (52)) for silica monolith 843.

the PPM and the PNM. This reason for this result is straight forward due to the fact that the larger pores contribute more to the mesopore volume than the smaller pores and, thus, the pore volume distributions depict a larger average pore diameter, $p_{dv,ave}$. Furthermore, the PDVs obtained from the PNM are less disperse (narrower) than the PDVs obtained from the PPM. Although the error associated with the standard deviation values obtained from ISEC measurements are much more prone to errors than the average diameters [57], this trend is consistent for silica monoliths 787, 800, 811, and 842 and, thus, one could tentatively conclude that the incorporation of the network effects in the PNM can lead to the calculation narrower PVDs than the PVDs obtained from calculations using the PPM since the PPM has to account for network effects by increasing the width of the PVD and/or decreasing the average diameter of the PVD. The pore size distributions obtained for silica monoliths 803 and 843 shown in Figs. 8 and 11, respectively, show a very narrow PVD that was calculated from the PPM, while the PND and PDV are wider. Due to the fact that obtaining the PVD and PND parameters (along with ε_b and n_T) from the PPM and PNM presented in this work is an ill-posed problem [57], the solution is completely dependent on the continuity and density of the experimental data points [57,58]. By examining the experimental exclusion curves in Figs. 4 and 5, it is apparent that the curvature of the concave up portion of the exclusion curve, which is most critical to defining the width of the PVDs and PNDs, is not well defined by the experimental data. The difference between the widths of the PVD obtained from the PPM and the PVD obtained from the PNM could probably be due simply to the stopping criteria of the regression routines. However, this leads to a discussion of the drawbacks of ISEC as a porosimetry method. The reliability of ISEC characterization parameters is highly dependant on the continuity of the experimental data as pointed out by Gorbunov et al. [57] and Hagel et al. [58] and, thus, one needs to use as many high quality polymer standards as possible to obtain a smooth experimental exclusion curve. The ability to obtain enough data points to provide a smooth characterization curve is not a problem for other indirect porosimetry methods such as mercury intrusion or gas sorption, but for ISEC the batch to batch quality of polymer standards or polymer standards of various molecular weights obtained from different sources could yield very erratic experimental exclusion curves. Furthermore, as the molecular weight of the polymer standards increase, then it becomes more probable that the polymers are branched and not straight chain, and thus, the functional form of Eqs. (6a) and (6b) would have to be modified [66]. In any case, despite these drawbacks, ISEC is still an attractive technique for porosimetry due to the fact that the porosimetric measurements are performed with the materials in a practical column under actual chromatographic conditions; this is especially attractive for polymeric materials that may shrink or swell depending on the composition of the mobile phase [60].

5. Conclusions and remarks

In this work, a parallel pore model and a pore network model were developed to provide a state-of-art method for the calculation of: (a) the mesopore and macropore void volume fractions, (b) the pore connectivity, (c) the pore number distribution, and (d) the pore volume distribution, from inverse size-exclusion chromatography (ISEC) experiments. A general mathematical model for the exclusion curve of a homologous set of flexible straight-chain polymer standards was developed based on the first moments of the column response to a pulse injection for the molecules involved in the calculation. The model was formulated in a manner that is similar to typical experimental calculations of the ISEC exclusion curve [57,61,73,75]. The general model was then translated into a PPM (Eq. (49)) and a PNM (Eq. (52)) that could be applicable to both monoliths and columns packed with porous particles. This is due to the fact that the general model was based on the first moments of the column response to a pulse injection, which is independent of the morphology of the stationary phase (Eq. (41)). The PPM and PNM proposed in this work both were able to predict the second inflection point in the experimental exclusion curve that has been observed for monolithic materials [60,75] by accounting for the volume partitioning of the polymer standards in the macropores of the monolith. The appearance and prominence of the second inflection point in the exclusion curve was determined to depend strongly on the following parameters: (a) the void fraction, ε_b, of the macropores (flow-through pores), (b) the nominal diameter, $p_{d,m}$, of the macropores, and (c) the radius of gyration, $r_{g,N}$, of the largest polymer standard employed in the determination of the experimental ISEC exclusion curve. It was shown that the second inflection point appears and becomes prominent when the ratio ($r_{g,N}/p_{d,m}$) of the radius of gyration, $r_{g,N}$, of the largest polymer standard employed in the ISEC experiment to the nominal diameter, $p_{d,m}$, of the macropores was larger than 0.0025 when the macropore void fraction, ε_b, is equal to 0.30, and when $r_{g,N}/p_{d,m}$ was larger than 0.0017 when ε_b is equal to 0.50.

ISEC exclusion curves were measured for six silica monoliths having different macropore and mesopore diameters and every exclusion curve measured had two inflection points. The PPM proposed in this work was employed in a non-linear regression of the experimental ISEC exclusion curves to determine value of the macropore void fraction, ε_b, along with the values of the average diameter, $p_{dv,ave}$, and the standard deviation, $p_{dv,std}$, of the pore volume distribution; the void fraction, ε_p, of the porous skeleton could then be obtained from the values of ε_b and the total column void fraction, ε_t. It should be noted here that if one has obtained the value of ε_b from an independent experiment, then the value of the nominal macropore diameter, $p_{d,m}$, could be obtained from the regression using the PPM in place of the macropore void fraction, ε_b; however, the values of ε_b and $p_{d,m}$ cannot be simultaneously obtained along with the values of $p_{dv,ave}$ and $p_{dv,std}$. The PNM proposed in this work was also employed in a non-linear regression of the experimental ISEC exclusion curves to determine value of the pore connectivity, n_T, along with the values of the average diameter, $p_{dn,ave}$, and the standard deviation, $p_{dn,std}$, of the pore number distribution; the average diameter, $p_{dv,ave}$, and the standard deviation, $p_{dv,std}$, of the PVD could then be obtained from the PND. The agreement between the theoretical predictions and the experimental ISEC exclusion curve was excellent for both models. The results

obtained from the PNM indicated that the values of the pore connectivity, n_T, for all the monoliths studied were 10 or greater which indicates that the mesopore topology within the silica skeleton could be considered to be almost infinitely connected with respect to volume partitioning phenomenon. This result is confirmed by comparing the values of the average diameter, $p_{dv,ave}$, of the PVDs that were obtained from the PPM and the PNM which, for all practical purposes, were similar. Due to the fact that the PPM assumes an infinite pore connectivity, n_T, the confirmation that the PNM (which accounts for the finite connectivity of the mesopore structure) produces results similar to the PPM could lead one to conclude that the mesopore structure is almost infinitely connected with respect to volume partitioning phenomenon. Furthermore, in most cases studied, the PVD obtained from the PNM was slightly less disperse than the PVD obtained from the PPM which could lead one to tentatively conclude that the PPM still slightly lumps the network effects into its distribution parameters since the intrinsic modeling structure of the PPM does not include any network effects. However, due to the two exceptions to this rule that were shown in this work and the analysis done elsewhere [57,58], the differences in the PVDs could simply arise from the fact that ISEC characterization is an ill-posed problem [57] and, thus, the results are highly dependant on the continuity and density of the data points on the experimental exclusion curves, especially with respect to the values obtained for the standard deviation of the PVD and PND.

It is important to note that the individual void fractions of the macropores and the skeleton, ε_b and ε_p, respectively, could be obtained directly from the models presented in this work that are based on first principles. Therefore, the proposed model represents a significant improvement over the method to determine ε_b and ε_p proposed by Al-Bokari et al. [60] because one does not have to extrapolate a linear empirical model of a non-linear curve beyond the range of the experimental data points. Furthermore, due to the fact that the experimental exclusion curves had two inflection points, the model of Gorbunov et al. [57] could not provide a satisfactory fit to the data. The fact that the modeling methodology presented in this work can indeed provide a satisfactory fit to the experimental data, indicates the potential value of the models proposed in this work with respect to the characterization of the mesoporous structure of chromatographic columns (monoliths or packed beds) with a large value of ε_b and/or small values of $p_{d,m}$. It should be noted that the PNM can always be applied without the use of the PPM, since the PPM is an idealization that considers an infinitely connected porous medium and for materials having a low (<6) pore connectivity the PPM would force the PVD to a lower average diameter and larger distribution width as opposed to properly accounting for the network effects present in the real porous medium.

Acknowledgements

B.A.G., R.S., and K.K.U. are grateful to Merck KGaA for financial, material, and intellectual support for this work. B.A.G. would also like to thank Prof. A.I. Liapis from the University of Missouri-Rolla, in Rolla, MO, and Dr. L.M. Bryntesson of GE Healthcare in Uppsala, Sweden, for useful discussions related to this work.

References

[1] S. Hjerten, J.-L. Liao, J. Chromatogr. 457 (1988) 333.
[2] S. Hjerten, J.-L. Liao, R. Zhang, J. Chromatogr. 473 (1989) 273.
[3] S. Hjerten, K. Nakazato, J. Mohammad, D. Eaker, Chromatographia 37 (1993) 287.
[4] F. Svec, J.M.J. Frechet, Anal. Chem. 64 (1992) 820.
[5] Q.C. Wang, F. Svec, J.M.J. Frechet, Anal. Chem. 65 (1993) 2243.
[6] J. Matsui, T. Kato, T. Takeuchi, M. Suzuki, K. Yokoyama, E. Tamiya, I. Karube, Anal. Chem. 65 (1993) 2223.
[7] Q.C. Wang, F. Svec, J.M.J. Frechet, J. Chromatogr. A 669 (1994) 230.
[8] M. Petro, F. Svec, J.M.J. Frechet, J. Chromatogr. A 752 (1996) 59.
[9] S. Xie, F. Svec, J.M.J. Frechet, J. Chromatogr. A 775 (1997) 65.
[10] S. Xie, R.W. Allington, F. Svec, J.M.J. Frechet, J. Chromatogr. A 865 (1999) 169.
[11] A. Podgornik, M. Barut, A. Strancar, D. Josic, T. Koloini, Anal. Chem. 72 (2000) 5693.
[12] M. Vodopivec, A. Podgornik, A. Berovic, A. Strancar, J. Chromatogr. Sci. 38 (2000) 489.
[13] M. Merhar, A. Podgornik, M. Barut, S. Jaksa, M. Zigon, A. Strancar, J. Liq. Chromatogr. Relat. Technol. 24 (2001) 2429.
[14] B. Mayr, R. Tessadri, E. Post, M. Buchmeiser, Anal. Chem. 73 (2001) 4071.
[15] X. Huang, S. Zhang, G.A. Schulz, J.D. Henion, Anal. Chem. 73 (2001) 4918.
[16] P. Coufal, M. Cihak, J. Suchanova, E. Tesarova, Z. Bosakova, K. Stulik, J. Chromatogr. A 946 (2002) 99.
[17] H. Oberacher, A. Premstaller, C.G. Huber, J. Chromatogr. A 1030 (2004) 201.
[18] F. Svec, J. Sep. Sci. 27 (2004) 747.
[19] K. Nakanishi, N. Soga, J. Am. Ceram. Soc. 74 (1991) 2518.
[20] K. Nakanishi, N. Soga, J. Non-Cryst. Solids 139 (1992) 1.
[21] K. Nakanishi, N. Soga, J. Non-Cryst. Solids 139 (1992) 14.
[22] H. Minakuchi, K. Nakanishi, N. Soga, N. Ishizuka, N. Tanaka, Anal. Chem. 68 (1996) 3498.
[23] K. Nakanishi, H. Minakuchi, N. Soga, N. Tanaka, J. Sol-Gel. Sci. Technol. 8 (1997) 547.
[24] H. Minakuchi, K. Nakanishi, N. Soga, N. Ishizuka, N. Tanaka, J. Chromatogr. A 762 (1997) 135.
[25] K. Nakanishi, H. Minakuchi, N. Soga, N. Tanaka, J. Sol-Gel. Sci. Technol. 13 (1998) 163.
[26] N. Ishizuka, H. Minakuchi, K. Nakanishi, N. Soga, K. Hosoya, N. Tanaka, J. Chromatogr. A 797 (1998) 133.
[27] K. Cabrera, G. Wieland, D. Lubda, K. Nakanishi, N. Soga, H. Minakuchi, K.K. Unger, Trends Anal. Chem. 17 (1998) 50.
[28] K. Nakanishi, J. Sol-Gel Sci. Technol. 19 (2000) 65.
[29] N. Ishizuka, K. Nakanishi, K. Hirao, J. Sol-Gel. Sci. Technol. 19 (2000) 371.
[30] K. Cabrera, D. Lubda, H. Minakuchi, K. Nakanishi, J. High Resolut. Chromatogr. Commun. 23 (2000) 81.
[31] K. Nakanishi, K. Cabrera, D. Lubda, J. High Resolut. Chromatogr. 23 (2000) 111.
[32] P. Zoellner, A. Leitner, D. Lubda, K. Cabrera, W. Lindner, Chromatographia 52 (2000) 818.
[33] D. Lubda, K. Cabrera, H. Minakuchi, K. Nakanishi, J. Sol-Gel Sci. Technol. 23 (2002) 185.
[34] M. Motokawa, H. Kobayashi, N. Ishizuka, H. Minakuchi, K. Nakanishi, H. Jinnai, K. Hosoya, T. Ikegami, N. Tanaka, J. Chromatogr. A 961 (2002) 53.
[35] N. Tanaka, H. Kobayashi, N. Ishizuka, H. Minakuchi, K. Nakanishi, K. Hosoya, T. Ikegami, J. Chromatogr. A 965 (2002) 35.
[36] N. Tanaka, H. Kobayashi, Anal. Bioanal. Chem. 376 (2003) 298.
[37] A.-M. Siouffi, J. Chromatogr. A 1000 (2003) 801.
[38] K. Cabrera, J. Sep. Sci. 27 (2004) 843.
[39] F. Gritti, W. Piatkowski, G. Guiochon, J. Chromatogr. A 978 (2002) 81.

II

[40] F.C. Leinweber, D.G. Schmid, D. Lubda, K.-H. Wiesmüller, G. Jung, U. Tallarek, Rapid Commun. Mass Spectrom. 17 (2003) 1180.
[41] D. Lubda, K. Cabrera, N. Nakanishi, W. Lindner, Anal. Bioanal. Chem. 377 (2003) 892.
[42] D. Lubda, W. Lindner, J. Chromatogr. A 1036 (2004) 135.
[43] B. Chankvetadze, T. Ikai, C. Yamamoto, Y. Okamoto, J. Chromatogr. A 1042 (2004) 55.
[44] F.C. Leinweber, U. Tallarek, J. Chromatogr. A 1006 (2003) 207.
[45] K.-C. Loh, D.I.C. Wang, J. Chromatogr. A 718 (1995) 239.
[46] K.-C. Loh, A. Geng, Chem. Eng. Sci. 58 (2003) 3439.
[47] J.J. Meyers, A.I. Liapis, J. Chromatogr. A 827 (1998) 197.
[48] J.J. Meyers, A.I. Liapis, J. Chromatogr. A 852 (1999) 3.
[49] A.I. Liapis, J.J. Meyers, O.K. Crosser, J. Chromatogr. A 865 (1999) 13.
[50] B.A. Grimes, J.J. Meyers, A.I. Liapis, J. Chromatogr. A 890 (2000) 61.
[51] J.J. Meyers, S. Nahar, D.K. Ludlow, A.I. Liapis, J. Chromatogr. A 907 (2001) 57.
[52] L.M. Bryntesson, J. Chromatogr. A 945 (2002) 103.
[53] M.E. van Kreveld, N. van den Hoed, J. Chromatogr. 83 (1973) 111.
[54] M.E. van Kreveld, N. van den Hoed, J. Chromatogr. 149 (1978) 71.
[55] I. Halasz, K. Martin, Angew. Chem. Int. Ed. Engl. 17 (1978) 901.
[56] J.H. Knox, H.P. Scott, J. Chromatogr. 316 (1984) 311.
[57] A.A. Gorbunov, L.Ya. Solovyova, V.A. Pasechnik, J. Chromatogr. 448 (1988) 307.
[58] L. Hagel, M. Östberg, T. Andersson, J. Chromatogr. A 743 (1996) 33.
[59] M. Goto, B.J. McCoy, Chem. Eng. Sci. 55 (2000) 723.
[60] M. Al-Bokari, D. Cherrak, G. Guiochon, J. Chromatogr. A 975 (2002) 275.
[61] Y. Yao, A.M. Lenhoff, J. Chromatogr. A 1037 (2004) 273.
[62] B.A. Grimes, C. du Fresne von Hohenesche, M. Quaglia, D. Lubda, K.K. Unger, Presented at the 10th International Symposium on Preparative and Industrial Chromatography and Allied Techniques (SPICA 2004), Aachen, October 17–20, 2004 (Lecture session 1).
[63] E.F. Casassa, J. Polym. Sci. Part B 5 (1967) 773.
[64] J.C. Giddings, E. Kucera, C.P. Russell, M.N. Myers, J. Phys. Chem. 72 (1968) 4397.
[65] E.F. Casassa, Y. Tagami, Macromolecules 2 (1969) 14.
[66] E.F. Casassa, Macromolecules 9 (1976) 182.
[67] R.G. Priest, J. Appl. Phys. 52 (1981) 5390.
[68] M.G. Davidson, U.W. Suter, W.M. Deen, Macromolecules 20 (1987) 1141.
[69] K. Miyabe, G. Guiochon, J. Phys. Chem. B 106 (2002) 8898.
[70] A.E. Rodrigues, J.C. Lopes, Z.P. Lu, J.M. Loureiro, M.M. Dias, J. Chromatogr. 590 (1992) 93.
[71] D.D. Frey, E. Schweinheim, Cs. Horvath, Biotechnol. Prog. 9 (1993) 273.
[72] B.A. Grimes, S. Lüdtke, K.K. Unger, A.I. Liapis, J. Chromatogr. A 979 (2002) 447.
[73] M. Ousalem, X.X. Zhu, J. Hradil, J. Chromatogr. A 903 (2000) 13.
[74] J.J. Meyers, Ph.D. Thesis, Department of Chemical Engineering, University of Missouri-Rolla, Rolla, MO, 2000.
[75] D. Lubda, W. Lindner, M. Quaglia, C. du Fresne von Hohenesche, K.K. Unger, J. Chromatogr. A 1083 (2005) 14.
[76] IMSL FORTRAN Library User's Guide STAT/LIBRARY, vol. 1 of 2, Visual Numerics, San Ramon, CA, 2003.
[77] X. Zhang, J.-C. Wang, K.M. Lacki, A.I. Liapis, J. Phys. Chem. B 109 (2005) 21028.
[78] T.A. Klar, S. Jakobs, M. Dyba, A. Egner, S.W. Hell, Proc. Natl. Acad. Sci. U.S.A. 97 (2000) 8206.
[79] A. Egner, S. Jakobs, S.W. Hell, Proc. Natl. Acad. Sci. U.S.A. 99 (2002) 3370.
[80] V. Levi, Q.Q. Ruan, E. Gratton, Biophys. J. 88 (2005) 2919.
[81] V. Levi, Q.Q. Ruan, M. Plutz, A.S. Belmont, E. Gratton, Biophys. J. 89 (2005) 4275.

II

Available online at www.sciencedirect.com
ScienceDirect
Journal of Chromatography A, 1144 (2007) 72–84
JOURNAL OF CHROMATOGRAPHY A
www.elsevier.com/locate/chroma

Impact of pore structural parameters on column performance and resolution of reversed-phase monolithic silica columns for peptides and proteins

Romas Skudas [a], Brian A. Grimes [a], Egidijus Machtejevas [a], Vilma Kudirkaite [a], Olga Kornysova [a], Tom P. Hennessy [a], Dieter Lubda [b], Klaus K. Unger [a,*]

[a] *Institut für Anorganische Chemie und Analytische Chemie, Johannes Gutenberg Universität-Mainz, Duesbergweg 10-14, D-55099 Mainz, Germany*
[b] *PLS R&D Merck KGaA, Frankfurterstrasse 250, D-64271 Darmstadt, Germany*

Available online 3 November 2006

III

Abstract

In this work, monolithic silica columns with the C4, C8, and C18 chemistry and having various macropore diameters and two different mesopore diameters are studied to access the differences in the column efficiency under isocratic elution conditions and the resolution of selected peptide pairs under reversed-phase gradient elution conditions for the separation of peptides and proteins. The columns with the pore structural characteristics that provided the most efficient separations are then employed to optimize the conditions of a gradient separation of a model mixture of peptides and proteins based on surface chemistry, gradient time, volumetric flow rate, and acetonitrile concentration. Both the mesopore and macropore diameters of the monolithic column are decisive for the column efficiency. As the diameter of the through-pores decreases, the column efficiency increases. The large set of mesopores studied with a nominal diameter of ~25 nm provided the most efficient column performance. The efficiency of the monolithic silica columns increase with decreasing *n*-alkyl chain length in the sequence of C18 < C8 < C4. The resolution of proteins and peptides by reversed-phase gradient liquid chromatography on *n*-octadecyl, *n*-octyl, and *n*-butyl bonded monolithic silica columns is optimized. The results obtained imply the use of acetonitrile concentration gradient up to 75% for *n*-octadecyl and *n*-octyl bonded monolithic silica columns, and the use of acetonitrile concentration gradient up to 85% for *n*-butyl bonded monolithic silica columns. With the respect to the gradient times and flow rates, the optimum conditions are the best with *n*-octyl and *n*-butyl bonded monolithic silica columns, where the range of optimum gradient times is up to ~30 min and mobile phase flow rates in the range of 0.5–1 ml/min. Consequently, the best performance towards peak resolution is obtained with *n*-octyl bonded monolithic silica column with the respect to low concentration of organic phase gradient, fast separations and low solvent consumptions due to low flow rates.

Keywords: Silica monolith; Efficiency; Resolution; Gradient elution

1. Introduction

Apart from the fast separation of low molecular weight analytes in high throughput drug analysis, the resolution of peptides from protein digests is one of the most striking tasks in the field of proteomics. Recently adapted separation techniques such as reversed-phase liquid chromatography (RPLC) have shown potential to significantly enhance the resolution efficiency.

With the pioneering work of Gruber et al. [1], Frei et al. [2] and Horvath et al. [3], RPLC was applied to separate a mixture of peptides, and not long after, a mixture of proteins [4]. Through the following years, the technique rapidly developed due to (a) alterations in retention times and improved reproducibility through introduction of ion-paring agents [5,6], (b) increased resolution and recovery through introduction of high-porosity, high-purity silica supports [7], and (c) altered column selectivity and longevity due to the optimization of the stationary phase via elimination of residual silanols [8].

The enhanced reproducibility, selectivity and, lately, speed of liquid based separation process led to the development of novel supports. Among the variety of stationary phases being

* Corresponding author. Tel.: +49 6151 728 209; fax: +49 6151 729 535.
E-mail address: k.k.unger@web.de (K.K. Unger).

0021-9673/$ – see front matter © 2006 Elsevier B.V. All rights reserved.
doi:10.1016/j.chroma.2006.09.096

III

used for RPLC [9–14], monolithic silica-based columns offered opportunities to meet the challenging requirements [15–17]. Though the development of the monolithic polymer based supports [18,19] was started earlier than the silica based monolithic supports [20–23], the wide variety of available polymeric supports [24–27] did not find its application in the field of RPLC due to the lack of mechanical strength [18] and swelling or shrinkage in organic solvents [28]. That was the main reasons for developing silica based monolithic supports, consisting of a mesoporous silica skeleton and through-pores that allow a rapid transit of an eluent through the chromatographic bed [20–23]. If compared to the conventional columns packed with 5 μm particles, where the size of interstitial openings in the packed bed [29–31] should be similar to through-pores of 1.5–1.8 μm of the monolithic sorbent, monolithic silica-based columns enhanced the high flow-rates by reducing the column back pressure [15–17,32–34] and reduced the separation time [33,35–38]. These benefits led to the recognition of the monolithic silica based column suitability in the separation of peptides and proteins [39–43] in the wide range of other stationary phases used for RPLC [13,14].

Monolithic silica columns proved to be useful in the separation of simple polypeptide mixtures as well as on complicated tryptic digests [39,40,44–47]. Minakuchi et al. [39] presented the first results of polypeptide separation on an octadecylsilylated continuous porous silica column. Soon after it was followed by other scientists, such as Leinweber et al. [46], who measured the retention thermodynamics of insulin and angiotensin II on a C18 silica monoliths, Spoof and Meriluoto [45], who achieved to obtain a fast separation of microcystins and nodularin using a monolithic C18-bonded silica rod column, Hennessy et al. [40], who performed a separation of various peptide fragments obtained by tryptic digestion of various Cytochrome *c* species, Pham-Tuan et al. [44], who developed a method for high-throughput profiling and metabonomic studies of biofluid samples using short monolithic columns, and Tolstikov et al. [47], who applied C18 monolithic silica capillary columns for studying of the metabolome of the model plant *Arabidopsis thaliana*. It was recognized, that the main features of monolithic silica columns were the rapid mass transfer and high flow rates. This concept was adapted in two-dimensional RPLC [48,49].

Even though the potential of using monolithic silica columns for peptide and protein separation was recognized [42,50–52], the pore structure of the monoliths was needed to be adapted to the peptidic analytes to ensure a rapid mass transfer and a high accessibility of the stationary surface. Numerous theoretical models proved this assumption of high porosity, high homogeneity and small-sized skeletons with mesopores large enough not to hinder the passage of the molecules in and out of the pore [53–58].

In this work, monolithic silica columns with a C4, C8, and C18 chemistry having various macropore diameters and gradated mesopore diameters are studied to access the differences in the plate height versus linear velocity curves under isocratic elution conditions and the resolution of selected peptide pairs under reversed-phase gradient elution conditions. The behavior of the monolithic columns based on through-pore diameter, mesopore diameter, and surface chemistry are studied to determine the characteristics of an optimal monolithic stationary phase for the separation of peptides and proteins.

2. Materials and methods

2.1. Chemicals

Thiourea, trifluoroacetic acid (for spectroscopy) and were purchased from Merck KGaA (Darmstadt, Germany). Acetonitrile (HPLC grade) was obtained from Rathburn (Walkerburn, UK). Uracil (99%+) was purchased from Acros Organics (Geel, Belgium). Water (18.2 MΩ cm^3) was prepared using a model Milli-Q (Millipore, Bedford, MA, USA) water-purification system. All eluents were filtered on-line through 0.22 μm pore size membrane filters (Millex, Millipore) prior to use.

2.2. Samples

Peptides and proteins used for the chromatographic measurements were Ala-Gly (M_r 146), ferritin from horse spleen (M_r 450 000) (all from Serva, Heidelberg, Germany), transferin from human serum (M_r 75 000) (from Boehringer Ingelheim, Germany), [Val^5]angiotensin II synthetic (M_r 1032), angiotensin I, human, synthetic (M_r 1296), insulin from bovine pancreas (M_r 5733), Cytochrome *c* from horse heart (M_r 12 384), lysozyme from chicken egg white (M_r 14 300), albumin from bovine serum (M_r 63 000) (all from Sigma-Aldrich, Steinheim, Germany), oxytocin, antiserum from rabbit (M_r 1007) and desmopressin, human, synthetic (M_r 1069) (all from Bachem Distribution Services, Weil am Rhein, Germany).

2.3. Columns

Measurements were performed on three sets of monolithic silica (100 × 4.6 mm) research columns, provided by Merck KGaA. The first set of columns had approximately the same nominal mesopore diameter of 10 nm (calculated using nitrogen sorption data) and the through-pore diameter varied from 1.8 to 5.74 μm (calculated using mercury porosimetry data). The second set of research monolithic silica columns had approximately the same nominal mesopore diameter of 25 nm (calculated using nitrogen sorption data) and the through-pore diameter varied from 1.9 to 6 μm (calculated using mercury porosimetry data). The surface of both sets of the research columns were functionalized with *n*-octadecyl groups. The third set of monolithic silica columns had the same mesopores of approximately 25 nm (calculated using nitrogen sorption data), the same macropores of approx. 1.9 μm (calculated using mercury porosimetry data), but different surface functional groups: *n*-octadecyl, *n*-octyl, or *n*-butyl. The monolithic silica columns were cladded with polyether ether ketone (PEEK) by a propriety process by Merck KGaA. The characteristic values of the columns are presented in Table 1.

2.4. Instrumentation

The measurements at isocratic conditions were performed using a standard fully automated HP 1090 HPLC system (Agi-

Table 1
Summary of structural through-pore and mesopore properties of the used eight silica monolithic research columns

Material ID	Through-pore diameter (μm) (*mercury intrusion*)	Mesopore size (nm) (*nitrogen sorption*)	Functional group (*n-octadecyl, n-octyl, n-butyl*) e[a]
787	1.8	10.9	C18e
800	1.9	25	C18e
803	3.5	10.9	C18e
811	3.4	24	C18e
842	5.74	10	C18e
843	6	24.4	C18e
906	1.9	25	C8e
1104	1.9	25	C4e

[a] Endcapped.

lent Technologies, Waldbronn, Germany). The measurements at gradient conditions were performed using a standard fully automated HP 1100 HPLC system (Agilent Technologies). The ChemStation software (Agilent Technologies) was used to serve for data acquisition and to control the system.

2.5. Chromatographic conditions

2.5.1. Assessment of column efficiency curves using protein samples in RPLC

RPLC using protein samples was performed to assess column efficiency (plate height vs. mobile phase linear velocity) curves for the investigated adsorbents. Cytochrome *c* (from horse heart) and lysozyme (from chicken egg white) were dissolved in a 5% (v/v) acetonitrile and 0.1% trifluoroacetic acid (TFA) mixture at a concentration of 0.01 mg/ml. The composition of the mobile phase was adjusted for each monolithic silica column with different surface functional groups. A reversed-phase gradient elution was performed in each necessary step, with a mobile phase composition of eluent A: 5% acetonitrile, 0.1% TFA, eluent B: 95% acetonitrile, 0.09% TFA and gradient time from 0 to 100% of eluent B in 100 min. From the elution of the sample, the necessary amount of acetonitrile was calculated for the isocratic elution of the protein on the selected adsorbent. The measured values were as follows: (a) for the n-octadecyl group surface modified monolithic silica columns the mobile phase composition for Cytochrome *c* was 34.6% acetonitrile and 0.1% TFA and for lysozyme, it was 38% acetonitrile and 0.1% TFA, (b) for the n-octyl group surface modified monolithic silica columns the mobile phase composition for Cytochrome *c* was 33.6% acetonitrile and 0.1% TFA and for lysozyme, it was 37.1% acetonitrile and 0.1% TFA, (c) for the *n*-butyl group surface modified monolithic silica columns the mobile phase composition for Cytochrome *c* was 33% acetonitrile and 0.1% TFA and for lysozyme, it was 36% acetonitrile and 0.1% TFA.

The measurements were performed under isocratic elution for each peptide or protein by injecting 5 μl of sample with thiourea (1 μg/ml) as the t_0 marker at a flow rate of 0.5 ml/min. The detector used was a UV detector measuring the adsorption at a wavelength of 254 nm. The measurements were made in triplicate in order to ensure repeatability.

2.5.2. Assessment of resolution dependencies using gradient elution of peptide and protein samples in RPLC

RPLC was used for the assessment of resolution dependencies for the peptide and protein samples under gradient elution. The composition of the mobile phase A was 5% acetonitrile and 0.1% TFA, while the mobile phase B consisted of 95% acetonitrile and 0.09% TFA. The gradient elution was performed from 0% of the mobile phase B, to 100, 90, 80, 70, and 60%. Protein and peptide samples were dissolved in the mobile phase at a concentration of 0.01 mg/ml. The measurements were performed by injecting 5 μl sample at a flow rate of 0.5, 1.0, 2.0, and 4.0 ml/min. The detector used was a diode array detector measuring the adsorption from 210 to 300 nm, where the chromatographic parameters were determined at 214, 254, and 280 nm. As a dead volume marker, uracil (0.01 mg/ml of mobile phase A) was repeatedly injected and monitored at 254 nm. The measurements were carried out three times. Data emerge as mean values from three independent runs in order to ensure repeatability.

2.6. Characterization by gas adsorption and liquid intrusion

The nitrogen adsorption measurements were carried out with an ASAP 2400 from Micromeritics (Norcross, GA, USA) at 77 K. The surface area of the measured sample was calculated according to the BET method, while the mesopore size distribution and total volume was calculated according to the BJH method. Mercury porosimetry measurements were accomplished with a Pascal 440 equipment from CE-Instruments (Wigan, UK). For the estimation of the corresponding through-pore diameter from the applied pressure, the Washburn equation with the surface tension of mercury of 480 dynes/cm and a contact angle of mercury on a silica surface of 140°. All measurements were performed by Merck KGaA.

3. Results and discussion

Silica-based monoliths have been implemented more frequently in chromatographic separation systems due to their favorable properties such as high-efficiency and fast separation that arise from fast mass transfer kinetics in the mesoporous

void space of the skeleton and high column permeability. However, silica monoliths have been mainly applied to separations of low molecular weight analytes [58]. The potential of the pore structure of silica monoliths to provide efficient column performance for peptide and protein probes in RPLC was recognized by Tanaka et al. [33] and Leinweber et al. [46], but there is still need for further quantitative investigation. In the following paragraphs, the impact of the pore structural characteristics and the surface functionality of *n*-alkyl bonded silica monoliths employed in the analysis of peptides and proteins will be presented and discussed in terms of the height equivalent of a theoretical plate (HETP) for isocratic elution and resolution for gradient elution.

3.1. The impact of the pore structural characteristics on the performance of n-octadecyl bonded monolithic silica columns

Based on the work of Tanaka et al. [33], Leinweber et al. [46] and Ishizuka [59], the impact of the pore structural characteristics of *n*-octadecyl bonded silica monoliths on the column performance for peptide and protein probes in RPLC were quantitatively determined. Monolithic silica columns of various through-pore and mesopore size were evaluated. HETP curves for lysozyme and Cytochrome *c* were measured for columns 787, 800, 803, 811, 842, and 843 (see Table 1).

In Fig. 1, the influence of the mesopore diameter of the monolithic silica columns was investigated. Two nominal mesopore diameters of ~10 and ~25 nm were investigated. Based on the value of the minimum plate height and the slope of the mass transfer dominated portion of the HETP curves, the efficiency of each column was related to the value of the mesopore diameter. As indicated in Fig. 1, the measured minimum plate height values for lysozyme and Cytochrome *c* were similar (49–53 μm) for monolithic silica columns having mesopores of ~10.9 and ~25 nm, but the average linear velocity through the bed (u_{av}) where the minimum plate height occurred was higher for the monolithic silica columns having a mesopore diameter of ~25 nm. The minimum plate height values occurred at linear velocities of ~0.6 mm/s for the monolithic silica columns having a nominal mesopore diameter of ~25 nm, while for the columns having a nominal mesopore diameter of ~10.9 nm, the minimum plate height occurred at ~0.2 mm/s. Furthermore, it is clear from Fig. 1 that the slope of the HETP curves at higher velocities is smaller for columns having nominal mesopore diameters of ~25 nm than the slope of the HETP curves for monoliths having nominal mesopore diameters of ~10.9 nm in the same velocity domain. These results indicate that the monolithic silica columns with the larger mesopore diameter (~25 nm) provided less mass transfer resistance in the mesoporous structure of the skeleton due to the fact that there is less steric hindrance and frictional resistance to diffusion of the large lysozyme and Cytochrome *c* molecules when the mesopores are considerably larger (~5 times) than the analytes. Thus, the monolithic columns having larger mesopore diameters (~25 nm) enables one to operate the column at higher flow rates, which allows for shorter analysis times without loosing separation efficiency.

The same behavior with respect to the nominal mesopore diameter was observed for monolithic silica columns having larger through-pore diameters, as depicted in Fig. 2. In Fig. 2, two columns having similar through-pore sizes of 3.5 and 3.4 μm, but different nominal mesopore diameters of ~10.9 and ~24 nm were compared. The measured minimum HETP values were similar for both analytes, but the minimum plate height of the columns having a ~10.9 nm nominal mesopore diameter occurred at a linear velocity of ~0.2 mm/s, while for the columns having a ~25 nm nominal mesopore diameter, the minimum HETP value occurred at a linear velocity of ~0.4 mm/s.

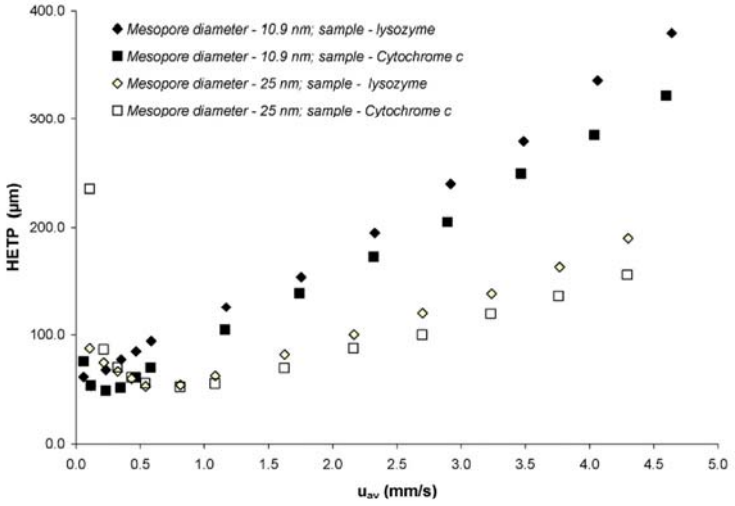

Fig. 1. Plate height curves for lysozyme and Cytochrome *c* with C18e monolithic silica columns of average through-pore diameter of 1.8–1.9 μm.

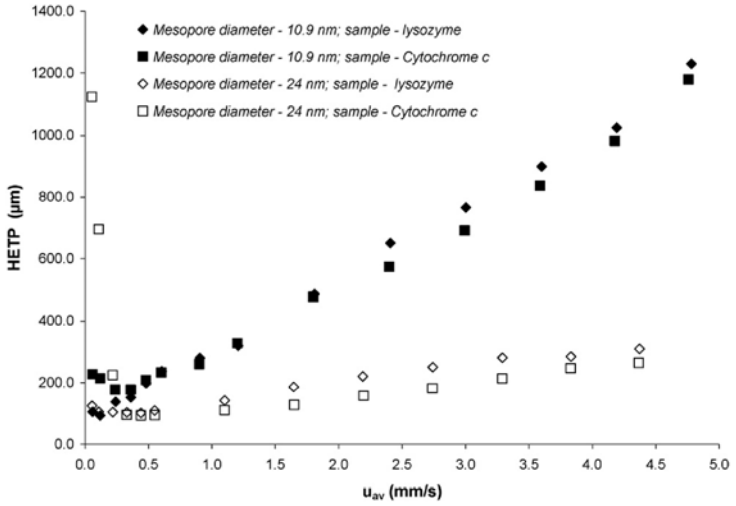

Fig. 2. Plate height curves for lysozyme and Cytochrome *c* with C18e monolithic silica columns of average through-pore diameter of 3.5–3.4 μm.

However, the values of the plate height for the columns having a through-pore diameter of ~3.5 μm were significantly larger over the entire linear velocity domain than the plate height for the columns having a through-pore diameter of ~1.8 μm.

Apart from providing high column efficiency at high flow rates, the most prominent feature of the HETP versus velocity curves for monolithic silica columns having nominal mesopore diameters of ~25 nm was a very shallow curvature near the minimum. This is due to the low mass transfer resistance and short diffusion path lengths in the mesoporous structure of the silica skeleton. For the monolithic silica column having ~25 nm mesopores, the measured HETP values varied between ~100 and ~250 μm as average linear velocity through the bed increased from 0.5 to 4 mm/s, while for the monolithic silica column having mesopores of 10.9 nm, the measured HETP values increased from ~150 to ~1000 μm over the same linear velocity domain. As mentioned above, the smaller mesopores (~10.9 nm) tended to hinder the movement of the large molecules through the pores, thereby leading to peak broadening and higher plate height values, while monolithic silica columns with bigger mesopores

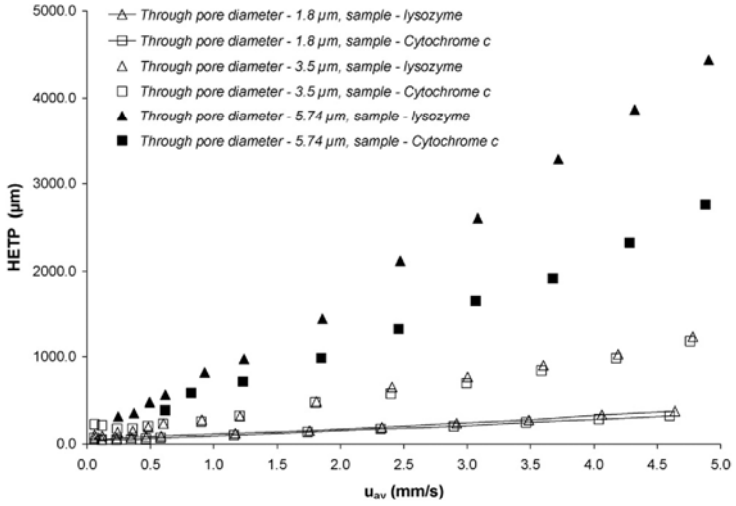

Fig. 3. Plate height curves for lysozyme and Cytochrome *c* with C18e monolithic silica columns of average mesopore diameter of 10.0–10.9 nm.

III

III

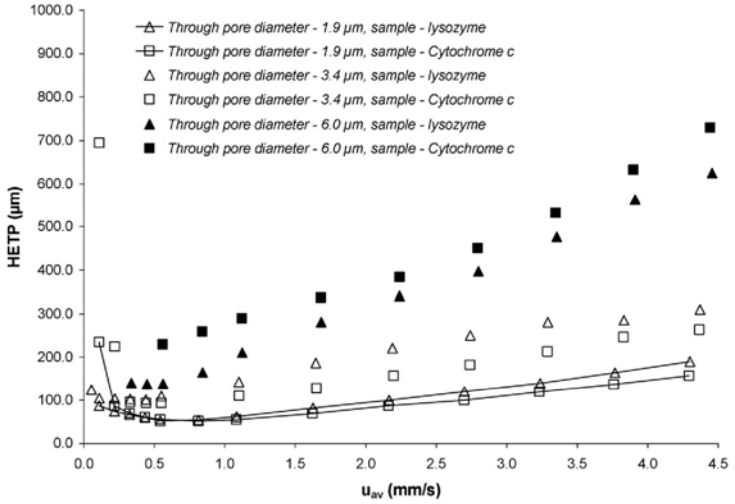

Fig. 4. Plate height curves for lysozyme and Cytochrome *c* with C18e monolithic silica columns of average mesopore diameter of 25.0–24.4 nm.

reduced contribution of mass transfer in the mesoporous structure of the skeleton to plate height values, and allowed faster the separation without sacrificing resolution and efficiency.

In Fig. 3, the effect of the through-pore size on HETP behavior is presented for the columns having a nominal mesopore diameter of ~10.9 nm. It is clear from Fig. 3 that increasing the through-pore diameter leads to a significant reduction in the column efficiency over the entire linear velocity domain studied. For column 787 having a nominal through-pore diameter of ~1.8 μm, the measured plate height value for Cytochrome *c* at a linear velocity of 1.8 mm/s was ~150 μm, while for column 842 having a nominal through-pore diameter of ~5.74 μm, the measured plate height value for Cytochrome *c* at a linear velocity of 1.8 mm/s was ~1500 μm. Clearly, since the average transverse dimensions of the skeleton was increasing with increasing through-pore diameter, the diffusion path length through the mesoporous skeleton was increasing which lead to the loss of column efficiency as the nominal through-pore diameter increased. This result is analogous to increasing the particle diameter in a packed bed.

In Fig. 4, the effect of the through-pore size on HETP behavior is presented for the columns having a nominal mesopore diameter of ~25 nm. The minimum HETP values obtained with lysozyme for the monolithic silica columns hav-

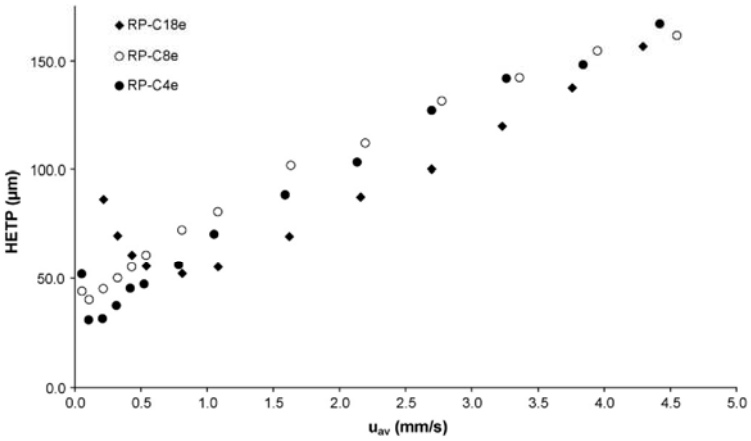

Fig. 5. Plate height curves for Cytochrome *c* with monolithic silica columns having ~1.9 μm through-pores and ~25 nm mesopores where the surface functional group is C18, C8, or C4.

ing through-pores of 1.9, 3.5, and 6.0 μm were ~50, ~100, ~150 μm, respectively. The same tendencies were obtained for Cytochrome *c*. Similar to the results presented for Fig. 3, the magnitude of band broadening was dependant on the average through-pore diameter, and tended to decrease with decreasing through-pore size. Again, this result is due to the fact that the diffusion path length through the mesoporous void space of the skeleton increases as the diameter of the through-pores increases.

By comparing the results presented in Figs. 1–4, the monolithic silica columns with larger mesopores and smaller through-pores showed higher separation efficiency than those with smaller mesopores and larger through-pores. The best column performance within the tested RP-18e columns for lysozyme was found for RP-18e column 800 (HETP = 45 μm). The results obtained in this work corresponded well to the conclusions of Minakuchi et al. [17] and numerous theoretical models [53–58], such that the columns with the small-sized skeletons and mesopores large enough not to hinder the mass transfer rate of molecules in the mesoporous void space of the skeleton would give the lowest HETP values.

3.2. The impact of the surface functionality on the performance of the n-alkyl bonded monolithic silica columns

In Fig. 5, HETP versus linear velocity curves are presented for Cytochrome *c* on monoliths having various *n*-alkyl surface functionalities. Results are presented for (a) column 800 (the column determined to have the highest efficiency in the above analysis) having an *n*-octadecyl bonded surface chemistry, (b) column 906 having an *n*-octyl bonded surface chemistry, and (c) column 1104 having an *n*-butyl bonded surface chemistry. It should be noted here that each column (800, 906, and 1104) has a similar nominal through-pore diameter and a similar nominal mesopore diameter, and the surface functionality modification was performed after the formation of the skeleton by a proprietary procedure developed by Merck. The efficiency of the column, based on the location of the minimum HETP value and the slope of the mass transfer dominated portion of the plate height curves, was related to the values of the functional group on the stationary phase surface. As mentioned above, column 800 was determined to provide the best column performance within the set of RP-18e modified columns and the minimum HETP value for lysozyme was 45 μm. It is clear from the results presented in Fig. 5 that the minimum HETP values tended to decrease as the length of the bonded *n*-alkyl chain decreased as demonstrated for Cytochrome *c* where the minimum HETP value was 52 μm for RP-18e column 800, while the minimum HETP value was 40 μm for RP-8e column 906, and the minimum HETP value was 30 μm for RP-4e column 1104. These results support the investigation of Liu et al. [60], who found that the adsorption enthalpies of proteins with *n*-octyl functional group at constant ligand density were higher than with *n*-butyl functional group by the difference of 7–8 kJ/mol. They also proved, that the heat required to dehydrate the *n*-octyl chain was 10 kJ/mol higher than that required to dehydrate the *n*-butyl chain.

In RPLC, the slow diffusion and kinetics of desorption and other equilibria of protein retention, induced by the strong hydrophobic solute surface interaction with the hydrocarbon stationary phase, led to low column efficiency. Though monolithic silica columns showed the possibility to overcome these obstacles of slow diffusion and kinetics by increased mesopore size, reduced through-pore diameter (altogether with reduced skeleton size) and shorter ligand chain length on the support surface.

3.3. The impact of the pore morphology and surface functionality on the resolution of the n-alkyl bonded monolithic silica columns in gradient elution

The optimization of peak resolution in gradient elution reversed-phase HPLC is essential for the separation of multicomponent samples such as those encountered in proteomic research. It is necessary to study the effect of the surface functional group (*n*-alkyl chain) length, gradient time, t_G, flow rate, Q, and acetonitrile concentration on the peak resolution for separations of a model peptide and protein mixture. The choice of the columns was dictated by the findings of the most efficient monolithic silica column according the separation efficiency, as presented in the results above. As shown in the preceding discussion, the monolithic silica columns, which had a small through-pore diameter of 1.9 μm and a large mesopore diameter of 25 nm were the most efficient for the separation of the chosen protein samples. Even though the results presented clearly elucidated the behavior of the column efficiency with respect to the *n*-alkyl chain length, the *n*-octadecyl, *n*-octyl, and *n*-butyl modified columns of similar pore structure were evaluated to determine the performance of the different surface chemistries for a multi-component separation. Such a decision was made since the target of this research was not only the efficiency of the separation under isocratic elution conditions, but the optimization of the chromatographic resolution of a gradient separation as well.

The chromatographic resolution, R_S, was calculated according to the following expression:

$$R_S = \frac{t_{R,i+1} - t_{R,i}}{B_i + A_{i+1}} \quad (1)$$

where $t_{R,i+1}$ and $t_{R,i}$ represent the retention times of two consecutive peaks, and B_i and A_{i+1} denote the baseline widths of the respective peaks. Such adaptation of the chromatographic resolution calculation enabled the representation of the threshold of baseline separation. For the optimization of the gradient elution, the following two peak pairs were chosen: oxytocin and desmopressin, and [Val^5]angiotensin II and angiotensin I. The main reason for choosing such samples as the representatives of the overall resolution map was that in all measured conditions, baseline separation of those peaks was obtained. As the optimization of gradient conditions based on the separation of the poorest resolved peak only represents the results for the critical peak pair, it was deemed necessary to show important differences in the separation of non-critical peaks as an overall tendency of the optimization of the gradient elution conditions.

III

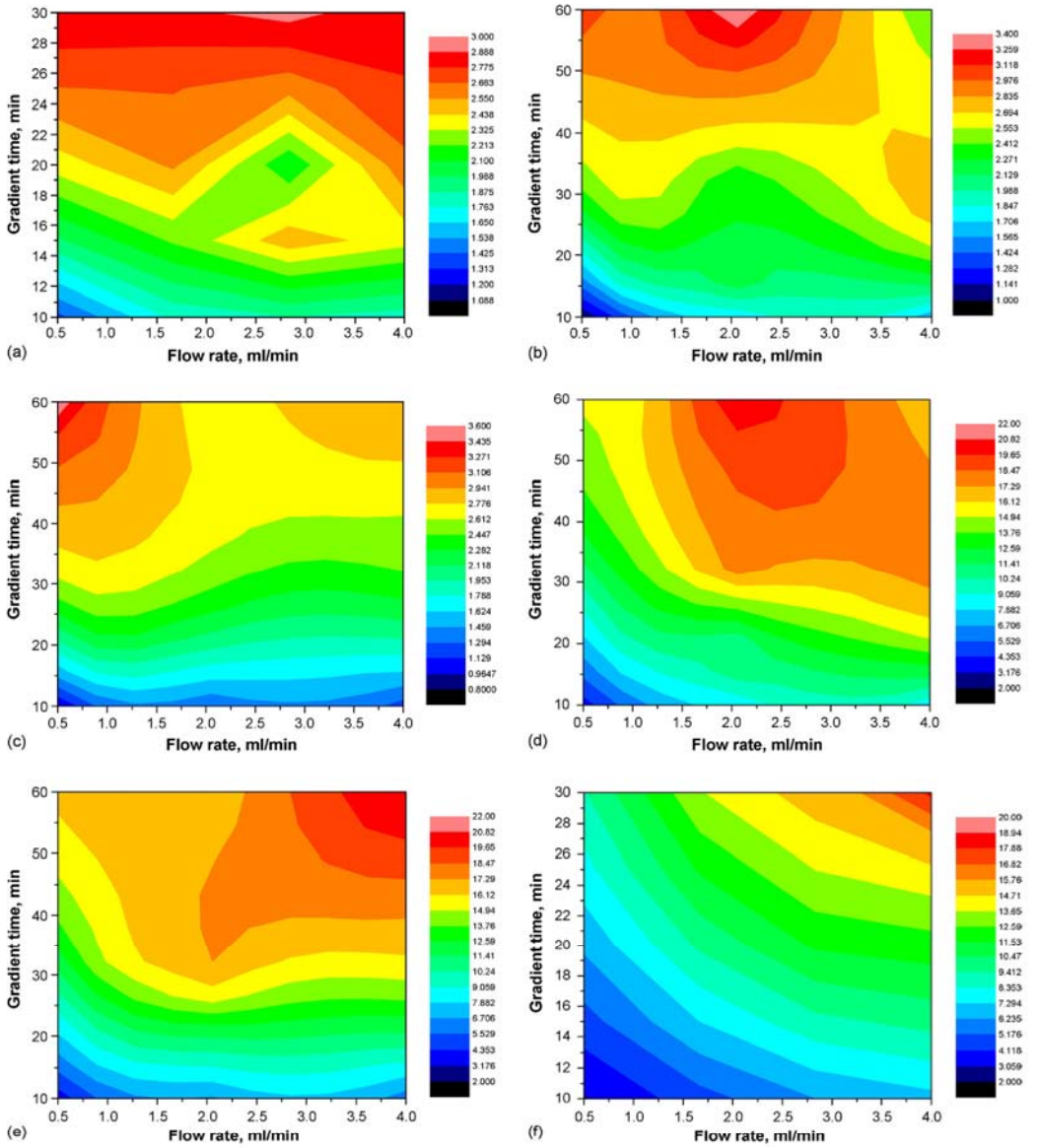

Fig. 6. Chromatographic resolution as a function of the volumetric flow rate and gradient time for the C18e monolithic silica column. (a–c) Peak pair of oxytocin and desmopressin; (d–f) peak pair of [Val^5]angiotensin II and angiotensin I. The acetonitrile concentration is as follows: (a) 55%, (b) 75%, (c) 85%, (d) 75%, (e) 85%, and (f) 95%.

In Fig. 6, the effect of the gradient time, t_G, the flow rate, Q, and acetonitrile concentration on the peak resolution for separations on the RP-18e monolithic silica column 800 is shown. Fig. 6a–c represent the results obtained for the resolution of the first analyzed peak pair of oxytocin and desmopressin, while Fig. 6d–f represent the results obtained for the resolution of the second analyzed peak pair of [Val^5]angiotensin II and angiotensin I.

The effect of gradient time on the increasing value of peak resolution was the same for both analyzed peak pairs. As the gradient time increased, the value of resolution increased. Furthermore, as the concentration of acetonitrile was increased, the maximum resolution values were shifted even to longer gradient times. If the acetonitrile concentration gradient was 55%, the optimum gradient time was 30 min (see Fig. 6a), and if the acetonitrile concentration gradient was 85%, the optimum gradient time was 50 min (see Fig. 6c) with respect to maximum resolution values reached for the peak pair of oxytocin and desmopressin. For the maximum resolution values of the second peak pair of [Val^5]angiotensin II and angiotensin I, the gradient times were not as dependent on the acetonitrile concentration gradient and were reached at the maximum gradient time value of 60 min. Though, if the optimum resolution values (~3–5) should be taken into account, the effect of gradient time on the optimum peak resolution was also not dependent on the acetonitrile concentration gradient, but occurred in the range of shorter gradient times up to 25 min.

The effect of the flow rate on the peak resolution was different for each analyzed peak pair, but the tendency for the optimum peak resolution values of ~3–5 was the same. Fig. 6a–c for the first peak pair of oxytocin and desmopressin indicate that as the acetonitrile concentration gradient increases from 55 to 85%, maximum resolution values move to lower flow rates from 3 to 0.5 ml/min and increase in magnitude with respect to maximum resolution values reached for the peak pair (see Fig. 6a–c). While Fig. 6d–f for the second peak pair of [Val^5]angiotensin II and angiotensin I, the maximum resolution values were reached with increasing flow rate if the acetonitrile concentration gradient increased, but the optimum peak resolution values (~3–5) were found at lower flow rates as the acetonitrile concentration gradient increased (see Fig. 6d–f).

The obtained results for optimum peak pair resolution values suggest, that the optimum resolution for both peak pairs was reached at acetonitrile concentration gradient to 75%, flow rate of ~2 ml/min and gradient times up to 40 min for the *n*-octadecyl bonded monolithic silica column 800.

In Fig. 7, the effect of the gradient time, t_G, the flow rate, Q, and acetonitrile concentration on the peak resolution for separations on the RP-8e monolithic silica column 906 is shown. Fig. 7a–c represent the results obtained for the resolution of the first analyzed peak pair of oxytocin and desmopressin, while Fig. 7d–f represent the results obtained for the resolution of the second analyzed peak pair of [Val^5]angiotensin II and angiotensin I.

The effect of gradient time on the value of the peak resolution was the same for the analyzed peak pairs. In Fig. 7a and b for the first peak pair of oxytocin and desmopressin, the maximum resolution occurs in the range of 30–40 min when the acetonitrile gradient concentration was 55 and 75%, respectively. However, as Fig. 7c clearly indicates, when the acetonitrile gradient concentration was raised from 75 to 95%, the optimum gradient times were shifted to higher values of 60 min (see Fig. 7c) with respect to the first peak pair of oxytocin and desmopressin. With respect to maximum resolution values for second peak pair, the optimum gradient time was not dependent on the increasing acetonitrile gradient concentration (see Fig. 7d and e), but when the acetonitrile gradient concentration was increased from 75 to 95%, the maximum peak resolution values were shifted to higher gradient times of 60 min (see Fig. 7e). However, it should be noted here that if optimum values (~3–5) of the resolution of the second peak pair should be taken into account, the resolution values were not dependent on the increasing acetonitrile gradient concentration, and stayed the range of 20 min with respect to the gradient time (see Fig. 7a–c). The effect of gradient time with the increasing value of acetonitrile gradient concentration was not influencing the optimum peak resolution if the range of acetonitrile gradient concentration was not increased above 75%. The increase of acetonitrile gradient concentration above 75% led to increase of gradient times for the chromatographic resolution of the first peak pair.

The effect of the flow rate on the increasing value of peak resolution was different for the analyzed peak pairs, but the tendency for the optimum peak resolution values of ~3–5 was the same. The maximum resolution values of the first peak pair were not influenced with respect to flow rate in increasing acetonitrile gradient concentrations and stayed in the range of ~0.5–1.0 ml/min (see Fig. 7a–b). The maximum resolution values of the second peak pair was independent of the flow rate if the acetonitrile concentration gradient was not above 85% (see Fig. 7d and e). With higher acetonitrile gradient concentration values, the maximum resolution values for the second peak pair were shifted to higher flow rates (see Fig. 7f). But the optimum peak resolution values (~3–5) for the second peak pair were independent of the flow rate and stayed in the range of ~0.5–1.0 ml/min.

The obtained results for optimum peak pair resolution values suggest, that the optimum resolution for both peak pairs was not dependent on the flow rate, but was reached at acetonitrile concentration gradient lower then 75% and gradient times up to 20 min for the *n*-octyl bonded monolithic silica column 906.

In Fig. 8, the effect of the gradient time, t_G, the flow rate, Q, and acetonitrile concentration on the peak resolution for separations on the RP-4e monolithic silica column 1104 is shown. Fig. 8a–c represent the results obtained for the resolution of the first analyzed peak pair of oxytocin and desmopressin, while Fig. 8d–f represent the results obtained for the resolution of the second analyzed peak pair of [Val^5]angiotensin II and angiotensin I.

The effect of gradient time on the value of the peak resolution was the same for the analyzed peak pairs. In Figs. 8a and c for the first peak pair of oxytocin and desmopressin, the maximum resolution occurs at the highest value of 60 min when the acetonitrile gradient concentration was 75 and 95%, respectively. However, as Fig. 8b clearly indicates, when the acetonitrile gradient concentration was 85%, the optimum gradient times were shifted to a lower 30 min with respect to the first peak pair of oxytocin and desmopressin. With respect to the maximum resolution values for the second peak pair, the optimum gradient time showed the same dependency on the acetonitrile gradient concentration of 75 and 95% (see Fig. 8d and f) as the first analyzed peak pair, but with the acetonitrile gradient concentration of 85% the optimum gradient times were shifted to a lower range of ~30–40 min (see Fig. 8e). The same tendencies were

III

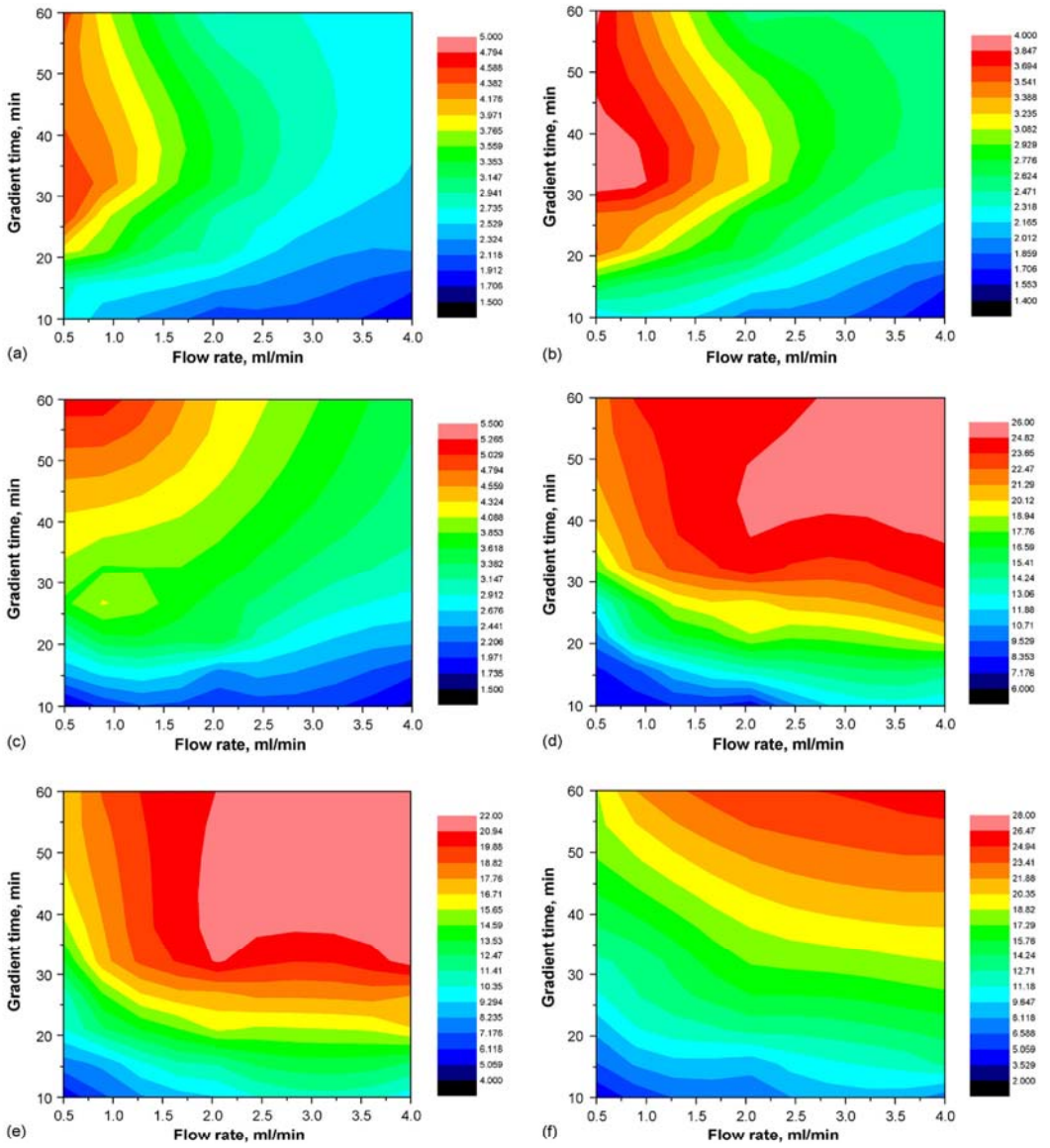

Fig. 7. Chromatographic resolution as a function of the volumetric flow rate and gradient time for the C8e monolithic silica column. (a–c) Peak pair of oxytocin and desmopressin; (d–f) peak pair of [Val^5]angiotensin II and angiotensin I. The acetonitrile concentration is as follows: (a) 55%, (b) 75%, (c) 95%, (d) 55%, (e) 75%, and (f) 95%.

noticed and for the optimum peak resolution values of the second peak pair, staying in the range of 20 min for an acetonitrile concentration of 75 and 95%, and lowering down to 10 min, when the acetonitrile gradient concentration was 85%. The effect of gradient time with the increasing value of acetonitrile gradient concentration was not constant on the optimum peak resolution. If used acetonitrile gradient concentration was 75 or 95%, the optimum gradient times were 60 min for the first peak pair and 20 min for the second peak pair, but if acetonitrile gradient concentration was 85%, the optimum gradient times were shifted

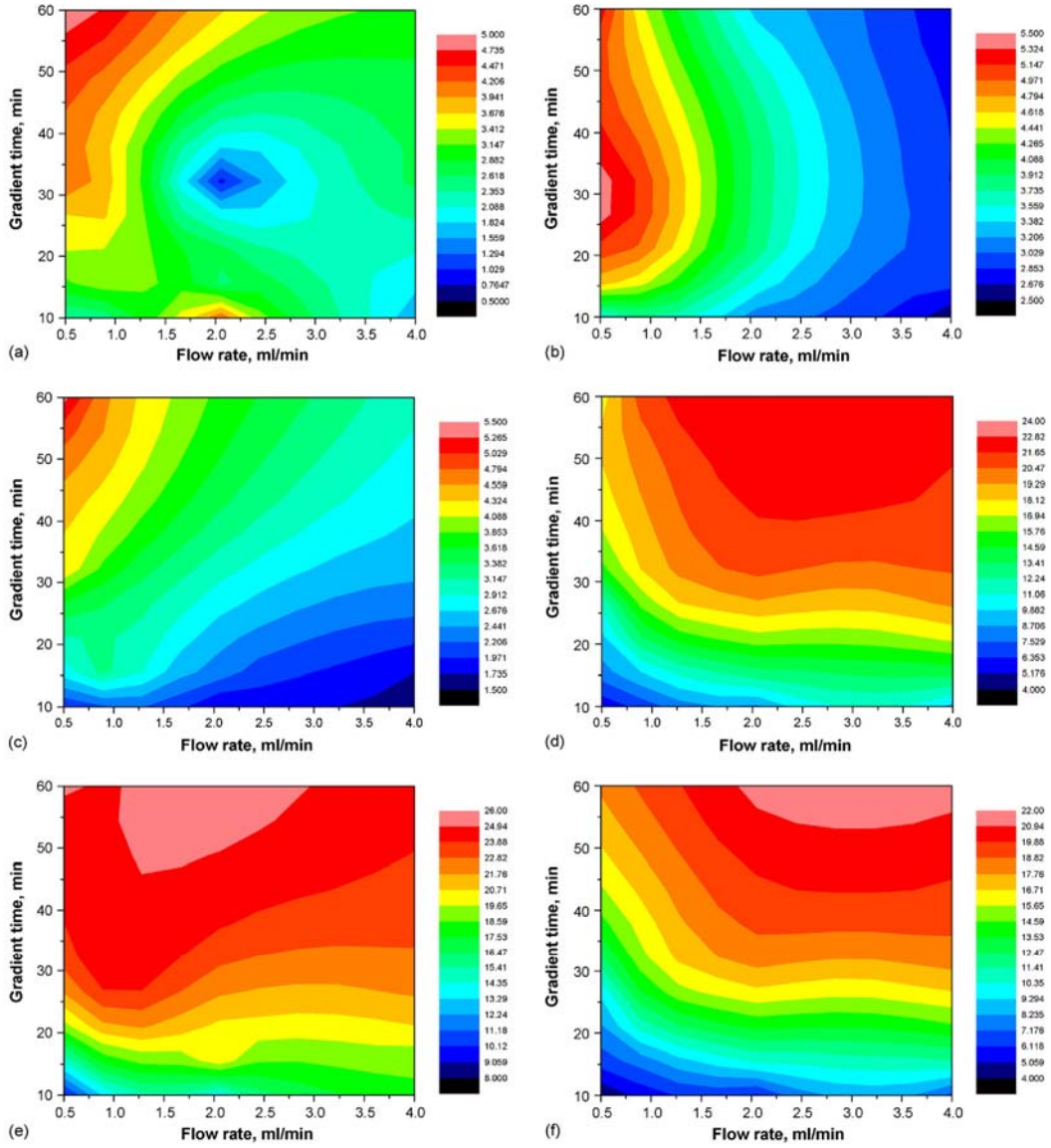

Fig. 8. Chromatographic resolution as a function of the volumetric flow rate and gradient time for the C4e monolithic silica column. (a–c) Peak pair of oxytocin and desmopressin; (d–f) peak pair of [Val^5]angiotensin II and angiotensin I. The acetonitrile concentration is as follows: (a) 75%, (b) 85%, (c) 95%, (d) 75%, (e) 85%, and (f) 95%.

to lower values of 30 min for the first peak pair and 10 min for the second peak pair. With the respect to the measured gradient time values, the optimum acetonitrile gradient concentration was 85%, giving the smallest values of gradient times and the fastest separation.

The effect of the flow rate on the increasing value of peak resolution was different for the analyzed peak pairs, but the tendency for the optimum peak resolution values of ~3–5 was the same. The maximum resolution values of the first peak pair were not influenced with respect to flow rate as the acetoni-

trile gradient concentration increased and stayed in the range of ~0.5–1.0 ml/min (see Fig. 8a–c). The maximum resolution values of the second peak pair were independent of the flow rate. If the acetonitrile concentration gradient was 75 or 95% (see Fig. 8d and f), the maximum resolution values were obtained in high flow rates of >1.5 ml/min, but if the acetonitrile gradient concentration was 85%, the maximum resolution values were obtained in the range of 1.0–2.5 ml/min (see Fig. 8e). But the optimum peak resolution values for the second peak pair were independent of the flow rate and stayed in the range of ~0.5–1.0 ml/min.

The obtained results for optimum peak pair resolution values suggest that the optimum resolution for both peak pairs was not dependent on the flow rate, but was reached at acetonitrile concentration gradient of 85% and gradient times up to 30 min for the *n*-butyl bonded monolithic silica column 1104.

4. Conclusions and remarks

In this work, monolithic silica columns with a C4, C8, and C18 chemistry and having various macropore diameters and two different mesopore diameters were studied to access the differences in the column efficiency under isocratic elution conditions and the resolution of selected peptide pairs under reversed-phase gradient elution conditions. The behavior of the monolithic columns based on through-pore diameter, mesopore diameter, and surface chemistry were studied to determine the characteristics of an optimal monolithic stationary phase for the separation of peptides and proteins. The columns with the pore structural characteristics that provided the most efficient separations were then employed to optimize the conditions of a gradient separation of a model mixture of peptides and proteins based on surface chemistry, gradient time, volumetric flow rate, and acetonitrile concentration.

Both the mesopore and macropore diameters of the monolithic column are decisive for the column efficiency. As the diameter of the through-pores decreases, the column efficiency increases. The mesopore sizes have to be adapted to the molecular size of the analyte in particular to peptides and proteins. Consequently, the larger set of mesopores studied with a nominal diameter of ~25 nm provided the most efficient column performance because they provided less resistance to mass transfer in the mesoporous void space of the skeleton. Further analysis could be performed to determine the effect of increasing the mesopore diameter on the overall dynamic adsorption capacity of the column. The efficiency of the monolithic silica columns increase with decreasing *n*-alkyl chain length in the sequence of C18 < C8 < C4.

The resolution of proteins and peptides by gradient RPLC on *n*-octadecyl, *n*-octyl, and *n*-butyl bonded monolithic silica columns was optimized. The obtained results imply the use of acetonitrile concentration gradient up to 75% for *n*-octadecyl and *n*-octyl bonded monolithic silica columns, and the use of acetonitrile concentration gradient up to 85% for *n*-butyl bonded monolithic silica columns. With the respect to the gradient times and flow rates, the optimum conditions were the best with *n*-octyl and *n*-butyl bonded monolithic silica columns, where the range of optimum gradient times was up to ~30 min and mobile phase flow rates in the range of 0.5–1 ml/min. So the best performance towards peak resolution was obtained with *n*-octyl bonded monolithic silica column with the respect to low organic phase gradient, fast separations and low solvent consumptions due to low flow rates.

Acknowledgment

The authors are grateful to Merck KGaA for financial, material, and intellectual support for this work.

References

[1] K.A. Gruber, S. Stein, L. Brink, A. Radhakrishnan, S. Udenfriend, Proc. Natl. Acad. Sci. U S A 73 (1976) 1314.
[2] R.W. Frei, L. Michel, W. Santi, J. Chromatogr. 126 (1976) 665.
[3] C. Horvath, W. Melander, I. Molnar, J. Chromatogr. 125 (1976) 129.
[4] W. Moench, W. Dehnen, J. Chromatogr. 147 (1978) 415.
[5] W.S. Hancock, C.A. Bishof, R.L. Prestidge, D.R.K. Harding, M.T.W. Hearn, J. Chromatogr. 153 (1978) 391.
[6] M.T.W. Hearn, W.S. Hancock, C.A. Bishof, J. Chromatogr. 157 (1978) 337.
[7] J.D. Pearson, N.T. Lin, F.E. Regnier, Anal. Biochem. 124 (1982) 217.
[8] K.A. Cohen, J. Chazaud, G. Calley, J. Chromatogr. 282 (1983) 423.
[9] H. Poppe, J. Chromatogr. A 778 (1997) 3.
[10] J.E. McNair, K.C. Lewis, J.W. Jorgenson, Anal. Chem. 69 (1997) 983.
[11] P.P.H. Tock, C. Boshoven, H. Poppe, J.C. Kraak, K.K. Unger, J. Chromatogr. 477 (1989) 95.
[12] B. Slentz, N. Penner, F.E. Regnier, J. Chromatogr. A 984 (2003) 97.
[13] U.D. Neue, B.A. Alden, T.H. Walter, J. Chromatogr. A 849 (1999) 101.
[14] M.R. Euerby, P. Petersson, J. Chromatogr. A 994 (2003) 13.
[15] H. Minakuchi, K. Nakanishi, N. Soga, N. Ishizuka, N. Tanaka, Anal. Chem. 68 (1996) 3498.
[16] H. Minakuchi, K. Nakanishi, N. Soga, N. Ishizuka, N. Tanaka, J. Chromatogr. A 762 (1997) 135.
[17] H. Minakuchi, K. Nakanishi, N. Soga, N. Ishizuka, N. Tanaka, J. Chromatogr. A 797 (1998) 121.
[18] S. Hjerten, J.-L. Liao, R. Zhang, J. Chromatogr. 473 (1989) 273.
[19] L.C. Hansen, R.E. Sievers, J. Chromatogr. 99 (1974) 123.
[20] K. Nakanishi, N. Soga, J. Am. Ceram. Soc. 74 (1991) 2518.
[21] K. Nakanishi, N. Soga, J. Non-Cryst. Solids 139 (1992) 1.
[22] K. Nakanishi, N. Soga, J. Non-Cryst. Solids 139 (1992) 14.
[23] K. Nakanishi, Y. Sagawa, N. Soga, J. Non-Cryst. Solids 134 (1991) 39.
[24] G. Iberer, R. Hahn, A. Jungbauer, LC–GC Eur., Feb. (2000) 88.
[25] A. Strancar, A. Podgornik, M. Barut, R. Necina, Adv. Biochem. Eng./Biotechnol. 76 (2002) 49.
[26] H. Zou, X. Huang, M. Ye, Q. Luo, J. Chromatogr. A 954 (2002) 5.
[27] A. Maruska, O. Kornysova, J. Biochem. Biophys. Methods 59 (2004) 1.
[28] N. Tanaka, T. Ebata, K. Hashizume, K. Hosoya, M. Araki, J. Chromatogr. 475 (1989) 195.
[29] J.H. Knox, H.P. Scott, J. Chromatogr. 316 (1984) 311.
[30] K.K. Unger, Porous Silica, Elsevier, Amsterdam, 1979, Chapter 5.
[31] L.K. Frevel, L.J. Kressley, Anal. Chem. 35 (1963) 1492.
[32] N. Ishizuka, H. Minakuchi, K. Nakanishi, N. Soga, K. Hosoya, N. Tanaka, J. Chromatogr. A 797 (1998) 133.
[33] N. Tanaka, H. Kobayashi, N. Ishizuka, H. Minakuchi, K. Nakanishi, K. Hosoya, T. Ikegami, J. Chromatogr. A 965 (2002) 35.
[34] D. Lubda, K. Cabrera, K. Nakanishi, H. Minakuchi, J. Sol–Gel Sci. Tech. 23 (2002) 23.
[35] K. Cabrera, G. Wieland, D. Lubda, K. Nakanishi, N. Soga, H. Minakuchi, K.K. Unger, Trends Anal. Chem. 17 (1998) 50.
[36] K. Cabrera, D. Lubda, H. Minakuchi, K. Nakanishi, J. High Resolut. Chromatogr. 23 (2000) 93.

[37] N. Tanaka, H. Nagayama, H. Kobayashi, T. Ikegami, K. Hosoya, N. Ishizuka, H. Minakuchi, K. Nakanishi, K. Cabrera, D. Lubda, J. High Resolut. Chromatogr. 23 (2000) 111.
[38] A.-M. Siouffi, J. Chromatogr. A 1000 (2003) 801.
[39] H. Minakuchi, N. Ishizuka, K. Nakanishi, N. Soga, N. Tanaka, J. Chromatogr. A 828 (1998) 83.
[40] T.P. Hennesy, R.I. Boysen, M.I. Huber, K.K. Unger, M.T.W. Hearn, J. Chromatogr. A 1009 (2003) 15.
[41] B. Barroso, D. Lubda, R. Bischoff, J. Proteome Res. 2 (2003) 633.
[42] L. Xiong, R. Zhang, F.E. Regnier, J. Chromatogr. A 1030 (2004) 187.
[43] D. Josic, A. Buchacher, A. Jungbauer, J. Chromatogr. B 752 (2001) 191.
[44] H. Pham-Tuan, L. Kaskavelis, C.A. Daykin, H.-G. Janssen, J. Chromatogr. B 789 (2003) 283.
[45] L. Spoof, J. Meriluoto, J. Chromatogr. A 947 (2002) 237.
[46] F.C. Leinweber, D. Lubda, K. Cabrera, U. Tallarek, Anal. Chem. 74 (2002) 2470.
[47] V.V. Tolstikov, A. Lommen, K. Nakanischi, N. Tanaka, O. Fiehn, Anal. Chem. 75 (2003) 6737.
[48] N. Tanaka, H. Kimura, D. Tokuda, K. Hosoya, T. Ikegami, N. Ishizuka, H. Minakuchi, K. Nakanishi, Y. Shintani, M. Furuno, K. Cabrera, Anal. Chem. 76 (2004) 1273.
[49] T. Ikegami, T. Hara, H. Kimura, H. Kobayashi, K. Hosoya, K. Cabrera, N. Tanaka, J. Chromatogr. A 1106 (2006) 112.
[50] B. Barroso, D. Lubda, R. Bischoff, J. Proteome Res. 2 (2003) 633.
[51] L. Rieux, H. Niederländer, E. Verpoorte, R. Bischoff, J. Sep. Sci. 28 (2005) 1628.
[52] K. Cabrera, J. Sep. Sci. 27 (2004) 843.
[53] P. Gzil, N. Vervoort, G.V. Baron, G. Desmet, Anal. Chem. 76 (2004) 6707.
[54] A.I. Liapis, J.J. Meyers, O.K. Crosser, J. Chromatogr. A 865 (1999) 13.
[55] J.J. Meyers, A.I. Liapis, J. Chromatogr. A 852 (1999) 3.
[56] A.-M. Siouffi, J. Chromatogr. A, in press.
[57] N. Vervoort, P. Gzil, G.V. Baron, G. Desmet, J. Chromatogr. A 1030 (2004) 177.
[58] F. Gritti, W. Piatkowski, G. Guiochon, J. Chromatogr. A 978 (2002) 81.
[59] N. Ishizuka, H. Minakuchi, K. Nakanishi, K. Hirao, N. Tanaka, Colloids Surf. A 187 (2001) 273–279.
[60] F.-Y. Lin, W.-Y. Chen, R.-C. Ruaan, H.-M. Huang, J. Chromatogr. A 872 (2000) 37.

Journal of Chromatography A, 1191 (2008) 57–66

Contents lists available at ScienceDirect

Journal of Chromatography A

journal homepage: www.elsevier.com/locate/chroma

Textural characterization of native and *n*-alky-bonded silica monoliths by mercury intrusion/extrusion, inverse size exclusion chromatography and nitrogen adsorption

M. Thommes[a,*], R. Skudas[b], K.K. Unger[b], D. Lubda[c]

[a] Quantachrome Instruments, Applied Sciences, R&D, 1900 Corporate Drive, Boynton Beach, FL 33426, USA
[b] Institut für Anorganische Chemie und Analytische Chemie, Johannes Gutenberg Universität-Mainz, Duesbergweg 10-14, D-55099 Mainz, Germany
[c] PLS and Global Production, Merck KGaA, Frankfurter Land Str. 250, 64293 Darmstadt, Germany

IV

ARTICLE INFO

Article history:
Available online 1 April 2008

Keywords:
Monolithic columns
Mercury porosimetry
Hysteresis
Entrapment
Adsorption
Density functional theory (DFT)
Inverse size exclusion chromatography (ISEC)

ABSTRACT

Native and *n*-alkyl-bonded (*n*-octadecyl) monolithic silica rods with mesopores in the range between 10 and 25 nm and macropores in the range between 1.8 and 6.0 μm were examined by mercury intrusion/extrusion, inverse size exclusion chromatography (ISEC) and nitrogen sorption. Our results reveal very good agreement for the mesopore size distribution obtained from nitrogen adsorption (in combination with an advanced NLDFT analysis) and ISEC. Our studies highlight the importance of mercury porosimetry for the assessment of the macropore size distribution and show that mercury porosimetry is the only method which allows obtaining a combined and comprehensive structural characterization of macroporous/mesoporous silica monoliths. Our data clearly confirm that mercury porosimetry hysteresis and entrapment have different origin, and indicate the intrinsic nature of mercury porosimetry hysteresis in these silica monoliths. Within this context some silica monoliths show the remarkable result of no entrapment of mercury after extrusion from the mesopore system (i.e. for the first intrusion/extrusion cycle). The results of a systematic study of the mercury intrusion/extrusion behavior into native silica monoliths and monoliths with bonded *n*-alkyl groups reveals that the macro (through) pore structure, which controls the mass transfer to and from the mesopores, here mainly controls the entrapment behavior. Our data suggest that mercury intrusion/extrusion porosimetry does not only allow to obtain a comprehensive pore structure analysis, but can also serve as a tool to estimate the mass transport properties of silica monoliths to be employed in liquid-phase separation processes.

1. Introduction

The development of novel monolithic materials as columns, rods and discs provided a promising alternative for fast and efficient separations in high-performance liquid chromatography (HPLC) as compared to particle packed beds. Two types of the monolithic supports were developed: polymer-based monoliths, which were applied in the field of biopolymer analysis and biopolymer isolation and purification [1–7], and monolithic silica rods which were preferably employed for the fast analysis of low-molecular compounds [8–17].

Further developments of silica-based monolithic columns [18–27] have led to excellent performance in terms of high-plate numbers, low-column pressure drop and fast analysis. These achievements were due to the high accessibility of the stationary surface through the micron size flow-through macropores and due to the rapid mass transfer of the analytes in the diffusional mesopores being located in the skeleton of the monoliths. One of the key features in the manufacture of such monoliths was to generate a homogeneous flow-through pore network as well as large enough diffusional pores to provide a fast mass transfer kinetics of the analytes in and out of the pores [28–31]. Thus a thorough characterization of this flow-through pore network of the monolithic supports was essential. This could be achieved by applying microscopy and image analysis [32], as well as techniques such as mercury porosimetry and gas adsorption [33–35].

Notable progress has been achieved in recent years with regard to the understanding of adsorption phenomena in narrow pores (for recent reviews on this topic, please see [36,37]), which has led to significant improvements in the pore size characterization. This progress was supported by a number of developments: (i) the discovery of novel highly ordered micro–mesoporous model substances such as MCM-41, MCM-48, SBA-15, which exhibit a

* Corresponding author. Tel.: +1 561 731 4999; fax: +1 561 732 9888.
E-mail address: Matthias.Thommes@quantachrome.com (M. Thommes).

0021-9673/$ – see front matter © 2008 Elsevier B.V. All rights reserved.
doi:10.1016/j.chroma.2008.03.077

uniform pore structure and morphology and can therefore be used as model adsorbents to test theories of gas adsorption; (ii) carefully performed adsorption experiments; (iii) the application of methods, such as the non-local density functional theory (NLDFT) and computer simulation methods (e.g. Monte-Carlo and molecular-dynamic simulations). These methods are based on statistical mechanics and allow describing the configuration of adsorbed molecules in pores on a molecular level (e.g. [38,39]), in contrast to classical methods, which are based on macroscopic thermodynamic assumptions (e.g. Dubinin–Radushkevitch, Barrett–Joyner–Halenda (BJH)). Further, they take into account that the shape of the adsorption isotherm does not depend only on the texture of the porous material, but also on the difference of thermodynamic states between the confined fluid and bulk fluid phase. Pore size analysis data for microporous and mesoporous molecular sieves obtained with these novel methods agree very well with the results obtained from independent methods (based on X-ray diffraction (XRD); transmission electronic microscopy (TEM)), and allow to characterize a sample over the complete micropore/mesopore size range. Appropriate methods for pore size analysis based on NLDFT and molecular simulation are meanwhile commercially available for many adsorptive/adsorbent systems.

Gas adsorption allows assessing pore sizes from the micropore range (pore widths <2 nm) and mesopore range (pores widths between 2 and 50 nm). The generally accepted method for textural analysis of macroporous materials (pore widths >50 nm) is mercury porosimetry. The main attraction of the latter technique is that it allows pore size analysis to be undertaken over a wide range of mesopore–macropore widths (routinely, from ca. 4 nm to ca. 400 μm). Mercury porosimetry is used also to determine the surface area and particle size distribution and to assess the tortuosity, permeability, fractal dimension and compressibility of porous materials. Furthermore, the technique can provide useful information relating to the pore shape, network effects and density (skeletal and bulk density) [35,40]. In contrast to capillary condensation, where the pore fluid wets the pore walls (i.e. the contact angle <90°), mercury porosimetry describes a non-wetting situation (contact angle >90°) and therefore pressure must be applied to force mercury into the pores. Thus, a progressive increase in hydrostatic pressure is applied to enable the mercury to enter the pores in decreasing order of width. Accordingly, there is an inverse relationship between the applied pressure p and the pore diameter d_p, which in the simplest case of cylindrical pores is given by the Washburn equation [41]:

$$d_p = -\left(\frac{4\gamma}{p}\right)\cos\theta \quad (1)$$

where γ is the surface tension and θ is the contact angle.

To apply Eq. (1) for the calculation of d_p, it is necessary to insert values for γ and θ. Generally, γ is assumed to be 484 mN m^{-1}, which is the surface tension of pure mercury. If no detailed information about the contact θ is available, a value of 140° is customarily used [42]. The contact angles of mercury for many materials are also reported [43].

A significant feature of mercury porosimetry curves is the occurrence of hysteresis between the intrusion and extrusion branch. In addition, entrapment is often observed, i.e. mercury remains contained in the porous network after extrusion.

The importance of understanding hysteresis and entrapment phenomena has been recognized since a long time [44–49], in particular because it is most important to be able to obtain an unambiguous pore size analysis (e.g. [49–60]). Different mechanisms have been proposed to explain intrusion/extrusion hysteresis. The single pore mechanism implies that hysteresis can be understood as an intrinsic property of the intrusion/extrusion process due to nucleation barriers associated with the formation of an vapor–liquid interface during extrusion [52,53]. The phenomenon is also discussed based on the differences in advancing and receding contact angles (e.g. [54,55]). In addition, the network models take into account the inkbottle and percolation effects in pore networks [56–60]. It is now generally accepted that pore blocking effects, which can occur on the intrusion branch, are similar to the percolation effects involved in the desorption of gases from porous networks.

It is noteworthy to mention that the shape of a mercury intrusion/extrusion hysteresis loop often agrees quite well with that of the corresponding gas adsorption loop caused by capillary condensation. Thus, the mercury intrusion and the capillary evaporation appear to follow similar pathways (e.g. [61,63]). The pore blocking/percolation effects are dominant in disordered pore networks, and a reliable pore size distribution can only be calculated from the intrusion branch by applying complex network models based on percolation theory. The application of such models also allows one to obtain a limited amount of structural information from the intrusion/extrusion hysteresis loop [56]. Scanning the hysteresis loop in combination with the application of advanced network models can also provide information about the pore network and the solid structure [49].

Very often entrapment is observed, i.e. mercury remains contained in the porous network. Classically, the entrapment phenomenon is believed to be associated with kinetic effects during mercury extrusion, coupled with the tortuosity of disordered pore network and the surface chemistry of the material [48]. Experiments with model pore networks and molecular simulation studies (e.g. [49–51]) indicate that mercury entrapment is often associated with the rupture of mercury bridges in pore constrictions during extrusion leading to mercury entrapment in inkbottle pores. This is in agreement with recent studies involving grand canonical Monte Carlo simulations using both Glauber dynamics and Kawasaki dynamics [51–63], which suggest that mercury entrapment is caused by a decrease in the rate of mass transfer associated with the fragmentation of liquid during extrusion. This leads to a configuration where droplets of mercury are surrounded by a vapor phase. The fragmentation slows down the rate of mass transfer of fluid from the porous material. It reflects a mechanism of evaporation of liquid from the entrapped droplets and diffusion of this vapor to the external surface.

A promising and novel method for pore structural investigations of chromatographic adsorbents is inverse size exclusion chromatography (ISEC). Unlike nitrogen sorption, mercury intrusion or microscopic techniques, ISEC is performed at liquid-phase conditions similar to those, used in liquid chromatographic separations. The particular advantage of ISEC is that it is a chromatographic method, which provides a comparative statistical representation of the pore space that is accessible to a solute transport. The values derived correspond to the pore volume that is accessible in liquid-based separations, rather then the ones obtained from static characterization methods. Aggerbrandt and Samuelson [64] developed the principle of the ISEC, followed by Halasz and Martin [65] who used the method to determine the pore size of chromatographic stationary phases. Knox and Scott [66] proposed a theoretical model for ISEC for the assessment of the pore size distribution of chromatographic supports. After this breakthrough, additional theoretical models were developed for the assessment of pore structural data via ISEC [67–72]. In 2002, Polymer Standard Service (Mainz, Germany) distributed a software called PSS PoroCheck™.

The first attempts to compare the pore characterization data obtained by ISEC to the one obtained by static characterization methods was done by Hagel [73]. He found a good agreement between pore size data obtained by electron microscopy, nitrogen

sorption and ISEC. Later Guan et al. [74–76] compared pore size data obtained from mercury intrusion porosimetry, nitrogen sorption and ISEC for various particulate adsorbents. The data obtained by all the named methods were in excellent agreement with differences in the order of 1–2% for the internal porosity.

Although ISEC proved its high potential in the pore structural characterization of particulate supports, certain drawbacks were acknowledged when the method was applied to the characterization of monolithic supports. Numerous authors stated that pore characterization data obtained by ISEC [77,70,78] were not in agreement with the data obtained by nitrogen sorption, mercury porosimetry and transmission electron microscopy [78]. This confusion was due to the misinterpretation of the data obtained by ISEC. The exclusion of the solutes from the flow-through pores of monoliths was interpreted as a result of a secondary mesoporosity. Grimes et al. [79] cleared this misunderstanding by applying the pore network model to obtain the pore structural data from the ISEC measurement on monolithic silica columns. Grimes stated that an exclusion of high-molecular weight solutes is due to the exclusion mechanism in the flow-through pores (separation by flow).

Another potential of ISEC was recognized by Kuga [80], who stated, that the most important feature of ISEC is its applicability to polymeric gels in the swollen state to which the conventional porosimetry cannot be applied. This feature was extensively studied in numerous publications as the only method for obtaining reliable pore characterization data on polymer-based supports [81–83].

By applying the techniques of gas adsorption, mercury porosimetry and ISEC on selected silica monoliths (native and functionalized with *n*-alkyl groups) we address in this work the problem of a comprehensive textural characterization of such supports. Mesopore size analysis is performed by combining nitrogen sorption, ISEC and mercury porosimetry, whereas mercury porosimetry is used to assess macroporosity. We used well-characterized silica monoliths as model materials to study the mercury intrusion/extrusion hysteresis and entrapment behavior, which allows correlating details of the monolith pore structure with the mercury porosimetry data. A detailed understanding of the underlying mechanism of mercury intrusion/extrusion into silica monoliths is crucial for a comprehensive textural characterization of both the macropore and mesopore system and will help to further optimize the properties of monolithic materials in view of column performance, column pressure drop, speed of analysis in liquid separation processes.

2. Materials and experiments

2.1. Monolithic materials and columns

Measurements were performed on a set of monolithic silica columns (length and ID of 100 mm × 4.6 mm), provided as research samples by Merck KGaA (Darmstadt, Germany). The inter-skeleton flow-through pore sizes of the silica monoliths were in the range from 1.8 to 6.0 μm and the intra-skeleton pore sizes were from 10 to 25 nm. Samples were available as native silica and as *n*-octadecyl, *n*-octyl or *n*-butyl derivates. The structural properties of such monolith supports and their impact on column performance are given in Ref. [27]. In this study we focused on selected native silica samples as well as *n*-octadecyl derivatives. In order to obtain columns that could be used in HPLC, the monolithic silica rods were gladded with poly-ether-ether-ketone (PEEK) by a proprietary process of Merck KGaA (Darmstadt, Germany).

The manufacturing process of monolithic silica research samples consisted of: preparation of the starting solution, phase separation and gelation, aging and drying. The starting silica sources usually were tetramethoxysilane or tetraethoxysilane, which were subjected to acid catalysed hydrolysis and condensation in the presence of water-soluble polymers, such as polyethyleneglycol and polyacrylic acid and surfactants as additives. Phase separation and gelation was controlled by the kinetics of two competitive processes: the domain coarsening and the structure freezing by the sol–gel transition. The resulting gels were aged and solvent exchange was performed to tailor the mesopore structure. The flow-through porous gel domains were filled with the polymer, which was burned out by calcination after drying. In this way the process enabled to generate two continuous pore systems and to adjust and control the pore size, and porosity of flow-through pores and mesopores independently [48].

2.2. Characterization methods

2.2.1. Inverse size exclusion chromatography

Tetrahydrofuran (for liquid chromatography) and 2-propanol (for liquid chromatography) were obtained from Merck KGaA (Darmstadt, Germany). Polymer standards of poly(styrene) – molecular weight of 162, 309, 514, 707, 795, 1920, 3460, 51,500, 524000, and polystyrol – molecular weight of 5610, 12,500, 27,500, 125,000, 271,000 were obtained from Polymer Standards Service (Mainz, Germany). Polystyrene standard of molecular weight 950 (lipophilic gel permeation chromatography) was obtained from Merck KGaA (Darmstadt, Germany). All samples had polydispersity values lower than 1.10.

All experiments were run on a Bischoff liquid chromatographic system (LC-CaDI controller with two HPLC compact pumps 2250, UV detector Lambda 1010, autosampler Model 718 AL), obtained from Bischoff Chromatography (Leonberg, Germany). The configuration was controlled by McDAcq32 software (Bischoff Chromatography, Leonberg, Germany).

All ISEC experiments were performed under isocratic elution conditions for each polymer standard sample. The pump was operated at volumetric flow rates of 0.2 ml min^{-1}. The injection volume was 2 μl and UV detection was carried out at 254 nm. The measurements were carried out three times. Data emerged as mean values from three independent runs.

The pore size distribution curve was obtained by separation of the polymer standards in the liquid chromatography mode and measuring the elution volumes of the named analytes. The ISEC measurement was carried out under such conditions that the elution behavior of known size solutes was influenced only by the steric effects in the porous system of the column. A proper mathematical treatment of solute elution volumes by the PSS PoroCheck™ program was used to calculate the pore size distribution.

2.2.2. Mercury porosimetry experiments

Mercury intrusion and extrusion experiments on silica monoliths samples were performed over a wide range for pressures starting in vacuum up to 60,000 psi (1 psi = 6.895 × 10^{-3} MPa by a Quantachrome Poremaster 60 (Quantachrome, Boynton Beach, USA) instrument. Data acquisition was performed in the so-called continuous scanning mode, in which the rate of pressurization is controlled by the motor speed of the pressure generator system. However, it was possible (with the help of a microcomputer) to adjust the pressurization and depressurization rate in inverse proportion to the rate of intrusion or extrusion, respectively. Thus, the porosimeter provides maximum speed in the absence of intrusion or extrusion and maximum resolution and in most cases sufficient relaxation time (sampling time) when most required, i.e. when intrusion or extrusion is occurring rapidly with changing pressure. The use of this scanning mode allows obtaining high-resolution

intrusion/extrusion curves and up to ca. 2000 data points were acquired for a combined intrusion/extrusion cycle (please note that for reasons of clarity only every 10th data point is being displayed in some figures where intrusion/extrusion curves of various silica monoliths samples are being compared).

2.2.3. Gas adsorption

The nitrogen adsorption isotherm (at 77.4 K) on sample Tr2783/1 silica was performed at Merck KGaA with a conventional automated adsorption analyzer (ASAP 2400, Micromeritics, Norcross, USA). The sample was outgassed overnight at 150 °C prior to the adsorption measurement. The analysis of the adsorption data was performed with the Quantachrome As 1.54 software package (Quantachrome, Boynton Beach, USA).

3. Results and discussion

3.1. Pore size analysis of a native silica monolith by mercury porosimetry, gas adsorption and inverse size exclusion chromatography

A typical mercury intrusion/extrusion curve on a native silica monolith (here silica Tr2783/1) is shown in Fig. 1. The volume of intruded/extruded mercury of two consecutive intrusion/extrusion cycles runs is here shown as a function of pore diameter (as obtained by applying the Washburn equation on the experimental hydraulic pressure/volume curves). Fig. 1 clearly reveals the bimodal nature of this silica monolith sample, i.e. it consist of macropores with a (mode) pore diameter of 1800 nm and a mesopore system of mode pore diameter 10 nm (the mode pore diameter, or modal pore diameter, is defined as the most frequent pore diameters, or pore diameter associated with the maximum of the pore size distribution curve).

The first cycle clearly indicates no entrapment for intrusion/extrusion into the mesopores (ca. 10 nm, see Fig. 4 for a detailed pore size distribution curve), but there is clearly some remaining entrapment for intrusion/extrusion into the macropores. The lack of appreciable entrapment for the first intrusion/extrusion cycle into the mesopore systems is indeed remarkable. Usually mercury intrusion/extrusion is always accompanied by entrapment [35]. In line with the findings in Refs. [61–63], the lack of entrapment would indicate that the rate of mass transfer in and out of the mesopores appears to be fast enough to avoid fragmentation of liquid during extrusion (which would lead to entrapment). We will discuss this finding in more detail in Section 3.3. Contrary to the situation for the silica monolith mesopore system, entrapment is observed for intrusion/extrusion into the macropores of the silica monolith. However, similar as observed for instance for other porous glasses [63] entrapment completely vanishes also here in the second intrusion/extrusion cycle. The perfect reproducibility of the hysteresis loops for both the macro- and mesopores in subsequent intrusion/extrusion cycles (we have performed sometimes up to three intrusion/extrusion experiments on the same material) does not only indicate that the structure of the silica monolith was not affected in the first cycle (i.e. no fracture of the material), but also confirms that entrapment and hysteresis have a different origin [35,40,63].

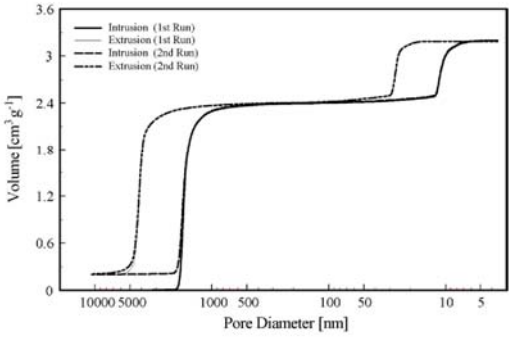

Fig. 1. Intrusion/extrusion cycles into the native silica monolith Tr2783/1. The specific pore volume is displayed as a function of pore diameter.

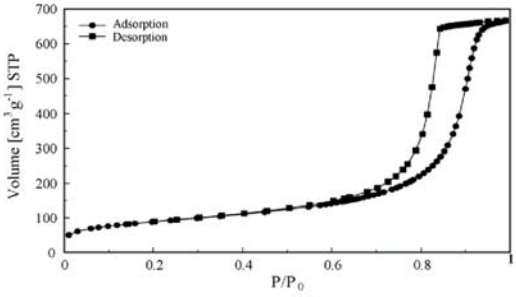

Fig. 2. Nitrogen adsorption at 77.4 K on the native silica monolith Tr2783/1.

Nitrogen adsorption/desorption data obtained at 77.4 K on the native silica monolith Tr2783/1 are displayed in Fig. 2. The type IV isotherm (IUPAC classification) reveals a hysteresis loop indicative of pore condensation. The hysteresis loop can be classified as to between type H1 and H2. This would indicate that in addition to intrinsic reasons for hysteresis (i.e. the delay in condensation is caused by metastable pore fluid), also pore blocking/percolation effects are present which lead to a delay in the position of the desorption branch. This conclusion is in agreement with the shape of the hysteresis loop observed in the mercury intrusion/extrusion experiment, i.e. also here the shape of the loop can be classified as to be between types H1 and H2. It is widely accepted that the underlying mechanism of mercury intrusion in mercury porosimetry hysteresis is analogue to the mechanism of capillary evaporation (i.e. the desorption branch in capillary condensation hysteresis [61,63]). Thus, mercury intrusion and capillary evaporation appear to follow a similar pathway. Pore blocking/network effects could principally also affect the position of the intrusion branch and the resulting pore size distribution curve in a similar way. Fig. 3 reveals a good agreement between the pore size distribution curves obtained by applying the BJH method [84] (which is based on the Kelvin equation) on the desorption branch with the pore size distribution curve obtained from mercury intrusion by applying the Washburn equation with an assumed contact angles of 140° (the "standard value", see [42]). The agreement of the pore size distributions obtained from both methods is even better if a contact angle of 145° is being used (this value was found on recent contact angle measurements of mercury on amorphous silica [85]). Similar good agreement of the pore size distribution curves obtained from nitrogen adsorption and mercury porosimetry has also been recently reported for porous Vycor and controlled glasses [63]. However, it is important to note that both the Washburn equation and the Kelvin equation (which is the basis for the BJH method) are macroscopic, thermodynamic approaches. It is meanwhile well known that these classic methods fail to describe correctly the adsorption and phase behavior of fluids in small mesopores, which leads to a significant underestimation of pore size (for

IV

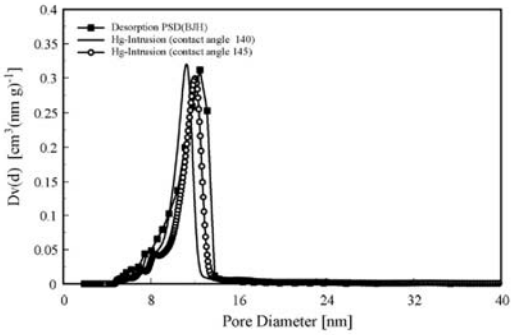

Fig. 3. Pore size analysis from gas adsorption (BJH method applied to the desorption branch) and mercury porosimetry (calculated for contact angles of 140° and 145°).

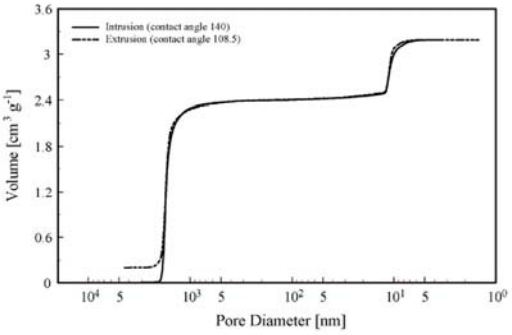

Fig. 5. Mercury intrusion/extrusion curves over the complete macro/mesopore size range as a function of pore diameter. The pore diameter was calculated by applying the Washburn equation, assuming a contact angle of 140° for intrusion and 108,5° for extrusion.

pore widths which are smaller than ca. 20 nm [37–39]). As already mentioned in Section 1, theoretical approaches such as the NLDFT [38,39] are able to describe the configuration of the adsorbed phase on a molecular level, and therefore allow (as already described in the introduction) to obtain an accurate pore size distribution. This has been extensively confirmed in recent years (see [37] and references therein). In addition, the application of the NLDFT correctly predicts that the adsorption branch of a hysteretic adsorption isotherm is not at thermodynamic equilibrium, i.e. pore condensation occurs with a delay due to metastable pore fluid. Hence, in case hysteresis is only caused by metastable pore fluid and no networking effects are present, the desorption branch of the hysteresis loop reflects the thermodynamic equilibrium transition and the pore size distribution calculated from the desorption branch by applying the NLDFT equilibrium method, and from the adsorption branch by applying the so-called NLDFT metastable adsorption branch kernel (which takes into account the delay in condensation) should agree. This has indeed been confirmed in various studies [37–39]. Applying these two kernels on the adsorption and desorption branches of the nitrogen isotherm of sample Tr2783/1 reveals that the mode pore diameter obtained from the desorption branch is slightly shifted to smaller values. Furthermore, the pore size distribution (PSD) curve is much narrower as compared to the PSD obtained from the adsorption branch indicating the presence of some network/pore blocking effects. These NLDFT pore size distribution curves are displayed together with the PSD curves from other techniques (mercury intrusion, ISEC) in Fig. 4. The data shown

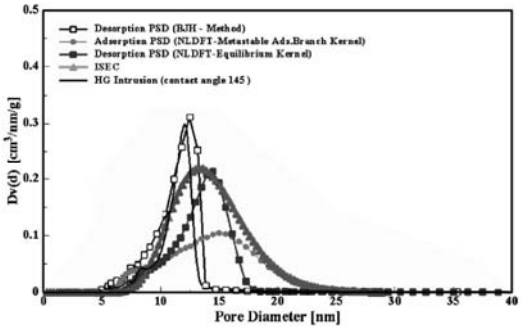

Fig. 4. Comparison of mesopore size distribution curves for the native silica monolith Tr2783/1 obtained from nitrogen adsorption (by applying NLDFT and BJH methods), ISEC and mercury porosimetry.

in Fig. 4 also reveal that (as to be expected) the BJH method significantly underestimates the pore size compared to the NLDFT pore size. The pore size distribution curve obtained from the adsorption branch is wider as compared to the pore size distribution curve obtained from the desorption branch, indicating that pore blocking/network effects contribute here to the hysteresis. Interestingly, the width of the pore size distribution curve obtained by ISEC agrees reasonably well with the pore size distribution curve obtained from the NLDFT adsorption branch.

The analysis of the nitrogen adsorption results indicates the presence of some pore blocking/network effects. This is in accord with the shape of mercury intrusion/extrusion hysteresis loop, which is between types H1 and H2 as in case of the nitrogen adsorption hysteresis for silica monolith Tr2783/1. In order to test to which extend mercury intrusion/extrusion hysteresis is not only of intrinsic origin (e.g. cavitations induced evaporation, contact angle hysteresis), or is also affected by networking (pore blocking/percolation) effects, one can apply the idea of contact angle hysteresis in a sense that if hysteresis completely disappears just by changing an intrinsic parameter (such as the extrusion contact angle), then hysteresis is caused by intrinsic parameters. By lowering the effective extrusion contact angle one obtains a narrowing of the hysteresis because the extrusion branch "moves" to smaller pore diameters. By doing this one has to make sure that intrusion occurs at least at the same or higher pressure than extrusion, i.e. this criteria determines the lowest possible extrusion contact angle, which is here 108.5° (for an intrusion contact angle of 140°). In the case of the native silica monolith Tr2783/1 (see Fig. 5) the hysteresis widely disappears by reducing the extrusion contact angle, with the exception of a small portion in the high-pressure range. This reveals that hysteresis in the sample Tr2783/1 is mainly caused by intrinsic factors. However, the fact that one cannot obtain a perfect overlay between the intrusion and extrusion branches in the range of narrow mesopores (pores of diameters <8 nm) by changing the contact angle indicates that some (although minor) contributions of structural hysteresis in form of pore blocking/percolation effects are also present.

It needs to be stressed that changing the extrusion contact angle is here only used for assessing the intrinsic nature of the observed mercury porosimetry hysteresis as demonstrated in Fig. 5. Our results obtained on silica monoliths are also in agreement with the so-called energy barrier model of hysteresis (see here also Ref. [53]) Because of the specific nature of this silica monoliths, which allows mass transport into and out of the mesopores only through the

IV

macroporous through pores (e.g. [27]), extrusion may occur via cavitation (i.e. vapor bubble formation). Associated with the cavitation phenomenon are nucleation barriers which have to be overcome; as a consequence extrusion occurs with a delay, which contributes significantly to the observed mercury porosimetry hysteresis.

Summarizing, our data show that the mesopore size distribution obtained from ISEC agrees well with the NLDFT pore size distribution determined from the adsorption branch of the nitrogen adsorption isotherm. The pore size obtained from mercury intrusion data by using a realistic contact angle underestimates the true pore size and width of distribution because of the reasons discussed above (i.e. macroscopic thermodynamic method, i.e. surface tension depends on radius of curvature; network effects). It is worthwhile to emphasize that the mercury porosimetry results agree with the pore size distribution according to BJH. This finding is not surprising because the Kelvin equation and the Washburn equation are based on the same macroscopic, thermodynamic assumptions. However, such macroscopic approaches are expected to become more accurate for larger mesopores (pore diameter >20 nm) and macropores [35,37,38,51,63]. It can be concluded that mercury porosimetry is the method of choice for a comprehensive pore size assessment of larger mesopores and macropores, and thus is an important tool for the textural analysis of silica monoliths.

3.2. Textural analysis of n-alkyl-grafted silica monoliths

In order to apply silica monoliths in liquid separation techniques a chemical functionalization of the surface is mandatory. The most common surface modification is the bonding of *n*-alkyl groups via silanization [27,86] prepared and subjected to pore texture analysis.

It is of key interest in which way the pore texture is changed by the bonding and how these changes might effect the column performance of the materials.

The native silica monolith (Tr2783/1) was converted to monolith Fr787 by grafting with *n*-octadecyl chains on surface (see Section 2). A comparison of the cumulative specific pore volume curves for the native and *n*-octadecyl-grafted monolith as obtained from mercury porosimetry is shown in Fig. 6a. It should be emphasized that, the intrusion/extrusion curves into the mesopores of the grafted sample still do not reveal any appreciable entrapment. This serves as an indication that the functionalization of the silica monolith Tr2783/1 and the resulting changes in effective pore size and specific pore volume (which we will discuss below) might have no influence on the mass transfer kinetics into and out of the mesopore system.

However, Fig. 6a also clearly reveals that the effective specific pore volume of the functionalized silica monolith is significantly decreased for both the macro- and the mesopore system as a consequence of the grafting. Further it appears that the shape of the intrusion/extrusion hysteresis has become more of type H2 as compared to the native silica monoliths indicating a wider pore size distribution. The inspection of the mercury intrusion/extrusion curves reveal that the macropore size distribution is essentially not affected by the grafting with *n*-alkyl groups (the small shift to larger values might be due to an effective change in contact angle of mercury in contact with the grafted surface as compared to a pure silica surface) whereas the mode pore size for the mesopores has been slightly shifted to smaller values (here the reduction in effective pore size due to the surface groups is significant, despite the possibility of a contact angle change).

The decrease in specific pore volume for the *n*-octadecyl-grafted monoliths is also visible from the cumulative pore volume plots as obtained from ISEC (see Fig. 6b). Also ISEC confirms that the grafting with *n*-alkyl groups reduce the effective pore diameter, and that the pore size distribution of the *n*-octadecyl-grafted monolith is much wider as compared to the native silica monolith. Interest-

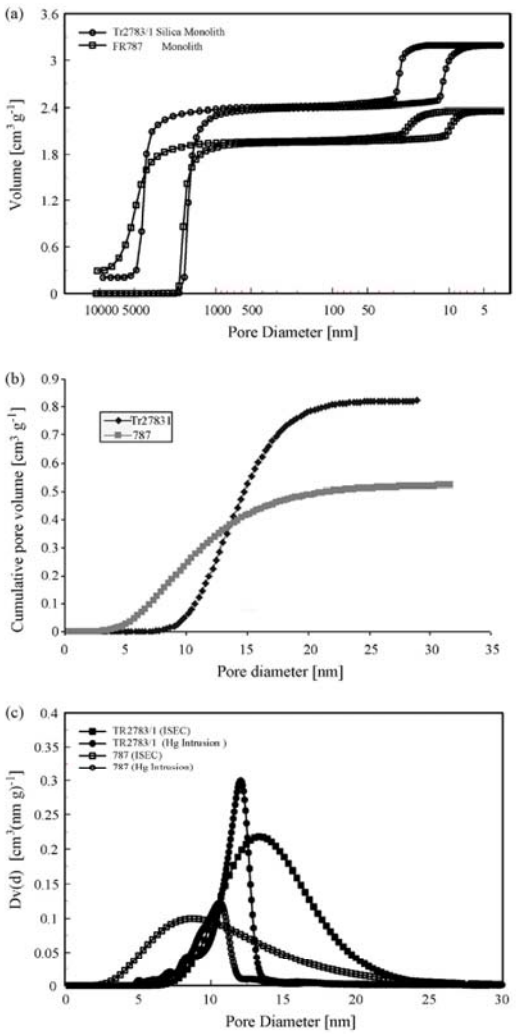

Fig. 6. (a) Mercury intrusion/extrusion into the native silica monolith (Tr2783/1) and into silica monolith Fr787 with bonded *n*-octadecyl groups made from monolith Tr2783/1 as base material. (b) Cumulative pore volume curves obtained by ISEC of the native silica monoliths Tr2783/1 and its derivative with bonded *n*-octadecyl groups (silica monolith Fr787). (c) Comparison of pore size distribution curves obtained from ISEC and mercury porosimetry for the native silica monolith (Tr2783/1) and the silica monolith Fr787 with bonded *n*-octadecyl groups.

ingly, ISEC data reveal a much more pronounced shift to smaller pore diameter values, as compared to the pore size obtained from mercury porosimetry (see Fig. 6c). It should be mentioned in this context that mercury intrusion principally underestimate the pore size for such narrow mesopores (see discussion associated with Fig. 4). Hence, it is therefore a bit surprising that the shift of the mercury porosimetry PSD for the *n*-octadecyl-grafted monolith (in comparison with the corresponding native silica monolith) is less pronounced than the shift of the ISEC pore size distribution. One

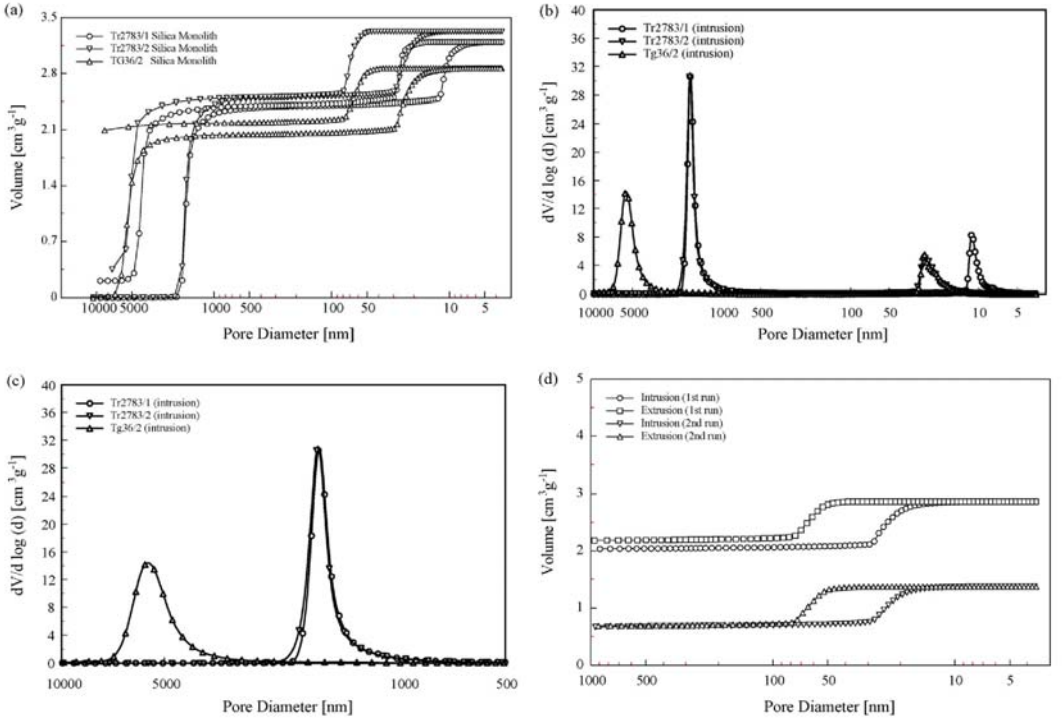

Fig. 7. (a) Mercury intrusion/extrusion hysteresis into some characteristic native silica monoliths. (b) Differential pore size distributions curves for silica monoliths shown in (a) obtained from the intrusion branch. (c) Pore size distribution of macropores for Tr2783/1, Tr2783/2 and TG36/2 monolithic silica rods obtained from the intrusion branch. (d) Mercury intrusion/extrusion experiments into the native silica monolith (sample TG36/2). The second run was performed after the first experiments on the identical sample. The smaller amount of intrusion is due to the entrapment observed for the first experiment in both pore systems, i.e. the mesopore and the macropore system.

cannot rule out that the bonded phase may interact with the testing polymers, which would lead to a larger elution volume and would contribute to the observed shift of the ISEC pore size distribution to smaller values. In case of mercury porosimetry one would expect that the effective contact angle and surface tension for mercury on a *n*-octadecyl-grafted monolith is different as compared to a pure silica surface, which may also affect the position of the pore size distribution curve. Another possible explanation for the observed differences between ISEC and mercury porosimetry is that the orientation of the functional groups grafted on the pore walls maybe be different under the high pressures applied in mercury intrusion, as compared to the ISEC measurement conditions. One expects that the *n*-octadecyl groups have a vertical orientation on the pore walls, but it appears that the high pressure applied in mercury porosimetry may partially change the orientation of the *n*-octadecyl groups from vertical to more or less parallel to the pore walls. This would lead to a somewhat larger effective pore diameter as compared to the situation where all *n*-alkyl groups are vertically oriented. Hence, this would suggest that the ISEC method appears to be better suited than mercury porosimetry to assess the mesopore size distribution of silica monolith, which is grafted with *n*-octadecyl groups.

3.3. Effect of monolith macropore/mesopore structure on mercury intrusion/extrusion behavior

As mentioned before, the advantage of mercury intrusion/extrusion porosimetry is that it allows assessing both the mesopore and macropore structure. Textural characteristics of micropore and mesopores are important for transport properties of silica monoliths, which are crucial for their application in HPLC. We will discuss in the following section to which extend the mercury intrusion/extrusion behavior into silica monoliths (native and functionalized) can be correlated with the macropore/mesopore structure. As discussed already before, the origin of intrusion/extrusion hysteresis and entrapment are different. Whereas hysteresis is caused by intrinsic as well as by structural effects, the entrapment phenomenon is believed to be associated with kinetic effects during mercury extrusion, coupled with the tortuosity and surface chemistry of the pores in the porous network [61–63].

Recent experimental and simulation work has clearly revealed the dynamic nature of entrapment, i.e. it indicates that the origin of entrapment is the slowdown of the dynamics associated with the fragmentation of the liquid in the void space that makes vapor transport an important part of the extrusion process [61–63]. As a consequence it has been observed that for (given equilibration characteristics) samples with small pores, low porosity and highly tortuous nature exhibit larger amounts of entrapment as compared to samples with large pores and high porosity [63]. Hence, in principle it should be possible to correlate the entrapment behavior with characteristic transport properties of a sample.

The striking feature of the intrusion/extrusion behavior into native silica monoliths (Tr2783/1) and *n*-octadecyl-grafted silica monolith samples is the fact that they do not show any appreciable

IV

amount of entrapment. This indicates that the rate of mass transfer in and out of the mesopores appears to be fast enough to avoid fragmentation of liquid during extrusion (which would lead to entrapment). The reason for this interesting behavior has to be correlated with the texture of both the mesopore system and the macroporous through pores and the connection between them. One would expect that the mercury extrusion process from the mesopores is affected by both the mesopore structure as well as the texture of the macropore systems, whereas the latter controls the fluid transport into and out of the mesopore system. Hence, we compare first the intrusion/extrusion behavior of mercury into three native silica monoliths, which have either different mesopore size but an identical macropore system (silica monoliths Tr2783/1 and Tr2783/2), or identical mesopore size distribution but different macropore size (silica monoliths TG36/2 and Tr2783/1). As shown in Fig. 7a no entrapment occurs for monolith Tr2783/2, which has a larger mesopore diameter of ca. 28 nm compared to 12 nm for Tr2783/1. Both monoliths have almost an identical macropore system with regard to porosity and pore size distribution. This is also clearly visible in Fig. 7b, which depicts the differential pore size distribution curves for the samples featured in Fig. 7a. Contrary to the previous observation, silica monolith TG36/2 clearly shows an entrapment into mesopores. The mesopore size of sample TG36/2 agrees well with that of sample Tr2783/1. The macroporosity, however, is significantly reduced despite the fact that through pores are larger in pore diameter. Fig. 7c highlights the macropore size distribution of the three samples and clearly reveals that the macropore size distribution for silica monolith TG36/2 is wider as compared with the samples Tr2783/1 and Tr2783/2. This indicates also that the macroporous framework of sample TG36/2, which controls the transport/extrusion of mercury from the mesopores to the bulk phase, appears to be more heterogeneous/disordered as compared to the silica monoliths samples which do not show entrapment. As to be expected, if the intrusion/extrusion experiment is repeated just after the first intrusion/extrusions runs on the same sample of TG36/2, entrapment disappears. This is demonstrated in Fig. 7d, which shows the intrusion/extrusion cycles into the mesopores of sample TG36/2 (the lesser amount of intrusion and therefore available pore volume for the second intrusion/extrusion cycle is due to the entrapment observed for the first experiment in both pore systems, i.e. the mesopore and the macropore system).

The above discussed results concerning the effect of macropore structure on the mercury extrusion entrapment for native silica monoliths is also supported by intrusion/extrusion experiments performed on various silica monoliths functionalized all with *n*-octadecyl groups (samples Fr800, Fr843, Fr787), but with different pore structure. The corresponding intrusion/extrusion data are displayed in Fig. 8a. Samples Fr787 and Fr800 show no entrapment. These two monoliths differ in mesopore diameter, but have identical macropore size distribution. On the other hand, the monoliths Fr800 and Fr843 agree with regard to their mesopore size distribution, but differ appreciably with regard to their macropore systems. This is clearly visible in Fig. 8b and c which show the pore size distribution for these *n*-alkyl-grafted samples. In particular Fig. 8c reveals that for monolith Fr 843 the macropore size distribution is wider as compared to samples Fr800 and Fr787. Contrary to samples Fr800 and FR787, sample Fr843 shows significant entrapment for intrusion/extrusion into the mesopores. Hence, similar as in case of the native silica monolith (see Fig. 7), the monoliths with the most disordered and heterogeneous macropore system reveal mercury entrapment.

These results obtained on native and *n*-alkyl-bonded silica monoliths suggest that the macropore structure, which controls the access to the mesopore system, is crucial for the occurrence of mercury entrapment. It appears that details of the well defined mesopore structure do not significantly influence the entrapment behavior, although the nitrogen sorption and mercury porosimetry data for the native silica monolith Tr2783/1 clearly suggest the existence of a small fraction of inkbottle pores or pore constrictions in the mesopore system. However, our results clearly show that the structure of the macroporous through pores controls the entrapment behavior for the mesopore intrusion/extrusion cycle.

The importance of the macroporous through pores for the extrusion process and possible entrapment of mercury from mesopores

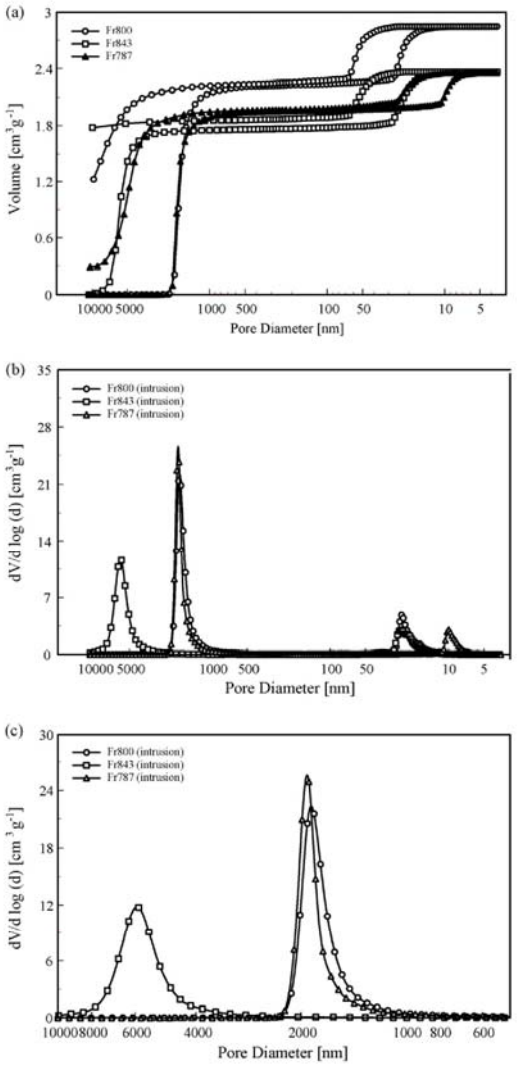

Fig. 8. (a) Mercury intrusion/extrusion curves in various *n*-alkyl (i.e. *n*-octadecyl)-bonded silica monoliths. (b) Differential macro/mesopore size distributions curves for silica monoliths shown in (a) obtained from the intrusion branch. (c) Pore size distribution of macropores for Fr800, Fr843 and Fr787 monolithic silica rods from the intrusion branch.

IV

is also clearly visible for samples where the intrusion/extrusion hysteresis loop for the mesopores is of perfect type H1 character as it can be found for instance for some controlled pore glasses (type H1 hysteresis indicates that the hysteresis is mainly of intrinsic nature). An example is shown in Fig. 9a, which compares mercury intrusion/extrusion into the mesopores of a controlled pore glass of type CPG-10-75 and silica monolith Tr2783/1. Contrary to intrusion/extrusion into silica monolith Tr2783/1, the CPG sample clearly reveals significant entrapment. It is interesting to note, that the mesopore size of this CPG sample agrees well with that of silica monolith Tr2783/1. However, as shown in Fig. 9b the two materials differ mainly with regard to their macropore system, which in case of CPG sample consist of interparticle voids between the CPG particles. One can also clearly see that the porosity of these macropore system as well as the mesopore system is significantly smaller than for the silica monolith. It follows further from Fig. 9b that the pore size distribution of the interparticle pores (voids) is as to be expected much wider as compared to the silica monolith. Hence, the occurrence of entrapment in controlled pore glass or is there in qualitative agreement with our findings on silica monoliths with disordered macro-(through)pore systems.

The lack of entrapment for extrusion from mesopores (such as Tr2783/1 and Tr2783/2, see Fig. 7) indicates enhanced transport properties, which is in accord with the results of Skudas et al. who reported in previous work that these samples exhibit good separations performance [27]. Interestingly, the monolith sample TG36-2 which shows clear entrapment for extrusion from the mesopores (see Fig. 7) revealed poor separation performance [27]. Hence, mercury intrusion/extrusion porosimetry does not only allow to obtain a comprehensive pore structure analysis over the complete range of macro- and mesopores, but also can be used as tool to assess the transport properties of silica monolith to be used for separation processes.

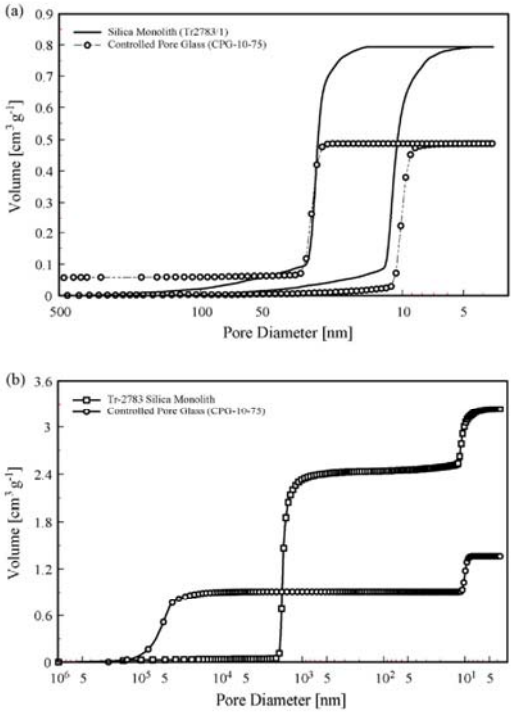

Fig. 9. (a) Mercury intrusion/extrusion curves into the mesopore systems of controlled pore glass (CPG-10-75) and the native silica monolith (Tr2783/1; please note that only the mesopores system is shown here). The specific pore volume is shown as a function of the pore diameter. (b) Mercury intrusion curves into the mesopore system of controlled pore glass (CPG-10-75) and the native silica monolith (Tr2783/1). The cumulative specific pore volume is shown as a function of the pore diameter.

4. Summary and conclusions

Native and *n*-alkyl-bonded (*n*-octadecyl) monolithic silica rods with mesopores in the range between 10 and 25 nm and macropores in the range between 1.8 and 6.0 μm were examined by mercury intrusion/extrusion, ISEC and nitrogen sorption. Our results reveal very good agreement for the mesopore size distribution obtained from nitrogen adsorption (in combination with an advanced NLDFT analysis) and ISEC, but indicate that mercury porosimetry underestimates the pore size for narrow mesopores. However, on the other hand, mercury porosimetry allows not only obtaining a detailed assessment of the macropore size distribution, but also allows to obtain structural information over the complete range of macro- and mesopores of silica monoliths.

Our data confirm that mercury porosimetry hysteresis and entrapment have different origin, and indicate the intrinsic nature of mercury porosimetry hysteresis in these silica monoliths. Within this context some silica monoliths show the remarkable result of no entrapment of mercury after extrusion from the mesopore system (i.e. for the first intrusion/extrusion cycle). The results of a systematic study of the mercury intrusion/extrusion behavior into native silica monoliths and monoliths with bonded *n*-alkyl groups reveals that the macropore (or through pore) structure, which controls the mass transfer to and from the mesopores, here mainly controls the entrapment behavior. It appears that entrapment is more likely to occur if the macropore system is heterogeneous and disordered (which would restrict mass transfer) as indicated by a wide pore size distribution coupled with relatively low porosity. Vice versa, the lack of entrapment after extrusion from monolith mesopore system indicates enhanced transport properties, which is in accord with an ordered, highly porous macropore system. Hence, mercury intrusion/extrusion porosimetry does not only allow to obtain a complete pore structure analysis over the complete range of macro- and mesopores, but also might serve as tool to estimate the mass transport properties of silica monoliths to be employed in liquid-phase separation processes.

Acknowledgement

We would like to thank Mr. Riaz Ahmad for his help with the mercury porosimetry experiments.

References

[1] S. Hjerten, J.-L. Liao, J. Chromatogr. 457 (1988) 165.
[2] J.-L. Liao, S. Hjerten, J. Chromatogr. 457 (1988) 175.
[3] S. Hjerten, J.-L. Liao, R. Zhang, J. Chromatogr. 473 (1989) 273.
[4] F. Svec, J.M.J. Frechet, Anal. Chem. 64 (1992) 820.
[5] Q.C. Wang, F. Svec, J.M.J. Frechet, J. Chromatogr. A 669 (1994) 230.
[6] A. Podgornik, M. Barut, A. Strancar, D. Josic, T. Koloini, Anal. Chem. 72 (2000) 5693.
[7] H. Oberacher, A. Premstaller, C.G. Huber, J. Chromatogr. A 1030 (2004) 201.
[8] K. Nakanishi, N. Soga, J. Am. Ceram. Soc. 74 (1991) 2518.
[9] K. Nakanishi, N. Soga, J. Non-Cryst. Solids 139 (1992) 1.
[10] K. Nakanishi, N. Soga, J. Non-Cryst. Solids 139 (1992) 14.
[11] H. Minakuchi, K. Nakanishi, N. Soga, N. Ishizuka, N. Tanaka, Anal. Chem. 68 (1996) 3498.
[12] K. Cabrera, G. Wieland, D. Lubda, K. Nakanishi, N. Soga, H. Minakuchi, K.K. Unger, Trends Anal. Chem. 17 (1998) 133.

IV

[13] F. Gritti, W. Piatkowski, G. Guiochon, J. Chromatogr. A 978 (2002) 81.
[14] F.C. Leinweber, D.G. Schmid, D. Lubda, K.-H. Weismüller, G. Jung, U. Tallarek, Rapid Commun. Mass Spectrom. 17 (2003) 1180.
[15] D. Lubda, K. Cabrera, N. Nakanishi, W. Lindner, Anal. Bioanal. Chem. 377 (2003) 892.
[16] D. Lubda, W. Lindner, J. Chromatogr. A 1036 (2004) 135.
[17] B. Chankvetadze, T. Ikai, C. Yamamoto, Y. Okamoto, J. Chromatogr. A 1042 (2004) 55.
[18] N. Tanaka, H. Nagayama, H. Kobayashi, T. Ikegami, K. Hosoya, N. Ichizuka, H. Minakuchi, K. Nakanishi, K. Cabrera, D. Lubda, J. High Resolut. Chromatogr. 23 (2000) 111.
[19] M. Motokawa, H. Kobayashi, N. Ishizuka, H. Minakuchi, K. Nakanishi, H. Jinnai, K. Hosoya, T. Ikegami, N. Tanaka, J. Chromatogr. A 961 (2002) 53.
[20] N. Tanaka, H. Kobayashi, N. Ishizuka, H. Minakuchi, K. Nakanishi, K. Hosoya, T. Ikegami, J. Chromatogr. A 965 (2002) 35.
[21] N. Tanaka, H. Kobayashi, Anal. Bioanal. Chem. 376 (2003) 298.
[22] H. Minakuchi, N. Ishizuka, K. Nakanishi, N. Soga, N. Tanaka, J. Chromatogr. A 828 (1998) 83.
[23] T.P. Hennesy, R.I. Boysen, M.I. Huber, K.K. Unger, M.T.W. Hearn, J. Chromatogr. A 1009 (2003) 15.
[24] B. Barroso, D. Lubda, R. Bischoff, J. Proteom. Res. 2 (2003) 633.
[25] L. Xiong, R. Zhang, F.E. Regnier, J. Chromatogr. A 1030 (2004) 187.
[26] D. Josic, A. Buchacher, A. Jungbauer, J. Chromatogr. B 752 (2001) 191.
[27] R. Skudas, B.A. Grimes, E. Machtejevas, V. Kudirkaite, T.P. Hennessy, D. Lubda, K.K. Unger, J. Chromatogr. A 1144 (2007) 72.
[28] P. Gzil, N. Vervoort, G.V. Baron, G. Desmet, Anal. Chem. 76 (2004) 6707.
[29] A.I. Liapis, J.J. Meyers, O.K. Crosser, J. Chromatogr. A 865 (1999) 13.
[30] J.J. Meyers, A.I. Liapis, J. Chromatogr. A 852 (1999) 3.
[31] N. Vervoort, P. Gzil, G.V. Baron, G. Desmet, J. Chromatogr. A 1030 (2004) 177.
[32] B. Tesche, in: F. Schüth, K.S.W. Sing, J. Weitkamp (Eds.), Handbook of Porous Solids, Wiley-VCH, Weinheim, 2002, p. 106.
[33] H.L. Ritter, L.C. Drake, Ind. Eng. Chem. Anal. Chem. 17 (1945) 782.
[34] L.C. Drake, H.L. Ritter, Ind. Eng. Chem. Anal. Ed. 17 (1945) 787.
[35] S. Lowell, J. Shields, M.A. Thomas, M. Thommes, Characterization of Porous Solids and Powders: Surface Area, Pore Size and Density, Springer, The Netherlands, 2004.
[36] M. Thommes, J. Cejka, H. van Bekkum, Corma FA., F. Schüth (Eds.), Introduction to Zeolite Science and Practice (3rd revised edition). Studies in Surface Science and Catalysis, vol. 168, Elsevier, 2007, p. 495 (Chapter 15).
[37] M. Thommes, in: G.Q. Lu, X.S. Zhao (Eds.), Nanoporous Materials, Science & Engineering, Imperial College Press, 2004 (Chapter 11).
[38] V.A. Neimark, P.I. Ravikovitch, Micropor. Mesopor. Mater. 44 (2001) 697.
[39] P.I. Ravikovitch, A.V. Neimark, Colloids Surf. A 187 (2001) 11.
[40] León y León, Adv. Colloid Interf. Sci. 76 (1998) 341.
[41] E.W. Washburn, Proc. Natl. Acad. Sci. U.S.A. 7 (1921) 115.
[42] ISO 15901-1, Pore Size Distribution and Porosity of Solid Materials by Mercury Porosimetry and Gas Adsorption. Part 2. Analysis of Macropores by Mercury Porosimetry.
[43] J.C. Groen, L.A.A. Peffer, J. Perez-Ramirez, Stud. Surf. Sci. Catal. 144 (2002) 91.
[44] L.M. Pismen, Doklady Akademii Nauk SSSR 211 (1973) 1398.
[45] A.V. Neimark, Colloid J. USSR 46 (1984) 639.
[46] Tsakiroglou, A.C. Payatakes, Adv. Colloid Interf. Sci. 75 (1998) 215.
[47] A.V. Neimark, Colloid J. USSR 47 (1985) 67.
[48] L. Moscou, S. Lub, Powder Technol. 29 (1981) 45.
[49] S. Rigby, in: F. Rodriguez-Reinoso, B. Mac Enaney, J. Rouquerol, K. Unger (Eds.), Characterization of Porous Solids VI. Studies in Surface Science and Catalysis, vol. 144, Elsevier, Amsterdam, 2002, p. 185.
[50] S.P. Rigby, I.O. Evbuoumwan, M.J. Watt-Smith, K. Edler, R.S. Fletcher, Part. Part. Syst. Charact. (2006) 82.
[51] C. Felipe, F. Rojas, I. Kornhauser, M. Thommes, G. Zgrablich, Adsorpt. Sci. Technol. 24 (2006) 623.
[52] H. Giesche, Part. Part. Syst. Charact. 23 (2006) 9.
[53] H. Giesche, Mater. Res. Soc. Symp. Proc. 431 (1996) p.151.
[54] (a) S. Lowell, J.E. Shields, J. Colloid Interf. Sci. 80 (1981) 192;
(b) S. Lowell, J.E. Shields, J. Colloid Interf. Sci. 83 (1981) 273.
[55] G. Salmas, G.J. Androutsopolous, J. Colloid Interf. Sci. 239 (2001) 178.
[56] M. Day, I.B. Parker, J. Bell, M. Thomas, R. Fltecher, J. Duffie, in: J. Rouquerol, F. Rodriguez-Reinoso, K.S.W. Sing, K.K. Unger (Eds.), Characterization of Porous Solids II, Amsterdam, 1991, p. 75.
[57] M. Day, I.B. Parker, J. Bell, R. Fletcher, J. Duffe, K.S.W. Sing, D. Nicholson, in: J. Rouquerol, F. Rodriguez-Reinoso, K.S.W. Sing, K.K. Unger (Eds.), Characterization of Porous Solids III. Studies in Surface Science and Catalysis, vol. 87, Elsevier, Amsterdam, 1994, p. 225.
[58] G. Zgrablich, S. Mendioroz, L. Daza, J. Pajares, V. Mayagotia, F. Rojas, W.C. Conner, Langmuir 7 (1991) 779.
[59] C. Felipe, S. Cordero, I. Kornhauser, G. Zgrablich, R. Lopez, F. Rojas, Part. Part. Syst. Charact. 48 (2006) 60.
[60] K.L. Murray, N.A. Seaton, M.A. Day, Langmuir 15 (1999) 8155.
[61] F. Porcheron, P.A. Monson, M. Thommes, Langmuir 20 (2004) 6482.
[62] F. Porcheron, P.A. Monson, Langmuir 21 (2005) 3179.
[63] F. Porcheron, M. Thommes, R. Ahmad, P.A. Monson, Langmuir 23 (2007) 3372.
[64] L.G. Aggerbrandt, O. Samuelson, J. Appl. Polym. Sci. 8 (1964) 2801.
[65] I. Halasz, K. Martin, Angew. Chem. Int. Ed. Engl. 17 (1978) 901.
[66] J.H. Knox, H.P. Scott, J. Chromatogr. 316 (1984) 311.
[67] A.A. Gorbunov, L.Ya. Solovyova, V.A. Pasechnik, J. Chromatogr. 488 (1988) 307.
[68] L. Hagel, M. Ostberg, T. Andersson, J. Chromatogr. A 743 (1996) 33.
[69] M. Goto, B.J. McCoy, Chem. Eng. Sci. 55 (2000) 723.
[70] M. Al-Bokari, D. Cherrak, G. Guiochon, J. Chromatogr. A 975 (2002) 275.
[71] Y. Yao, A.M. Lenhoff, J. Chromatogr. A 1037 (2004) 273.
[72] B.A. Grimes, C. du Fresne von Hohenesche, M. Quaglia, D. Lubda, K.K. Unger, Presented at the 10th International Symposium on Preparative and Industrial Chromatography and Allied Techniques (SPICA 2004), Aachen, October 17–20, 2004 (Lecture Session 1).
[73] L. Hagel, in: P.L. Dublin (Ed.), Aqueous Size-Exclusion Chromatography, Elsevier, Amsterdam, 1988, p. 119.
[74] H. Guan, G. Guiochon, J. Chromatogr. A 731 (1996) 27.
[75] H. Guan, G. Guiochon, D. Coffey, E. Davis, K. Gulakowski, D.W. Smith, J. Chromatogr. A 736 (1996) 21.
[76] H. Guan-Sajonz, G. Guiochon, E. Davis, K. Gulakowski, D. Smith, J. Chromatogr. A 773 (1997) 33.
[77] N. Ishizuka, H. Minakuchi, K. Nakanishi, N. Soga, H. Nagayama, K. Hosoya, N. Tanaka, Anal. Chem. 72 (2000) 1275.
[78] D. Lubda, W. Lindner, M. Quaglia, C. du Fresne von Hohenesche, K.K. Unger, J. Chromatogr. A 1083 (2005) 14.
[79] B.A. Grimes, R. Skudas, K.K. Unger, D. Lubda, J. Chromatogr. A 1144 (2007) 14.
[80] S. Kuga, in: P.L. Dublin (Ed.), Aqueous Size-Exclusion Chromatography, Elsevier, Amsterdam, 1988, p. 157.
[81] J. Hradil, D. Horak, Z. Pelzbauer, E. Votavova, F. Svec, J. Kalal, J. Chromatogr. 259 (1983) 269.
[82] T.P. Rao, R.S. Praveen, S. Daniel, Crit. Rev. Anal. Chem. 34 (2004) 177.
[83] M. Ousalem, X.X. Zhu, J. Hradil, J. Chromatogr. A 903 (2000) 13.
[84] E.P. Barrett, L.G. Joyner, P.P. Halenda, J. Am. Chem. Soc. 73 (1951) 373.
[85] J. Simon, S. Saffer, C.J. Kim, J. Microelectromech. Syst. 6 (1997) 2.
[86] K.K. Unger, Porous Silica, Elsevier, Amsterdam, 1979.

IV

Journal of Chromatography A, 1216 (2009) 2625–2636

Contents lists available at ScienceDirect

Journal of Chromatography A

journal homepage: www.elsevier.com/locate/chroma

Flow-through pore characteristics of monolithic silicas and their impact on column performance in high-performance liquid chromatography

R. Skudas[a], B.A. Grimes[b], M. Thommes[c], K.K. Unger[a,*]

[a] Institut für Anorganische Chemie und Analytische Chemie, Johannes Gutenberg University, Duesbergweg 10-14, D-55099 Mainz, Germany
[b] Norwegian University of Natural Science and Technology, Department of Chemical Engineering, Sem Sælandsvej 4, 7491 Trondheim, Norway
[c] Quantachrome Instruments, 1900 Corporate Drive, Boynton Beach, FL 33426, USA

ARTICLE INFO

Article history:
Available online 29 January 2009

Keywords:
Monolithic columns
Mercury porosimetry
Permeability
Flow-through pores
Porosity

ABSTRACT

In order to elucidate the role of the flow-through characteristics with regard to the column performance in high-performance liquid chromatography (HPLC) native and *n*-octadecyl bonded monolithic silica rods and columns, respectively of 100 mm length and 4.6 mm ID with mesopores in the range between 10 and 25 nm and macropores in the range between 0.7 and 6.0 μm were examined by mercury intrusion/extrusion, scanning electron microscopy, image analysis and permeability. The obtained data of the flow-through pore sizes and porosity values as well as surface-to-volume ratio of the stationary phase skeleton enabled to predict their influence to the chromatographic separation efficiency. Our data demonstrate that mercury porosimetry is a reliable technique to obtain all the characteristic parameters of the flow-through pores of silica monoliths. An important result of our examination was that the surface-to-volume ratio of monolithic silica skeletons had more significant impact to the separation process, rather than the average flow-through pore sizes. We could also show the essential differences between the particulate and monolithic stationary phases based on theoretical computation. The results, obtained from other characterization methods also indicated the structural complexity of monolithic silica samples. Permeability of columns is a generally applicable parameter to characterize all chromatographic phases no matter the chemistry or format. The correlation coefficient obtained for mercury intrusion and permeability of water was 0.998, though our investigation revealed that the surface modification is more likely influencing the obtained results. Further, the assumption of the cylindrical morphology of flow-through pores is not relevant to the investigated monolithic silica columns. These results on the morphology of the flow-through pores and of the skeletons were confirmed by the image analysis as well. Our main finding is that the flow-through pore sizes are not relevant for the estimation of the chromatographic separation efficiency of monolithic silica columns.

1. Introduction

The application of high-performance liquid chromatography (HPLC) has gained a substantial interest in solving daily analytical problems. Though this analytical technique is so randomly used, the knowledge about the complexity of this process is usually rather low. It is known that the performance of chromatographic separation depends on numerous stationary phase and analyte properties, and chosen separation conditions. Minor changes of any of these constituents bring a radical influence to the obtained results. Therefore, the optimization of chromatographic system constituents could lead to enhanced separation performance. One can distinguish five main key parameters of the chromatographic system that are influenced by several chromatographic system properties [1]: the flow velocity parameter, the axial dispersion coefficient, the mass transfer coefficient, the adsorption capacity and the effective diffusion coefficient.

The mobile phase could be optimized by changing its composition and the separation temperature. The analyte properties are case dependent and usually are less influenced, while the stationary phase properties could be enhanced for the optimum performance of the chromatographic system. The chromatographic column is usually characterized by the packing/adsorbent properties such as the internal porosity, pore size, surface area, base material, surface chemistry and the column properties such as the external porosity, length and diameter, and flow resistance. The internal porosity, pore size and surface chemistry influence the adsorption capacity and the effective diffusion coefficient of the chromatographic system, while external porosity and flow resistance influence the flow velocity parameter, the axial dispersion coefficient and the mass

* Corresponding author. Tel.: +49 6151 152630; fax: +49 6151 152631.
E-mail address: k.k.unger@web.de (K.K. Unger).

0021-9673/$ – see front matter © 2009 Elsevier B.V. All rights reserved.
doi:10.1016/j.chroma.2009.01.079

transfer coefficient. The investigation of these column properties has a high potential, but could be hardly performed on the particulate supports. They are, in this case, limiting, since the external porosity and flow resistance are influenced by the particle size and the voids between the particles of the packing. When the external porosity of the packed bed is increased, it causes a proportional increase of defects in its packing leading to an unstable bed and reduced column efficiency [2]. The monolithic supports, in this case, enable the optimization of external porosity and the flow resistance through the control of the flow-through pore size, its distribution, the external porosity and surface-to-volume ratio of the monolithic skeleton.

Two different types of monolithic supports, polymer-based monoliths and silica-based monoliths were developed and introduced into HPLC as a promising alternative to particle packed columns for fast and efficient separations [3,4].

In the case of silica monoliths this was achieved through the independent control of the flow-through pores, which are formed by the polymer template during the synthesis. Contrary to the particulate supports, where the mobile phase flow is taking place through the spaces between the particles of the packed bed, the mobile phase flow in the monolithic support is taking place through the spaces between the skeleton of the stationary phase, namely through the flow-through pores.

Although the key role of the flow-through pore size was already recognized [3,4]; however, a detailed analysis on the influence on the flow-through pore characteristics on the chromatographic separation was not performed.

Viewing the literature, one can recognize diverging results on how the pore structural properties of monolithic silicas influence the column performance. Gzil et al. [5] stated that the optimization of the separation process on the monolithic supports with respect to column performance will require the diminution of the domain sizes while preserving the same relative degree of heterogeneity or if the same domain sizes are preserved, to improve the structural homogeneity. Though the attempt to reduce the domain size will eventually reach a lower limit band of kinetic performances, that can no longer be suppressed significantly by further decreasing the domain sizes [6]. Liapis et al. [7] suggested that the optimum monolithic column performance would be obtained having relatively large flow-through pores with a high-pore connectivity and small sized skeletons. Later Guiochon [4] stated that the efficiency of monoliths is controlled by the domain size and that the random fluctuations of the flow-through pore size might explain largely the relatively poor level of performance of current monolithic columns as compared to their potentiality. The optimization of the structural homogeneity of the monoliths would certainly enhance their column performance.

In order to prove these statements it is mandatory to apply characterization methods to monolithic silicas, which are reliable and will provide solid data.

There are several characterization methods that could be used to distinguish the external porosity and flow resistance of the monolithic supports. Mercury porosimetry enables to determine the average pore diameter in the range between 40 μm and 4 nm, the porosity of these pores and their specific surface area. Furthermore, the technique can provide useful information with respect to the pore shape, network effects and the skeleton and bulk density [8–12].

Additional characterization of the flow-through pore network of the monolithic supports could be performed with microscopy and image analysis [13]. Microscopy is a valuable tool for the investigation of the flow-through pore diameter and the skeleton diameter of monolithic silicas [14,15]. One can obtain the distribution of those characteristic parameters, but these values would then be more dependent on the chosen image analysis method rather then representing the actual values [16,17].

Recent development of three-dimensional (3D) images of the structure from the magnetic resonance imaging [18,19] and microscopic images enables one to transfer these data to the computer simulation platform [20,21]. Such approaches enable to choose routes to improve the performance of monolithic structures using the computational estimation of the plate height data [5], domain size-induced heterogeneity effects [6,15] optimal external porosity effects [22] and a correlation of the column pressure drop [23].

Other characterization methods have been applied to a lesser extent although they bear a high potential of information. For example, the flow resistance of monolithic silica columns is known to dependant on the surface-to-volume ratio of the monolith. Therefore, data from permeability measurements of a liquid could be directly applied for the calculation of the monolithic surface when the volume is known. Pioneering work in this field has been done by Washburn [24], who studied the dynamic invasion of a fluid into capillaries and by Carman [25], who used the concept of hydraulic radius to define equilibrium positions of fluid–fluid interfaces in tubes of different cross-section. The flow of a liquid through a porous material was described by the Hagen–Poiseuille and by Kozeny–Carman [26] equations. The Hagen–Poiseuille approach was based on the assumption of cylindrical pores whereas the Kozeny–Carman approach assumed pores as voids between closely packed spheres of equal size.

Various papers were published dealing with potential of the Kozeny–Carman approach in characterization of silica-based monolithic supports. The most fundamental work was done by Minakuchi [14], Leinweber [27,28], and Vervoort [15,23] resulting in various interpretations of the flow resistance values. The same relative particle diameters were obtained, but certain individual approximations were done for the calculation of the flow-through pore sizes. A notable progress was made by introducing the term of domain size being the sum of the skeleton diameter and the diameter of the flow-through pore [22]. Though this assumption was not reflecting the real silica-based monolithic support, it enabled to use the liquid permeability data to characterize the monolith regardless its format and chemistry.

Though many different characterization methods were widely used, the comparison between the data and their validity, however, is still lacking and the influence of each of these parameters on column performance is under discussion. The limits of the method application are even narrowed by the irrelevant comparison and interpretation of the measured data. Therefore, a comprehensive investigation on the validity, reliability and comparison of these characteristic parameters would help to choose the right characterization method and to thoroughly discuss their influence on the column performance.

In this work we will apply the named methods for the characterization of flow-through pores of monolithic silicas with respect to the validity of the obtained data, its comparison between the different methods and its influence on column performance in HPLC.

The objective of this study was to search for the optimum method with respect to the data reliability and assessment of the average flow-through pore size data, interstitial porosity and the surface-to-volume ratio of the skeleton of the monolithic support of the monolithic silica research columns.

2. Experimental

2.1. Monolithic materials and columns

Measurements were performed on a set of monolithic silica columns (length and ID of 100 mm × 4.6 mm), provided as research

Table 1
Survey on investigated research monolithic silica columns and their properties.

Monolithic silica research sample	Surface functionality (native, *n*-octadecyl bonded and endcapped)	Flow-through pore diameter in μm (mercury intrusion)	Mesopore diameter in nm (mercury intrusion)
787	C18e	1.93	10.1
800	C18e	1.86	24.1
803	C18e	3.52	10.2
811	C18e	3.62	23.5
842	C18e	5.74	9.5
843	C18e	6.13	23.9
KN 253	C18e	1.44	11.9
KN 341	C18e	0.96	11.6
KN 255	C18e	1.77	11.0
KN 349	C18e	0.73	12.2
KN 345	C18e	2.52	10.0
KN 344	C18e	1.01	11.1
KN 252	C18e	1.58	11.7
Tr2783/1	Native	1.81	10.9
Tr2783/2	Native	1.76	25.1
Tr2786/1	Native	3.52	10.9
Tr2786/2	Native	3.40	24.0
TG36/1	Native	5.74	10.1
TG36/2	Native	5.64	24.4

samples by Merck (Darmstadt, Germany). The (inter-skeleton) flow-through pore diameters of the silica monoliths were in the range from 0.7 to 6.0 μm and the (intra-skeleton) pore diameters were from 10 to 25 nm. In this study we focused on selected monolithic silica samples with bonded *n*-octadecyl groups and endcapped. Six native monolithic silica columns (L = 100 mm, ID = 4.6 mm) were also included (see Table 1). In order to obtain columns that could be used in HPLC, the monolithic silica rods were gladded with polyether ether ketone (PEEK) by a proprietary process of Merck.

The manufacturing process of monolithic silica samples generating two continuous pore systems, adjusting and controlling the pore size, and porosity of flow-through pores and mesopores independently is discussed in numerous references [29–43].

2.2. Characterization methods

2.2.1. Mercury porosimetry

Mercury intrusion and extrusion experiments on the silica monolithic samples were performed over a wide range for pressures starting in vacuum up to 60,000 psi (1 psi = 6.895 × 10^{-3} MPa) by a Poremaster 60 instrument (Quantachrome Instruments, Boyton Beach, FL, USA). Data acquisition was performed in *Autospeed* continuous scanning mode enabling maximum speed in the absence of intrusion or extrusion and maximum resolution and sufficient equilibration time (sampling time) when most required, that was, when intrusion or extrusion was occurring rapidly with changing pressure. Such method prevented mistakes that could have been made of volume penetration readings taken before equilibrium had been reached [10].

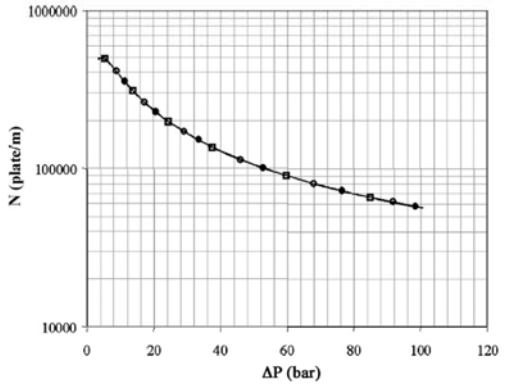

Fig. 1. The plate number of monolithic silica columns as a function of column back-pressure for different flow-through pore diameters. The analyte radius (r) was 0.50 nm; K_{eq}, 10; ε_t, 0.800; ε_b, 0.500; ε_p, 0.600; $P_{d,mes}$, 10 nm were kept constant. D_f was changed in the range from 1 to 10 μm: (○) 1 μm, (●) 4 μm, (■) 10 μm.

In order to obtain the pore volume distribution curve from the mercury porosimetry curve the Washburn equation was applied on the intrusion curve:

$$\Delta P_s = \frac{(2\gamma \cos \theta)}{r_{pore}} \quad (1)$$

where ΔP_s is a pressure difference across the element of surface area, γ the interfacial (or surface) tension of mercury, θ the contact angle between mercury and the solid (pore wall) and r_{pore} is the radius of the pore [44].

Mercury surface tension value of 480 dynes/cm was taken from the ISO standard [45]. The reference contact angle of 140° between the mercury and surface of the monolithic silica sample was taken from the ISO standard [45] and article by Groen et al. [46].

2.2.2. Scanning electron microscopy

For the scanning electron microscopy we employed a JSM-6300F instrument from JEOL (Tokyo, Japan). For the samples preparation, we deposited a piece of silica monolith onto the Au/Pd (80:20, w/w) target. The silica monoliths were sputtered with a 5 nm thick gold layer under vacuum to improve conductivity, using a SCD 040 instrument from Balzers.

The average flow-through pore diameter and skeleton diameter were obtained from images using two methods: direct scale measurement and the "Pixcavator" program. The direct measurement was performed via segmenting each image into relative areas and measuring the characteristic parameters via given scale. The average values were withdrawn from all measured values. The values estimated by the "Pixcavator" program were based on the area estimation via integrating the number of pixels in that area. The area was defined by the colour. Since the flow-through pores were in most cases black, the estimation of all the pixels in the area was performed by calculation the number of them and multiplying by the area of one pixel. The obtained relative area of a single flow-through pore was then assumed to be equal to the area of circle (meaning a round shaped pore) and the diameter of this circle was taken as the

diameter of the flow-through pore. Contrary to the flow-through pores the skeleton diameter was not obtained via "Pixcavator" program, due to a fact, that analyzed SEM images had various contrast colours of skeletons and the margins could not be clearly indicated.

2.2.3. Permeability

The permeability measurements were done at room temperature (22 °C), using pure water (for liquid chromatography, Merck) or methanol (for liquid chromatography, Merck) as the permeating fluid and using flow rates ranging from 0.1 to 2.0 ml/min. All experiments were done with a Bischoff liquid chromatographic system HPLC compact pump 2250. Since the pressure drop value on the read-out display of the pump contains system pressure in addition to column pressure, each reported pressure drop value is obtained by subtracting the pressure drop of the empty column from the measured value of the packed column. The permeability was calculated from the slope of the plot of the pressure drop versus the linear velocity of the liquid (eluent).

3. Results and discussion

3.1. Influence of the flow-through pore characteristics on the column efficiency in HPLC

In a previous paper [47] we have developed an equation which links the plate height of monolithic columns with the common mass transfer kinetics of an analyte and the properties of the monolithic supports:

$$H = \frac{K_b D_L}{2u} + \left[2L\left(\frac{K_b D_L}{uL}\right)^2 \left(e^{(-uL)/(K_b D_L)} - 1\right)\right] + \left[\frac{\varepsilon_b(1-\varepsilon_b)(\varepsilon_p K_p + K_{eq})^2}{[\varepsilon_b K_b + (1-\varepsilon_b)(\varepsilon_p K_p + K_{eq})]^2}\frac{R_p}{k_f}\right] u + \left[\frac{\varepsilon_b(1-\varepsilon_b)(\varepsilon_p K_p + K_{eq})^2}{4[\varepsilon_b K_b + (1-\varepsilon_b)(\varepsilon_p K_p + K_{eq})]^2}\frac{R_p^2}{\varepsilon_p K_p D_p}\right] u \quad (2)$$

where H stands for the height equivalent of a theoretical plate (HETP), or plate height, u is the linear flow velocity of the eluent, R_p denotes the radius of the skeletons, ε_b is the void fraction of the macroporous void space in the column, the K_b represents the volume partition coefficient of the finite sized molecule in the flow-through porous void space of the monolithic column, ε_p is the void fraction of the monolithic skeleton, K_p represents the volume partition coefficient of the finite sized molecule in the mesoporous void space of the skeleton, D_p denotes the effective diffusion coefficient of the analyte in the confined mesoporous space of the skeleton, K_{eq} represents the equilibrium adsorption constant of the linear adsorption isotherm, k_f denotes the film mass transfer coefficient of the analyte, D_L represents the axial dispersion coefficient of the solute in the mobile phase, and L is the length of the column.

The column flow resistance or back-pressure, ΔP, according the Ergun equation [48] and assuming no turbulent flow, depends on the surface-to-volume ratio of the skeletons of monolithic supports as

$$\Delta P = L\left[4167u\mu\left(\frac{s}{v}\right)^2\frac{(1-\varepsilon_b)^2}{\varepsilon_b^3}\right] \quad (3)$$

where μ stands for the mobile phase viscosity.

When measuring the column efficiency, the surface-to-volume ratio of the skeletons of the monolithic support should be taken into account whereas the flow-through pore diameter of these supports is not decisive [49]. This partly explains the confusing previous results on the comparison of particulate stationary phase with the monolithic ones. Studies showed that a relative average particle size

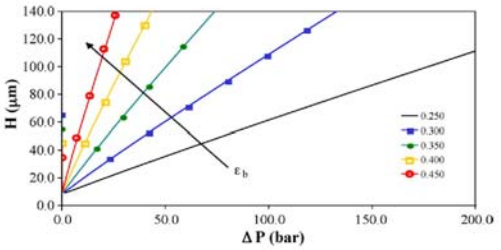

Fig. 2. The dependency of the theoretical plate height on the column back-pressure drop for different external porosity values. The external porosity (ε_b) values were: (—) 0.250, (■) 0.300, (♦) 0.350, (□) 0.400, (○) 0.450.

was found if one compared the efficiency values obtained by the particulate and monolithic stationary phases, and different relative average particle size values if one compared the permeability of the particulate and monolithic stationary phases [27,28]. The flow resistance, in this case, is only dependent on the surface-to-volume ratio of the skeletons or the particles. Therefore much higher relative average particle sizes correspond to the monolithic stationary phase skeletons. The column efficiency is more influenced by the void fraction of the interstitial pores (ε_b), the volume partition coefficient of the molecule in the interstitial pore (K_b) and film mass transfer coefficient (k_f) rather than just by the average flow-through pore size (D_f). The combined influence of named parameters lead to much lower comparable relative average particle sizes of the particulate stationary phases. Therefore, monolithic supports have unique features of efficient but low-flow resistant stationary phases that particulate stationary phases do not implement.

The same counts for the axial dispersion coefficient that is equal to the idealized diameter of the monolithic skeleton element D_0. If a cylindrical geometry of the skeletons is assumed, then D_0 depends on the surface-to-volume ratio as $s/v = 4/D_0$. The parameter D_0 should not be considered as the skeleton diameter per se, but the characteristic diameter of a cylinder that provides the same surface-to-volume ratio as the real material, then equation given above adequately represents the plate height in monoliths. The parameter D_0 can be obtained from the back-pressure versus flow curves using the linear term of the Ergun equation.

Fig. 1 shows the calculated dependency (Eqs. (2) and (3)) of the column back-pressure on the number of the theoretical plates for an unretained solute of 0.5 nm molecular radius. The graph indicates no significant changes in plate count numbers when the flow-through pore diameter D_f is varied at constant s/v and ε_b. The lines represent results from modelling where the curves of various flow-through pore diameters do not scatter. This indicates, that the column efficiency is scarcely dependent on the flow-through pore diameter when the surface-to-volume ratio of the skeletons and external porosity are fixed.

Fig. 2 displays the plate height value dependency of the column pressure drop for different values of external porosity. Increasing the external porosity from 0.25 to 0.45 not only decreases the column pressure drop, but also decreases the plate height values achieved at the same higher column pressure drop values. The mass transfer resistance for small molecular mass samples is noticed to increase with enhanced flow-through porosity at the same column resistance.

The flow resistance of monolithic supports is influenced by the external monolithic structure parameters as well. The comparison of the monolith skeleton diameter and external porosity on the back-pressure ratio between 3 μm packed bed and monolith is shown in Fig. 3. Decreasing the skeleton diameter increases the back-pressure, while increasing the flow-through pore void fraction

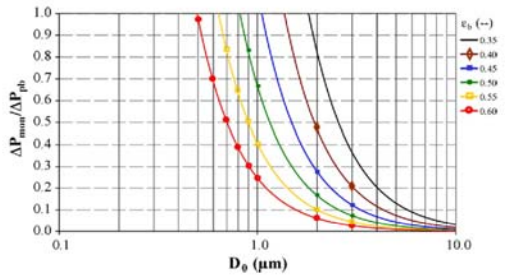

Fig. 3. Pressure drop ratio between monoliths and packed beds (3 μm) comparison with the skeleton diameter (D_θ) at different external porosity values. The external porosity (ε_b) values were: (—) 0.350, (ε) 0.400, (■) 0.450, (●) 0.500, (□) 0.550, (○) 0.600.

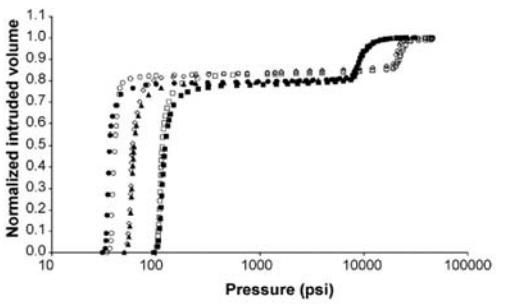

Fig. 4. Mercury intrusion curves for the six monolithic silica rods with grafted *n*-octadecyl chains: (□) "787" monolithic silica rod grafted with *n*-octadecyl chains, (■) "800" monolithic silica rod grafted with *n*-octadecyl chains, (ε) "803" monolithic silica rod grafted with *n*-octadecyl chains, (▲) "811" monolithic silica rod grafted with *n*-octadecyl chains, (○) "842" monolithic silica rod grafted with *n*-octadecyl chains, (●) "843" monolithic silica rod grafted with *n*-octadecyl chains.

allows one to have smaller skeleton sizes at the same back-pressure values. However, when higher column permeability as compared to 3 μm packed beds is required, the skeleton size should be between 1 and 2 μm.

The discussed theoretical approach names four column parameters, that are important for the efficiency of monolithic columns: the surface area-to-volume ratio of the monolithic skeleton, the external porosity, the skeleton size and the flow-through pore size. If these parameters are measured, the prediction of the optimum performance could be done.

3.2. Monolith characterization via mercury porosimetry

The mercury intrusion curves (Fig. 4) indicate, that the pore structure of the investigated monolithic silica is bimodal, having pores located in the silica skeleton (mesopores) and flow-through pores. The plateau region at pressures of 1000 psi in the mercury intrusion curves clearly separates the two pore size regimes and allows one to calculate the corresponding surface area and porosity values of the flow-through pores (see Table 2).

Since the surface of major tested monolithic samples was modified with *n*-octadecyl chains, mercury intrusion method was used to investigate some native silica monolithic rods that later were grafted with *n*-octadecyl chains and characterized again.

Small differences in pore size distribution curves can be seen between the native and *n*-octadecyl grafted monolithic silica rods as displayed in Fig. 5. Contrary to what one would expect, the average pore diameter values are smaller for the non-grafted monoliths, namely 5.64 μm for TG36/2 monolithic sample and 1.76 μm for Tr2783/2 monolithic sample. This might be due to the underes-

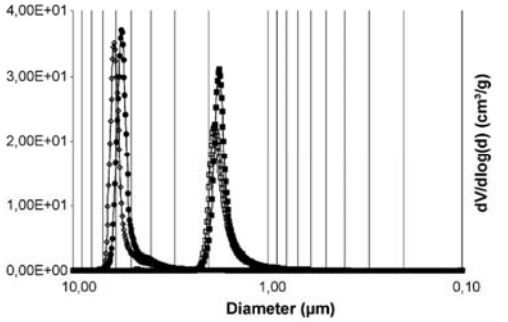

Fig. 5. Differential flow-through pore diameter distribution curves of selected monolithic silica rods: (○) "843" monolithic silica rod grafted with *n*-octadecyl chains, (●) "TG36/2" native monolithic silica rod, (□) "800" monolithic silica rod grafted with *n*-octadecyl chains, (■) "Tr2783/2" native monolithic silica rod.

timation of the mercury contact angle in the evaluation of the pore size distribution of the *n*-octadecyl grafted monolithic silica rods due to a hydrophobic surface. The slight decrease in the porosity values of the flow-through pores was recognized, while the pore size distribution stayed the same.

The estimation of the specific skeleton surface area and specific flow-through pore volume was performed from the cumula-

Table 2
Flow-through pore characteristics of the research silica monoliths assessed by mercury intrusion.

Monolithic silica research sample	Flow-through pore diameter (μm)	Specific flow-through pore volume (cm^3/g)	Surface/volume of the skeletons (Mm^{-1})	Skeleton diameter* (μm)
787	1.93	1.96	1.638	2.44
800	1.86	2.23	1.946	2.06
803	3.51	2.16	1.247	3.21
811	3.62	2.27	0.999	4.01
842	5.74	1.85	0.673	5.94
843	6.13	1.76	0.772	5.18
KN 253	1.44	2.32	3.922	1.02
KN 341	0.96	2.31	4.819	0.83
KN 255	1.77	2.08	3.200	1.25
KN 349	0.71	1.85	7.018	0.57
KN 345	2.52	2.02	1.951	2.05
KN 344	1.04	1.73	3.883	1.03
KN 252	1.58	2.35	3.604	1.11

The skeleton diameter* was calculated assuming a cylindrical pore morphology, then $s/v = 4/D_\theta$.

V

Table 3
Flow-through pore characteristics of silica monoliths distinguished via image analysis.

Monolithic silica sample	Direct image analysis			"Pixcavator"
	Flow-through pore diameter, D_f (μm)	Monolithic skeleton diameter, D_s (μm)	Surface/volume of the skeletons* (Mm^{-1})	Flow-through pore diameter, D_f (μm)
787	2.26	1.81	2.210	1.89
800	2.04	1.56	2.564	1.78
803	3.66	2.47	1.619	3.28
811	3.78	3.19	1.254	3.77
842	5.41	4.66	0.858	5.56
843	5.87	3.96	1.010	6.13
KN 253	1.44	0.75	5.333	1.39
KN 341	1.16	0.66	6.061	0.96
KN 255	1.59	0.87	4.598	1.82
KN 349	0.69	0.43	9.302	0.67
KN 345	2.02	1.48	2.703	2.67
KN 344	1.27	0.78	5.128	1.05
KN 252	1.54	0.86	4.651	1.67

The surface/volume ratio of the skeletons* was calculated assuming a cylindrical pore morphology then $s/v = 4/D_s$.

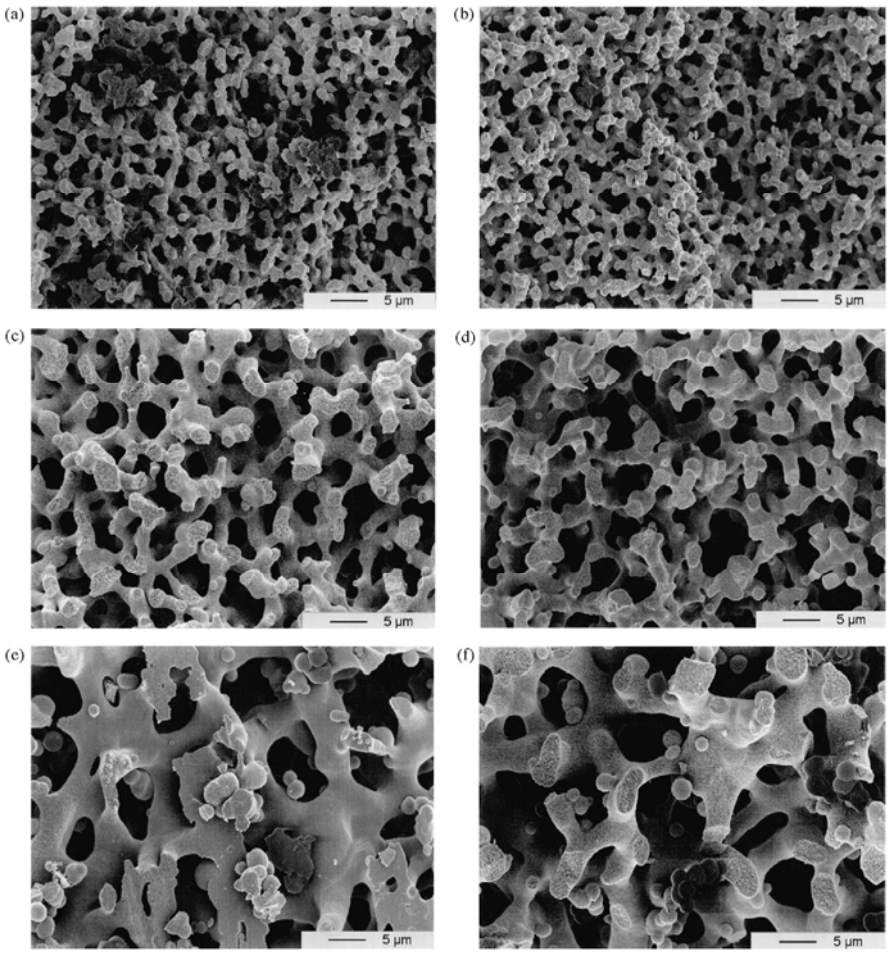

Fig. 6. The electron scanning micrographs of monolithic research silica samples: (a) 787, (b) 800, (c) 803, (d) 811, (e) 842, (f) 843.

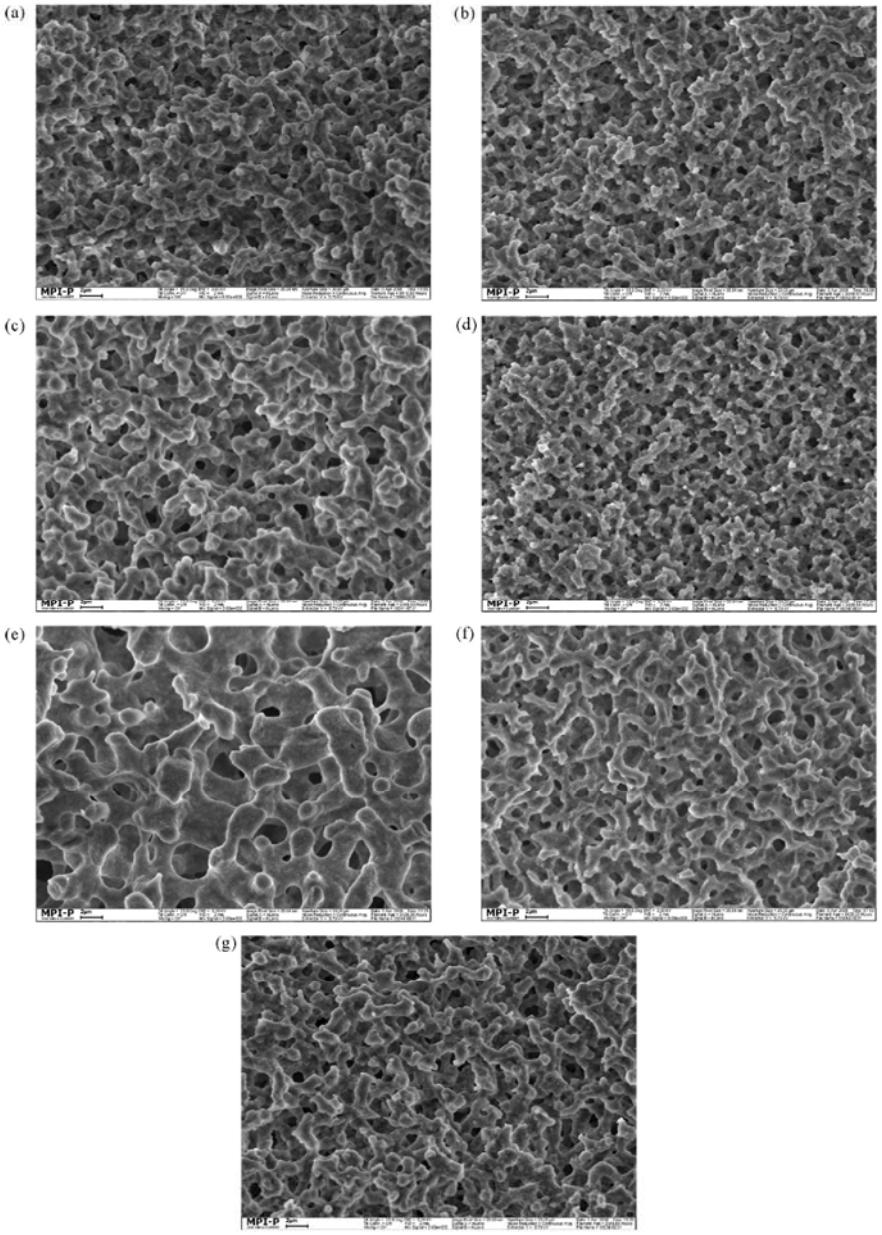

Fig. 7. The electron scanning micrographs of monolithic research silica samples: (a) KN 253, (b) KN 341, (c) KN 255, (d) KN 349, (e) KN 345, (f) KN 344, (g) KN 252.

tive pore volume curves (see Table 2). The cumulative surface area plots clearly revealed that the specific surface area of the flow-through pores is below 20 m^2/g. Hence, the mesopores (pores in the skeleton) contribute mainly to the relative high-specific surface area (>100 m^2/g) of the monoliths. Knowing the porosity values of the monoliths, it was possible to calculate the measured specific flow-through pore volume values to the specific skeleton volume values, that enabled the calculation of surface-to-volume ratios of monolithic silica samples (see Table 2).

Due to relative insensitivity of mercury porosimetry to pore network morphology when the porosity, and hence the accessibility, is high [50], we were able to obtain the flow-through pore diameter, the specific flow-through pore volume and the surface/volume ratios of the monolithic skeletons of the tested samples. The skeleton diameter was then calculated assuming that it is cylindrical.

3.3. Monolith characterization via scanning electron microscopy

Images obtained via scanning electron microscopy (SEM) technique were used for the assessment of the flow-through pore diameters and the skeleton diameters (see Figs. 6a–f and 7a–g).

Direct analysis and the "Pixcavator" program were employed for the estimation of the skeleton diameter and the flow-through pore diameter. It should be emphasized, that the "Pixcavator" program was inapplicable to the estimation of the average skeleton sizes, due to the changes in the contrast of used images (see Section 2). The obtained results are displayed in Table 3 where the actual skeleton diameter is expressed as the D_s (skeleton diameter per se).

When one compares the data obtained from the mercury intrusion (Table 2) and image analysis (Table 3), the agreement between the flow-through pore diameter values is rather good, especially the values obtained from the "Pixcavator" program and the mercury intrusion curves. If one sees the values from mercury intrusion as 100%, then the average flow-through pore diameter value obtained via "Pixcavator" method was in the range of $94\% < x < 107\%$, with the summed up difference between the used methods smaller then 0.5%. The values from the direct investigation showed a wider spread. According to good average flow-through diameter value correlation between the image analysis and mercury intrusion, the s/v ratio values were compared as well. The s/v ratios of different monolithic samples are directly obtained from the mercury intrusion method (Table 2). The s/v ratios from the image analysis were calculated from D_s, skeleton diameter per se, values. To obtain good correlation between the results of used characterization methods we obtained that $s/v = 3/D_s$ instead of $s/v = 4/D_0$. As mentioned before, the parameter D_0 is not considered as the skeleton diameter per se, while D_s is. Therefore, the s/v ratios in real system are also different as compared to the ideal case of cylinders. This is noticed in the images as well, where one sees not only cylindrical skeletons, but also various forms where these skeletons connect. This causes a wide distribution of skeleton diameter values as well. Therefore, the external surface area of this monolithic structure would be smaller when compared to the particulate or cylindrical stationary phase morphology when the volume and the average structural diameters are equal, since the s/v ratio for the investigated silica monolith structure was $s/v = 3/D_s$, for the cylindrical structure $s/v = 4/D_c$ and for the particulate structure $s/v = 6/D_p$.

The 3D structure of the tested samples could be reconstructed from the two-dimensional digital images, which need to be binarized and then stacked together to get a quantitative 3D structure [51]. Unfortunately, the obtained images lack in resolution and quantity for such investigation. This work is still ongoing and therefore, for this study, we limited our studies to the estimation of the flow-through pore diameter and monolithic skeleton diameter.

The direct results, obtained via imaging and image analysis were in good agreement with results from mercury intrusion, suggesting minor differences between the data from both methods.

3.4. Monolith characterization via liquid permeability measurements

When the plot of the pressure drop versus the linear velocity of the fluid show a linear relationship, Darcy's law for laminar flow-through porous media is applicable for the calculation of the permeability B [52]:

$$B^0 = \mu L \frac{Q}{A\Delta P} \tag{4}$$

where Q is the flow-rate and A is the cross-sectional area of the conduit normal to the direction of flow.

The Kozeny–Carman equation is then employed for the calculation of the effective diameter of the equivalent pores in the porous bed from the permeability and porosity data [52]:

$$D_f = 2\left(\frac{5B^0}{\varepsilon_b}\right)^{1/2} \tag{5}$$

where D_f is the mean flow-through pore diameter.

An equivalent sphere diameter of the porous bed from permeation of liquid could also be obtained through the Ergun equation [48]:

$$f_p = \frac{150}{Re_p} + 1.75 \tag{6}$$

where the friction factor f_p for the packed bed is defined as follows:

$$f_p = \frac{\Delta P}{L}\frac{D_p}{\rho V_s^2}\left(\frac{{\varepsilon_b}^3}{1-\varepsilon_b}\right) \tag{7}$$

The various symbols appearing in the above equations can be defined as follows, that D_p is the equivalent spherical diameter of the particle, V_s is the superficial viscosity (which is equal to Q/A where Q is the volumetric flow rate of the fluid).

Eqs. (6) and (7) could be simplified to obtain the flow-through pore diameter of the porous bed from the permeation of liquid while relating the hydraulic diameter of a monolithic bed to the diameter of an equivalent sphere [14,23,27,53]. The Reynolds number in packed beds and monolithic columns is in the order of 0.01 or lower. Therefore it is insignificant to the whole permeability. The simplified permeability equation, where D_{perm} is the equivalent particle diameter for monoliths, could be expressed as

$$\frac{V_s}{D_{perm}^2} = -\frac{\varepsilon_b^3}{180\mu(1-\varepsilon_b)^2}\frac{\Delta P}{L} \tag{8}$$

The Kozeny constant could be changed from 150 to 180, since it is related to the average diameter of the flow-through pores, their size distribution, their tortuosity and constriction [4].

The application of Eq. (8) leads to the value of an equivalent sphere diameter. The link between the relative particle diameter and the flow-through pore diameter could be expressed by [14]

$$D_{perm} = \frac{3}{2}D_f \tag{9}$$

or as [54]:

$$D_{perm} = 3\frac{(1-\varepsilon_b)}{\varepsilon_b}D_f \tag{10}$$

The calculation of the skeleton diameter D_s based on the diameter of the permeability pores was proposed by Vervoort et al. [15]:

$$\frac{D_f}{D_s} = \sqrt{\frac{32}{55}}\left(\frac{1}{1-\varepsilon_b}\right)^{1.55} \tag{11}$$

A direct approach of using the Kozeny–Carman equation to characterize the monolithic porous bed might be incorrect since it is based on the empirical data that were required for random-close packings of nearly spherical particles, having a narrow particle size distribution and an interstitial porosity of about 0.4 [28]. Therefore the average flow-through pore sizes displayed in Table 3 were obtained using two different approaches: Eqs. (4) and (5) [52] and Eq. (8) [14]. The fact that the investigated silica monoliths were composed of flow-through pores with different pore sizes, as seen

Table 4
Flow-through pore characteristics of silica monoliths assessed by the permeability of a liquid.

Monolithic silica sample	Gusev				Minakuchi				Skudas			
	Average flow-through pore diameter, D_f (μm)		Average skeleton diameter, D_s (μm)		Equivalent particle diameter, D_{perm} (μm)		Average flow-through pore diameter, D_f (μm)		Average flow-through pore diameter, D_f (μm)		Average skeleton diameter, D_s (μm)	
787	1.931	2.409*	1.682	2.098*	8.352	10.51*	5.563	7.013*	1.934	2.436*	1.685	2.123*
800	1.879	2.381*	1.571	1.991*	7.161	8.99*	4.771	5.990*	1.871	2.363*	1.569	1.990*
803	3.490	3.383*	2.445	2.362*	8.475	8.36*	5.652	5.571*	3.524	3.475*	2.466	2.433*
811	3.821	4.410*	3.192	3.690*	14.771	16.84*	9.851	11.234*	3.874	4.411*	3.243	3.692*
842	6.051	5.823*	4.832	4.633*	20.484	19.96*	13.662	13.302*	6.133	5.974*	4.891	4.761*
843	6.542	6.124*	5.136	4.814*	20.542	19.48*	13.691	12,993*	6.424	6.093*	5.043	4.783*
KN 253	1.183	1.201*	0.687	0.696*	1.908	1.94*	1.272	1.290*	1.181	1.201*	0.687	0.696*
KN 341	0.959	0.958*	0.603	0.602*	1.817	1.81*	1.211	1.209*	0.959	0.957*	0.603	0.601*
KN 255	1.568	1.640*	0.934	0.977*	2.673	2.77*	1.782	1.849*	1.574	1.635*	0.938	0.974*
KN 349	0.661	0.664*	0.468	0.471*	1.642	1.64*	1.095	1.092*	0.666	0.665*	0.471	0.474*
KN 345	2.549	2.755*	1.722	1.861*	5.518	6,03*	3.679	4.021*	2.488	2.719*	1.681	1.837*
KN 344	0.917	0.936*	0.664	0.678*	2.398	2.43*	1.599	1.623*	0.921	0.934*	0.666	0.676*
KN 252	1.338	1.365*	0.795	0.811*	2.249	2.32*	1.499	1.545*	1.333	1.374*	0.791	0.816*

Values with '*' were obtained using methanol as a solvent.

by the results of the microscopy and mercury intrusion analysis, and considering that the flow rate through the larger pores could be more than proportionally larger than the flow-through the smaller pores (flow rate ~ (pore diameter)^4), it was expected that the observed flow resistance in this case will be smaller than the flow resistance calculated on the basis of the average pore size [28]. The displayed flow-through pore diameter values were calculated from the total flow resistance or pressure drop, and a slight shift by approx. 5% towards the larger pore sizes was noticed due to the effect of pore size distribution.

The link between the relative flow-through pore diameter and relative skeleton diameter was distinguished in each case according to Eq. (11). The best value correlation with the obtained mercury intrusion and image analysis results (Table 4) was found by the flow-through pore size estimation according to Gusev et al. [52] and Skudas et al. [54] with 3% higher average values when compared to the mercury intrusion, and with 5% higher average values when compared to image analysis ("Pixcavator" analysis). Note, that water was used as a permeable fluid. The estimation of the monolithic skeleton diameter was more case dependent with a total error of approx. 3% for both methods as compared to the image analysis.

A certain disagreement was found between the results and the modifications when the back-pressure was measured using various solvents. The displayed results showed relatively larger values obtained for certain columns when methanol was used as a permeating fluid as compared to water. This might be explained by the fact, that using methanol for assessment of the permeability on a reversed-phase column might be influenced by the orientation of the surface functional groups and their hydrophobicity. In methanol, the flow resistance should be smaller, and the average calculated flow-through pore diameters should be enhanced, since a hydrophobic surface does not hinder the flow of the hydrophobic mobile phase. Though, when water is used as a permeating fluid, the hydrophobic surface of the adsorbent hinders the diffusion of liquid towards the surface and relatively smaller flow-through pore diameters are obtained. It is highly possible that differences in the solvent viscosity might play a role in this estimation, since methanol is less viscous and consequently a larger measurement error is obtained. The Pearson correlation coefficient r_p, was calculated for the flow-through pore size values obtained via mercury intrusion, image analysis and permeability of a liquid (see Table 5). The best correlation coefficient values were obtained for mercury intrusion and image analysis using the "Pixcavator" program, $r_p = 0.998$; mercury intrusion and permeability of water using Gusev's model [52] gave $r_p = 0.998$ and the Skudas model [54], $r_p = 0.998$.

In conclusion all named methods could be used to distinguish reliable flow-through pore size for the monolithic research silica columns. Therefore, the pore characteristic values of the permeability using water will be used for further discussion, since they correlate better with the mercury intrusion and image analysis data.

When comparing the calculated flow-through pore values by Gusev and Skudas approaches, and mercury intrusion, one notices slight differences (Fig. 8). This might be due to the fact, that not all the pores were permeable at the same extent. The larger pores

Table 5
Pearson correlation coefficient (r_p), calculated for the flow-through pore diameters obtained by mercury intrusion, image analysis and permeability of a liquid methods for monolithic research silica columns.

Used characterization methods	Mercury intrusion	Image analysis		Permeability of a liquid					
		Direct analysis	"Pixcavator"	Gusev (H_2O)	Gusev (CH_3OH)	Minakuchi (H_2O)	Minakuchi (CH_3OH)	Skudas (H_2O)	Skudas (CH_3OH)
Mercury intrusion		*0.991*	*0.998*	*0.998*	0.985	0.958	0.918	*0.998*	0.986
Image analysis									
Direct analysis	*0.991*		0.986	*0.991*	0.985	0.971	0.939	*0.992*	0.987
"Pixcavator"	*0.998*	0.986		*0.997*	0.987	0.957	0.919	*0.996*	0.986
Permeability of a liquid									
Gusev (H_2O)	*0.998*	*0.991*	*0.997*		0.989	0.968	0.930	*1.000*	*0.990*
Gusev (CH_3OH)	0.985	0.985	0.987	0.989		0.983	0.965	*0.990*	*1.000*
Minakuchi (H_2O)	0.958	0.971	0.957	0.968	0.983		0.989	0.970	0.983
Minakuchi (CH_3OH)	0.918	0.939	0.919	0.930	0.965	0.989		0.933	0.965
Skudas (H_2O)	*0.998*	*0.992*	*0.996*	*1.000*	*0.990*	0.970	0.933		*0.991*
Skudas (CH_3OH)	0.986	0.987	0.986	*0.990*	*1.000*	0.983	0.965	*0.991*	

Values given in italic represent good correlation.

V

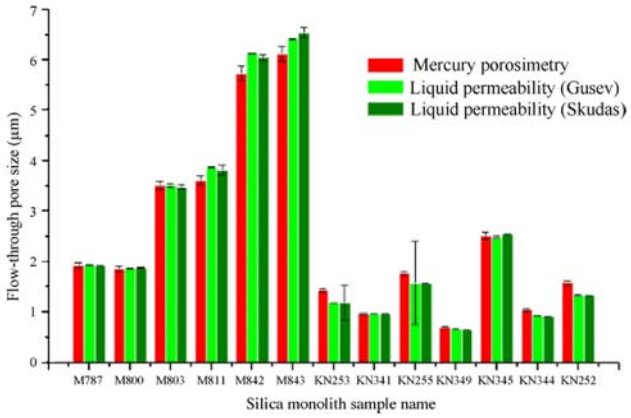

Fig. 8. Average flow-through pore size values and standard deviation of silica monoliths obtained by mercury porosimetry, liquid permeability method according to Gusev [52], and liquid permeability method according to Skudas [54].

Table 6
Characteristic values of the monolithic silica research columns.

Monolithic silica research sample	Plate count (N/m)	Skeleton diameter (μm)	Surface/volume of the skeletons (Mm^{-1})	Total porosity	Mesopore size (nm)	Macrorosity
KN 341	128,100	0.6221	4.819	0.787	21.98	0.617
KN 253	121,300	0.7221	3.922	0.821	19.59	0.671
KN 349	96,500	0.4490	7.018	0.740	21.84	0.558
KN 255	92,900	0.9198	3.200	0.787	16.78	0.643
KN 252	92,800	0.8196	3.604	0.841	12.45	0.652
KN 344	92,700	0.7205	3.883	0.715	18.72	0.539
KN 345	44,200	1.6055	1.951	0.708	15.34	0.578
787	25,400	1.7521	1.638	0.860	11.01	0.500
800	22,600	1.5602	1.946	0.919	23.32	0.478
811	19,300	3.1558	1.247	0.900	25.04	0.478
803	11,400	2.4467	0.999	0.849	11.53	0.607
843	7200	4.5063	0.673	0.878	36.51	0.536
842	4900	4.7099	0.772	0.819	11.52	0.524

The plate count values are calculated at the maximum efficiency for lysozime as solute.

(that explicit columns 842 and 843) have higher permeability since the flow rate is proportional to the pore diameter[4]. Therefore the estimated flow-through pore diameter values are larger as well. It could be concluded that obviously not all of the surface area is accessed via mobile phase at the same ratio.

The results clearly reveal that the permeability method could be used for the flow-through characterization, allowing one to obtain flow-through pore values and skeleton diameters. The calculated s/v ratios also showed a good correlation between the mercury intrusion data and data from the permeability method.

3.5. The application of the characteristic data obtained and their impact on column performance

The comprehensive characterization of the flow-through pores of selected monolithic silicas and previous results of the mesopore characterization [47,54] as well as the results of modelling of the column efficiency enabled us to compare the experimental and predicted results (Fig. 9). For the predicted results Eq. (2) was used, where the axial dispersion coefficient and the dimension of the skeletons was obtained as an average value from mercury intrusion, image analysis and permeability of a liquid. The graphic data indicate a fairly good agreement between the theoretical and the experimental data. This means in addition that our assumptions on the impact of the s/v ratio of the skeletons and external porosity influence on the column efficiency were correct. This enables to assess the conditions for the maximum plate height values for the investigated monolithic silica research columns.

In monoliths, the axial dispersion is significant since it increases with increasing flow-through pore size and their porosity and this will lead to a significant decrease of the column efficiency. The diameter of the monolithic skeleton strongly depends on the

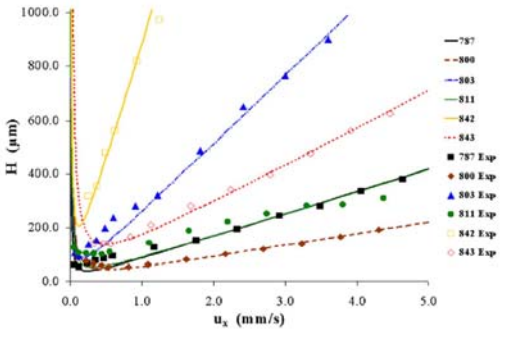

Fig. 9. Theoretical and experimental HETP vs. linear velocity curves for the monolithic silica columns for lysozime as solute, where lines represent the modeling results and points the experimental results.

flow-through pore size (it increases with increasing flow-through pore size) and this leads to a diminution of the column efficiency. Thus, for the optimum column efficiency one needs to reduce the flow-through pore porosity and flow-through pore size and increase the mesoporosity to maintain the overall porosity. The results of maximum column efficiency values (see Table 6) suggest that there is a limit of optimum performance of tested monolithic silica research columns. The best performance was obtained with a column that did not feature the smallest skeleton diameter values or highest s/v ratios. This finding corresponds to the earlier conclusions by Billen et al. [6] on a limit of column performance. In our case, this limit is between 0.45 and 0.62 μm of the skeleton size. The same corresponds to the s/v ratio from 4.819 to 7.018 Mm^{-1}. Regarding the dependency of the column efficiency on the ε_b values and on the total porosity of monolithic silicas, no clear tendency could be established through our studies.

According to Billen et al. [6], whose data were based on the computed simulations, the domain size-induced heterogeneity was found as the column performance limitation of small-domain monolithic columns. They proposed, that due to the heterogeneity of the skeletons and flow-through pores it appears nearly impossible to prepare small-domain monolithic silica columns that have the same column performance as compared to a column packed with sub-2 μm silica particles.

Our results confirm such conclusion and give experimental evidence that if the s/v ratios of the skeletons are maximized by decreasing the average skeleton sizes of the monolithic columns, the efficiency of such supports also reach a limit. However, this assumption remains questionable because we did not take into account the influence of the mesopore diameter, the porosity of the mesopores and the mesopore size distribution on the column efficiency of the selected analyte lysozyme.

4. Summary and conclusion

Our study demonstrated that mercury porosimetry, imaging and image analysis as well as permeability of a liquid are reliable techniques to obtain the characteristic parameters of the flow-through pores of silica monoliths. The results obtained from modelling suggested that the surface to volume ratio of the skeletons and external porosity should be decisive for the column efficiency and the latter should be totally independent from the flow-through pore diameter. We assessed the flow-through pore characteristics by direct and indirect approaches and derived theoretical efficiency curves. Our study showed that the skeleton diameter being a significant parameter affecting the column efficiency. Next to the skeleton diameter, the total porosity and its distribution of the flow-through pores and mesopores has a substantial effect on the plate count, especially as the extent of adsorption increases. The column efficiency is increasing with decreasing skeleton diameter, decreasing external porosity and increasing total porosity. Though this tendency has a limit due to heterogeneity of the studied monolithic samples, we found that the maximum efficiency of the studied monolithic research columns could be reached at a skeleton diameter of ~0.5 μm. Furthermore when maximizing the column efficiency, more homogeneous monoliths should be prepared.

In case that the aim will be directed towards the maximizing of the column through-put at the given back-pressure, then the pore size distribution of the flow-through pores should be wide (not uniform) and weighted to larger pores.

Even though, it might be true, that the efficiency values of sub-2 μm particle columns are hard to reach with the currently studied monolithic silica research columns, having rather high level of heterogeneity, the sub-2 μm packed columns will never be able to compete with monolithic columns in respect to permeability, low-flow resistance and robustness, that weights the overall separation performance to the side of monoliths.

Nomenclature

A	the cross-sectional area of the conduit normal to the direction of flow
c	a constant accounting for secondary effects
D	the effective diffusion coefficient of the analyte in the confined mesoporous space of the skeleton
D_c	the cylinder diameter
D_f	the mean flow-through pore diameter
D_L	the axial dispersion coefficient of the solute in the mobile phase
D_m	the molecular diameter of the analyte
D_p	the equivalent spherical diameter of the particle
D_{perm}	the equivalent particle diameter for monoliths
D_s	the skeleton diameter per se or directly measured silica skeleton diameter
D_0	idealized diameter of the monolithic skeleton element
f_p	the friction factor for the packed bed
H	the height equivalent of a theoretical plate (HETP), or plate height
HDC	hydrodynamic chromatography
HPLC	high-performance liquid chromatography
k_f	the film mass transfer coefficient of the analyte
k_{SEC}	the accessible fraction of the intra-particle pores
K	constant
K_b	the volume partition coefficient of the finite sized molecule in the flow-through porous void space of the monolithic column
K_{eq}	the equilibrium adsorption constant of the linear adsorption isotherm
K_p	the volume partition coefficient of the finite sized molecule in the mesoporous void space of the skeleton
L	the length of the column
L_{app}	approximated length of the pore
L_p	the length of the cylindrical pore
ΔP	the column flow resistance or back-pressure
$P_{d,mes}$	the diameter of mesopores
ΔP_s	a pressure difference across the element of surface area
PEEK	polyether ether ketone
Q	the volumetric flow rate of the fluid
r	the molecular radius of the test sample
r_{pore}	the radius of the pore
R	the gas constant
R_g	the radius of gyration of the polymer
R_p	the radius of the cylindrical pore
Re_p	the Reynolds number
s/v	the surface-to-volume ratio of the skeletons of the monolith
SEC	size-exclusion chromatography
t_m	migration time of infinite small marker
t_p	a migration time of the polymer
T	the absolute temperature
u	the linear flow velocity of the eluent
V_s	the superficial viscosity
V_x	the velocity profile in a cylindrical pore
3D	three-dimensional

Greek letters

γ	the interfacial (or surface) tension of mercury
ε	the porosity of porous support

ε_b	the void fraction of the flow-through porous void space in the column
ε_p	the void fraction of the monolithic skeleton
η	the viscosity coefficient
θ	the contact angle between mercury and the solid (pore wall)
λ	aspect ratio
μ	the mobile phase dynamic viscosity
μm	micrometer
v	the solvent linear velocity
v_i	the intra-particle (pore) volume
v_0	inter-particle solvent volume
ρ	the mobile phase density
τ	relative migration rate in HDC-SEC
τ_f	the tortuosity of the flow-through pores
τ_{HDC}	the relative migration rate in HDC
φ	the Flory–Fox parameter

References

[1] M.W. Dong, Modern HPLC for Practicing Scientists, Wiley, Hoboken, NJ, 2006.
[2] M.R. Schure, R.S. Maier, presented at the 30th International Symposium on High Performance Chromatography and Related Techniques, San Francisco, CA, June 17–22, 2006, paper L-0502.
[3] K.K. Unger, R. Skudas, M.M. Schulte, J. Chromatogr. A 1184 (2008) 393.
[4] G. Guiochon, J. Chromatogr. A 1168 (2007) 101.
[5] P. Gzil, J.D. Smet, G. Desmet, J. Sep. Sci. 29 (2006) 1675.
[6] J. Billen, P. Gzil, G. Desmet, Anal. Chem. 78 (2006) 6191.
[7] A.I. Liapis, J.J. Meyers, O.K. Crosser, J. Chromatogr. A 865 (1999) 13.
[8] H.L. Ritter, L.C. Drake, Ind. Eng. Chem. Anal. Chem. 17 (1945) 782.
[9] L.C. Drake, H.L. Ritter, Ind. Eng. Chem. Anal. Ed. 17 (1945) 787.
[10] S. Lowell, J. Shields, M.A. Thomas, M. Thommes, Characterization of Porous Solids and Powders: Surface Area, Pore Size and Density, Springer, Dordrecht, 2004.
[11] C.A. León y León, Adv. Colloid Interf. Sci. 76 (1998) 341.
[12] M. Thommes, R. Skudas, K.K. Unger, D. Lubda, J. Chromatogr. A 1191 (2008) 57.
[13] D. Lubda, W. Lindner, M. Quaglia, C.F. von Hohenesche, K.K. Unger, J. Chromatogr. A 1083 (2005) 14.
[14] H. Minakuchi, K. Nakanischi, N. Soga, N. Ishizuka, N. Tanaka, J. Chromatogr. A 797 (1998) 121.
[15] N. Vervoort, H. Saito, K. Nakanischi, G. Desmet, Anal. Chem. 77 (2005) 3986.
[16] Y.H. Yang, M.J. Buckley, T.P. Speed, Brief Bioinform. 4 (2001) 341.
[17] A.E. Carpenter, T.R. Jones, M.R. Lamprecht, C. Clarke, I.H. Kang, O. Friman, D.A. Guertin, J.H. Chang, R.A. Lindquist, J. Moffat, P. Golland, D.M. Sabatini, Genome Biol. 7 (2006) R100.1.
[18] M.D. Montminy, A.R. Tannenbaum, C.W. Macosko, J. Colloid Interf. Sci. 280 (2004) 202.
[19] C.A. Baldwin, A.J. Sederman, M.D. Mantle, P. Alexander, L.F. Gladden, J. Colloid Interf. Sci. 181 (1996) 79.
[20] H. Jinnai, K. Nakanishi, Y. Nishikawa, J. Yamanaka, T. Hashimoto, Langmuir 17 (2001) 619.
[21] J. Courtois, M. Szumski, F. Georgsson, K. Irgum, Anal. Chem. 79 (2007) 335.
[22] P. Gzil, N. Vervoort, G.V. Baron, G. Desmet, Anal. Chem. 76 (2004) 6707.
[23] N. Vervoort, P. Gzil, G.V. Baron, G. Desmet, Anal. Chem. 75 (2003) 843.
[24] E.W. Washburn, Phys. Rev. 17 (1921) 273.
[25] P.C. Carman, Soil Sci. 52 (2) (1941) 1.
[26] P.C. Carman, Flow of Gases through Porous Media, Butterworths, London, 1956 (Chapter 1).
[27] F.C. Leiweber, D. Lubda, K. Cabrera, U. Tallarek, Anal. Chem. 74 (2002) 2470.
[28] F.C. Leinweber, U. Tallarek, J. Chromatogr. A 1006 (2003) 207.
[29] K. Nakanishi, N. Soga, J. Am. Ceram. Soc. 74 (1991) 2518.
[30] K. Nakanishi, N. Soga, J. Non-Cryst. Sol. 139 (1992) 1.
[31] K. Nakanishi, N. Soga, J. Non-Cryst. Sol. 139 (1992) 14.
[32] H. Minakuchi, K. Nakanishi, N. Soga, N. Ishizuka, N. Tanaka, Anal. Chem. 68 (1996) 3498.
[33] K. Cabrera, G. Wieland, D. Lubda, K. Nakanishi, N. Soga, H. Minakuchi, K.K. Unger, Trends Anal. Chem. 17 (1998) 133.
[34] F. Gritti, W. Piatkowski, G. Guiochon, J. Chromatogr. A 978 (2002) 81.
[35] F.C. Leinweber, D.G. Schmid, D. Lubda, K.-H. Weismüller, G. Jung, U. Tallarek, Rapid Commun. Mass Spectrom. 17 (2003) 1180.
[36] D. Lubda, K. Cabrera, N. Nakanishi, W. Lindner, Anal. Bioanal. Chem. 377 (2003) 892.
[37] D. Lubda, W. Lindner, J. Chromatogr. A 1036 (2004) 135.
[38] B. Chankvetadze, T. Ikai, C. Yamamoto, Y. Okamoto, J. Chromatogr. A 1042 (2004) 55.
[39] N. Tanaka, H. Nagayama, H. Kobayashi, T. Ikegami, K. Hosoya, N. Ichizuka, H. Minakuchi, K. Nakanishi, K. Cabrera, D. Lubda, J. High Resolut. Chromatogr. 23 (2000) 111.
[40] M. Motokawa, H. Kobayashi, N. Ishizuka, H. Minakuchi, K. Nakanishi, H. Jinnai, K. Hosoya, T. Ikegami, N. Tanaka, J. Chromatogr. A 961 (2002) 53.
[41] N. Tanaka, H. Kobayashi, N. Ishizuka, H. Minakuchi, K. Nakanishi, K. Hosoya, T. Ikegami, J. Chromatogr. A 965 (2002) 35.
[42] N. Tanaka, H. Kobayashi, Anal. Bioanal. Chem. 376 (2003) 298.
[43] H. Minakuchi, N. Ishizuka, K. Nakanishi, N. Soga, N. Tanaka, J. Chromatogr. A 828 (1998) 83.
[44] H. Giesche, in: F. Schüth, K.S.W. Sing, J. Weitkamp (Eds.), Handbook of Porous Solids, Wiley-VCH, Toronto, 2002, pp. 309–351.
[45] ISO 15901-1:2005 Pore Size Distribution and Porosity of Solid Materials by Mercury Porosimetry and Gas Adsorption. Part I. Mercury Porosimetry, International Organization of Standardization (ISO), Geneva, December 7, 2005.
[46] J.C. Groena, L.A.A. Peffer, J. Perez-Raminez, in: F. Rodriguez-Reinoso, B. McEnaney, J. Rouquerol, K. Unger (Eds.), Characterization of Porous Solids VI, Proceedings of the 6th International Symposium on the Characterization of Porous Solids (COPS-VI), Alicante, Spain, May 8–11, 2002 (Studies in Surface Science and Catalysis, vol. 144), Elsevier, Amsterdam, 2002, p. 91.
[47] B.A. Grimes, R. Skudas, K.K. Unger, D. Lubda, J. Chromatogr. A 1144 (2007) 14.
[48] S. Ergun, Chem. Eng. Prog. 48 (1952) 89.
[49] A.M. Siouffi, J. Chromatogr. A 1126 (2006) 86.
[50] S.P. Rigby, R.S. Fletcher, S.N. Riley, J. Colloid Interf. Sci. 240 (2001) 190.
[51] H. Jinnai, K. Nakanischi, Y. Nishikawa, J. Yamanaka, T. Hashimoto, Langmuir 17 (2001) 619.
[52] I. Gusev, J. Chromatogr. A 855 (1999) 273.
[53] R. Hahn, Anal. Chem. 72 (2000) 4853.
[54] R. Skudas, B.A. Grimes, O. Kornysova, D. Lubda, K.K. Unger, presented at the 30th International Symposium on High Performance Chromatography and Related Techniques, Stockholm, Sweden, June 25–28, 2005.